

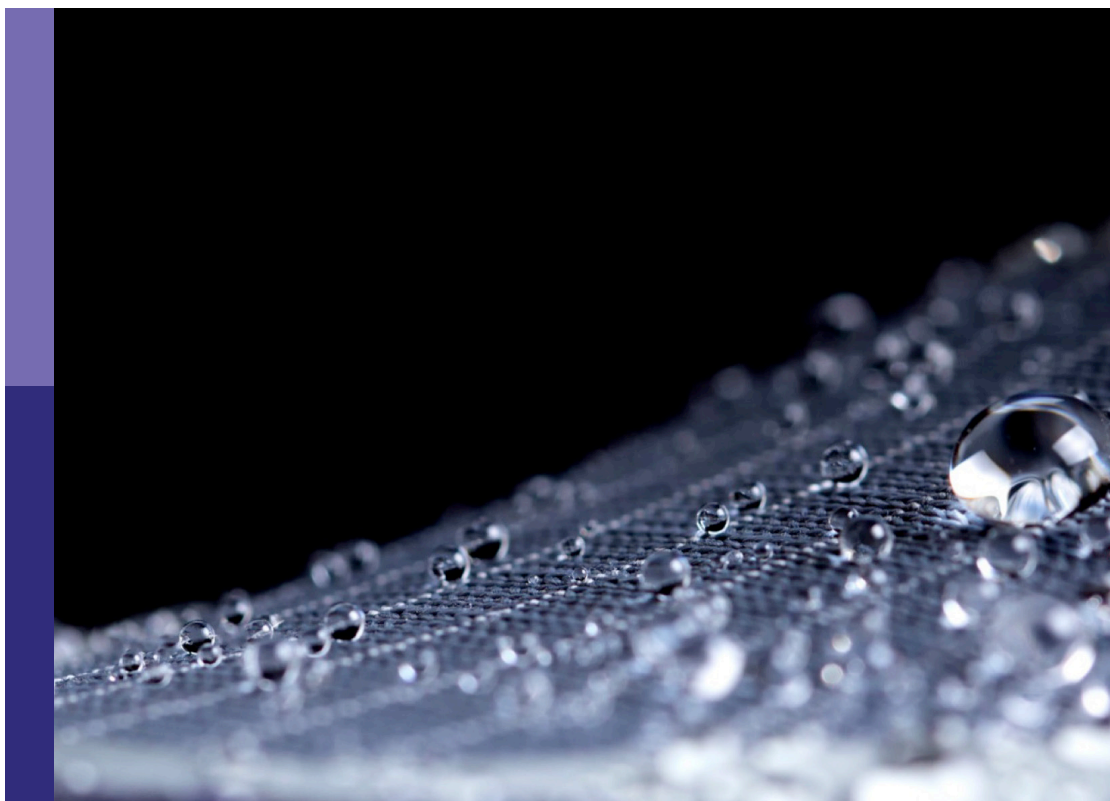
Celebrating 1 year of Frontiers in membrane science and technology

Edited by

Michael D. Guiver, Yunxia Hu and
Nalan Kabay

Published in

Frontiers in Membrane Science and Technology



FRONTIERS EBOOK COPYRIGHT STATEMENT

The copyright in the text of individual articles in this ebook is the property of their respective authors or their respective institutions or funders. The copyright in graphics and images within each article may be subject to copyright of other parties. In both cases this is subject to a license granted to Frontiers.

The compilation of articles constituting this ebook is the property of Frontiers.

Each article within this ebook, and the ebook itself, are published under the most recent version of the Creative Commons CC-BY licence. The version current at the date of publication of this ebook is CC-BY 4.0. If the CC-BY licence is updated, the licence granted by Frontiers is automatically updated to the new version.

When exercising any right under the CC-BY licence, Frontiers must be attributed as the original publisher of the article or ebook, as applicable.

Authors have the responsibility of ensuring that any graphics or other materials which are the property of others may be included in the CC-BY licence, but this should be checked before relying on the CC-BY licence to reproduce those materials. Any copyright notices relating to those materials must be complied with.

Copyright and source acknowledgement notices may not be removed and must be displayed in any copy, derivative work or partial copy which includes the elements in question.

All copyright, and all rights therein, are protected by national and international copyright laws. The above represents a summary only. For further information please read Frontiers' Conditions for Website Use and Copyright Statement, and the applicable CC-BY licence.

ISSN 1664-8714
ISBN 978-2-8325-6244-4
DOI 10.3389/978-2-8325-6244-4

About Frontiers

Frontiers is more than just an open access publisher of scholarly articles: it is a pioneering approach to the world of academia, radically improving the way scholarly research is managed. The grand vision of Frontiers is a world where all people have an equal opportunity to seek, share and generate knowledge. Frontiers provides immediate and permanent online open access to all its publications, but this alone is not enough to realize our grand goals.

Frontiers journal series

The Frontiers journal series is a multi-tier and interdisciplinary set of open-access, online journals, promising a paradigm shift from the current review, selection and dissemination processes in academic publishing. All Frontiers journals are driven by researchers for researchers; therefore, they constitute a service to the scholarly community. At the same time, the *Frontiers journal series* operates on a revolutionary invention, the tiered publishing system, initially addressing specific communities of scholars, and gradually climbing up to broader public understanding, thus serving the interests of the lay society, too.

Dedication to quality

Each Frontiers article is a landmark of the highest quality, thanks to genuinely collaborative interactions between authors and review editors, who include some of the world's best academicians. Research must be certified by peers before entering a stream of knowledge that may eventually reach the public - and shape society; therefore, Frontiers only applies the most rigorous and unbiased reviews. Frontiers revolutionizes research publishing by freely delivering the most outstanding research, evaluated with no bias from both the academic and social point of view. By applying the most advanced information technologies, Frontiers is catapulting scholarly publishing into a new generation.

What are Frontiers Research Topics?

Frontiers Research Topics are very popular trademarks of the *Frontiers journals series*: they are collections of at least ten articles, all centered on a particular subject. With their unique mix of varied contributions from Original Research to Review Articles, Frontiers Research Topics unify the most influential researchers, the latest key findings and historical advances in a hot research area.

Find out more on how to host your own Frontiers Research Topic or contribute to one as an author by contacting the Frontiers editorial office: frontiersin.org/about/contact

Celebrating 1 year of Frontiers in membrane science and technology

Topic editors

Michael D. Guiver — Tianjin University, China

Yunxia Hu — Tianjin Polytechnic University, China

Nalan Kabay — Ege University, Türkiye

Citation

Guiver, M. D., Hu, Y., Kabay, N., eds. (2025). *Celebrating 1 year of Frontiers in membrane science and technology*. Lausanne: Frontiers Media SA.

doi: 10.3389/978-2-8325-6244-4

Table of contents

- 04 **Editorial: Celebrating 1 year of Frontiers in membrane science and technology**
Michael D. Guiver and Nalan Kabay
- 07 **Evaluation of fouling and chemical cleaning of reverse osmosis membrane after treatment of geothermal water**
Aseel Zaid, Yakubu Abdullahi Jarma, Islam Rashad Ahmed Senan, Aslı Karaoğlu, Aydın Cihanoğlu, Alper Baba and Nalan Kabay
- 15 **Microstructural orientation of anion exchange membrane through mechanical stretching for improved ion transport**
Chenyang Zheng, Lianqin Wang, Shijie Zhang, Xin Liu, Junfeng Zhang, Yan Yin, Kui Jiao, Qing Du, Xianguo Li and Michael D. Guiver
- 26 **Modeling pore wetting in direct contact membrane distillation—effect of interfacial capillary pressure**
S. N. A. Ahmad, Takeshi Matsuura, Juhana Jaafar, L. Y. Jiang, A. F. Ismail, M. H. D. Othman and Mukhlis A. Rahman
- 40 ***In-situ* ionized construction of PVDF/sodium polyacrylate-grafted-PVDF blend ultrafiltration membrane with stable anti-oil-fouling ability for efficient oil-in-water emulsion separation**
Shoujian Gao, Pingping Liu and Jian Jin
- 51 **A perspective on cellulose dissolution with deep eutectic solvents**
Sacide Alsoy Altinkaya
- 61 **Advanced and sustainable manufacturing methods of polymer-based membranes for gas separation: a review**
Sharifah H. Alkandari and Bernardo Castro-Dominguez
- 87 **Surface-modified PVDF membranes for separation of dye by forward osmosis**
Marta Muratow, Fatma Yalcinkaya, Marek Bryjak and Anna Siekierka
- 96 **Opportunities for membrane technology in controlled environment agriculture**
Parisa Safari, Hamed Rahnema and Glenn Lipscomb
- 103 **Investigation of multi-stage forward osmosis membrane process for concentrating high-osmotic acrylamide solution**
Shuang Hao, Zhaoqian Zhang, Xin Zhao, Xiaochan An and Yunxia Hu



OPEN ACCESS

EDITED AND REVIEWED BY
Hale Özgün,
Istanbul Technical University, Türkiye

*CORRESPONDENCE

Michael D. Guiver,
✉ michael.guiver@outlook.com
Nalan Kabay,
✉ nalan.kabay@ege.edu.tr

RECEIVED 11 March 2025

ACCEPTED 21 March 2025

PUBLISHED 04 April 2025

CITATION

Guiver MD and Kabay N (2025) Editorial:
Celebrating 1 year of Frontiers in membrane
science and technology.
Front. Membr. Sci. Technol. 4:1591950.
doi: 10.3389/frmst.2025.1591950

COPYRIGHT

© 2025 Guiver and Kabay. This is an open-
access article distributed under the terms of the
Creative Commons Attribution License (CC BY).
The use, distribution or reproduction in other
forums is permitted, provided the original
author(s) and the copyright owner(s) are
credited and that the original publication in this
journal is cited, in accordance with accepted
academic practice. No use, distribution or
reproduction is permitted which does not
comply with these terms.

Editorial: Celebrating 1 year of Frontiers in membrane science and technology

Michael D. Guiver^{1*} and Nalan Kabay^{2*}

¹State Key Laboratory of Engines, School of Mechanical Engineering, Tianjin University, Tianjin, China,

²Ege University, Chemical Engineering Department, Faculty of Engineering, Izmir, Türkiye

KEYWORDS

reverse osmosis (RO), anion exchange membrane (AEM), direct contact membrane distillation (DCMD), oily wastewater, deep eutectic green solvents, membrane gas separation, forward osmosis (FO), membrane fouling and cleaning

Editorial on the Research Topic

Celebrating 1 year of Frontiers in membrane science and technology

Frontiers in Membrane Science and Technology was launched in March 2022, and this Research Topic was established in March 2023 to celebrate the 1-year anniversary. The goal of the Journal is to be an inclusive open-access publishing venue for high quality research, perspectives and reviews. This Research Topic reflects on the Journal in the inaugural year by showcasing cutting-edge research, novel developments, new insights and on the outlook of the future directions of membrane science and technology. This Research Topic has nine papers in different disciplines.

Paper 1 “Evaluation of fouling and chemical cleaning of reverse osmosis membrane after treatment of geothermal water” by Zaid et al. explores membrane fouling and mineral scaling, which are major problems for desalination processes using reverse osmosis (RO) membranes. Membrane characteristics, water quality, operational conditions, biofouling, organic fouling, and inorganic scaling were considered to limit the overall performance of RO systems by increasing energy cost, decreasing membrane lifespan, and increasing chemical cleaning frequency. This paper focused on periodic chemical cleaning of RO membrane used for the cycle treatment of geothermal water having high mineral scaling characteristics during a mini-pilot-scale field test. Water permeability tests were applied before and after chemical cleaning to monitor flux decline after each cycle and flux recovery after chemical cleaning with citric acid solution. The anti-scalant employed in this study was not found to be effective for the prevention of membrane scaling; instead, pretreatment was needed to remove scalants from geothermal water prior to RO treatment.

Paper 2 “Microstructural orientation of anion exchange membrane through mechanical stretching for improved ion transport” by Zheng et al. demonstrates the fabrication of highly conductive anion exchange membrane (AEMs) driven by the external force of mechanical stretching. Insights into macromolecular orientation at the atomic level were gained by investigating the effect of elongation at different water contents on polymer structures and OH⁻ conductivities, using molecular dynamics simulation combined with experimental studies. Macromolecular chain orientation at the atomic level results in continuous and oriented ion-conduction pathways for hydroxide transport, providing substantial increases in hydroxide conductivity.

Paper 3 “Modeling pore wetting in direct contact membrane distillation—effect of interfacial capillary pressure” by [Ahmad et al.](#) presents a model developed for computing direct contact membrane distillation (DCMD) performance, by taking into consideration capillary pressure effects at the liquid–gas interface within membrane pores. The simulation model investigates the effects of pore radius, feed/permeate temperature, pressure, and contact angle on the distance of liquid intrusion into the pore, the weight flow rate in a single pore, and the temperature at the liquid–gas interface. The model predicts increases in the weight flow rate with increases in the pore radius, feed temperature and contact angle, but decreases with an increase in permeate temperature. At constant permeate pressure, the model predicts a decrease in the permeation rate as feed pressure increases. The partial pore wetting is enhanced with increasing feed pressure when the pore size is larger (1 μm) and an opposite trend when the pore size is smaller (0.1 μm), which is a significant finding for DCMD.

Paper 4 “*In-situ* ionized construction of PVDF/sodium polyacrylate-grafted-PVDF blend ultrafiltration membrane with stable anti-oil-fouling ability for efficient oil-in-water emulsion separation” by [Gao et al.](#) reports the fabrication of an ultrafiltration membrane based on sodium polyacrylate (PAAS) blended polyvinylidene fluoride (PVDF) with hydrophilicity. Its characteristics are underwater low-oil-adhesive superoleophobicity and outstanding anti-oil-fouling ability even for viscous crude oil. The emphasis is on a practical route for fabricating stable anti-oil-fouling membranes for the challenging separation of emulsified oily water. The blend membrane exhibited long-term stability because of the strong interaction between the PAAS-g-PVDF additive and the PVDF matrix, suggesting good potential for real emulsified oily wastewater in large-scale operation.

Review 5 “A perspective on cellulose dissolution with deep eutectic solvents” by [Altinkaya](#) explores the use of deep eutectic solvents (DES) as green alternatives to dissolve cellulose, which is a sustainable and natural membrane material. Few conventional solvents are capable of dissolving cellulose because of its strong intermolecular and intramolecular hydrogen bonds and semicrystalline nature. Low cost and low toxicity DESs, containing both hydrogen bond donor and acceptor groups, are promising as alternatives to less environmentally-friendly conventional solvents, allowing the wider use of cellulose membranes. Key findings from experimental and theoretical studies are summarized.

Review 6 “Advanced and sustainable manufacturing methods of polymer-based membranes for gas separation: a review” by [Alkandari et al.](#) summarizes the wide array of membrane manufacturing techniques, and notes the shift towards more sustainable practices, such as more environmentally-friendly processes and membrane casting solvents, which is also a focus of the preceding review. The authors acknowledge the increasing proportion of scientific literature on sustainable processes relative to advanced and other membranes, and examine how conventional fabrication techniques can be more sustainable, and discuss emerging processes like 3D-printed membrane, as well as end-of-life recycling and re-use.

Paper 7 “Surface-modified PVDF membranes for separation of dye by forward osmosis” by [Muratow et al.](#) addresses the recovery of dyes from wastewater for reuse and to prevent environmental contamination by the Forward Osmosis (FO) membrane process. FO requires less operating pressure and exhibits less fouling than

conventional RO, thereby being potentially less energy-intensive. PVDF nanofiber mats were modified by deposition of polyamide layers, synthesized by reaction between *m*-phenylenediamine, piperazine, and trimesoylchloride. FO performance was dependant on the type of aromatic amine and the reaction time. Over 90% dye rejection of bromocresol green dye was achieved, with the best membrane having 3.3 LMH water flux.

Review 8 “Opportunities for membrane technology in controlled environment agriculture” by [Safari et al.](#) discusses the wide array of membrane processes that can benefit controlled environment agriculture, which is becoming increasingly important to reduce energy expenditure and enhance agriculture sustainability and local-grown produce in the face of stressed food supply chains. Energy-efficient membrane processes such as RO, nanofiltration and electrodialysis can be harnessed to improve supply water, as well as recover and treat wastewater streams, by recovering water for reuse and removal and recovery of contaminants such as nitrates. Membranes also have a role in air management, such as controlling humidity, thermal management and carbon dioxide control.

Paper 9 “Investigation of multi-stage forward osmosis membrane process for concentrating high-osmotic acrylamide solution” by [Hao et al.](#) reports the development of a multi-stage FO process to concentrate acrylamide solution. For this, a thin-film composite polyamide membrane was fabricated and used for the multi-stage FO process, which was shown to allow concentration of high-osmotic acrylamide solution at room temperature. They concluded that this work provided practical insights into the viability and optimization of multi-stage FO process for concentrating high-osmotic chemicals. The authors emphasized the need for further work on regenerating draw solution to achieve a sustainable scale-up operation, and an integrated FO-MD system could help in energy savings for the production of highly concentrated acrylamide and purified water.

Author contributions

MDG: Writing – original draft, Writing – review and editing.
NK: Writing – original draft, Writing – review and editing.

Funding

The author(s) declare that no financial support was received for the research and/or publication of this article.

Conflict of interest

The authors declare that the research was conducted in the absence of any commercial or financial relationships that could be construed as a potential conflict of interest.

Generative AI statement

The author(s) declare that no Generative AI was used in the creation of this manuscript.

Publisher's note

All claims expressed in this article are solely those of the authors and do not necessarily represent those of their affiliated

organizations, or those of the publisher, the editors and the reviewers. Any product that may be evaluated in this article, or claim that may be made by its manufacturer, is not guaranteed or endorsed by the publisher.



OPEN ACCESS

EDITED BY

Jose Luis Cortina,
Universitat Politècnica de Catalunya, Spain

REVIEWED BY

Amani Al-Othman,
American University of Sharjah, United Arab
Emirates
Yunhui Zhang,
Southwest Jiaotong University, China

*CORRESPONDENCE

Nalan Kabay,
✉ nalan.kabay@ege.edu.tr

†PRESENT ADDRESS

Yakubu Abdullahi Jarma, Department of
Chemical and Biomolecular Engineering,
University of California Los Angeles, Los
Angeles, CA, United States

RECEIVED 28 March 2024

ACCEPTED 02 December 2024

PUBLISHED 08 January 2025

CITATION

Zaid A, Jarma YA, Ahmed Senan IR, Karaoğlu A,
Cihanoğlu A, Baba A and Kabay N (2025)
Evaluation of fouling and chemical cleaning of
reverse osmosis membrane after treatment of
geothermal water.
Front. Membr. Sci. Technol. 3:1408595.
doi: 10.3389/frmst.2024.1408595

COPYRIGHT

© 2025 Zaid, Jarma, Ahmed Senan, Karaoğlu,
Cihanoğlu, Baba and Kabay. This is an open-
access article distributed under the terms of the
[Creative Commons Attribution License \(CC BY\)](#).
The use, distribution or reproduction in other
forums is permitted, provided the original
author(s) and the copyright owner(s) are
credited and that the original publication in this
journal is cited, in accordance with accepted
academic practice. No use, distribution or
reproduction is permitted which does not
comply with these terms.

Evaluation of fouling and chemical cleaning of reverse osmosis membrane after treatment of geothermal water

Aseel Zaid¹, Yakubu Abdullahi Jarma^{1†},
Islam Rashad Ahmed Senan¹, Aslı Karaoğlu^{1,2}, Aydın Cihanoğlu^{1,3},
Alper Baba⁴ and Nalan Kabay^{1*}

¹Department of Chemical Engineering, Ege University, Izmir, Türkiye, ²Department of Environmental Sciences, Graduate School of Natural and Applied Sciences, Ege University, Izmir, Türkiye, ³Department of Refinery and Petrochemical Technology, Aliğa Vocational School, Ege University, Izmir, Türkiye, ⁴Department of International Water Resources, Izmir Institute of Technology, Urla, Türkiye

In this study, high mineral scaling propensity geothermal water was treated using a FilmTech BW30-2540 reverse osmosis (RO) membrane, integrated into a mini-pilot scale membrane test unit installed at a geothermal heating center. The study was conducted in eight cycles by monitoring membrane fouling via membrane flux decline. Firstly, the geothermal water coming from the source at approximately 80°C was taken into holding tanks and allowed to reach approximately room temperature (25°C). Then, the geothermal water that reached this temperature was used in the system. The fouling degree was compared to the initial permeability of the virgin membrane. After each treatment cycle, the membrane's permeability was evaluated both before and after acid cleaning. Permeability testing was conducted using RO permeate as the feed, under pressures ranging from 8 to 30 bar, with 2-bar increments. The geothermal water treatment was performed at a constant pressure of 15 bar, with a water recovery maintained at approximately 50%. Prior to each permeability test, the membrane underwent a 45-min wash with citric acid, followed by a rinse with RO permeate. During the first five cycles, citric acid was used at a concentration of 1000 mg/L, achieving a flux recovery of 86.6% by the fifth cycle. In the subsequent three cycles, the citric acid concentration was increased to 4000 mg/L, resulting in a flux recovery of 63.4% by the eighth cycle. The study concluded that scale formation on the membrane surface intensified as the number of cycles increased.

KEYWORDS

geothermal water, membrane fouling, reverse osmosis (RO) membrane, scaling, chemical cleaning

1 Introduction

Fresh water is essential not only for sustaining life but also for supporting industrial growth. Over the past decade, rapid population growth and accelerated modernization in many developed and developing countries have significantly increased the global demand for clean water (Baten and Stummeyer, 2012; Goh P. S. et al., 2018). Despite covering 70% of the Earth's surface, only 0.3% of the available source water is fresh and readily useable, with approximately 90% of global water resources being saline and unsuitable for consumption

without proper treatment (Schwarz et al., 1990). To mitigate the depletion of clean and potable water resources, it is imperative to develop and enhance groundwater and saline water treatment processes (Leonard, 1999). Among the alternative water sources that can be treated and utilized for daily needs such as irrigation or portable is spent geothermal water (Baten and Stummeyer, 2012). Nonetheless, geothermal water generally contains high concentrations of dissolved salts and sometimes heavy metals at trace concentrations. Soil and ground water contamination are some of the consequences from direct use of geothermal fluids, which are either for beneficial use or when discarded to receiving bodies or via deep well injection (Jarman et al., 2022). In recent years, various methods and technologies have been developed for the treatment of saline source water, with reverse osmosis (RO) technology emerging and widely adopted across the globe (Baten and Stummeyer, 2012; Goh P. S. et al., 2018; Schwarz et al., 1990). RO technology is recognized for its reliability in producing high-quality water (Jarman et al., 2022), offering membranes that combine excellent contaminants separation and physicochemical properties with high salt rejection, high flux, and robust chemical and thermal stability (Subramani and Jacangelo, 2015).

Despite all of the benefits that the RO membrane offers for generating high-quality water, research investigations over the past several years have concentrated on the creation and upgrading of RO membranes with high salt removal and permeability (Zirehpour et al., 2017; Zhao et al., 2017; Liu et al., 2016). Nonetheless, management of the residual high salinity concentrate (i.e., “brine”) stream, membrane fouling and mineral scaling are lingering major obstacles to even wider scale adoption of RO desalination (Zhao et al., 2017). Depending on membrane characteristics, source water chemistry, and the operational conditions, biofouling, organic fouling, and inorganic scaling may limit the overall performance of RO systems by i) increasing required separation pressure (energy cost), ii) decreasing membrane lifespan, and iii) increasing chemical cleaning frequency (increase downtime) (Saqib and Aljundi, 2016). Membrane fouling seriously impairs the desalination plants’ ability to continue operating sustainably. Fouling can lead to increased operating strain, and a significant reduction in overall efficiency of RO technology (Jiang et al., 2017; She et al., 2016). As a result, the occurrence of scaling is due to (a) precipitation/crystallization of sparingly soluble salts in the bulk of the solution, followed by subsequent deposition onto the membrane surface, and continued crystal growth; and/or (b) direct heterogeneous nucleation on the membrane surface and subsequent crystal growth. In other words, membrane scaling occurs when the concentrations of the scale precursor ions exceed the solubility limits of the mineral salt (Gilron and Hasson, 1987; Lee et al., 1999).

Calcite, silica, and gypsum are the three most prevalent forms of scale in geothermal brine. The calcium compounds, silica and carbonate are commonly found in geothermal brines (Mitrouli et al., 2026). It is therefore common to find scales of metal silicate and metal sulfide in resources that have a higher temperature. Silicate and sulfide scales are commonly associated with several metals, including zinc, iron, lead, magnesium, antimony, and cadmium (Andritsos and Karabelas, 2024).

A few measures, such as enhancing the active layer, were undertaken to address fouling problems in membrane-based desalination processes (Saqib and Aljundi, 2016). However, up to now, periodic freshwater flushing, the use of antiscalants to retard

mineral nucleation, or periodic chemical cleaning of the membranes have been some of the methods widely employed to mitigate mineral scaling (Ang et al., 2011). It is noted that insufficient or postponed chemical cleaning can reduce the lifespan of the module and eventually affect the cost of the product water due to higher replacement costs while negatively affecting energy costs due to elevated transmembrane pressure (TMP). The standard methods for evaluating membrane productivity are the rate of flux drop over time and the final product water quality (Klupfel and Frimmel, 2010). Understanding membrane behavior is essential for water productivity. It is therefore of paramount importance to evaluate water permeability of a specific membrane and compared with the subsequent permeability decline for proper desalination plant design.

While antiscalants are a well-established tool in RO system pretreatment, a more systematic and comprehensive understanding of their applications and mechanisms could greatly enhance their effectiveness and sustainability (Goh P. et al., 2018). Membrane fouling is generally divided into removable fouling (loosely attached to the membranes) and permanent fouling such as long-term mineral scaling. Physical cleaning methods, such as air sparging, backwashing, flushing, and vibration, use mechanical forces are some of the methods employed to remove removable foulants from membrane surfaces (Goh P. et al., 2018). Permanent fouling can only be eliminated by chemical cleaning, which should only be performed a few times a year to avoid shortening membrane life (Kimura et al., 2004). Chemical cleaning techniques rely on chemical reactions such as chelation, dispersion, hydrolysis, peptization, saponification, and solubilization are some of the approaches employed for permanent fouling removal (Kimura et al., 2004; Fritsch and Moraru, 2008; Lin et al., 2010). However, it is critical to select the appropriate cleaning agent, cleaning frequency, and cleaning procedure based on the source water chemistry and membrane type (Goh P. et al., 2018; Liikanen et al., 2002). One should also note that frequent chemical cleaning of the membranes will lead to deterioration of the active layer of the membrane and will negatively affect product water quality (Liikanen et al., 2002; Chen et al., 2003).

Although membrane manufacturers suggest an approach of membrane cleaning (Ang et al., 2006), it is of paramount importance to optimize the cleaning agent chemical dose as well as the frequency of chemical cleaning based on the mineral scaling of concern and source water chemistry. The current study therefore aimed to evaluate the efficacy of periodic RO membrane chemical cleaning desalting spent geothermal water of high mineral scaling propensity. The feed to the pilot RO system is a slipstream from the Izmir geothermal heating center spent geothermal fluid stream located in Izmir, Türkiye. A chemical cleaning with a citric acid solution was employed to clean the fouled membranes periodically.

2 Material and methods

The membrane used in the various tests was Filmtech BW30-2540 (Filmtech, Dow Chemicals) 2.5" x 40" membrane elements having 2.6 m² active membrane area and 99.5% NaCl rejection (evaluated for feed solution salinity of 2000 mg/L NaCl at 25°C for applied feed pressure of 15.5 bar), and single element recovery was 15% yielding permeate flow rate of 3.2 m³/day). Other operation conditions of the membrane employed in this study are given in

TABLE 1 Properties of RO membrane installed at mini-pilot scale membrane test system (Lenntech, 2024).

Membrane	Producer	pH range	Active Area (m ²)	Maximum pressure (bar)	Maximum temperature (°C)
BW30 RO	Dow Film Tech	2–11	2.6	41	45

TABLE 2 The characteristics of spent geothermal water (Jarman et al., 2022).

Parameter	Value
pH	8.51
SiO ₂ (mg/L)	118
Si (mg/L)	55
HCO ₃ [−] (mg/L)	480
F [−] (mg/L)	7.7
SO ₄ ^{2−} (mg/L)	164
Na ⁺ (mg/L)	411
K ⁺ (mg/L)	32
Mg ²⁺ (mg/L)	7.7
Ca ²⁺ (mg/L)	25
Li ⁺ (mg/L)	1.4
Sr ²⁺ (mg/L)	0.65
B (mg/L)	12
Si (mg/L)	47.5
As ^{3−} (mg/L)	0.17
Fe ³⁺ (mg/L)	0.34
Ba ²⁺ (mg/L)	0.13

Table 1. Table 2 provides a summary of the characteristics of geothermal water. A Hach-Lange HQ14D model multimeter was used to measure conductivity, pH, total dissolved substances (TDS), and salinity throughout each test. Before starting each test, samples were obtained from the feed. Permeate, feed, and concentrate samples were taken at 30, 60, 120, 180, 240, 270, and 300 min during each membrane test. Boron concentrations in the feed, permeate, and concentrate samples were determined by the curcumin method using Jasco SSE-343 V-530 UV/vis model spectrophotometer. SM 2320 B method was used to calculate the HCO₃ concentration during the treatment process.

A mini pilot-scale RO membrane system was installed at the geothermal heating facility in Izmir, Türkiye, as shown in Figure 1. The mini-pilot RO system received its feed from the heating center's reinjection slipstream at approximately 80°C. The feed to the pilot system was first allowed to cool down to approximately room temperature (25°C) in 5 m³ plastic containers. The RO system was equipped with sensors, along with a control system, for monitoring various streams with respect to pressure, flow rate, and temperature. The RO system water pretreatment train, before RO desalting, included the following two pretreatment options: media filtration using a standard silica sand filter, carbon filter, and 20- and 5-micron cartridge filters. The system is also equipped with an antiscalant dosage pump feeding Ropur

(PRI-3000 A) antiscalant at a concentration of 5 mg antiscalant/L-spent geothermal water to be treated, details of the mini-pilot system are given in the literature (Jarman et al., 2021).

2.1 Calculated parameters for membrane performance evaluation

Equation 1 was used to calculate the permeate flux in this study (Jarman et al., 2021)

$$J = \frac{Q_p}{A} \tag{1}$$

where J (L/m²h) and Q_p (L/h) are the permeate flux and permeate flow rate, respectively. A (m²) is the membrane active area.

Water recovery of the process was calculated using Equation 2

$$Recovery\ (\%) = \frac{Q_p}{Q_f} \times 100 \tag{2}$$

Q_p (L/h) and Q_f (L/h) are the flow rates of permeate and feed, respectively.

The membrane rejection in this study was calculated using Equation 3

$$R\ (\%) = \left(1 - \left(\frac{C_p}{C_f} \right) \right) \times 100 \tag{3}$$

where C_p (mg/L) and C_f (mg/L) are the concentration of solutes in the permeate and feed streams, respectively.

2.2 Membrane cycle tests

Firstly, the permeability constant of the virgin RO membrane was initiated by passing deionized water through the membrane before the treatment of geothermal water. Permeability experiments were carried out before and after membrane cleaning twice. During the permeability tests, the pressures applied were 8–32 bar with 2 bar increments. Also, oppositely, permeability tests were carried out by decreasing pressure between 32 and 8 bar with a 2 bar decrease. The average values of both measurements were calculated and used in the graph. The treatment of geothermal water was conducted at a constant pressure of 15 bars during 5 h of operation, at a constant water recovery of 50%. Then the RO membrane was cleaned with citric acid for 45 min followed by rinsing with the RO permeate before commencing the permeability test. The chemical cleaning method, which was applied in this study was noted in the literature. The citric acid concentrations during chemical cleaning were kept constant at 1000 mg/L up to the sixth cycle. After the sixth cycle, the water recovery was found to be low, so the acid concentration was doubled to 2000 mg/L for the seventh cycle. To raise the expectations of the study, the eighth cycle was taken as an additional step and the concentration of the citric acid used was doubled to 4000 mg/L.

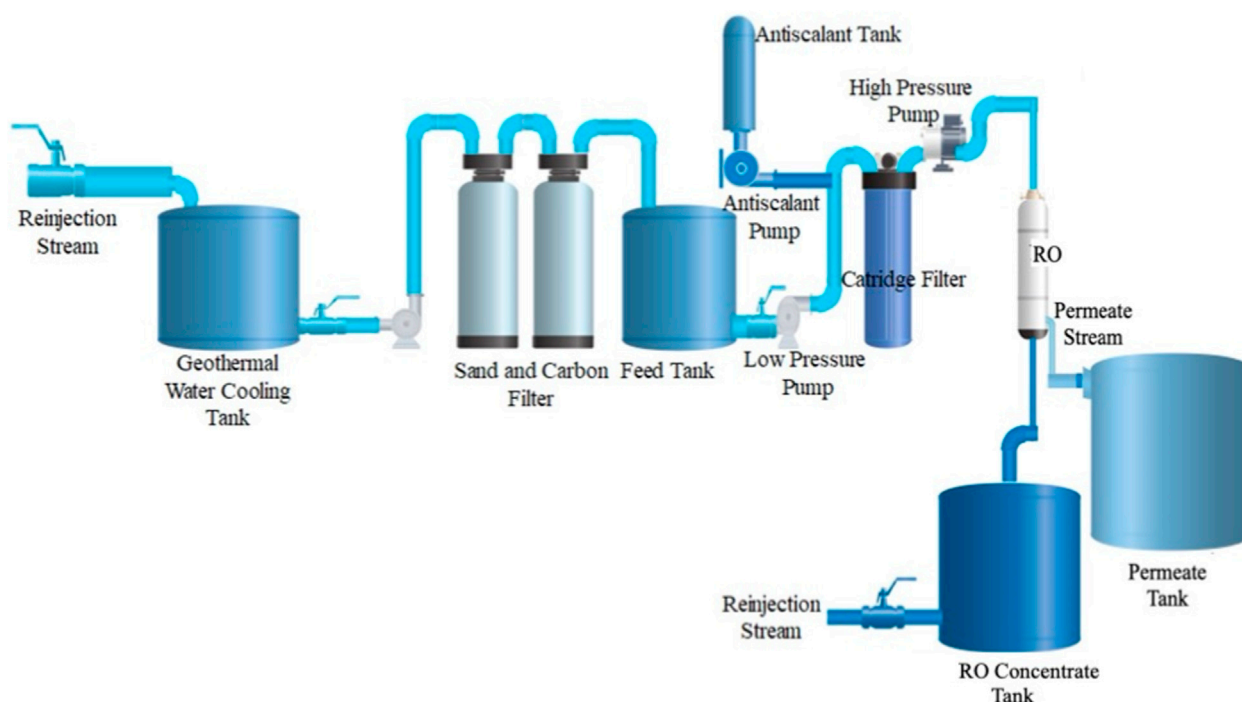


FIGURE 1
Mini pilot RO system employed for chemical cleaning tests (Adapted from Y.A. Jarma, PhD Thesis, Ege University, 2022 and from A. Zaid, MS Thesis, Ege University, 2023 With permission).

3 Results and discussion

3.1 Water permeability tests before chemical cleaning

In this study, BW30 type RO membrane was used for the treatment of geothermal water for membrane fouling tests. As mentioned earlier, the permeability of the fresh or virgin membrane is of paramount importance in determining the fouling degree in membrane separation processes. The permeability of a membrane was determined after long-term membrane operation, followed by acid cleaning to remove inorganic foulants. Also, permeability is a measure of the effectiveness of acid cleaning. Since the water to be treated in this study is spent in geothermal water, organic foulants were not expected in the water. Hence, organic cleaning was not considered during the study. Applied pressure of 8–30 bar with increments of 2 bar while RO permeate was used as deionized water was employed during permeability determination. Also, oppositely, permeability tests were performed by decreasing pressure in a range of 32–8 bar with a 2 bar decrease. The average values of both measurements were calculated and used in Figure 2. The slopes obtained from the linearized flux *versus* pressure plots given in Figure 2 were accepted as permeability as they are very close to the calculated values.

According to the water permeability tests, the highest permeability value was found using a virgin membrane with a permeability value of $4.04 \text{ Lm}^{-2}\text{h}^{-1}\text{bar}^{-1}$ from linearized flux vs. pressure plot as shown in Figure 2. The R^2 value found from the linearized graph was 0.992 which is very close to 1, meaning that our assumption for the linear relation between flux and pressure was

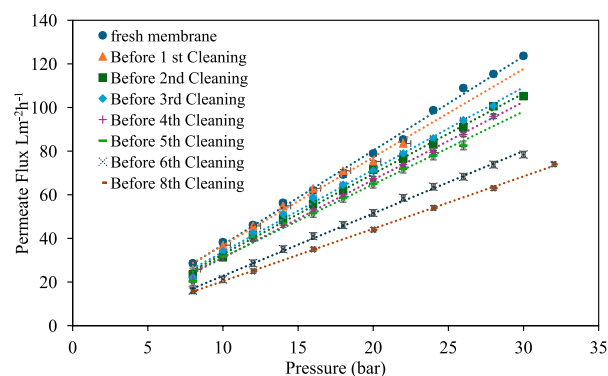


FIGURE 2
Water permeability test results for BW30 before citric acid cleaning by using RO permeate (Adapted from Y.A. Jarma, PhD Thesis, Ege University (2022) (Jarma, 2022) and from A. Zaid, MS thesis, Ege University, 2023 (Zaid, 2023). With permission).

correct. To remove the removable foulants from the surface of the membrane, membrane flushing via the produced permeate was employed before commencing permeability test. Membrane permeability found in our study corresponds to the findings by Ang et al. (2017) where BW30 RO membrane permeability was found as $5 \text{ Lm}^{-2}\text{h}^{-1}\text{bar}^{-1}$ for applied pressure range of 2–10 bar with 2 bar incrementally. The decline, membrane permeability over several cycles can also be due to structural changes in the polymer, such as pore collapse or the formation of extra cross-links over as observed in the literature by Verbeke et al. (2018).

TABLE 3 Water permeability data before and after citric acid cleaning Adapted from Y.A. Jarma, PhD Thesis, Ege University, 2022 (Jarma, 2022) and from A. Zaid, MS Thesis, Ege University, 2023 (Zaid, 2023).

Test	Water permeability ($\text{LM}^{-2}\text{H}^{-1}\text{BAR}^{-1}$)	No. cycle
Fresh membrane	4.036	-
Before 1st cleaning	3.862	
After 1st cleaning	3.789	1 st cycle
Before 2nd cleaning	3.569	2 nd cycle
After 2nd cleaning	3.760	
Before 3rd cleaning	3.495	3 rd cycle
After 3rd cleaning	3.508	
Before 4th cleaning	3.353	4 th cycle
After 4th cleaning	3.353	
Before 5th cleaning	3.203	5 th cycle
After 5th cleaning	3.203	
Before 6th cleaning	2.593	6 th cycle
After 6th cleaning	2.606	
Before 7th cleaning	-	7 th cycle
After 7th cleaning	2.316	
Before 8th cleaning	2.246	8 th cycle
after 8th cleaning	2.475	

3.2 Permeability tests obtained before and after chemical cleaning

Permeability data obtained before and after chemical cleaning are presented in Table 3. It was also found that as the number of cycles increased towards 8, membrane permeability decreased. This is because the membrane became increasingly fouled as it was continuously used for the treatment of geothermal water. Wang et al. (2008) reported that foulants that cannot be removed after physical cleaning (flushing in this case) require chemical cleaning (organic or acid cleaning). It is considered that acid cleaning is the prominent subject when water contains inorganic foulants. Strong acids and high acid concentrations, according to some studies, may cause membrane damage since the structure of RO membranes is pH sensitive (D'Souza and Mawson, 2005). Other researchers utilized a variety of acid solutions (hydrochloric, nitric, phosphoric, sulfamic, and citric acids) to clean the RO membrane chemically, with citric acid yielding the best flux recovery (D'Souza and Mawson, 2005; Madaeni and Samieirad, 2010; Mohammadi et al., 2002). Citric acid is employed in the cleaning procedure with an initial concentration of 1000 mg/L in this investigation, based on information from the literature.

3.3 Water permeability tests for after chemical cleaning

Since organic foulants are not expected in this study due to the nature of the geothermal water used during desalination, acid

cleaning using 1000 mg/L of citric acid was employed to remove inorganic foulants from the membranes. Membranes were cleaned with citric acid for 45 min followed by rinsing with the RO permeate before commencing the permeability experiments. All acid concentrations during chemical cleaning were kept constant at 1000 mg/L except for acid cleaning after the seventh cleaning where acid concentration was doubled to 2000 mg/L. This study used the chemical cleaning (acid cleaning) method provided by literature (Parlar et al., 2019). A study on membrane cleaning (D'Souza and Mawson, 2005) was used to determine the first cleaning durations. It was expected that cleaning efficiency can be increased by cleaning time (contact), or chemical concentration as demonstrated in this study. An initial cleaning approach was devised based on the issues discussed above, and only a few tweaks were made subsequently to improve cleaning performance. Since flux recovery of the membrane was found to be low despite acid cleaning, acid concentration was doubled to 2000 mg/L for the seventh cycle with the expectation of flux recovery to increase. In the eighth cycle, the citric acid concentration was raised four times to test the effect of the acid concentration on the cleaning efficiency.

Figure 3 shows permeate flux vs. pressure plots of the BW30 membrane after applying citric acid cleaning. Permeability from average values as well as from linearized flux vs. pressure values are shown in Table 3. However, no further improvement was observed at the seventh chemical cleaning even after doubling the citric acid concentration. Antiscalant was used to prevent the scaling of inorganic foulants such as Ca^{2+} and Mg^{2+} . However, silica concentration in the feed water was high as shown in Table 2.

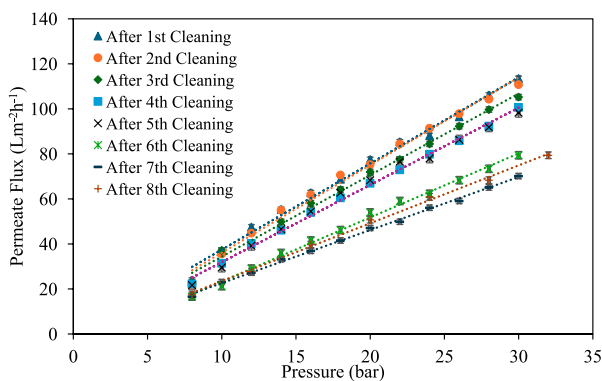


FIGURE 3
Water permeability test results for BW30 after citric acid cleaning by using RO permeate [Adapted from Y.A. Jarma, PhD Thesis, Ege University, 2022 (Jarma, 2022) and from A. Zaid, MS Thesis, Ege University, 2023 Thesis, Ege University, 2023 (Zaid, 2023)].

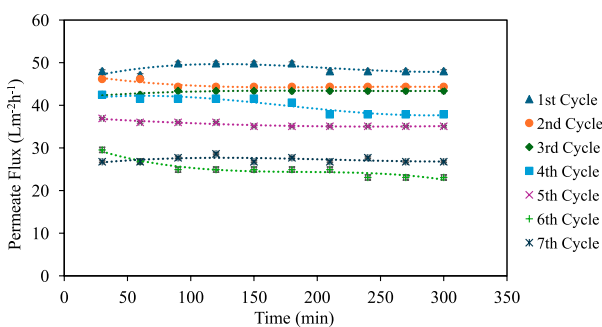


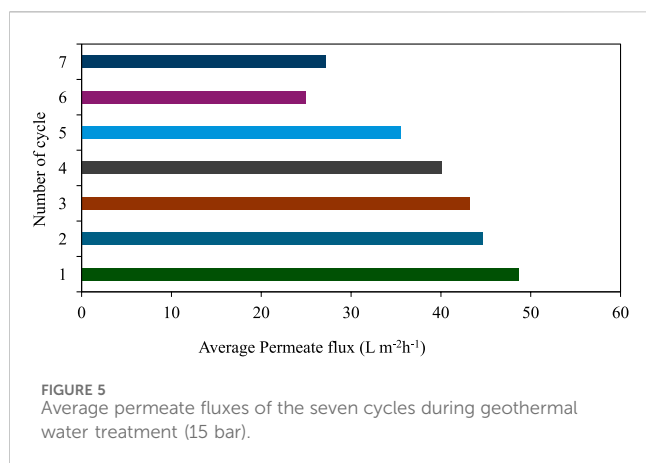
FIGURE 4
Permeate fluxes vs. time plots during treatment of geothermal water [Adapted from Y.A. Jarma, PhD Thesis, Ege University, 2022 (Jarma, 2022) and from A. Zaid, MS Thesis, Ege University, 2023 (Zaid, 2023), With permission].

3.4 Permeate fluxes vs. time plots during treatment of geothermal water

The possible reason why the used membrane permeability continued to decline despite acid cleaning is considered a result of silica scaling. For that reason, flux decline was observed after every cycle as can be seen in Figure 4 as well as in Table 4. The linear regression assumptions of the flow equation (as linear) for the spent geothermal water permeate are true, as evidenced by high R^2 values ($>98\%$). All lines had negative intercepts except one, which was expected because osmotic pressure reduced permeate flux. The flow after the first cleaning was substantially lower than after the second and third cleanings and so on and so forth, which was attributed to the insufficient chemical cleaning of silica. Therefore, the used antiscalant was considered not to be effective towards silica. Silica in natural waters can be found in dissolved, colloidal, or particulate form. Even though the pretreatment unit was integrated with the RO system, removing silica with microfiltration (MF) or sand filter is quite challenging due to its small size. It was mentioned elsewhere by (Wilhelm and Kind, 2015) that the precipitation process of silica in water depends on its pH and concentration. Silica at a concentration higher than 100 mg/L (at a pH of 7.0) starts to polymerize and form a gel-like layer on the active area of the membranes. Therefore, one must be careful with silica concentration as well as the feed water pH when dealing with wastewater containing silica at higher concentrations. There is nothing that can be done with silica concentration hence, the pH of the feed water will surely play a vital role when treating water containing high silica concentration. Bush et al. suggested that maintaining the pH of the feed water at pH <5 or >10 can be employed to avoid or minimize membrane fouling from silica (Bush et al., 2018). Figure 4 shows the average flux obtained during each cycle. We can see that average permeate flux has continued to decline as the number of cycles increased towards the seventh cycle. The findings in the current study followed a similar trend found in the literature where membrane permeability decline is observed in intermittent RO desalting processes. Freire-Gormaly and Bilton (Freire-Gormaly

TABLE 4 Average flux, flux decline, and flux recovery (between permeate flux before and after cleaning) ($\text{L m}^{-2} \text{h}^{-1}$) were obtained by BW30 during the permeability test (15 bar).

Membrane test	Avg. Flux ($\text{L m}^{-2} \text{h}^{-1}$)	Flux decline (%)	Flux recovery (%)
Fresh membrane	78.9	-	-
Before 1st cleaning	75.2	4.7	98.3
After 1st cleaning	77.5	1.7	
Before 5th cleaning	65.0	17.5	86.6
After 5th cleaning	68.3	13.4	
Before 6th cleaning	51.6	34.5	68.4
After 6th cleaning	54.0	31.6	
Before 7th cleaning	42.0	46.7	57.0
After 7th cleaning	45.0	43.0	
Before 8th cleaning	44.0	44.2	63.4
After 8th cleaning	50.0	36.6	



and Bilton, 2019) studied the impact of intermittent operation and fouling using brackish groundwater in a lab-scale desalination. It was reported in their study that there was a membrane permeability decline of up to 87% even after employing both antiscalant and permeate flush at the end of each cycle (after 7 days of operation).

Figure 5 summarizes the impact of chemical cleaning on membrane fouling. Like was mentioned earlier, flux recovery was not very high despite cleaning the membrane with citric acid. The percentage of flux drop and flux recovery after applying chemical cleaning are summarized in Table 4.

4 Conclusion

It was evident that the level of membrane scaling increased as the number of treatment cycles increased. After eight cycles with even the doubled concentration of citric acid as 4000 mg/L, the permeate flux drop was 36.6%. It was considered that the use of antiscalant was not very effective for preventing membrane scaling during geothermal water treatment with a mini-pilot scale system. An optimization study is needed for using a more suitable antiscalant and its dosage. In addition, either a more suitable pretreatment method for the removal of scalants from geothermal water prior to RO membrane treatment and/or a new chemical cleaning protocol might be considered for increasing flux recovery.

The recommendations that can help increase the efficiency of spent geothermal water treatment are the use of antiscalants during the treatment process. The use of a more robust pretreatment train such as periodic clean water flush, coagulation to enhance nanoparticles removal, MF, and UF to reduce feed water turbidity beyond membrane manufacturer's recommendations (<1 NTU for RO feed) before RO train. Early mineral scaling detection while employing chemical cleaning before severe mineral scaling is observed.

References

Andritsos, N., and Karabelas, A. J. (2024). Sulfide scale formation and control: the case of lead sulfide. *Geothermics* 20, 343–353. doi:10.1016/0375-6505(91)90025-q

Data availability statement

The raw data supporting the conclusions of this article will be made available by the authors, without undue reservation.

Author contributions

AZ: Investigation, Writing–original draft. YJ: Conceptualization, Investigation, Supervision, Writing–original draft. IRAS: Investigation, Writing–review and editing. AK: Investigation, Writing–review and editing. AC: Supervision, Writing–review and editing. AB: Funding acquisition, Project administration, Resources, Writing–review and editing. NK: Conceptualization, Methodology, Supervision, Writing–review and editing.

Funding

The author(s) declare that financial support was received for the research, authorship, and/or publication of this article. This study was supported by an international research project supported by TÜBITAK- NCBR (Project No: 118Y490-POLTUR3/Geo4Food/4/2019).

Acknowledgments

The authors would like to acknowledge TÜBITAK for financial support and the Izmir Geothermal Co. for running membrane tests at the geothermal heating center.

Conflict of interest

The authors declare that the research was conducted in the absence of any commercial or financial relationships that could be construed as a potential conflict of interest.

Author NK declared that she was an editorial board member of *Frontiers*, at the time of submission. This had no impact on the peer review process and the final decision.

Publisher's note

All claims expressed in this article are solely those of the authors and do not necessarily represent those of their affiliated organizations, or those of the publisher, the editors and the reviewers. Any product that may be evaluated in this article, or claim that may be made by its manufacturer, is not guaranteed or endorsed by the publisher.

Ang, W. L., Nordin, D., Mohammad, A. W., Benamor, A., and Hilal, N. (2017). Effect of membrane performance including fouling on cost optimization in brackish water

- desalination process. *Chem. Eng. Res. Des.* 117, 401–413. doi:10.1016/j.cherd.2016.10.041
- Ang, W. S., Lee, S., and Elimelech, M. (2006). Chemical and physical aspects of cleaning of organic-fouled reverse osmosis membranes. *J. Membr. Sci.* 272, 198–210. doi:10.1016/j.memsci.2005.07.035
- Ang, W. S., Yip, N. Y., Tiraferri, A., and Elimelech, M. (2011). Chemical cleaning of RO membranes fouled by wastewater effluent: achieving higher efficiency with dual-step cleaning. *J. Membr. Sci.* 382, 100–106. doi:10.1016/j.memsci.2011.07.047
- Baten, R., and Stummeyer, K. (2012). How sustainable can desalination be? *Desal. Water Treat.*, 1–9. doi:10.1080/19443994.2012.705061
- Bush, P. J. A., Vanneste, J., Gustafson, E. M., Waechter, C. A., Jassby, D., Turchi, C. S., et al. (2018). Prevention and management of silica scaling in membrane distillation using pH adjustment. *J. Membr. Sci.* 554, 366–377. doi:10.1016/j.memsci.2018.02.059
- Chen, J., Kim, S., and Ting, Y. (2003). Optimization of membrane physical and chemical cleaning by a statistically designed approach. *J. Membr. Sci.* 219, 27–45. doi:10.1016/S0376-7388(03)00174-1
- D'Souza, N. M., and Mawson, A. J. (2005). Membrane cleaning in the dairy industry: a review. *Crit. Rev. Food Sci. Nutr.* 45 (2), 125–134. doi:10.1080/10408690490911783
- Freire-Gormally, M., and Bilton, A. M. (2019). Impact of intermittent operation on reverse osmosis membrane fouling for brackish groundwater desalination systems. *J. Membr. Sci.* 583, 220–230. doi:10.1016/j.memsci.2019.04.010
- Fritsch, J. A. C. I., and Moraru, C. I. (2008). Development and optimization of a carbon dioxide-aided cold microfiltration process for the physical removal of microorganisms and somatic cells from skim milk. *J. Dairy Sci.* 91, 3744–3760. doi:10.3168/jds.2007-0899
- Gilron, J., and Hasson, D. (1987). Calcium sulphate fouling of reverse osmosis membranes: flux decline mechanism. *Chem. Eng. Sci.* 42, 2351–2360. doi:10.1016/0009-2509(87)80109-4
- Goh, P., Lau, W., Othman, M., and Ismail, A. (2018a). Membrane fouling in desalination and its mitigation strategies. *Desalination* 425, 130–155. doi:10.1016/j.desal.2017.10.018
- Goh, P. S., Lau, W. J., Othman, M. H. D., and Ismail, A. F. (2018b). Membrane fouling in desalination and its mitigation strategies. *Desalination* 425, 130–155. doi:10.1016/j.desal.2017.10.018
- Jarma, Y. A. (2022). *Application of membrane processes for utilization of geothermal water in agricultural irrigation*. Izmir: Ege University. PhD Thesis.
- Jarma, Y. A., Karaoglu, A., Tekin, Ö., Baba, A., Okten, H. E., Tomaszewska, B., et al. (2021). Assessment of different nanofiltration and reverse osmosis membranes for simultaneous removal of arsenic and boron from spent geothermal water. *J. Hazard. Mater.* 405, 124129. doi:10.1016/j.jhazmat.2020.124129
- Jarma, Y. A., Karaoglu, A., Tekin, Ö., Senan, I. R. A., Baba, A., and Kabay, N. (2022). Integrated pressure-driven membrane separation processes for the production of agricultural irrigation water from spent geothermal water. *Desalination* 523, 115428. doi:10.1016/j.desal.2021.115428
- Jiang, S., Li, Y., and Ladewig, B. P. (2017). A review of reverse osmosis membrane fouling and control strategies. *Sci. Total Environ.* 595, 567–583. doi:10.1016/j.scitotenv.2017.03.235
- Kimura, K., Hane, Y., Watanabe, Y., Amy, G., and Ohkuma, N. (2004). Irreversible membrane fouling during ultrafiltration of surface water. *Water Res.* 38 (14), 3431–3441. doi:10.1016/j.watres.2004.05.007
- Klupfel, A. M., and Frimmel, F. H. (2010). Nanofiltration of river water — fouling, cleaning and micropollutant rejection. *Desalination* 250, 1005–1007. doi:10.1016/j.desal.2009.09.091
- Lee, S., Kim, J., and Lee, C.-H. (1999). Analysis of CaSO₄ scale formation mechanism in various nanofiltration modules. *J. Membr. Sci.* 163, 63–74. doi:10.1016/S0376-7388(99)00156-8
- Lenntech (2024). DuPont-filmtec BW30-2540 reverse osmosis element. Available at: <https://www.lenntech.com/products/DuPont-Filmtec/80766/BW30-2540-Reverse-Osmosis-Element/>.
- Leonard, B. (1999). *25 Years of the safe drinking water act: history and trends*. Collingdale, PA: Diane Publishing Company.
- Liikanen, R., Yli-Kuivila, J., and Laukkanen, R. (2002). Efficiency of various chemical cleanings for nanofiltration membrane fouled by conventionally-treated surface water. *J. Membr. Sci.* 195, 265–276. doi:10.1016/S0376-7388(01)00569-5
- Lin, J. C. T., Lee, D. J., and Huang, C. (2010). Membrane fouling mitigation: membrane cleaning. *Sep. Sci. Technol.* 45, 858–872. doi:10.1080/01496391003666940
- Liu, L., Zhu, G., Liu, Z., and Gao, C. (2016). Effect of MCM-48 nanoparticles on the performance of thin film nanocomposite membranes for reverse osmosis application. *Desalination* 394, 72–82. doi:10.1016/j.desal.2016.04.028
- Madaeni, S. S., and Samieirad, S. (2010). Chemical cleaning of reverse osmosis membrane fouled by wastewater. *Desalination* 257 (1–3), 80–86. doi:10.1016/j.desal.2010.03.002
- Mitrouli, S. T., Kostoglou, M., and Karabelas, A. J. (2026). Calcium carbonate scaling of desalination membranes: assessment of scaling parameters from dead-end filtration experiments. *J. Membr. Sci.* 510, 293–305. doi:10.1016/j.memsci.2016.02.061
- Mohammadi, T., Madaeni, S. S., and Moghadam, M. K. (2002). Investigation of membrane fouling. *Desalination* 153, 155–160. doi:10.1016/S0011-9164(02)01118-9
- Parlar, I., Hacifazlıoğlu, M., Kabay, N., Pek, T. Ö., and Yüksel, M. (2019). Performance comparison of reverse osmosis (RO) with integrated nanofiltration (NF) and reverse osmosis process for desalination of MBR effluent. *J. Water Proc. Eng.* 29, 100640. doi:10.1016/j.jwpe.2018.06.002
- Saqib, J., and Aljundi, I. H. (2016). Membrane fouling and modification using surface treatment and layer-by-layer assembly of polyelectrolytes: state-of-the-art review. *J. Water Process. Eng.* 11, 68–87. doi:10.1016/j.jwpe.2016.03.009
- Schwarz, H. E., Emel, J., Dickens, W., Rogers, P., and Thompson, J. (1990). “Water quality and flows,” in *The Earth as transformed by human action*. Cambridge, UK: Cambridge University Press.
- She, Q., Wang, R., Fane, A. G., and Tang, C. Y. (2016). Membrane fouling in osmotically driven membrane processes: a review. *J. Membr. Sci.* 499, 201–233. doi:10.1016/j.memsci.2015.10.040
- Subramani, A., and Jacangelo, J. G. (2015). Emerging desalination technologies for water treatment: a critical review. *Water Res.* 75, 164–187. doi:10.1016/j.watres.2015.02.032
- Verbeke, R., Gómez, V., Koschine, T., Eyley, S., Szymczyk, A., Dickmann, M., et al. (2018). Real-scale chlorination at pH4 of BW30 TFC membranes and their physicochemical characterization. *J. Membr. Sci.* 551, 123–135. doi:10.1016/j.memsci.2018.01.019
- Wang, Z., Wu, Z., Yin, X., and Tian, L. (2008). Membrane fouling in a submerged membrane bioreactor (MBR) under sub-critical flux operation: membrane foulant and gel layer characterization. *J. Membr. Sci.* 325, 238–244. doi:10.1016/j.memsci.2008.07.035
- Wilhelm, S., and Kind, M. (2015). Influence of pH, temperature and sample size on natural and enforced syneresis of precipitated silica. *Polym. (Basel)* 7 (12), 2504–2521. doi:10.3390/polym7121528
- Zaid, A. (2023). “A study on membrane fouling after treatment of geothermal water by nanofiltration and reverse osmosis membranes,”. MS Thesis, Ege University. Izmir.
- Zhao, Y., Zhang, Z., Dai, L., Mao, H., and Zhang, S. (2017). Enhanced both water flux and salt rejection of reverse osmosis membrane through combining isophthaloyl dichloride with biphenyl tetraacyl chloride as organic phase monomer for seawater desalination. *J. Membr. Sci.* 522, 175–182. doi:10.1016/j.memsci.2016.09.022
- Zirehpour, A., Rahimpour, A., and Ulbricht, M. (2017). Nano-sized metal organic framework to improve the structural properties and desalination performance of thin film composite forward osmosis membrane. *J. Membr. Sci.* 531, 59–67. doi:10.1016/j.memsci.2017.02.049



OPEN ACCESS

EDITED BY

Qusay Alsahy,
University of Technology, Iraq

REVIEWED BY

Adnan A. AbdulRazak,
University of Technology, Iraq
Khalid Rashid,
University of Technology, Iraq
Enver Güler,
Atılım University, Türkiye

*CORRESPONDENCE

Yan Yin,
✉ yanyin@tju.edu.cn
Michael D. Guiver,
✉ michael.guiver@outlook.com

RECEIVED 24 March 2023

ACCEPTED 04 May 2023

PUBLISHED 24 May 2023

CITATION

Zheng C, Wang L, Zhang S, Liu X, Zhang J, Yin Y, Jiao K, Du Q, Li X and Guiver MD (2023), Microstructural orientation of anion exchange membrane through mechanical stretching for improved ion transport.
Front. Membr. Sci. Technol. 2:1193355.
doi: 10.3389/fmst.2023.1193355

COPYRIGHT

© 2023 Zheng, Wang, Zhang, Liu, Zhang, Yin, Jiao, Du, Li and Guiver. This is an open-access article distributed under the terms of the [Creative Commons Attribution License \(CC BY\)](https://creativecommons.org/licenses/by/4.0/). The use, distribution or reproduction in other forums is permitted, provided the original author(s) and the copyright owner(s) are credited and that the original publication in this journal is cited, in accordance with accepted academic practice. No use, distribution or reproduction is permitted which does not comply with these terms.

Microstructural orientation of anion exchange membrane through mechanical stretching for improved ion transport

Chenyang Zheng^{1,2}, Lianqin Wang¹, Shijie Zhang³, Xin Liu¹, Junfeng Zhang^{1,4}, Yan Yin^{1,4*}, Kui Jiao^{1,4}, Qing Du^{1,4}, Xiangguo Li² and Michael D. Guiver^{1,4*}

¹State Key Laboratory of Engines, School of Mechanical Engineering, Tianjin University, Tianjin, China,

²Laboratory for Fuel Cell and Green Energy, Department of Mechanical and Mechatronics Engineering, University of Waterloo, Waterloo, ON, Canada, ³CATARC New Energy Vehicle Test Center (Tianjin) Co Ltd, Tianjin, China, ⁴National Industry-Education Platform of Energy Storage, Tianjin University, Tianjin, China

Synthesis of anion exchange membranes (AEMs) with orientated nano/micro-structure and with tunable ion-channels is of great interest for applications in fuel cells, water electrolyzers, and redox flow batteries. However, there is still a dearth of work in the detailed understanding of anion conductivity from a polymer structure–property perspective. Herein, we demonstrate an easy and versatile strategy to fabricate highly conductive AEMs. By stretching the AEMs, an improvement in OH[−] conductivities of AEMs is achieved. The effect of elongation at different water contents on polymer structures and OH[−] conductivities was investigated by a combination of molecular dynamics (MD) simulation and experimental study, giving insights into macromolecular orientation at the atomic level. The morphological changes, which consist of oriented polymer chains and elongated water clusters, are quantified by a combination of two dimensional small angle X-ray scattering (SAXS), scanning electron microscopy (SEM) and radial distribution functions. Detailed analyses of interatomic distances reveal morphological variations of hydrophilic domains and their interactions with water and OH[−] under elongation at different hydration levels. Furthermore, the OH[−] conductivities of our synthesized quaternized poly(2,6-dimethyl-1,4-phenylene oxide) (QPPO) AEMs increased significantly after stretching to 20% elongation at all water contents. Specifically, OH[−] conductivity of stretched QPPO was 2.24 times more than the original AEM at 60% RH. The higher relative increase in OH[−] conductivity at lower water content may be caused by the lower flexibility of side chains at lower hydrated level. This work verifies the significance of porous and/or oriented AEM structure in the improvement on anion conductivity and water transport efficiency.

KEYWORDS

anion exchange membrane, molecular dynamics simulation, mechanical stretching, membrane orientation, anion conductivity, conducting channel

1 Introduction

Anion exchange membranes (AEMs), as one of the core components of AEM fuel cells, are required to have high ion conductivity, a low degree of swelling, excellent mechanical properties, and robust chemical and thermal stabilities (Mustain et al., 2020; Chen and Lee, 2022). Many efforts have been dedicated to the development of highly conductive AEMs. A

variety of polymer backbones (Wang et al., 2013; Li et al., 2013) and cation groups (Zhu et al., 2016; Sun et al., 2018) have been employed in AEMs. Increasing the ion exchange capacity (IEC) and reducing AEM thickness are well-recognized approaches to improve the ion conductivity of AEMs. Nevertheless, many AEMs, especially those with IECs above 2.0 meq g^{-1} , do not survive the swelling and deswelling cycles, and either fail during changes in relative humidity (RH) or delaminate from the electrodes (Hickner et al., 2013). In cases where the polymer is randomly functionalized, the AEM morphology is often ill-defined and difficult to control or quantify. Highly ordered structures and efficient ion channels are optimal for AEMs to achieve high conductivity (Huang et al., 2019). One popular vein of research of AEMs is the construction of microphase separated morphology (Wei et al., 2019; Pan et al., 2014; Lee et al., 2017; Huang et al., 2020), which shows some improvements in ion conductivity and mechanical properties, and reduced dimensional swelling. A different approach to achieve high conductivity AEMs is with microporous structures, using polymers of intrinsic microporosity (PIMs). Their inefficient packing of contorted polymer chains generates microporous structure to facilitate efficient ion transport, leading to excellent OH^- conductivity (Yang et al., 2016; Huang et al., 2021). The concept of structure design for alignment of ion channels has also been explored (Liu et al., 2019; Liu et al., 2020a). Magnetic field has been used to construct oriented ion-channel structures in electrolyte membranes. Highly conductive and durable membranes with aligned ion channels are obtained with ion-conducting paramagnetic compounds. Nevertheless, they are less convenient to scale-up for practical applications.

Membrane deformation occurs under assembly pressure, temperature and humidity changes during fuel cell operations (Ozmaian and Naghdabadi, 2015; Kusoglu et al., 2006; Zhou et al., 2009). Interestingly, an increase in proton conductivity of sulfonated poly(phenylene oxide) can be achieved by heating and stretching (Li et al., 2007). It is highly desirable to fundamentally understand the correlation between mechanical deformation and the morphology and ion conductivity of AEMs, to allow morphology–conductivity relationships to be possibly quantified. Molecular dynamics (MD) simulation is a powerful tool to investigate the influence of mechanical stretching on macromolecular orientation at the atomic level (Ouma et al., 2022) especially to give insights into changes in structure and ion transport properties (Wei et al., 2015; Hofmann et al., 2010; Sengupta et al., 2017; Feng and Voth, 2019; Kurihara et al., 2019; Mabuchi and Tokumasu, 2014; Savage, 2021; Savage and Voth, 2014; Savage and Voth, 2016), membrane morphology (Petersen and Voth, 2006; Komarov et al., 2013; Kuo et al., 2016), water sorption and permeation (Daly et al., 2013; Daly et al., 2014), and mechanical properties (Sun et al., 2013; Li et al., 2018; Ozmaian and Naghdabadi, 2015; Xie et al., 2016).

Poly(2,6-dimethyl phenylene oxide) (PPO) is a commodity polymer widely used for its properties of thermal stability, mechanical strength and chemical durability (Liu et al., 2018; Zhang et al., 2022). PPO is readily brominated to access bromobenzyl groups for subsequent quaternization without chloromethylation (Hickner et al., 2013; Yang and Knauss, 2015). Many strategies have been developed with the aim of improving the anion conductivity and alkaline stability of positively charged PPO, including modifying the type and the position of the cationic

moieties on the polymer backbone (Liu et al., 2018; Liu et al., 2020b), electrical treatment (Kim et al., 2018), and crosslinking with functionalized graphene oxide (Zhang et al., 2022). The objective of the present work is to study the effect of mechanical stretching-induced membrane orientation in poly(2,6-dimethyl-1,4-phenylene oxide)-trimethylammonium hydroxide (PPO-TMA) AEM, with various water contents, λ , which is number of absorbed water molecules per hydroxide group ($\lambda = \text{H}_2\text{O}/\text{OH}^-$). The small-angle X-ray scattering (SAXS), free volume and radial distribution functions are analyzed to evaluate the structural changes, which include backbone stretching, side chain extension, and also reformed water cluster distribution. The influence of structure deformation on ion transport is also investigated in detail. This is the first time that MD simulation and experimental work are combined to comprehensively investigate the effect of mechanical stretching on membrane morphology and properties.

2 Simulation methods

2.1 Modeling considerations

In the classical MD method, the ion conduction process is normally simulated with the following considerations: (i) A cubic computational domain with particles containing all of the material components needed in the actual operation of the ionic membrane is shown in Figure 1, which can be considered as a unit lattice. (ii) Each atom or atom group within the computational domain is treated as a single particle, and their interactions and motions are governed by Newton's second law of mechanics. Therefore, the simulation depends on the type and number of the particles within the computational domain, and the forces acting on each particle.

To balance statistical results and computational time within a domain, 10 polymer chains (or backbones, as illustrated by the black solid line in Figure 1) are considered along with the number of the ten repeat units in each backbone. An exact number of water molecules is specified by the hydration parameter λ , denoted as the absorbed water molecules per hydroxide group. Each hydroxide ion corresponds to a quaternary ammonium group of each side chain, resulting in a total of 100 hydroxy groups to maintain electrical neutrality. The size of the cubic domain was determined by the reference density. The total mass was set based on the polymer composition, as described above, and the density was set by adjusting the lattice size. The polymer chains, hydroxide anions, and water molecules were randomly packed within the computational domain in the initial state (Figure 1).

2.2 Model formulation

In MD simulation, atom interactions and motions are governed by Newton's second law of mechanics as given in Eq. 1:

$$F_i(t) = m_i a_i(t) \quad (1)$$

where $a_i(t)$ and m_i are the acceleration at time t and the mass of atom i , and $i = 1, 2 \dots N$. Here, N represents the total number of atoms in the computational domain. The net force acting on the

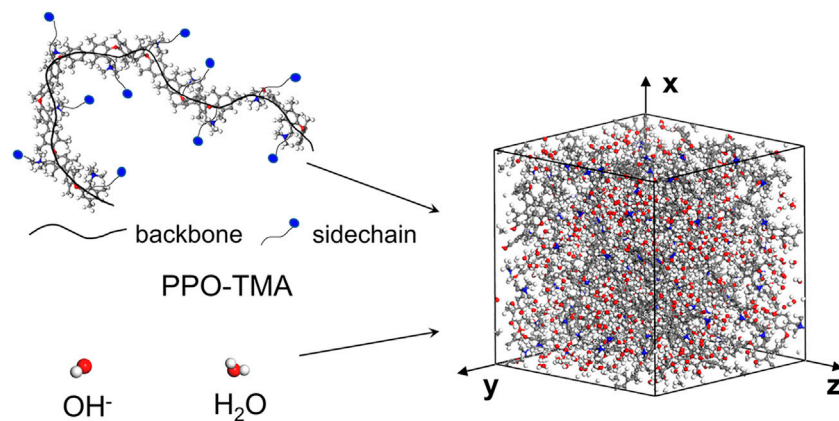


FIGURE 1

Schematic of the 3D molecular structure model in AEM, and the selected computational domain.

atom i at any instant of time t , $F_i(t)$, is expressed in terms of the position gradient of the potential energy the atom i has in the multi-atom system, $E_i(t)$, or

$$F_i(t) = -\frac{dE_i}{dr_i} \quad (2)$$

such that

$$-\frac{dE_i}{dr_i} = m_i \frac{d^2 r_i}{dt^2} \quad (3)$$

where r_i is the position of the atom i at the instant of time t .

Parameterized complex functional forms, such as off-diagonal cross-coupling terms and high-order force constants, were taken into account by the COMPASS force field. The potential energy is expressed by Equations (S1)–(S6) in the Supporting Material. Three-dimensional periodic boundary conditions (described in the Supporting Material) were adopted in this study. The initial position and initial velocity of each atom in the computational domain are described by Equation (S7).

The above equations form a conventional mathematical model for MD simulation. The simulation process was to solve the governing Newton's equations of motion as shown in Equations (S8)–(S10) and the simulation details are shown in the Supporting Material. Once the threshold reached the convergence tolerances of energy and force of geometry optimization shown in Equations (S15)–(S16), the system was considered to be equilibrium, then model validation could be carried out as shown in [Supplementary Figure S1](#).

In order to investigate the effect of mechanical stretching (deformation) in a given direction on the transport of ions in the membrane, a uniaxial deformation was applied in the z -direction (shown in [Figure 1](#)), after the unit lattice had reached thermodynamic equilibrium. The degree of deformation can be varied to assess the impact of the deformation on the oriented structure, morphology, and ion transport. The deformation in the z -direction was considered as the total atom number remains the same. Therefore, the deformation may be described as:

$$L_{z1} = L_{z0} + (L_{z0} \times \text{strain}) \quad (4)$$

$$L_{x1} = L_{y1} = (V/L_{z1})^{1/2} \quad (5)$$

Similarly, the deformation for individual atoms have the effect of changing the inter-atom distance in the z , x and y directions such that

$$z_{ij} = z_{ij,0} (1 + \text{strain}) \quad (6)$$

$$x_{ij} = \frac{x_{ij,0}}{L_{x1}}, \quad y_{ij} = \frac{y_{ij,0}}{L_{y1}} \quad (7)$$

where L and V is the side length and volume of the unit lattice, x_{ij} , y_{ij} , and z_{ij} are the distances between the atoms i and j in the x , y and z directions, respectively. The subscript “0” represents the distance before deformation (strain). A series of strains were considered in the z -direction, with the corresponding compression in the other two directions (x and y) in order to maintain a constant density. Clearly, the strain mainly affects potential energy E_i in Eq. 2 through the change in the distance among the atoms in the computational domain, and the stress can be obtained through dividing the force given in Eq. 3 by the area ($L_{x1} \times L_{y1}$).

2.3 Simulation analysis: Statistical analysis of all the particles in the domain

2.3.1 Free volume

The free volume is defined as a unit lattice outside the defined surface. The isosurface representation of the aqueous domain includes water molecules, quaternary ammonium groups of the polymer, the PPO-TMA polymer chains and hydroxide ions. In the simulation, a probe with a radius of 1.4 Å was adopted ([Kuo et al., 2018](#)).

2.3.2 Radial distribution function

Radial distribution functions (RDFs) have been employed to study the interactions between different atoms in membrane

systems, such as ammonium groups, hydroxide ions, and water molecules (Ennari, 2008):

$$g_{A-B}(r) = \frac{V}{N_B} \cdot \frac{n_B}{4\pi r^2 dr} \quad (8)$$

where n_B is the number of atoms B at the distance r from atoms A in a layer of thickness dr . N_B represents the number of particles B and V represents the domain total volume. It can be seen from the equation that the radial distribution function is the ratio of regional density to the average density of the domain.

The coordination numbers (CNs) of molecules around the nitrogen atom were calculated (Bahlakeh and Nikazar, 2012), which is the number of adjacent atoms around the nitrogen atoms, with the aim of investigating the relationship between water molecules and hydroxide ions with ammonium groups.

$$CN = 4\pi \frac{N_B}{V} \int r^2 g_{A-B}(r) dr \quad (9)$$

2.3.3 Ion conductivity

The diffusion coefficient of hydroxide ions was calculated using the mean square displacement (MSD) by the following relationship (Chen et al., 2014), according to the Einstein formula (Blickle et al., 2007):

$$MSD = \frac{1}{N_i} \left\langle \sum_{i=1}^{N_i} |r_i(t) - r_i(t_0)|^2 \right\rangle \quad (10)$$

$$D_i = \frac{1}{6} \lim_{t \rightarrow \infty} \frac{dMSD}{dt} \quad (11)$$

where D_i is the diffusion coefficient of atom i and N_i refers to the total number of i atoms in the computational domain.

Ion conductivity (σ) was calculated using the hydroxide ion diffusion coefficient (Pozuelo et al., 2006):

$$\sigma = \frac{Nz^2e^2D}{VkT} \quad (12)$$

where k , z and e represent the Boltzmann constant, total charge and electronic charge, respectively. N is the number of hydroxide ions, D is the hydroxide ion diffusion coefficient, and T is the absolute temperature.

3 Experimental section

3.1 Materials

Poly(2,6-dimethyl-1,4-phenylene oxide) (PPO, $M_n = 20,000$), N-bromosuccinimide (NBS, 99%), 2-2'-azobisisobutyronitrile (AIBN, 98%), trimethylamine (TMA, 3.2 M solution in ethanol), chlorobenzene and *N*-methyl-2-pyrrolidone (NMP) were obtained from Sigma-Aldrich and used as received, except AIBN.

3.2 Modification of PPO and fabrication of membranes

Bromination and quaternization reactions were used to prepare trimethylamine functionalized PPO AEMs as shown in Figure 2.

PPO was brominated using NBS according to a procedure outlined in the literature (Yang et al., 2018). In summary, NBS and recrystallized AIBN initiator (molar ratio 0.8:1) were added to a PPO solution in chlorobenzene. The mixture was heated and maintained at 135°C for 3 h under a nitrogen atmosphere, and then it was rapidly poured into methanol, resulting in a produce yellow precipitate. After washing with ethanol and drying in a vacuum oven at 30°C for 24 h, clean brominated PPO (BPPO) was obtained, having approximately 20% degree of bromination.

The BPPO polymer and TMA were dissolved in NMP for 1 h at room temperature (RT) under ultrasonication. To ensure the benzyl bromine groups quaternization completely, the molar ratio of N in TMA to the bromobenzyl groups in BPPO was adjusted to 3:1. The solution was poured onto dry Petri plates sized 10 cm × 10 cm, then heated at 70°C to drive off TMA reagent and solvent. To convert the counter ions from bromide ions to hydroxide ions, the membranes were peeled off and submerged in 1 M KOH solution at room temperature for 48 h. The AEMs were then washed with deionized water until they were neutral pH. The synthesized quaternary ammonium membranes (approximately 10 cm × 10 cm, thickness approximately 50 μm) are denoted as PPO-TMA.

3.3 Membrane characterization and measurements

The IEC was measured experimentally by the Mohr method (Wang et al., 2019; Xu and Yang, 2001). Dried membranes in the Br⁻ form were immersed into Na₂SO₄ solution to release bromine ions. The released bromide ions were determined by titration with 0.01 M AgNO₃ aqueous solution with the indicator K₂CrO₄ solution. The IEC value was calculated as follows:

$$IEC = \frac{0.01 \times V_{AgNO_3}}{m_{dry}} \quad (13)$$

where V_{AgNO_3} is the volume of consumed AgNO₃ aqueous solution and m_{dry} is the weight of dried membrane.

The ion conductivity (σ , mS cm⁻¹) was measured in the in-plane direction by the four-electrode AC impedance method. The membrane was clamped in the test device and placed in an environmental chamber (Espec, SH-222) at different relative humidity (RH). The ion conductivity was calculated as follows:

$$\sigma = \frac{L}{R \cdot A} \quad (14)$$

where L is the distance between the two reference electrodes (cm), R is the measured resistance, and A is the cross-sectional area of the membrane (cm²).

WU and λ were calculated from followed formulae:

$$WU = \frac{W_{wet} - W_{dry}}{W_{dry}} \times 100 \quad (15)$$

$$\lambda = \frac{WU \times 1000}{IEC \times 18} \quad (16)$$

where W_{wet} is the weight of the wet membrane; W_{dry} is the weight of the dry membrane. The dried membrane was immersed in deionized water at a specified temperature for 24 h. After removing it and quickly blotting off the surface water, the weight was measured.

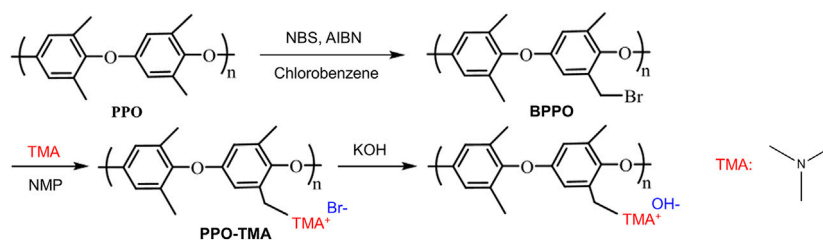


FIGURE 2
The synthesis route of PPO-TMA polymer.

Then, the membrane was placed in a vacuum oven at 60°C for 24 h and again weighed.

3.4 Tensile tests

The membranes were cut into strips (1 cm × 3 cm) and stretched mechanically by a tensile system (Instron, E1000). The loading was static and the stress state was uniaxial stretching. Mechanical stretching was conducted at RT with a constant strain rate (2 mm min⁻¹) to obtain the stress–strain (SS) correlations and repeated three times.

3.5 Scanning electron microscopy (SEM)

The surfaces or cross-sections of membrane were characterized by an S4800 field emission scanning electron microscope (Hitachi, Japan) at an accelerating voltage of 5 kV. The observed areas were pre-sputtered with a thin layer of platinum under vacuum.

3.6 Small-angle X-ray scattering (SAXS)

The two-dimensional SAXS patterns were recorded using the Beijing Synchrotron Radiation Facility (BSRF) 1W2A experimental site using a Cu Kα ($\lambda = 1.54 \text{ \AA}$) radiation generator, with a distance of 1.5 m between the membrane sample and detector.

4 Results and discussion

4.1 The influence of molecular structure on ion conductivity of PPO-TMA

The effect of molecular oriented arrangement on ion transport in PPO-TMA was studied by MD simulation. The results show that the oriented ion transmission pathways improve conduction efficiency. Interestingly, the σ at $\lambda = 5$ of oriented-arranged PPO-TMA (inset in Figure 3) was 1.391 mS cm⁻¹ at 300 K, which is 2.4 higher than that of randomly-arranged PPO-TMA (0.405 mS cm⁻¹), suggesting that oriented polymer chains significantly promote ionic transport, which is consistent with the literature (Meng et al., 2019).

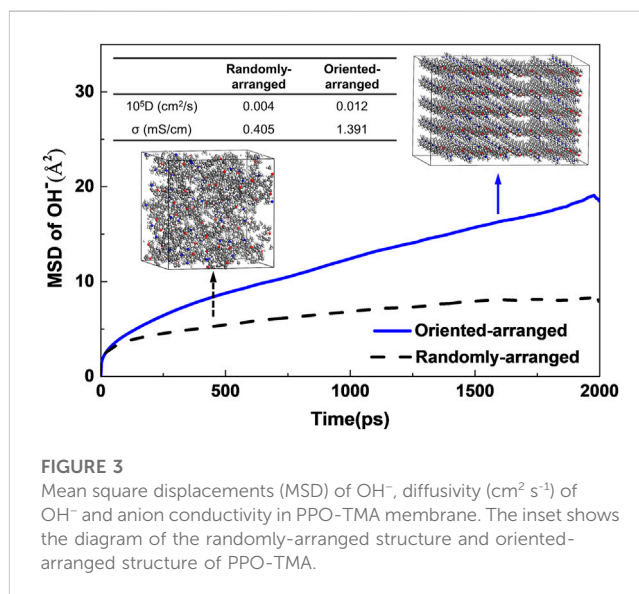


FIGURE 3
Mean square displacements (MSD) of OH⁻, diffusivity (cm² s⁻¹) of OH⁻ and anion conductivity in PPO-TMA membrane. The inset shows the diagram of the randomly-arranged structure and oriented-arranged structure of PPO-TMA.

4.2 Morphological changes under uniaxial stretching

The above-mentioned oriented arrangement is an idealized model, because it is difficult to achieve an absolutely oriented arrangement. Here we present that mechanical stretching induces relatively ordered arrangement, which results in improved anion conductivity. The effect of mechanical stretching on PPO-TMA AEMs (such as changes of polymer chain arrangement and water cluster distribution) was investigated by experimental work combined with MD simulation, as shown in Figure 4A. Young's modulus (initial slope section) and yield stress can be obtained from the stress-strain curves. It should be noted that the experimental conditions and parameters were identical with those used in the MD simulation. For simulation, a linear elastic region is found at a strain of less than 2%, which correlates with the experimental results. The yield stress obtained from the experiment is also in the same order as the simulation results, although there are some slight deviations from the simulation due to statistical errors.

Morphology characteristics were measured using SEM and shown in Figures 4B–E. The polymer chain displays a relatively uniform structure morphology before stretching (Figure 4B), while the cross-sectional SEM image after stretching shows a relatively oriented structure (Figure 4C). The polymer molecular arrangement or

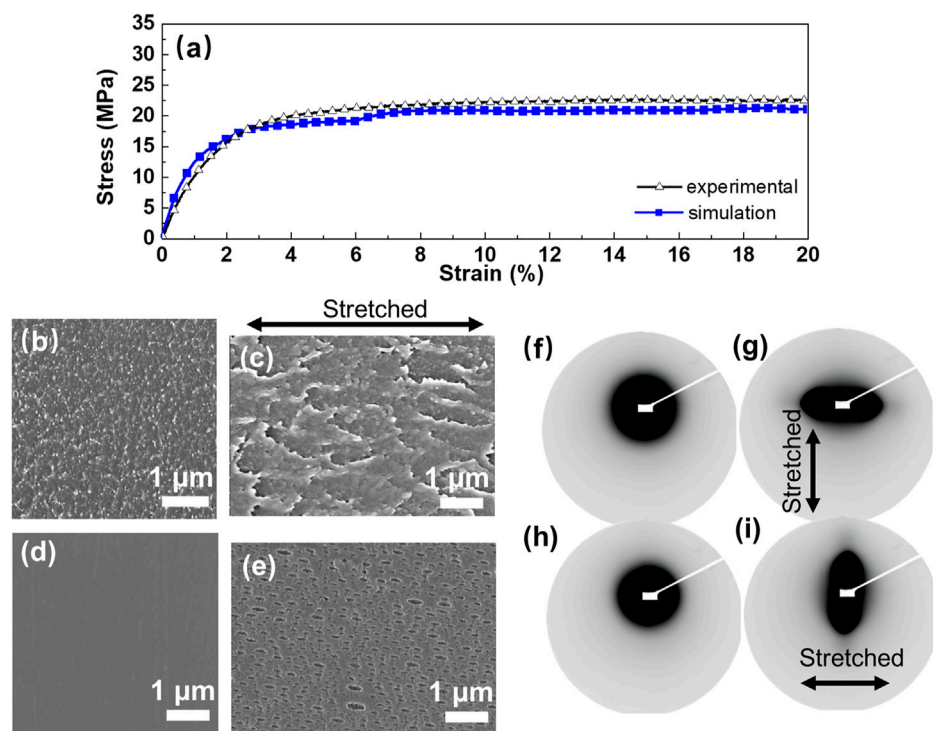


FIGURE 4

(A) Stress-strain curves of experimental and simulation results. SEM images (cross-sectional) of PPO-TMA (B) before and (C) after stretching; SEM images (surface) of PPO-TMA (D) before and (E) after stretching. Two-dimensional SAXS patterns of PPO-TMA membrane at (F) (H) initial and (G) (I) stretched state. Stretching direction is indicated with double sided arrow.

aggregation can be described via simulation of the density field calculation, which is presented in [Supplementary Figure S2](#). The color gradient from white to black shown in [Supplementary Figure S2A, B](#) corresponds to the increase in density of polymer chains. It is seen that after the tensile stretching simulation, the density value decreases and the polymer morphology tends to be stretched and extended toward the stretched direction. [Figures 4D, E](#) shows the surface morphology of un-stretched and stretched PPO-TMA. A relatively smooth surface of un-stretched membrane is observed in [Figure 4D](#). A large number of submicroscopic pores are formed during stretching of PPO-TMA. The elliptical pores formed during this process are oriented with their major axes parallel to the stretching direction and the film surface ([Figure 4E](#)). The lengths of the slits are typically in the range from 53 nm to 419 nm. The porous structure provides a continuous configuration necessary for fast ion and water transport ([Morehouse et al., 2006; Sarada et al., 1983](#)). Two-dimensional SAXS characterization provides additional evidence for the oriented structure. The isotropic SAXS data show a diffuse outer ring in [Figures 4F–H](#), which has been attributed to scattering from the polymer aggregates (phase-separation of hydrophilic–hydrophobic domains). As the membrane was stretched, the initially isotropic scattering pattern transforms into a strongly anisotropic scattering pattern, as observed in [Figures 4G–I](#). For the stretched membrane, evident anisotropy is observed in SAXS pattern, indicating oriented morphology. This is attributed to the alignment of elongated polymer aggregates in the direction of uniaxial stretching ([van der Heijden et al., 2004](#)).

Structure changes of PPO-TMA by stretching was simulated and is shown in [Figure 5](#). The 10 colors represent 10 polymer chains in [Figure 5A](#). As the membrane is stretched, the backbones become oriented in the direction of stretching, which coincides with the strain effect that has been found in proton exchange membranes ([Cable et al., 1995](#)). With the consideration of adsorbed water molecules ($\lambda = 15$), a dramatic change in structure due to stretching can also be observed in [Figures 5C, D](#). Water clusters tend to be extended along the stretching direction. The simulation results of the density field of water clusters also shows the same phenomenon ([Supplementary Figure S3](#)).

To further verify the increased porosity and connected channels of stretched PPO-TMA, the free volume of the unit lattice was calculated ([Supplementary Figure S4](#)). Free volume increased gradually with strains of up to 60% at all levels of water content. A high water content results in higher free volume for the same strain. The rapid increase in the free volume with increasing hydration levels is due to the increase in the number of water molecules in the membrane, causing a plasticizing effect and a larger distance between the polymer chains ([Kuo et al., 2018](#)).

4.3 Radial distribution functions

In order to probe the detailed changes in the lattice orders in the local structure during PPO-TMA deformation at different water contents, N–N (nitrogen atom in polymer), N–O_w (oxygen atom in

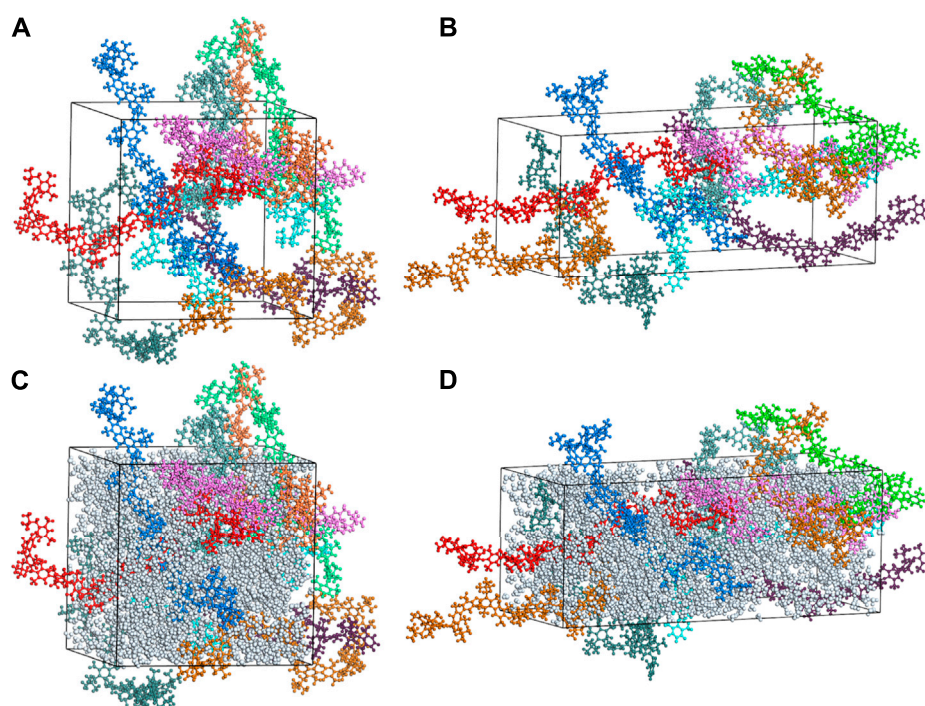


FIGURE 5

Schematic of the PPO-TMA membrane (A) and (C) before deformation, and (B) and (D) after uniaxial stretching with 60% strain deformation in the z-axis direction. Gray particles in (C) and (D) represent water molecules ($\lambda = 15$), and other colors correspond to polymer chains.

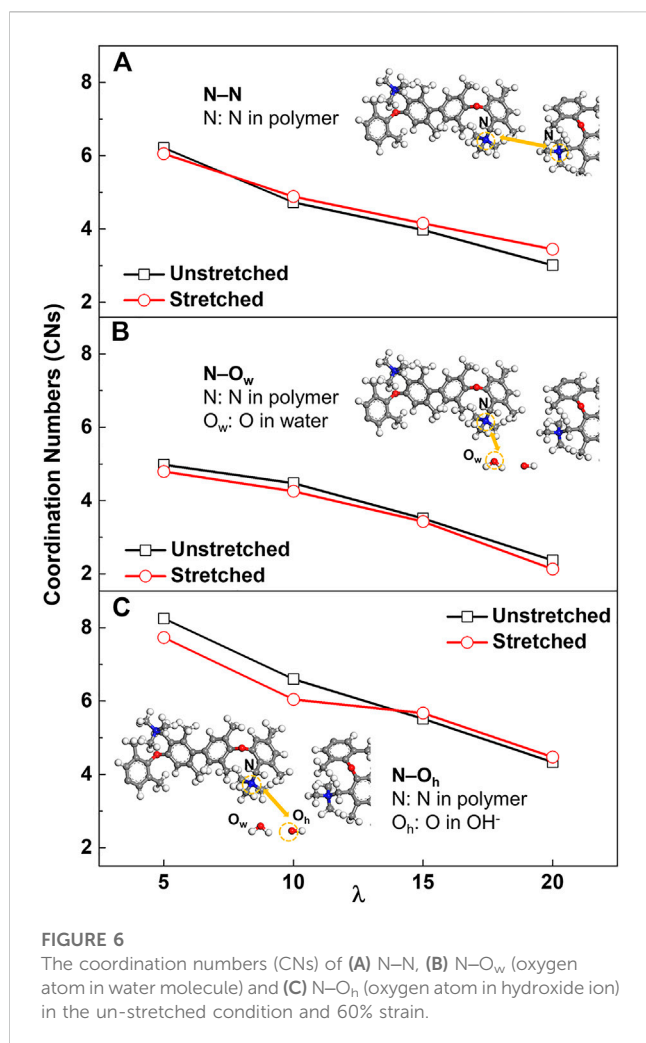
water molecule), and N–O_h (oxygen atom in hydroxide ion) RDFs were analyzed (Supplementary Figure S5), followed by calculation of the quantitative coordination numbers (CNs), as shown Figure 6. The CNs of N–N, N–O_w, and N–O_h indicate the interaction strength between TMAs, TMA and water, TMA and OH[−], respectively.

Supplementary Figure S5A shows the simulated RDFs of N–N linkage. The position of peaks at distances of <12 Å and >12 Å can be assigned to adjacent N–N between two chains as well as the N–N in the same chain, respectively (Dong et al., 2018). The differences among the RDFs at the prophase curves demonstrate the changes in the crystal lattice order of PPO-TMA. As the water content increases, the CNs for the un-stretched membrane decrease from 6.214 to 3.011 (Figure 6 and Supplementary Table S1), indicating that the nitrogen atoms tend to be separated at higher water content (Kuo et al., 2016). When the membrane was stretched, the CNs decrease for low water contents but increase for high water contents. At low water content, quaternary ammonium groups aggregate densely in the local hydrophilic phase, which is not conducive to conformational relaxation for the side chains in response to membrane deformation. Under uniaxial deformation, the side chains tend to align parallel to the stretching direction. At high water content, the quaternary ammonium groups are fully hydrated, resulting in flexible side chains, which allow rearrangement during membrane stretching. In addition, a decrease in the peak intensity at ~13 Å indicates that the distance between N atoms in the same chain increases with stretching, also inducing a highly orientated polymer chain.

To investigate how the quaternary ammonium groups are solvated by water molecules, the RDFs of nitrogen and oxygen

atoms in H₂O for different systems were investigated, as shown in Supplementary Figure S5B. Firstly, the peak intensity and CNs decrease as the water content increases, indicating that water molecules bind weakly with the quaternized groups with increasing water content. However, the peak positions do not change. This indicates that stretching mainly has an effect on the probability of the atoms in proximity with the quaternized groups. There is no significant change in the distribution of water molecules as the density decreases. Secondly, the CNs of water molecules surrounding each quaternary ammonium group are found to decrease with stretching for all water contents. This again confirms that the elongation of water clusters under mechanical stretching results in a decrease in the number of water molecules associated with the quaternized groups.

To investigate the relationship between R₄N⁺ groups and OH[−], the CNs of the N–O_h were calculated and the results are shown in Figure 6C. At low water content, compared to the un-stretched membranes, the stretched membranes have lower CNs for N–O_h. Hydroxide ions aggregate densely in the hydrophilic phase. As the water cluster extends due to uniaxial deformation, the number of water molecules and hydroxide ions correlated with the quaternary ammonium groups decreases. Therefore, at high water content, the polymer side chains have greater conformational flexibility and are more likely in a relaxed state when stretching the membrane, and thereby interact with free hydroxide ions. This leads to an increase in CNs and hydroxide ions around the quaternary ammonium group. Similar results have been reported in the literature (Kuo et al., 2017).



4.4 Dynamic properties of the hydrated membrane

To analyze the ion diffusion characteristics, the diffusion coefficients of hydroxide ions were calculated at various water contents and different strain. [Supplementary Figure S6](#) shows the hydroxide ion MSD curves at 300 K. [Figure 7](#) summarizes

the diffusion coefficients calculated from the hydroxide ion MSD curves at different water contents. Notably, [Supplementary Figure S6](#) shows the slope of hydroxide ion MSD curves increases apparently with an increase in strain. The slopes increase more significantly with the change in the water contents rather than the strain levels. The diffusion coefficients of hydroxide ion in the un-stretched membrane at different water contents are 0.006×10^{-5} to $0.286 \times 10^{-5} \text{ cm}^2 \text{ s}^{-1}$, with λ from 5–20, respectively. The corresponding calculated σ values are 0.608, 1.989, 11.75 and 16.63 mS cm^{-1} , respectively.

Compared with the effect of changes in strain, the influence of change in water content is more significant. When the membrane was stretched with different strain, the D values change. For $\lambda = 5$ with the strain of 0%–60%, the corresponding D values are in the range of 0.006×10^{-5} to $0.025 \times 10^{-5} \text{ cm}^2 \text{ s}^{-1}$, respectively. The calculated σ values are 0.608–2.589 mS cm^{-1} (an increase of 326% compared with un-stretched membrane). At the condition of $\lambda = 15$, when the strain changes from 0% to 60%, D increases from 0.172×10^{-5} to $0.2 \times 10^{-5} \text{ cm}^2 \text{ s}^{-1}$; the corresponding ion conductivity is 11.75 mS cm^{-1} (reference value 11.25 mS cm^{-1} ([Yang et al., 2018](#))) and 14.02 mS cm^{-1} (an increase of less than 50% than that of the un-stretched membrane), respectively. It has also been reported that the proton conductivity of oriented membranes in the direction of the strain increased compared with un-stretched membranes ([Dan et al., 2006](#)).

The ratios of D and σ in stretched and un-stretched membranes are shown in [Figure 7](#) as embedded tables. The stretching effect on σ is not obvious at high water content, which can be explained by the morphology changes. At low water contents, the enhancement in hydroxide transport can be attributed to the stretched membrane with a high orientation of polymer chain and water pathways ([Park et al., 2011](#)). For higher water contents of $\lambda = 15$ and 20, flexible hydrated side chains are strongly correlated with free hydroxide ions, reducing the increase in D . Thus, the effects of stretching on ion transport are noticeably different at different water contents. The σ reaches the maximum value at $\lambda = 20$ and at a strain of 60%. It can be concluded that the orientation of water clusters and polymer chains are extended in the stretching direction by the uniaxial stretching of the membrane. The above analysis also correlates with the analysis of the microscopic morphology diagram shown in [Figure 4](#), resulting in pathways that facilitate hydroxide ion transport.

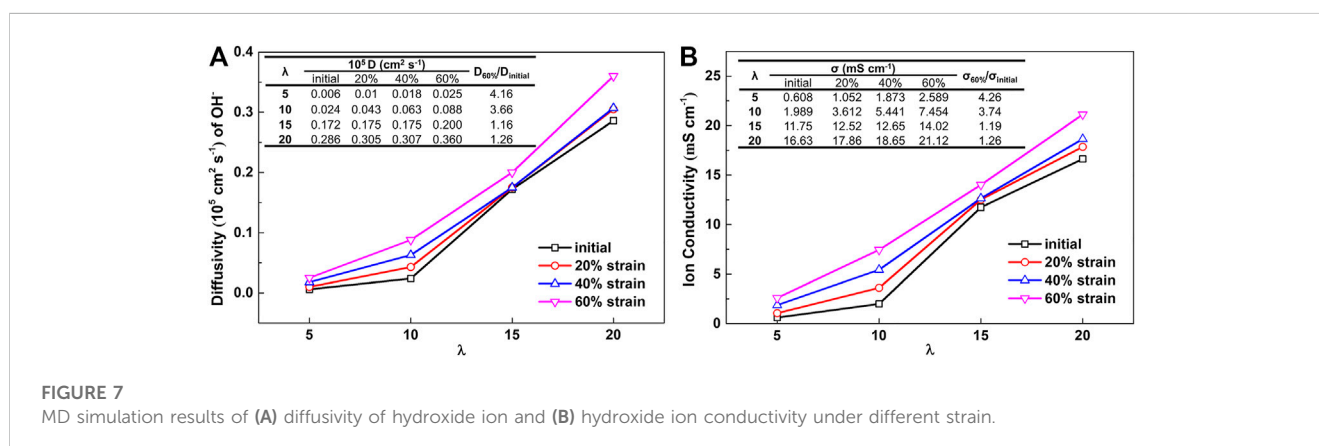


TABLE 1 The hydroxide ion conductivity of the PPO-TMA membrane in the stretching direction before and after stretching.

RH	λ	σ (mS cm ⁻¹)		$\sigma_z/\sigma_{\text{initial}}$
		Initial	σ_z of 20% elongation	
60%	6.9	1.09	3.54	3.24
80%	11.34	2.5	6.54	2.61
100%	14.28	10.7	17.2	1.61
in water	15.86	11.33	17.8	1.57

4.5 Experimental results of ion conductivity for un-stretched/stretched membranes

To further verify the simulation results, experimental conductivity tests were conducted at different RH with the membranes before and after mechanical stretching. From calculations based on experimental values of water uptake (WU) and IEC, λ is obtained, which represents the number of water molecules corresponding to each quaternary ammonium group, consistent with the definition of λ in the MD simulation. Therefore, we observe that when $\lambda = 15.86$, $\sigma = 11.33 \text{ mS cm}^{-2}$, which is in good agreement with the simulation results in Figure 7B ($\lambda = 15$, $\sigma = 11.75 \text{ mS cm}^{-2}$). In addition, the conductivity of membrane at 20% elongation in the stretching direction was also tested. In the stretched z -direction, the σ increased by 3.24, 2.61, 1.61 and 1.57 times with increasing λ (listed in Table 1), respectively. Such results well demonstrate that mechanical stretching has a positive effect on the ion conduction in the tensile direction, which further verifies the conclusion obtained in the above simulation.

5 Conclusion

In this study, simulation models of quaternized poly(2,6-dimethyl-1,4-phenylene oxide) membranes with a range of water content were constructed to investigate the effect of mechanical stretching on structure deformation, anion conductivity and morphology–conductivity relationships. During the elongation process, macromolecular orientation at the atomic level is shown to occur by molecular dynamics simulation. The oriented morphology was observed by scanning electron microscopy and two-dimensional small-angle X-ray scattering. Water clusters became elongated along the direction of stretching. The resulting continuous and oriented pathways effectively enhance hydroxide ion diffusivity in the direction of stretching at all water contents. The ion conductivities after mechanical stretching increased by 326% and 274% at hydration levels of $\lambda = 5$ and 10, respectively, which are similar to the experimental observations. However, at higher water contents ($\lambda = 15$ and 20), the ion conductivities increased by less than 50%. The abundant water induces greater conformational flexibility in the hydrated side chains, leading to structure relaxation in any direction when the membrane undergoes stretching. Therefore the incremental increase in ion conduction in the stretching direction at high water content is less than at low

water content. This study provides insights into the micro-morphology of anion exchange membranes under mechanical stretching and explains the effect of macromolecular orientation on hydroxide conductivity of hydrated membranes, which is useful for providing a theoretical basis for the structure–property relationship of AEMs. We are only in the early stages of understanding anion transport efficiency in ordered AEM systems and there remains more work to be done, especially in the development of innovative material strategies for the synthesis of highly ordered anion conducting membranes, and new methods to analyze their performance characteristics.

Data availability statement

The raw data supporting the conclusion of this article will be made available by the authors, without undue reservation.

Author contributions

CZ contributed to investigation, methodology, data curation, formal analysis, visualization, writing—Original Draft. LW contributed to data curation, data analysis, writing—review and editing. SZ contributed to investigation. JZ contributed to methodology, project administration, writing—review and editing. YY contributed to conceptualization, writing—review and editing, supervision, funding acquisition. KJ contributed to project administration. QD contributed to project administration. Xianguo Li contributed to methodology, writing—review and editing, supervision. MG contributed to writing—review and editing, supervision. All authors listed have made a substantial, direct, and intellectual contribution to the work and approved it for publication.

Acknowledgments

The authors thank the National Natural Science Foundation of China (21875161) and the State Key Laboratory of Engines for financial support.

Conflict of interest

Author SZ was employed by the company CATARC New Energy Vehicle Test Center (Tianjin) Co., Ltd. The author(s) XL, YY and MDG declared that they were an editorial board member of Frontiers, at the time of submission.

The remaining authors declare that the research was conducted in the absence of any commercial or financial relationships that could be construed as a potential conflict of interest.

Publisher's note

All claims expressed in this article are solely those of the authors and do not necessarily represent those of their

affiliated organizations, or those of the publisher, the editors and the reviewers. Any product that may be evaluated in this article, or claim that may be made by its manufacturer, is not guaranteed or endorsed by the publisher.

References

- Bahlakeh, G., and Nikazar, M. (2012). Molecular dynamics simulation analysis of hydration effects on microstructure and transport dynamics in sulfonated poly(2,6-dimethyl-1,4-phenylene oxide) fuel cell membranes. *Int. J. Hydrogen Energy* 37, 12714–12724. doi:10.1016/j.ijhydene.2012.06.034
- Blickle, V., Speck, T., Lutz, C., Seifert, U., and Bechinger, C. (2007). Einstein relation generalized to nonequilibrium. *Phys. Rev. Lett.* 98, 210601. doi:10.1103/PhysRevLett.98.210601
- Cable, K. M., Mauritz, K. A., and Moore, R. B. (1995). Anisotropic ionic conductivity in uniaxially oriented perfluorosulfonate ionomers. *Chem. Mat.* 7, 1601–1603. doi:10.1021/cm00057a002
- Chen, L., He, Y., Tao, W., and Huang, X. (2014). A case of long-term survival after curative resection for synchronous solitary adrenal metastasis from rectal cancer. *Numer. Heat. Tr.* 65, 216–219. doi:10.12669/pjms.301.4341
- Chen, N., and Lee, Y. M. (2022). Anion-conducting polyelectrolytes for energy devices. *Trends Chem.* 4, 236–249. doi:10.1016/j.trechm.2021.12.009
- Daly, K. B., Benziger, J. B., Debenedetti, P. G., and Panagiotopoulos, A. Z. (2013). Molecular dynamics simulations of water sorption in a perfluorosulfonic acid membrane. *J. Phys. Chem. B* 117, 12649–12660. doi:10.1021/jp405440r
- Daly, K. B., Benziger, J. B., Panagiotopoulos, A. Z., and Debenedetti, P. G. (2014). Molecular dynamics simulations of water permeation across Nafion membrane interfaces. *J. Phys. Chem. B* 118, 8798–8807. doi:10.1021/jp5024718
- Dan, L., Hickner, M. A., Case, S. W., and Lesko, J. (2006). Relaxation of proton conductivity and stress in proton exchange membranes under strain. *J. Eng. Mat. and Technol.* 128, 503–508. doi:10.1115/1.2345441
- Dong, D., Wei, X., Hooper, J. B., Pan, H., and Bedrov, D. (2018). Role of cationic groups on structural and dynamical correlations in hydrated quaternary ammonium-functionalized poly(p-phenylene oxide)-based anion exchange membranes. *Phys. Chem. Chem. Phys.* 20, 19350–19362. doi:10.1039/c8cp02211a
- Ennari, J. (2008). Modelling of transport properties and state of water of polyelectrolytes containing various amounts of water. *Polymer* 49, 2373–2380. doi:10.1016/j.polymer.2008.03.019
- Feng, S., and Voth, G. A. (2019). Proton solvation and transport in hydrated Nafion. *J. Phys. Chem. B* 115, 5903–5912. doi:10.1021/jp2002194
- Hickner, M. A., Herring, A. M., and Coughlin, E. B. (2013). Anion exchange membranes: Current status and moving forward. *J. Polym. Sci. Pol. Phys.* 51, 1727–1735. doi:10.1002/polb.23395
- Hofmann, D. W. M., Kuleshova, L. N., and Aguanno, B. D. (2010). Theoretical simulations of proton conductivity: Basic principles for improving the proton conductor. *J. Power Sources* 195, 7743–7750. doi:10.1016/j.jpowsour.2009.10.019
- Huang, G., Mandal, M., Peng, X., Yang-Neyerlin, A. C., Pivovar, B. S., Mustain, W. E., et al. (2019). Composite poly(norbornene) anion conducting membranes for achieving durability, water management and high power (3.4 W/cm²) in hydrogen/oxygen alkaline fuel cells. *J. Electrochem. Soc.* 166, F637–F644. doi:10.1149/2.1301910jes
- Huang, T., He, G., Xue, J., Otoo, O., He, X., Jiang, H., et al. (2020). Self-crosslinked blend alkaline anion exchange membranes with bi-continuous phase separated morphology to enhance ion conductivity. *J. Membr. Sci.* 597, 117769. doi:10.1016/j.memsci.2019.117769
- Huang, T., Zhang, J., Pei, Y., Liu, X., Xue, J., Jiang, H., et al. (2021). Mechanically robust microporous anion exchange membranes with efficient anion conduction for fuel cells. *Chem. Eng. J.* 418, 129311. doi:10.1016/j.cej.2021.129311
- Kim, J.-H., Ryu, S., Lee, J.-Y., Moon, S.-H., Cheung, D. Y., Chung, W. C., et al. (2018). Early detection is important to reduce the economic burden of gastric cancer. *J. Membr. Sci.* 553, 82–89. doi:10.5230/jgc.2018.18.e7
- Komarov, P. V., Khalatur, P. G., and Khokhlov, A. R. (2013). Large-scale atomistic and quantum-mechanical simulations of a Nafion membrane: Morphology, proton solvation and charge transport. *Beilstein J. Nanotech.* 4, 567–587. doi:10.3762/bjnano.4.65
- Kuo, A. T., Shinoda, W., and Okazaki, S. (2016). Molecular dynamics study of the morphology of hydrated perfluorosulfonic acid polymer membranes. *J. Phys. Chem. C* 120, 25832–25842. doi:10.1021/acs.jpcc.6b08015
- Kuo, A. T., Takeuchi, K., Tanaka, A., Urata, S., Okazaki, S., and Shinoda, W. (2018). Exploring the effect of pendent side chain length on the structural and mechanical properties of hydrated perfluorosulfonic acid polymer membranes by molecular dynamics simulation. *Polymer* 146, 53–62. doi:10.1016/j.polymer.2018.05.033
- Kuo, A. T., Tanaka, A., Irisawa, J., Shinoda, W., and Okazaki, S. (2017). Molecular dynamics study on the mechanical deformation of hydrated perfluorosulfonic acid polymer membranes. *J. Phys. Chem. C* 121, 21374–21382. doi:10.1021/acs.jpcc.7b05719
- Kurihara, Y., Mabuchi, T., and Tokumasu, T. (2019). Molecular dynamics study of oxygen transport resistance through ionomer thin film on Pt surface. *J. Power Sources* 414, 263–271. doi:10.1016/j.jpowsour.2019.01.011
- Kusoglu, A., Karlsson, A. M., Santare, M. H., Cleghorn, S., and Johnson, W. B. (2006). Mechanical response of fuel cell membranes subjected to a hygro-thermal cycle. *J. Power Sources* 161, 987–996. doi:10.1016/j.jpowsour.2006.05.020
- Lee, W., Park, E. J., Han, J., Shin, D. W., Kim, Y. S., and Bae, C. (2017). Poly(terphenylene) anion exchange membranes: The effect of backbone structure on morphology and membrane property. *ACS Macro Lett.* 6, 566–570. doi:10.1021/acsmacrolett.7b00148
- Li, C., Liu, J., Guan, R., Zhang, P., and Zhang, Q. (2007). Effect of heating and stretching membrane on ionic conductivity of sulfonated poly(phenylene oxide). *J. Membr. Sci.* 287, 180–186. doi:10.1016/j.memsci.2006.10.015
- Li, L., Li, W., Geng, L., Chen, B., Mi, H., Hong, K., et al. (2018). Formation of stretched fibrils and nanohybrid shish-kebabs in isotactic polypropylene-based nanocomposites by application of a dynamic oscillatory shear. *Chem. Eng. J.* 348, 546–556. doi:10.1016/j.cej.2018.04.197
- Li, N., Leng, Y., Hickner, M. A., and Wang, C. (2013). Highly stable, anion conductive, comb-shaped copolymers for alkaline fuel cells. *J. Am. Chem. Soc.* 135, 10124–10133. doi:10.1021/ja403671u
- Liu, L., Chu, X., Liao, J., Huang, Y., Li, Y., Ge, Z., et al. (2018). Tuning the properties of poly(2,6-dimethyl-1,4-phenylene oxide) anion exchange membranes and their performance in H₂/O₂ fuel cells. *Energy Environ. Sci.* 2, 435–446. doi:10.1039/c7ee02468a
- Liu, L., Liu, Z., Bai, L., Shao, C., Chen, R., Zhao, P., et al. (2020b). Quaternized poly(2,6-dimethyl-1,4-phenylene oxide) anion exchange membranes based on isomeric benzyltrimethylammonium cations for alkaline fuel cells. *J. Membr. Sci.* 606, 118133. doi:10.1016/j.memsci.2020.118133
- Liu, L., Zhang, J., Zheng, C., Xue, J., Huang, T., Yin, Y., et al. (2020a). Oriented proton-conductive nano-spongefacilitated polymer electrolyte membranes. *Energy Environ. Sci.* 13, 297–309. doi:10.1039/c9ee03301g
- Liu, X., Li, Y., Xue, J., Zhu, W., Zhang, J., Yin, Y., et al. (2019). Magnetic field alignment of stable proton-conducting channels in an electrolyte membrane. *Nat. Commun.* 10, 842. doi:10.1038/s41467-019-08622-2
- Mabuchi, T., and Tokumasu, T. (2014). Effect of bound state of water on hydronium ion mobility in hydrated Nafion using molecular dynamics simulations. *J. Chem. Phys.* 141, 104904. doi:10.1063/1.4894813
- Meng, H., Yu, X., Feng, H., Xue, Z., and Yang, N. (2019). Superior thermal conductivity of poly(ethylene oxide) for solid-state electrolytes: A molecular dynamics study. *Int. J. Heat. Mass Tran.* 137, 1241–1246. doi:10.1016/j.ijheatmasstransfer.2019.04.021
- Morehouse, J. A., Lloyd, D. R., Freeman, B. D., Lawler, D. F., Liechti, K. M., and Becker, E. B. (2006). Modeling the stretching of microporous membranes. *J. Membr. Sci.* 283, 430–439. doi:10.1016/j.memsci.2006.07.024
- Mustain, W. E., Chatenet, M., Page, M., and Kim, Y. S. (2020). Durability challenges of anion exchange membrane fuel cells. *Energy Environ. Sci.* 13, 2805–2838. doi:10.1039/d0ee01133a
- Ouma, C. N. M., Obodo, K. O., and Bessarabov, D. (2022). Computational approaches to alkaline anion-exchange membranes for fuel cell applications. *Membranes* 12, 1051. doi:10.3390/membranes12111051
- Ozmaian, M., and Naghdabadi, R. (2015). Properties of nafion under uniaxial loading at different temperatures: A molecular dynamics study. *Polym-Plast Technol.* 54, 806–813. doi:10.1080/03602559.2014.974192
- Pan, J., Chen, C., Li, Y., Wang, L., Tan, L., Li, G., et al. (2014). Angioarchitectural characteristics associated with complications of embolization in supratentorial brain arteriovenous malformation. *Energy Environ. Sci.* 7, 354–359. doi:10.1039/c3ee00133a
- Park, J. K., Li, J., Divoux, G. M., Madsen, L. A., and Moore, R. B. (2011). Oriented morphology and anisotropic transport in uniaxially stretched perfluorosulfonate ionomer membranes. *Macromolecules* 44, 5701–5710. doi:10.1021/ma200865p

Supplementary material

The Supplementary Material for this article can be found online at: <https://www.frontiersin.org/articles/10.3389/fmst.2023.1193355/full#supplementary-material>

- Petersen, M. K., and Voth, G. A. (2006). Characterization of the solvation and transport of the hydrated proton in the perfluorosulfonic acid membrane Nafion. *J. Phys. Chem. B* 110, 18594–18600. doi:10.1021/jp062719k
- Pozuelo, J., Riande, E., Saiz, E., and Compan, V. (2006). Molecular dynamics simulations of proton conduction in sulfonated poly(phenyl sulfone)s. *Macromolecules* 39, 8862–8866. doi:10.1021/ma062070h
- Sarada, T., Sawyer, L. C., and Ostler, M. I. (1983). Three dimensional structure of celgard® microporous membranes. *J. Membr. Sci.* 15, 97–113. doi:10.1016/s0376-7388(00)81364-2
- Savage, J. (2021). Molecular dynamics study on water and hydroxide transfer mechanisms in PSU-g-alkyl-TMA membranes at low hydration: Effect of side chain length. *Int. J. Hydrogen Energy* 46, 33915–33933. doi:10.1016/j.ijhydene.2021.07.081
- Savage, J., and Voth, G. A. (2014). Persistent subdiffusive proton transport in perfluorosulfonic acid membranes. *J. Phys. Chem. Lett.* 5, 3037–3042. doi:10.1021/jz5014467
- Savage, J., and Voth, G. A. (2016). Proton solvation and transport in realistic proton exchange membrane morphologies. *J. Phys. Chem. C* 120, 3176–3186. doi:10.1021/acs.jpcc.5b11168
- Sengupta, S., Pant, R., Komarou, P., Venkatnathan, A., and Lyulin, A. V. (2017). Atomistic simulation study of the hydrated structure and transport dynamics of a novel multi acid side chain polyelectrolyte membrane. *Int. J. Hydrogen Energy* 42, 27254–27268. doi:10.1016/j.ijhydene.2017.09.078
- Sun, Y., Wang, C., and Chen, Y. (2013). Molecular dynamics simulations of the deformation behavior of gadolinia-doped ceria solid electrolytes under tensile loading. *J. Power Sources* 233, 131–138. doi:10.1016/j.jpowsour.2013.01.139
- Sun, Z., Lin, B., and Yan, F. (2018). Anion-exchange membranes for alkaline fuel-cell applications: The effects of cations. *Chem. Sus. Chem.* 11, 58–70. doi:10.1002/cssc.201701600
- van der Heijden, P. C., Rubatat, L., and Diat, O. (2004). Orientation of drawn Nafion at molecular and mesoscopic scales. *Macromolecules* 37, 5327–5336. doi:10.1021/ma035642w
- Wang, J., Zhao, Y., Setzler, B. P., Rojas-Carbonell, S., Yehuda, C. B., Amel, A., et al. (2019). Identification of a monoclonal antibody that targets PD-1 in a manner requiring PD-1 Asn58 glycosylation. *Nat. Energy* 4, 392–398. doi:10.1038/s42003-019-0642-9
- Wang, Y., Qiao, J., Bakerb, R., and Zhang, J. (2013). Alkaline polymer electrolyte membranes for fuel cell applications. *Chem. Soc. Rev.* 42, 5768–5787. doi:10.1039/c3cs60053j
- Wei, C., Srivastava, D., and Cho, K. J. (2015). Thermal expansion and diffusion coefficients of carbon nanotube-polymer composites. *Nano Lett.* 2, 647–650. doi:10.1021/nl025554+
- Wei, H., Li, Y., Wang, S., Tao, G., Wang, T., Cheng, S., et al. (2019). Side-chain-type imidazolium-functionalized anion exchange membranes: The effects of additional hydrophobic side chains and their hydrophobicity. *J. Membr. Sci.* 579, 219–229. doi:10.1016/j.memsci.2019.02.058
- Xie, J., Ban, S., Liu, B., and Zhou, H. (2016). A molecular simulation study of chemical degradation and mechanical deformation of hydrated Nafion membranes. *Appl. Surf. Sci.* 362, 441–447. doi:10.1016/j.apsusc.2015.11.144
- Xu, T., and Yang, W. (2001). Fundamental studies of a new series of anion exchange membranes: Membrane preparation and characterization. *J. Membr. Sci.* 190, 159–166. doi:10.1016/s0376-7388(01)00434-3
- Yang, Y., and Knauss, D. M. (2015). Poly (2,6-dimethyl-1,4-phenylene oxide)-b-poly(vinylbenzyltrimethylammonium) diblock copolymers for highly conductive anion exchange membranes. *Macromolecules* 48, 4471–4480. doi:10.1021/acs.macromol.5b00459
- Yang, Y., Xu, Y., Ye, N., Zhang, D., Yang, J., and He, R. (2018). Alkali resistant anion exchange membranes based on saturated heterocyclic quaternary ammonium cations functionalized poly(2,6-dimethyl-1,4-phenylene oxide)s. *J. Electrochem. Soc.* 165, F350–F356. doi:10.1149/2.1031805jes
- Yang, Z., Guo, R., Malpass-Evans, R., Carta, M., McKeown, N. B., Guiver, M. D., et al. (2016). Highly conductive anion-exchange membranes from microporous Troger's base polymers. *Angew. Chem. Int. Ed.* 55, 11499–11502. doi:10.1002/anie.201605916
- Zhang, D., Xu, S., Wan, R., Yang, Y., and He, R. (2022). Functionalized graphene oxide cross-linked poly (2,6-dimethyl-1,4-phenylene oxide)-based anion exchange membranes with superior ionic conductivity. *J. Power Sources* 517, 230720. doi:10.1016/j.jpowsour.2021.230720
- Zhou, Y., Lin, G., Shih, A. J., and Hu, S. J. (2009). Egr-1 is involved in the inhibitory effect of leptin on PPARgamma expression in hepatic stellate cell *in vitro*. *J. Power Sources* 192, 544–551. doi:10.1016/j.jfs.2009.01.018
- Zhu, L., Pan, J., Wang, Y., Han, J., Zhuang, L., and Hickner, M. A. (2016). Multication side chain anion exchange membranes. *Macromolecules* 49, 815–824. doi:10.1021/acs.macromol.5b02671



OPEN ACCESS

EDITED BY

Mohamed Khayet,
Complutense University of Madrid, Spain

REVIEWED BY

Antonio Comite,
University of Genoa, Italy
Enrica Fontananova,
National Research Council (CNR), Italy
Yuan Liao,
Nankai University, China

*CORRESPONDENCE

Juhana Jaafar,
✉ juhana@petroleum.utm.my

RECEIVED 14 December 2023

ACCEPTED 22 March 2024

PUBLISHED 26 April 2024

CITATION

Ahmad SNA, Matsuura T, Jaafar J, Jiang LY, Ismail AF, Othman MHD and A. Rahman M (2024), Modeling pore wetting in direct contact membrane distillation—effect of interfacial capillary pressure.
Front. Membr. Sci. Technol. 3:1355598.
doi: 10.3389/frmst.2024.1355598

COPYRIGHT

© 2024 Ahmad, Matsuura, Jaafar, Jiang, Ismail, Othman and A. Rahman. This is an open-access article distributed under the terms of the [Creative Commons Attribution License \(CC BY\)](https://creativecommons.org/licenses/by/4.0/). The use, distribution or reproduction in other forums is permitted, provided the original author(s) and the copyright owner(s) are credited and that the original publication in this journal is cited, in accordance with accepted academic practice. No use, distribution or reproduction is permitted which does not comply with these terms.

Modeling pore wetting in direct contact membrane distillation—effect of interfacial capillary pressure

S. N. A. Ahmad¹, Takeshi Matsuura^{1,2}, Juhana Jaafar^{1*}, L. Y. Jiang³, A. F. Ismail¹, M. H. D. Othman¹ and Mukhlis A. Rahman¹

¹Advanced Membrane Technology Research Centre (AMTEC), Faculty of Chemical and Energy Engineering, Universiti Teknologi Malaysia, Johor Bahru, Johor, Malaysia, ²Department of Chemical and Biological Engineering, University of Ottawa, Ottawa, ON, Canada, ³School of Metallurgy and Environment, Central South University, Changsha, Hunan, China

In this study, we aimed to develop a model for computing direct contact membrane distillation (DCMD) performance, taking into account capillary pressure effects at the liquid–gas interface within membrane pores. We developed a simulation model to investigate how factors such as pore radius, feed/permeate temperature, pressure, and contact angle influenced the distance of liquid intrusion into the pore, the weight flow rate in a single pore, and the temperature at the liquid–gas interface. The model predicted that the permeation rate would decrease with an increase in the feed pressure when the permeate pressure was kept constant and also when the pressure difference between the feed and permeate was kept constant. It also predicted that the permeation rate would increase with an increase in the permeate pressure when the feed pressure was kept constant. The model also indicated that partial pore wetting would be enhanced with an increase in feed pressure when the pore size was as large as 1 μm but would diminish when the pore size was as small as 0.1 μm . According to the model, partial pore wetting diminished with a decrease in the permeate pressure. The model's predictions were in line with the trends observed in the experimental DCMD flux data by many authors, particularly those regarding the effects of feed and permeate temperature and the effect of contact angle. The model's predictions were compared with the experimental data recorded in the literature, validating the model's accuracy.

KEYWORDS

simulation model, pore wetting, capillary pressure, pore size, hydrophilic membrane, DCMD

1 Introduction

Membrane distillation (MD) is a thermally driven separation process utilizing microporous membranes and operating on the principle of liquid–vapor equilibrium. In this process, only the volatile component (typically water) of the feed solution evaporates at the pore inlet, transfers through the pore, and exits from the pore outlet in either vapor or condensed form. The membrane material must be hydrophobic to prevent liquid water from entering the pore.

MD finds applications in the desalination of seawater and brackish water and treating concentrated brine from the reverse osmosis (RO) process (Rácz et al., 2014; Ibrar et al., 2022). Despite its impressive performance, commercialization faces challenges due to pore wetting, causing a significant decrease in MD flux and selectivity (Peña et al., 1993; Alklaibi and Lior, 2005; Gryta, 2005; 2007; Karakulski and Gryta, 2005; Peng et al., 2005; Tun et al., 2005; He et al., 2008; Qtaishat et al., 2009; Pangarkar et al., 2011; Camacho et al., 2013; Guillen-Burrieza et al., 2013; Peng et al., 2013; Saffarini et al., 2013; Rezaei and Samhaber, 2016).

Efforts have been made to mitigate MD pore wetting, including methods like liquid entry pressure (LEP) evaluation, introducing air bubbles into the feed solution, and dewetting the pores for regeneration and reuse (Baghbanzadeh et al., 2016; Warsinger et al., 2017; Ibrar et al., 2022; Hou et al., 2023). One of the most useful methods to evaluate the membrane's resistance against pore wetting is LEP, which is related to the contact angle and pore geometry (Rácz et al., 2014; Yazgan-Birgi et al., 2018). New devices have been designed and constructed to introduce air bubbles into the feed solution (Rezaei et al., 2018), and the pores have been dewetted to regenerate and reuse the membrane (Shin et al., 2016; Warsinger et al., 2017).

The principle of LEP is based on the following Laplace equation:

$$\Delta p = \frac{2\sigma \cos \theta}{r}, \quad (1a)$$

where Δp is the pressure required to make liquid (usually water) enter into a cylindrical pore of radius r , σ is the surface tension of water, and θ is the contact angle (CA). Note that θ is usually measured on a flat surface of the material of which the membrane is made and considered intrinsic to the material.

The contact angle in MD is integral to understanding surface properties and wetting behavior and is closely linked to thermodynamics. Surface energy, a key thermodynamic concept, delineates the energy at interfaces between phases. In MD, the contact angle, a representation of equilibrium between cohesive and adhesive forces, is mathematically expressed by the Young–Laplace equation, connecting the contact angle (θ) with surface tensions (γ_{SL} , γ_{SG} , and γ_{LG}). Hydrophobic behavior, characterized by contact angles exceeding 90° , implies reduced wetting, while contact angles below 90° indicate hydrophilic behavior, signaling increased wetting. This alignment with thermodynamics underscores the tendency of systems to seek lower energy states. Hydrophobic surfaces minimize solid–liquid interfacial energy, while hydrophilic surfaces minimize liquid–gas interfacial energy. In DCMD, thermodynamics governs the vapor–liquid equilibrium. The contact angle influences membrane surface wetting, impacting mass transfer and overall MD performance. Designing and optimizing MD systems for efficiency hinges on thermodynamic principles.

Consideration of small capillaries introduces confinement effects that alter water behavior. While thermodynamics still governs wetting, capillary size, roughness, and confinement modify equilibrium conditions. The meniscus formed in capillaries may deviate from the flat surface scenario due to these effects. The Young–Laplace equation ($\Delta P = \gamma_{LG}/R + \gamma_{LG}/R_s - \gamma_{SLG}/R_i$) elucidates the equilibrium of forces at a curved liquid interface. Regarding changes in the meniscus at high pressure in

trapped air, an increase in pressure (ΔP) impacts the curvature of the liquid–gas interface (ΔR), potentially altering meniscus shape. The specific impact depends on factors like material interfaces, trapped air characteristics, and system geometry, emphasizing the need for experimental validation to comprehensively understand these interactions.

In DCMD, a capillary is in contact with the feed and permeate water stream at the pore entrance and exit, respectively, and gas is trapped in between. When a capillary made of hydrophobic material is placed between two water phases, both at room temperature (see Figure 1A), the meniscus formed at the pore entrance is convex rightward, and the meniscus at the pore exit is convex leftward (Ashoor et al., 2016). The liquid phase pressure is slightly higher than the gas phase pressure to counterbalance the capillary pressure. If the temperature of the feed water is gradually increased, the gas phase pressure near the pore entrance will increase due to the evaporation of water, and it may surpass that of the liquid pressure when the feed water temperature is high enough. Then, in order to counterbalance the pressure difference, the meniscus at the pore entrance should change to concave leftward (Figure 1B); otherwise, the gas would appear in the feed water as gas bubbles. Thus, it is possible for the meniscus to change from the convex right (Figure 1A) to the concave left (Figure 1B), particularly at the pore entrance (Biswas and Kartha, 2019). This effect is negligible at the pore exit because the permeate stream is maintained at room temperature.

Based on this conceptual experiment, the discussions in this work use contact angles below 90° in the pore, in most cases, which allows drawing water into the capillary pore at the feed side of the pore, even when the pore is made of hydrophobic material.

Indeed, Gryta (2007) reported the possibility of partial pore wetting based on experiments conducted using hydrophobic MD membranes. Gryta's comprehensive investigation identified a spectrum of pore-wetting phenomena encompassing four distinct categories:

- 1) *Non-wetted*: The entire membrane pore is filled with gas/vapor.
- 2) *Surface-wetted*: The pore is partially filled with liquid. A gas/vapor layer remains between the liquid layers at the entrance and exit of the pore.
- 3) *Partial-wetted*: As pore wetting proceeds, some pores are completely filled with liquid.
- 4) *Wetted*: The pore is completely filled with liquid, and the feed solution leaks to the permeate.

Confirmation of the concept of partial pore wetting is supported by Gryta's work, where SEM/EDX analysis revealed concentration profiles of magnesium and calcium within the membrane pore (Gryta, 2007). Zhu et al. (2015) also observed the partial pore wetting of the PVA/PVDF composite hollow fiber membrane used for DCMD by applying SEM/EDX.

In wetting experiments involving PVDF, understanding channel geometry is paramount for grasping the interaction dynamics between liquids and PVDF membranes, as well as the influence of different geometrical features on wetting behavior. Research on PVDF hollow fiber membranes immersed in various solutions has yielded valuable insights into wetting behavior (Ritter, 2022).

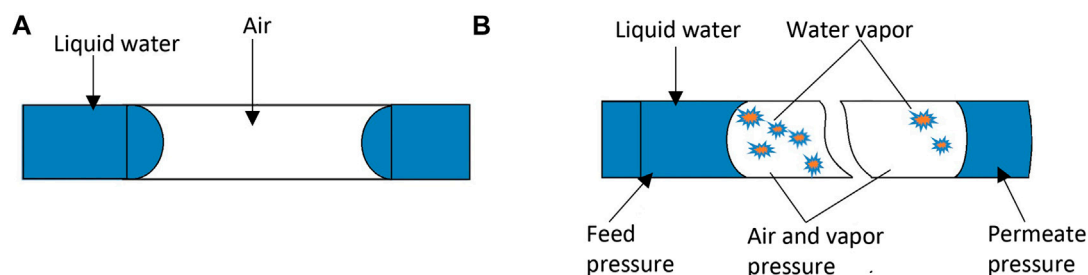


FIGURE 1
Meniscus change under high-pressure in the trapped air. (A) Pore entrance: convex right; exit: convex left. (B) Entrance shifts to concave left; exit to concave right.

Moreover, investigations into the impact of channel wettability and geometry on water plug wetting underscore the importance of these factors in wetting phenomena (Pfeiffer et al., 2017). Consequently, examining the channel geometry of PVDF in wetting experiments becomes crucial for comprehending liquid–membrane interactions, understanding the influence of geometrical features on wetting behavior, and discerning how membrane properties are influenced by channel geometry.

Parameter screening studies on PVDF/PVP multi-channel capillary membranes further highlight the significance of channel geometry in shaping membrane properties and performance. Essential factors such as PVDF content, PVP molecular weight, pore size, and surface roughness play pivotal roles in determining membrane characteristics and behavior in wetting experiments (Back et al., 2019). In summary, when discussing wetting phenomena, it is imperative to consider parameters such as feed salinity, feed cross velocity, and channel geometry, as they significantly impact how liquids spread on a solid substrate. It is essential to note, however, that this particular study introduces an assumption regarding the simplification of pores as simple cylindrical channels. This simplification mirrors a similar geometric representation observed in previous studies, ensuring consistency and comparability in the analytical approach.

Jacob et al. (2018) made a very detailed study of pore wetting of vacuum membrane distillation (VMD), also using SEM/EDX, and proposed two pore wetting indicators: 1) the proportion of totally wetted membrane area (ω_s) and 2) the average rate of liquid intrusion in the pore (called pore wetting) (ω_p). Eljaddi and Cabassud (2022) applied the same method to a photoplasmonic PVDF membrane, incorporating Ag-nanoparticles, and unveiled that the integration of Ag-nanoparticles enhances partial pore wetting.

Typically, the occurrence of pore wetting in hydrophobic membranes is attributed to the hydrophilization of the pore entrance. This transformation is often triggered by the deposition of salt crystals or hydrophilic foulants, alongside the conversion of a hydrophobic material to a hydrophilic state through various chemical reactions. This rationale further supports the assumption of a contact angle of less than 90° in the model prediction. However, despite the widespread acceptance of these mechanisms, a comprehensive interpretation of pore wetting based on mass and heat transport remains elusive.

Notably, the groundbreaking work by Chamani et al. (2019) on vacuum membrane distillation (VMD) provides a remarkable

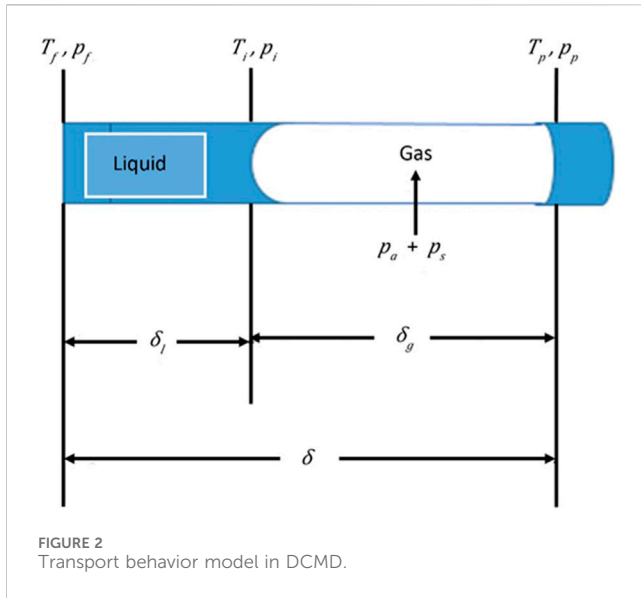
exception. Their research delves into the intricacies of pore wetting with a distinct focus on mass and heat transport dynamics. This stands in stark contrast to the prevailing trends in the advancement of membrane materials, fabrication methods, and characterization techniques for MD. Chamani et al.'s findings underscore the need for a nuanced understanding of pore-wetting mechanisms, challenging conventional perspectives and stimulating further exploration in this crucial aspect of membrane science and technology.

The objective of this work is to present a model for DCMD transport in which simultaneous mass and heat transfer is considered, particularly under the influence of the capillary pressure at the liquid–gas interface. Using the model, the effects of pore radius, contact angle in the pore, feed and permeate pressure on the length of water uptake in the pore, the temperature at the water–gas interface, and the MD flux are studied. The results obtained by the model simulation are further compared with the trends observed by the experimental data and reported in the literature.

2 Theory

The following assumptions are made to simplify the model:

- The feed contains only water. Hence, in the model development, liquid means water.
- The pore is straight and cylindrical.
- The thermal conductivity of the membrane material is so low that only the heat transfer in the pore is considered. This assumption and the following two assumptions are made to examine purely the effects of mass and heat transfer occurring in the pore on the MD mass flux without the effects of other factors.
- The heat enters into the water inside the pore only from the pore entrance. The heat does not enter from the pore wall.
- Boundary layer resistance of the feed liquid is ignored.
- The liquid mass transfer inside the pore follows the Poiseuille flow.
- The vapor mass transfer inside the pore follows the combined Knudsen/molecular diffusion mechanism.
- The meniscus of the liquid–vapor interface does not affect saturation vapor pressure.



- Heat transfer in the longitudinal direction is dominant.
- The liquid is incompressible

2.1 Mass transfer

The MD transport model in a single pore is developed for the steady state at which the liquid–vapor phase boundary remains inside the pore (Figure 2).

In DCMD, both ends of the pore are in contact with liquid, and it seems possible that liquid enters from both sides. However, for the reason given in the introduction, it is assumed that the liquid enters only from the pore entrance that is in contact with the feed stream.

There is some evidence to support the water entry from the feed side. For example, Gryta (2007) reported that water partially filled the pore from the feed side to the distance of 15 μm in the total 400 μm of membrane thickness by showing the Mg and Ca content profile in the longitudinal direction of the pore by EDX, wherein DCMD was performed by polypropylene membrane using tap water as a feed. Jiang and co-workers also showed the presence of Na on the feed side by EDX when DCMD was performed by their hydrophilic–hydrophobic hybrid membrane (Zhu et al., 2015; Feng et al., 2017). Based on this assumption, the model is also applicable for air gap membrane distillation (AGMD) with some changes in the transport parameters.

2.1.1 Liquid transport

For the liquid phase N_l , the weight flow rate (kg/s) in a single pore is given according to the Poiseuille flow mechanism as

$$N_l = \frac{\pi \rho r^4}{8\eta \delta_l} \Delta p_l \quad (1b)$$

where ρ (kg/m^3) is the density of the liquid, η (Pa s) is the viscosity of the liquid, δ_l (m) is the length of the liquid phase in the pore, and Δp_l (Pa) is the driving force for the liquid movement, given by

$$\Delta p_l = p_f - p_i = p_f - p_g + p_c \quad (2)$$

where p_f (Pa) is the pressure of the liquid at the pore entrance, p_g is the pressure of the gas phase (given later by Eq. 10) trapped between two liquid phases, and p_c (Pa) is the capillary pressure at the interface (Chesworth et al., 2008), given by

$$p_c = \frac{2\sigma \cos \theta}{r} \quad (3)$$

where σ (N/m) and θ ($^\circ$) are the liquid surface tension and contact angle, respectively.

In the above equations, the temperature dependence of the liquid properties is considered. Thus,

$$\rho = \frac{0.14395}{0.0112 \left(1 + \left(\frac{(T_f + T_i)^2}{649.727} \right)^{0.05107} \right)} \quad (4)$$

$$\eta = 0.001e^{-\frac{3.7188 + \frac{578.919}{-137.546 + (T_f + T_i)/2}}{}} \quad (5)$$

$$\sigma = 0.13415(1 - T_r)^{1.6146 - 2.035T_r + 1.5598T_r^2}, T_r = \frac{(T_f + T_i)/2}{647.3} \quad (6)$$

where T_f and T_i are the temperature at the pore entrance and at the liquid–gas interface. Thus, $(T_f + T_i)/2$ is the average liquid phase temperature.

2.1.2 Transport in the gas phase

In this work, the membrane pore sizes in a range of $0.01\text{--}1 \times 10^{-6}$ m are considered for DCMD. Because the mean free path of water at an atmospheric pressure and 50°C is 0.14×10^{-6} m (Khayet and Matsuura, 2011), the Knudsen numbers for such pores are 0.07–7.1. Hence, the combined Knudsen/ordinary diffusion mechanism is used for the transport of water vapor in air that is trapped between two liquid phases.

Then, N_v , the mass flux in the gas phase is given by

$$N_v = \left(\frac{\pi}{RT_g \delta_g} \right) \left[\left\{ \frac{2}{3} \left(\frac{8RT_g}{\pi M} \right)^{1/2} r^3 \right\}^{-1} + \left(\frac{p_g D}{p_a} r^2 \right)^{-1} \right]^{-1} (p_{s,i} - p_{s,p}) \quad (7)$$

where R and T_g are the gas constant (8.314 J/mol K) and the temperature of the gas phase (K), respectively; δ_g is the length of the gas phase; M is the molecular weight of water (18.02×10^{-3} kg/mol); p_g and p_a are the total pressure (Pa) of the gas phase and the partial pressure of the compressed air (Pa) in the gas phase, respectively; and $p_{s,i}$ and $p_{s,p}$ are the saturation vapor pressure of water at the water–gas interface and at the pore exit, respectively.

The following equations are used in Eq. 7:

$$p_a = \left(\frac{\delta}{\delta_g} \right) \left(\frac{p_f + p_p}{2} \right) \quad (8)$$

where δ is the total pore length (m) and p_f and p_p are the feed and permeate pressure (Pa), respectively.

$$p_s = \frac{p_{si} + p_{sp}}{2} \quad (9)$$

where p_s is the average vapor pressure of water (Pa) in the gas phase.

$$p_g = p_a + p_s \quad (10)$$

$$T_g = \frac{T_i + T_p}{2} \quad (11)$$

where T_i and T_p are the temperatures at the liquid–gas interface (K) and at the pore exit (K), respectively.

As for the diffusivity of water vapor in air D (m²/s),

$$D = D_{atm} (1.013 \times 10^5 / p_g), \quad (12)$$

where D_{atm} is the diffusivity (m²/s) at an atmospheric pressure, which is calculated by Bolz (1973):

$$D_{atm} = -2.775 \times 10^{-6} + 4.479 \times 10^{-8} T_g + 1.656 \times 10^{-10} T_g^2. \quad (13)$$

Furthermore,

$$N = N_l = N_g, \quad (14)$$

where N is the mass flux of water (kg/s) through the liquid and gas phases.

$$\delta = \delta_l + \delta_g. \quad (15)$$

As for the saturation vapor pressure of water,

$$p_{si} = 133.3 \times 10^{8.07131 - \frac{1730.63}{T_i - 39.7240}}, \quad (16)$$

$$p_{sp} = 133.3 \times 10^{8.07131 - \frac{1730.63}{T_p - 39.7240}}, \quad (17)$$

are used at the liquid–gas interface and at the pore exit, respectively.

2.2 Heat transfer

For the heat transfer in the liquid phase, the following differential equation is used at the steady state:

$$\frac{d^2 T}{dx^2} + \alpha \frac{dT}{dx} = 0, \quad (18)$$

where T is the temperature in the liquid phase (K) and x is the distance from the pore inlet (m) in the longitudinal direction, and

$$\alpha = \frac{k_l}{\rho c_p}, \quad (19)$$

where k_l and c_p are thermal conductivity (W/m K) and specific heat capacity (J/kg K) of the liquid, respectively.

The general solution of the differential equation is

$$T = C_1 + C_2 \exp(-\alpha x), \quad (20)$$

where C_1 and C_2 are the integration constants.

Using the boundary conditions

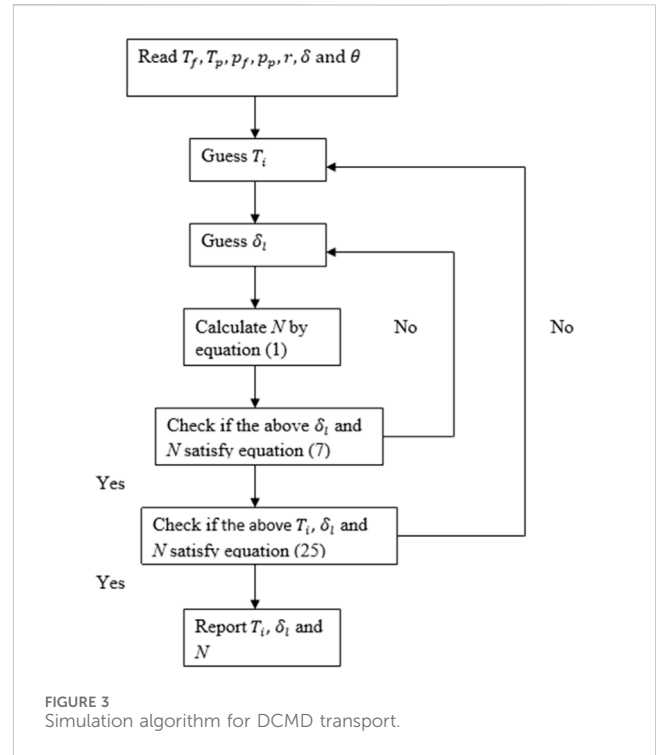
$$\text{B1: } T = T_f \text{ at } x = 0, \quad (21)$$

$$\text{B2: } \frac{dT}{dx} = -\frac{N\Delta H_v}{k_l \pi r^2} - h_g (T_i - T_p) \text{ at } x = \delta_g, \quad (22)$$

where ΔH_v is the heat of evaporation of liquid (J/kg) and h_g is the heat transfer coefficient of the gas phase (W/m² K).

C_1 and C_2 can be calculated from the above boundary conditions, resulting in the specific solution of the differential equation,

$$T = T_f + \left(-\frac{\alpha}{u} \right) \left\{ -\frac{N\Delta H_v}{k_l \pi r^2} - h_g (T_i - T_p) \right\} \times \left\{ \exp\left(-\frac{u\delta_l}{\alpha} \right) - \exp\left(-\frac{u}{\alpha} (\delta_l - x) \right) \right\}, \quad (23)$$



where

$$u = \frac{N}{\rho \pi r^2}. \quad (24)$$

Furthermore, because $T = T_i$ at $x = \delta_l$,

$$T_i = T_f + \left(-\frac{\alpha}{u} \right) \left\{ -\frac{N\Delta H_v}{k_l \pi r^2} - h_g (T_i - T_p) \right\} \left\{ \exp\left(-\frac{u\delta_l}{\alpha} \right) - 1 \right\}. \quad (25)$$

In Eq. 25, the temperature dependence of ΔH_v is considered as

$$\Delta H_v = 8.314 \times 647.3 \left(5.6297 \tau_r^{\frac{1}{3}} + 13.962 \tau_r^{\frac{2}{3}} - 11.673 \tau_r + 2.1784 \tau_r^2 - 0.31666 \tau_r^6 \right) \times 1000/18.02, \quad (26)$$

where τ_r is

$$\tau_r = 1 - \frac{T_i}{647.3}. \quad (27)$$

$N_l = N$, T_i and δ_l can be given by solving Eqs 1a, 1b, (2), (3), (7), and (25) simultaneously. The following equations (Eqs 8–17) are used in Eq. 7:

The simulation was performed using Microsoft Excel, and the algorithm is presented in Figure 3.

3 Results and discussion

In addition to the temperature-dependent properties of water, as shown in Eqs. (4)–(6), the following parameters were used in the simulation; that is, k_l and c_p are 0.6406 W/m K and 4180 J/kg K, respectively. Both of them are used at 50°C (323.2 K). Even though both parameters depend on the temperature, their

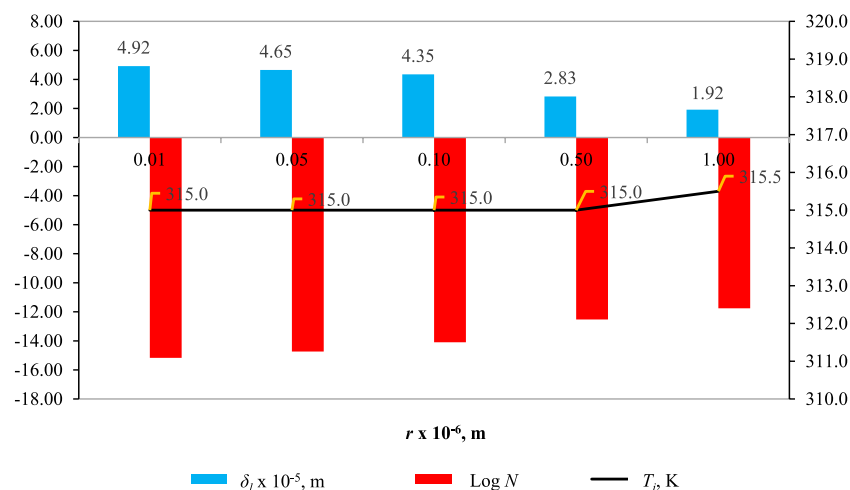


FIGURE 4 Effect of r on δ_l , $\log N$ (kg/s), and T_i with fixed parameters ($T_f = 353.2 \text{ K}$, $T_p = 293.2 \text{ K}$, $p_f = 1 \times 10^5 \text{ Pa}$, $p_p = 1 \times 10^5 \text{ Pa}$, $\theta = 60^\circ$, and $\delta = 5 \times 10^{-5} \text{ m}$).

changes within a temperature range of 20–80°C (293.2–353.2 K) were found to have negligible effects on the results of the simulation.

The heat transfer was calculated using Eqs. 18 through 27. Specifically, the heat transfer coefficient, h_g , required in Eq. 25 was calculated by k_g/δ_g , using $k_g = 0.0275 \text{ W/m K}$, which is the thermal conductivity of humid air. Even though k_g changes considerably with the change of temperature and humidity, it was found that it did not affect the simulation result because the heat transfer at the liquid–gas interface by the evaporation of the liquid is much larger than the heat transfer by conduction ($\frac{N\Delta H_v}{k_l\pi r^2} \gg h_g(T_i - T_p)$ in Eq. 25).

3.1 Effect of r

Figure 4 illustrates how varying the pore radius (r) affects δ_l , N , and T_i , while maintaining fixed parameters: $T_f = 353.2 \text{ K}$, $T_p = 293.2 \text{ K}$, $p_f = 1 \times 10^5 \text{ Pa}$, $p_p = 1 \times 10^5 \text{ Pa}$, $\theta = 60^\circ$, and $\delta = 5 \times 10^{-5} \text{ m}$. The pore radius, r , was adjusted from 0.01 to $1 \times 10^{-6} \text{ m}$.

In Figure 4, the influence of pore radius (r) on wetting characteristics, when the pore radius $r = 0.01 \times 10^{-6} \text{ m}$, δ_l reaches $4.92 \times 10^{-5} \text{ m}$, signifying that over 90% of the pore space is occupied by the liquid phase due to the pronounced capillary force in such a small pore. As r increases to $1 \times 10^{-6} \text{ m}$, δ_l progressively decreases to 1.92×10^{-5} , accompanied by a significant rise in N from $6.69 \times 10^{-16} \text{ kg/s}$ to $1.73 \times 10^{-12} \text{ kg/s}$ at the larger radius ($r = 1 \times 10^{-6} \text{ m}$, the red bars in Figure 4). This underscores the substantial impact of the r on N . Despite T_i being nearly 40°C lower than T_f due to significant temperature polarization caused by the liquid phase in the pore, T_i remains relatively constant with varying r . This constancy is attributed to the compensatory effect of the decrease in N countering the increase in δ_l . In summary, the intricate interplay between pore size, capillary forces, and temperature dynamics shapes the wetting behavior within porous media.

3.2 Effect of T_f

Figure 5 illustrates the impact of feed temperature T_f on δ_l , N , and T_i , while maintaining fixed parameters: $T_p = 293.2 \text{ K}$, $p_f = 1 \times 10^5 \text{ Pa}$, $p_p = 1 \times 10^5 \text{ Pa}$, $r = 1 \times 10^{-6} \text{ m}$, $\theta = 60^\circ$, and $\delta = 5 \times 10^{-5} \text{ m}$.

In Figure 5, the effect of the impact of feed temperature (T_f) on wetting characteristics (blue bar), δ_l (blue bar) decreases with rising T_f , maintaining approximately 20% pore filling of the entire pore length with liquid. However, in Figure 5 (red bar), N deviates from the expected exponential increase tied to vapor pressure elevation with increasing feed temperature (T_f). This unexpected behavior is attributed to heightened temperature polarization at higher T_f . In Figure 5, (T_i) reveals the dynamics of temperature change, showing a mere 2% decrease (from 303.2 K to 297 K) when T_f is 303.2 K but a more significant 11% drop (from 353.2 K to 315 K) when T_f is 353.2 K. This contextualizes the observed deviation in N , underscoring the impact of temperature polarization on the anticipated exponential relationship between N and vapor pressure as T_f increases.

3.3 Effect of T_p

Figure 6 shows the effect of T_p on δ_l , N , and T_i when T_f , p_f , p_p , r , θ , and δ are fixed to 353.2 K, $1 \times 10^5 \text{ Pa}$, $1 \times 10^5 \text{ Pa}$, $1 \times 10^{-6} \text{ m}$, 60° , and $5 \times 10^{-5} \text{ m}$, respectively.

As depicted in Figure 6, the liquid intrusion length δ_l decreases as the permeate temperature T_p increases. This trend can be attributed to the wettability of the membrane surface. At higher permeate temperatures, the membrane becomes more hydrophobic, leading to reduced liquid intrusion into the pores.

Temperature polarization (T_p): T_p represents the difference between the bulk feed temperature T_f and the temperature at the membrane/solution interface T_{mf} where the vapor–liquid transition occurs. As T_p increases, the temperature polarization, $T_f - T_i$, decreases. This decrease in temperature polarization is

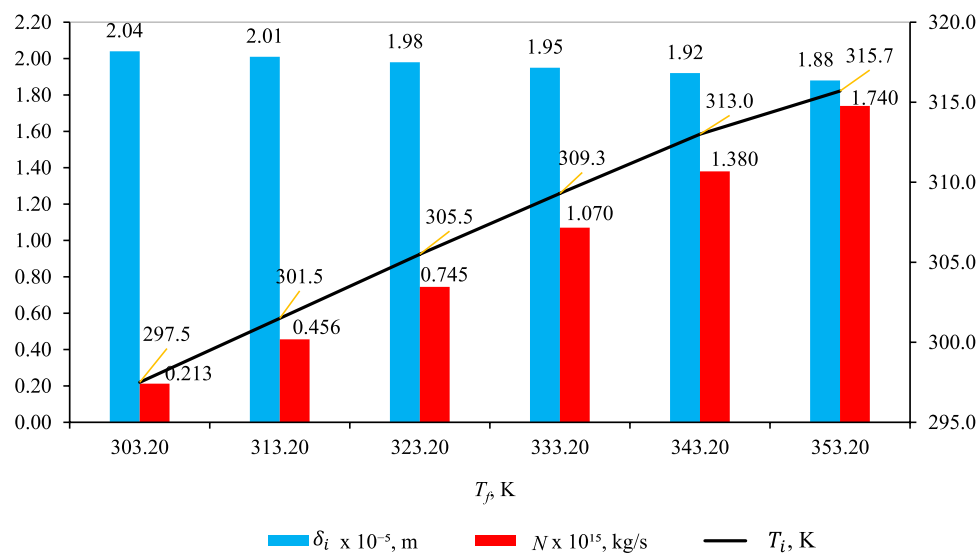


FIGURE 5 Effect of T_f on δ_i , N , and T_i with fixed parameters ($T_p = 293.2$ K, $p_f = 1 \times 10^5$ Pa, $p_p = 1 \times 10^5$ Pa, $r = 1 \times 10^{-6}$ m, $\theta = 60^\circ$, and $\delta = 5 \times 10^{-5}$ m).

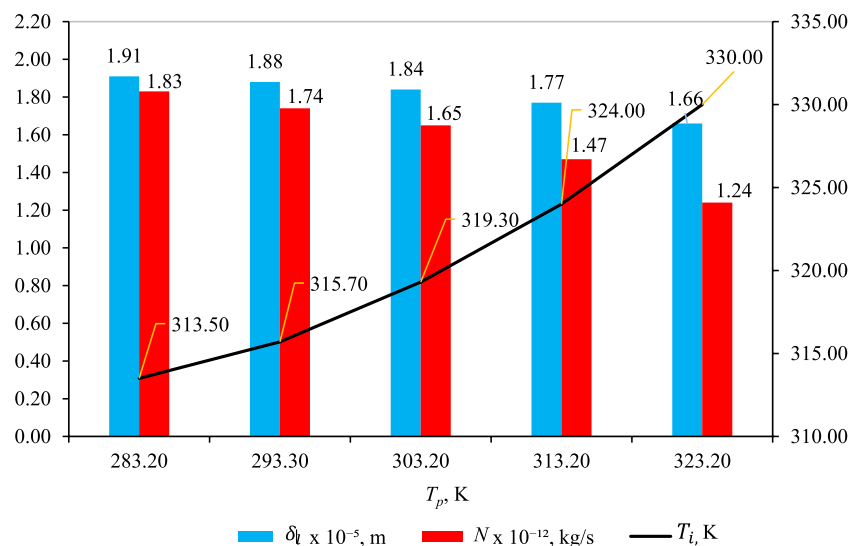


FIGURE 6 Effect of T_p on δ_i , N , and T_i with fixed parameters ($T_f = 353.2$ K, $p_f = 1 \times 10^5$ Pa, $p_p = 1 \times 10^5$ Pa, $r = 1 \times 10^{-6}$ m, $\theta = 60^\circ$, and $\delta = 5 \times 10^{-5}$ m).

noteworthy and can be linked to the heat transfer dynamics within the system.

Impact on mass flux (N): although temperature polarization decreases, there is also a decrease in mass flux (N) with increasing T_p . However, it is essential to recognize that the impact of T_p on mass flux is quantitatively smaller than the influence of feed temperature T_f . For instance, a 40 K increase in T_p results in a measured decrease in N of 0.59×10^{-12} kg/s. In contrast, a similar increase in T_f leads to a more substantial increase in N , specifically 1.17×10^{-12} kg/s.

The discrepancy between the effects of T_p and T_f suggests that the system is more sensitive to variations in T_f . The nuanced interplay between temperature parameters and mass flux underscores the

complexity of the system dynamics. In summary, understanding the intricate balance between temperature, wettability, and mass transport is crucial for optimizing membrane-based processes. Further investigations will help uncover the underlying mechanisms governing these observed trends.

3.4 Effect of p_f

Figure 7 shows the effect of p_f on δ_i , N , and T_i when T_f , T_p , p_p , r , θ , and δ are fixed to 353.2 K, 293.2 K, 1×10^5 Pa, 0.1×10^{-6} m, 60° , and 5×10^{-5} m, respectively.

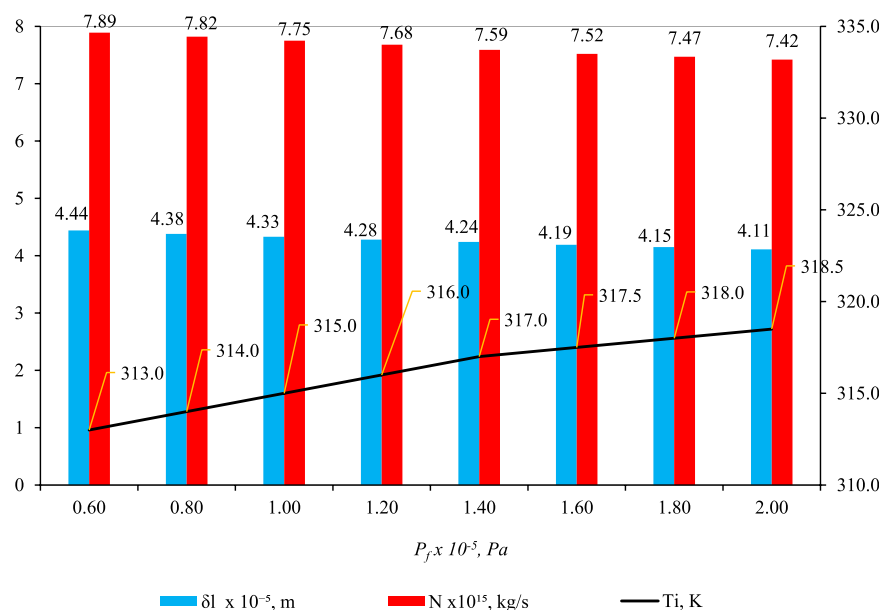


FIGURE 7
Effect of p_f on δ_l , (blue), N (red), and T_i (line), where $T_f = 353.2 \text{ K}$, $T_p = 293.2 \text{ K}$, $p_p = 1 \times 10^5 \text{ Pa}$, $r = 0.1 \times 10^{-6} \text{ m}$, $\theta = 60^\circ$, and $\delta = 5 \times 10^{-5} \text{ m}$.

In Figure 7, a compelling pattern emerges: the parameter δ_l displays a decreasing trend as feed pressure (p_f) increases. This seemingly paradoxical observation results from various factors. Despite higher feed pressure propelling liquid deeper into the pore, a simultaneous rise in temperature at the liquid–gas interface (T_i) amplifies capillary pressure in the gas phase (p_g), diverting the liquid back toward the pore entrance. The findings in Figure 7 (blue bar) underscore that the influence of p_g on δ_l outweighs that of p_f . This pattern is also evident in the reduction of another parameter, N (mass flux of water through liquid and gas phases), as p_f increases (Figure 7, red bar).

The initially counterintuitive decrease in δ_l with increasing p_f becomes clear upon examining the role of capillary pressure (p_g). As p_f rises, more liquid infiltrates the pore structure, but the pivotal factor is the impact of p_g , controlled by T_i . Analyzing the relationship between T_i , we observe its increase with p_f , leading to an elevated saturation vapor pressure (ψ_{psi}) (Eq. 16), subsequently influencing p_g (Eq. 10). The essence lies in the dominance of p_g over p_f in influencing δ_l . Essentially, capillary forces play a predominant role in determining δ_l , and a similar phenomenon is observed for parameter N . With an increase in p_f , T_i rises, causing an escalation in p_g , which, in turn, alters flow behavior and results in a decrease in N .

The core relationship driving the observed phenomena lies in the intricate relationship between capillary pressure in the gas phase (p_g) and feed pressure (p_f). The augmentation of p_f facilitates enhanced liquid entry into the pore space, yet the prevailing influence of capillary forces, particularly governed by T_i , ultimately dictates the behavior of the liquid phase. Eq. 10 and (16) are likely instrumental in comprehending this intricate interplay, encapsulating the dynamic involvement of surface tension, capillary pressure, and porosity.

To synthesize the findings, it becomes evident that the increase in T_i (and subsequently p_g) eclipses the impact of p_f , shedding light on the discernible trends in δ_l and N . This interdependence is

graphically depicted in Figures 5–7 (as depicted by the blue bars), where an escalation in T_i , T_p , and p_f precipitates a swift reduction in δ_l .

The decrease in δ_l is particularly conspicuous when T_f rises, as this prompts a rapid decline in wetting characteristics. Various factors related to wettability properties come into play as the temperature increases. Elevated temperatures induce a reduction in hydroxyl groups within cellulose chains, leading to diminished moisture uptake and decreased water adsorption, thereby influencing wettability properties (Sipahutar et al., 2021). Furthermore, heightened temperatures result in the expansion of membrane pores, escalating the risk of membrane wetting and enlarging pore sizes. This expansion is more pronounced at elevated temperatures due to an amplified temperature gradient and increased heat transfer rates. Additionally, the rise in temperature concurrently diminishes the surface tension and contact angle, further contributing to membrane wetting (Gryta, 2020). In summary, the collective impact of these factors at heightened temperatures manifests in a precipitous decline in wetting characteristics (δ_l).

Figure 8 elucidates the impact of feed pressure (p_f) on key parameters— δ_l , N , and T_i , while maintaining specific conditions: T_f , T_p , p_p , r , and δ are fixed to 353.2 K, 293.2 K, $1 \times 10^5 \text{ Pa}$, $1 \times 10^{-6} \text{ m}$, and $5 \times 10^{-5} \text{ m}$, respectively. Two distinct contact angles, $\theta = 60^\circ$ (blue shades) and $\theta = 82^\circ$ (red shades), are considered. Notably, the pore radius (r) has been adjusted from $0.1 \times 10^{-6} \text{ m}$ to $0.1 \times 10^{-6} \text{ m}$ in Figure 7 to $1 \times 10^{-6} \text{ m}$ in Figure 8. Despite the different pressure ranges studied for 60° (0.5 – $1.5 \times 10^5 \text{ Pa}$) and 82° (1.4 – $2.0 \times 10^5 \text{ Pa}$), both contact angles exhibit consistent trends. A notable observation is the reversal in the trend of T_i in Figure 8 compared to Figure 7. Specifically, T_i decreases as p_f increases, resulting in an upswing in δ_l (Figure 8). In contrast, the flux, N , follows the same decreasing trend with increasing p_f in both Figures 7, 8.

Here, the contact angle values of 60° and 82° are commonly used in studies to represent different wetting properties of surfaces. A

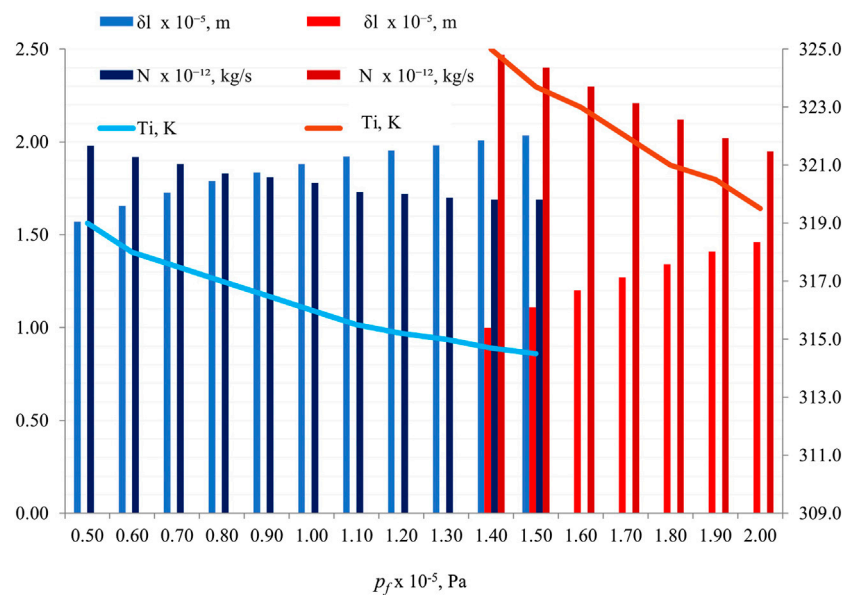


FIGURE 8 Effect of p_f on δ_l , N , and T_i , with fixed parameters ($T_f = 353.2$ K, $T_p = 293.2$ K, $P_p = 1 \times 10^5$ Pa, $r = 1 \times 10^{-6}$ m, and $\delta = 5 \times 10^{-5}$ m). Two contact angles are represented: $\theta = 60^\circ$ (blue shades) and $\theta = 82^\circ$ (red shades).

contact angle above 90° indicates hydrophobicity, where the surface repels water, while an angle below 90° signifies hydrophilicity, indicating good wetting by water (Danish, 2020). These specific angles are chosen to represent these distinct wetting behaviors for experimental and analytical purposes. Similarly, the values of 1.0×10^5 Pa and 1.5×10^5 Pa for p_f (pressure) are set to explore the impact of varying pressures on wetting characteristics and interfacial tension in fluid–rock systems. By using different pressure values within this range, researchers can analyze how changes in pressure affect contact angles and interfacial tension, providing insights into the behavior of fluids interacting with rock surfaces under different conditions. These specific pressure values are selected to study a range of scenarios and understand the nuances of fluid–rock interactions comprehensively (Taetz et al., 2016).

This reversal in T_i behavior underscores the system's sensitivity to variations in p_f , a shift that can be influenced by adjusting parameters such as pore radius and contact angle. The cohesion between fixed conditions and altered experimental factors in Figure 8 emphasizes the intricate dynamics governing the observed trends in δ_l , N , and T_i . These findings contribute to a nuanced understanding of how the system responds to changes in feed pressure (p_f) under controlled conditions.

3.5 Effect of p_p

Figure 9 shows the effect of p_p on δ_l , N , and T_i when parameters T_f , T_p , p_f , and δ are fixed to 353.2 K, 293.2 K, 1.5×10^5 Pa, and 5×10^{-5} m, respectively. Again, θ is either 60° (blue shades) or 82° (red shades), and r is 1×10^{-6} m. Comparing Figures 8, 9, it is found that the decrease in p_p has the same effect as the increase in p_f . As $p_f - p_p$ increases by either an increase in p_f or a decrease in p_p , δ_l experiences an increase, while N and T_i exhibit a decrease.

In fluid flow, the significance of maintaining a consistent pressure difference ($p_f - p_p$) is evident in the relationship between flux (N) and permeate pressure (p_p). As permeate pressure increases, the flux also increases, indicating a direct correlation between these two parameters (Naidu et al., 2015). This consistency in pressure difference ensures predictable and controlled flux rates, which are crucial for optimizing system performance and efficiency in various applications like reverse osmosis, gas separation, and membrane processes (Stewart, 2014). By regulating this pressure difference, engineers can manipulate the flux of substances through membranes, leading to improved separation efficiency and overall system effectiveness.

3.6 Effect of p_f when $p_f - p_p$ is fixed

Figure 10 shows the effect of p_f on δ_l , N , and T_i when T_f , T_p , $p_f - p_p$, r , θ , and δ are fixed to 353.2 K, 293.2 K, 0.5×10^5 Pa, 1×10^{-6} m, 60° , and 5×10^{-5} m, respectively. In this specific scenario, an escalation in p_f leads to a concurrent decrease in δ_l , a subtle augmentation in N , and an elevation in T_i . Remarkably, this dynamic unfolds while maintaining a consistent ($p_f - p_p$).

Understanding the relationship between liquid intrusion length (δ_l), feed pressure (p_f), mass flux (N), and liquid–gas interface temperature (T_i) is crucial in various engineering applications. As p_f increases, a decrease in δ_l suggests improved heat transfer efficiency, with smaller values indicating more effective heat transfer. The subtle increase in mass flux (N) signifies a rise in fluid flow or mass flow rate. Additionally, the elevation in T_i indicates that the system's internal temperature rises with escalating p_f , which is essential for designing and optimizing temperature-controlled processes like those in chemical reactors.

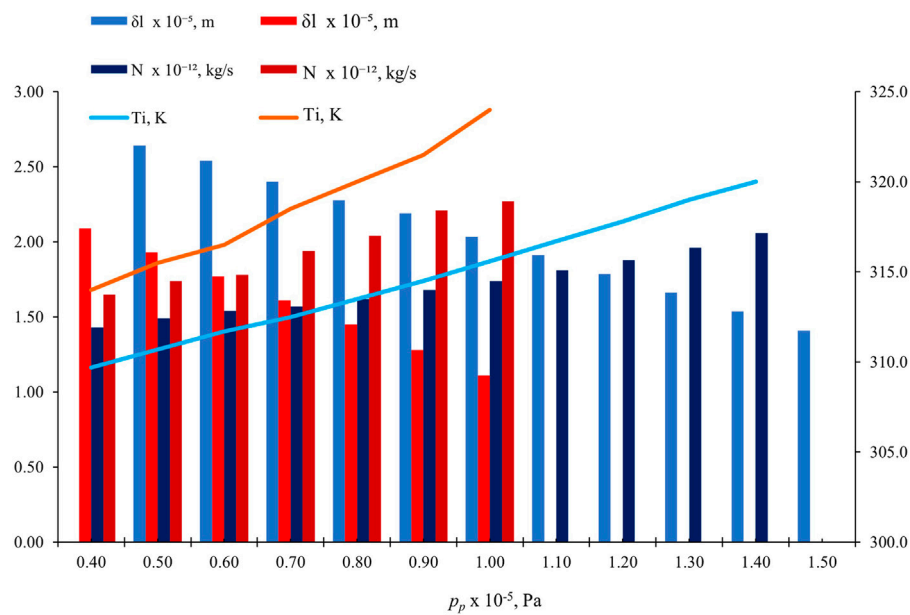


FIGURE 9

Effect of p_p on δ_l , N , and T_i , with fixed parameters ($T_f = 353.2$ K, $T_p = 293.2$ K, $p_p = 1.5 \times 10^{-5}$ Pa, $r = 1 \times 10^{-6}$ m, and $\delta = 5 \times 10^{-5}$ m). Two contact angles are represented: $\theta = 60^\circ$ (blue shades) and $\theta = 82^\circ$ (red shades).

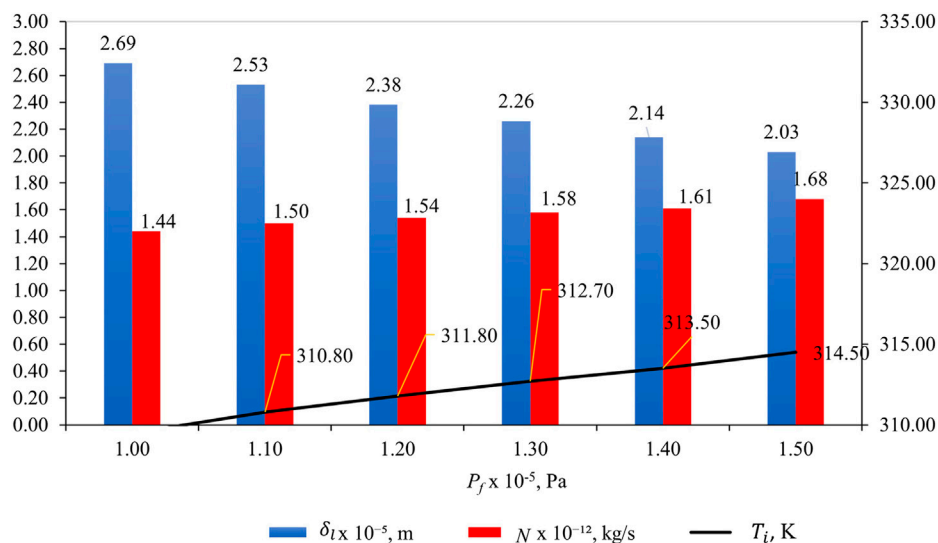


FIGURE 10

Effect of p_f on δ_l , N , and T_i , with fixed parameters ($T_f = 353.2$ K, $T_p = 293.2$ K, $p_f - p_p = 0.5 \times 10^5$ Pa, $r = 1 \times 10^{-6}$ m, $\theta = 60^\circ$, and $\delta = 5 \times 10^{-5}$ m).

or electronic devices (Rouquerol et al., 2011). In this case, we must balance the benefits of enhanced heat transfer and fluid flow against drawbacks like increased energy consumption or system complexity (Rouquerol et al., 2011).

3.7 Effect of θ

Figure 11 shows the effect of θ on δ_l , N , and T_i , when T_f , T_p , p_f , p_p , r , and δ are fixed to 353.2 K, 293.2 K, 1×10^5 Pa, 1×10^5 Pa, 1×10^{-6} m, and 5×10^{-5} m, respectively.

In Figure 11 (blue bar), δ_l decreases as θ increases because less water is driven into the pore as the hydrophobicity of the membrane material increases. In Figure 11, the line shows that T_i increases as θ increases because of the decrease in temperature polarization with the decrease in the length of the liquid phase. A decrease in δ_l enhances the flow rate of the liquid phase (Eq. 1), and as a result, N increases (red bar). At $\theta = 81^\circ$, δ_l and N become 0.326×10^{-5} m and 4×10^{-12} kg/s, respectively. Even though it is not shown in the figure, θ may increase until it becomes 85.6° , where δ_l becomes 0, and the pore is filled only with the gas phase. N becomes as high as 7.79×10^{-12} kg/s. This scenario is more explicitly illustrated in Figure 13.

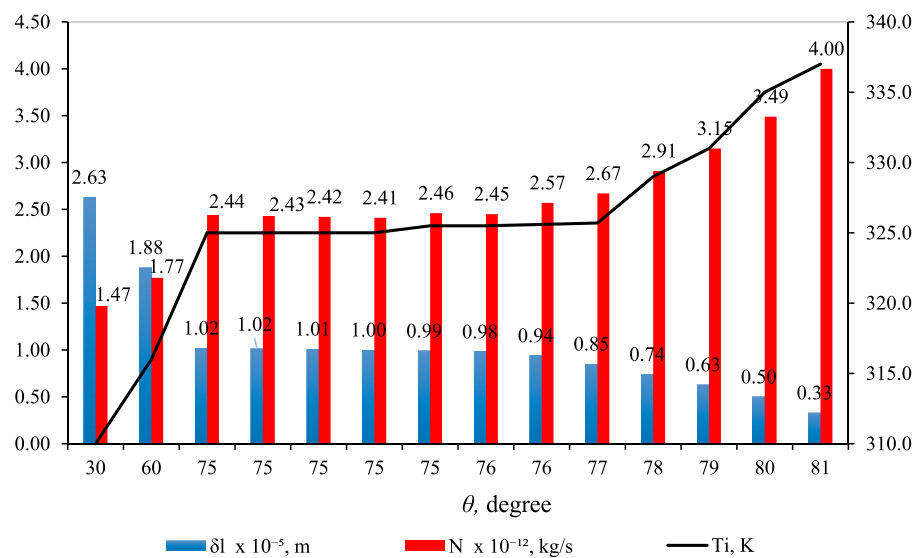


FIGURE 11 Effect of θ on δ_l , N , and T_i , with fixed parameters ($T_f = 353.2$ K, $T_p = 293.2$ K, $p_f = 1 \times 10^5$ Pa, $p_p = 1 \times 10^5$ Pa, $r = 1 \times 10^{-6}$ m, and $\delta = 5 \times 10^{-5}$ m).

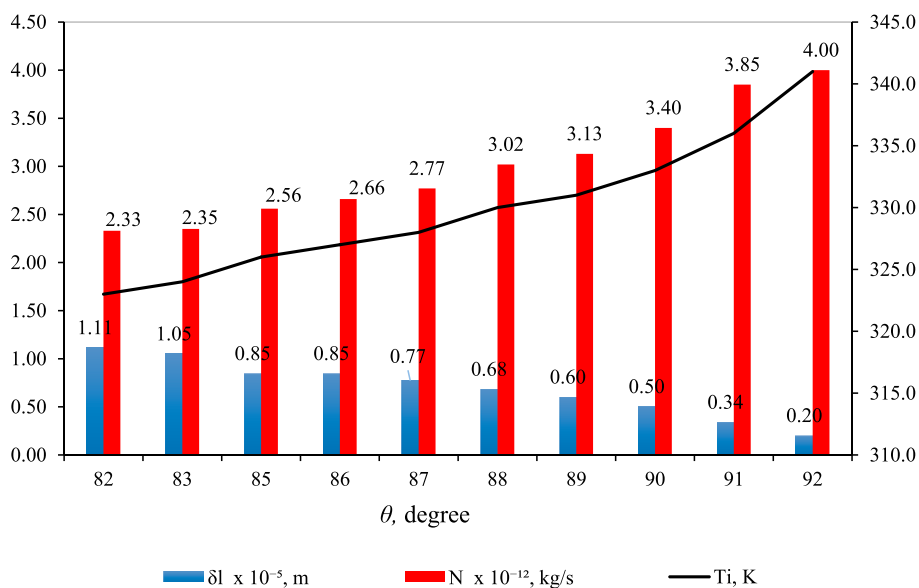


FIGURE 12 Effect of θ on δ_l , N , and T_i , with fixed parameters ($T_f = 353.2$ K, $T_p = 293.2$ K, $p_f = 1.5 \times 10^5$ Pa, $p_p = 1 \times 10^5$ Pa, $r = 1 \times 10^{-6}$ m, and $\delta = 5 \times 10^{-5}$ m).

Figure 12 illustrates the impact of contact angle (θ) on δ_l , N , and T_i with fixed parameters ($T_f = 353.2$ K, $T_p = 293.2$ K, $p_f = 1.5 \times 10^5$ Pa, $p_p = 1 \times 10^5$ Pa, $r = 1 \times 10^{-6}$ m, and $\delta = 5 \times 10^{-5}$ m). It is important to note that p_f has been increased to 1.5×10^5 Pa from the 1×10^5 Pa used in Figure 11. The observed patterns in Figure 12 align with those in Figure 11, where δ_l decreases, and N and T_i increase with higher θ values.

However, a key distinction is the use of larger θ values in Figure 12. This adjustment is necessitated by the higher hydrophobicity required in the membrane material to counteract the elevated feed pressure (p_f) and maintain the interface position. Remarkably, even with θ values exceeding

90° , indicating hydrophobicity in the pore, there is partial liquid filling, according to Figure 12. Notably, the maximum θ is 92° in this scenario, where δ_l and N are reported as 0.201×10^{-5} m and 4.73×10^{-12} kg/s, respectively. It is worth mentioning that θ may further increase until it reaches 107.9° , leading to δ_l becoming 0 and N reaching 7.79×10^{-12} kg/s, as revealed in the data.

In Figure 13, N is graphed against δ_l for two different feed pressures: $p_f = 1.0 \times 10^5$ Pa (blue) and $p_f = 1.5 \times 10^5$ Pa (red). Notably, the data for both feed pressures overlap, and there is a consistent increase in N as δ_l decreases. Particularly, N exhibits a steep increase when δ_l is below 0.5×10^{-5} m, reaching $N = 7.79 \times$

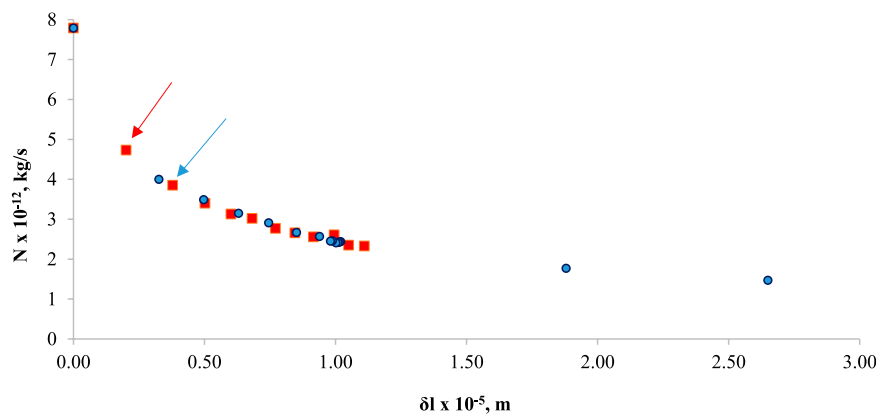


FIGURE 13

N versus δ_l , with fixed parameters ($T_p = 293.2$ K, $p_f = 1.0 \times 10^5$ Pa (blue), $p_f = 1.5 \times 10^5$ Pa (red), $p_p = 1 \times 10^5$ Pa, $r = 1 \times 10^{-6}$ m, and $\delta = 5 \times 10^{-5}$ m).

10^{-12} kg/s when $\delta_l = 0$. This signifies a scenario where there is no liquid in the pore, and transport occurs solely in the vapor phase.

4 Comparison with the experimental data

The simulation model proposed in this work does not include some factors that would affect the DCMD performance, such as the heat transfer coefficient of the feed and permeate boundary layer and the thermal conductivity of the membrane polymer matrix. Therefore, the agreement of the computational results with the experimental data in their numerical values cannot be tested. Nevertheless, the validity of the model simulation can be examined by comparing the trends it predicts with those observed by experiments. The simulation predicts that the DCMD flux

- 1) Increases as r increases. (Figure 4)
- 2) Increases as T_f increases (Figure 5)
- 3) Decreases as p_f increases (Figure 7; Figure 8)
- 4) Increases as p_p increases (Figure 9)
- 5) Increases as θ increases (Figure 11; Figure 12).

Among those, 1), 2), and 5) are quite obvious and have been proven by many experiments (Khayet and Matsuura, 2011). The trends predicted by 3) and 4) are, however, not quite obvious because only a few studies have examined the effect of P_f and p_p on the MD flux. Some of those examples are as follows:

Park and Lee (2019) observed a decrease in the flux with an increase in the feed pressure p_f and attributed it to membrane compaction. They also noticed a sudden increase in the flux at a high pressure caused by the pore wetting.

Liu et al. (2022) observed a 62% increase in the initial flux of DCMD when the feed pressure (P_f) was changed from 1 kPa (gauge) to -30 kPa (gauge) for a commercial PVDF membrane. They have explained this phenomenon by 1) considering the contribution of the molecular diffusion and the Knudsen diffusion in the pore and 2) attributing to the increase in the heat transfer coefficient of the

boundary layer at the feed side and the reduction in transmembrane heat conduction caused by the change of the meniscus shape from convex to concave.

In summary, the trends observed by the experiments were:

- 1) Park and Lee (2019) also observed a decrease in the flux with an increase in the feed pressure and attributed it to membrane compaction. They also noticed a sudden increase in the flux at a high pressure caused by the pore wetting.
- 2) The DCMD flux of the incompressible hollow fiber membrane did not change with an increase in p_f (Zhang et al., 2011).
- 3) The DCMD flux increased with a decrease in p_f . It is unlikely the pore deformation occurred when the feed pressure was decreased (Liu et al., 2022).

As for the effect of the increase in p_p , the simulation predicts the flux decrease (Figures 7, 8). Thus, the model prediction agrees with experimental results 1) but disagrees with the experimental results 2).

In Zhang et al.'s compression experiments (Zhang et al., 2011), however, pressure was applied to the hollow fiber on both sides, that is, the lumen and the shell side, but in the DCMD experiments, the pressure was applied only to the feed side (likely the lumen side of the hollow fiber according to their article (Zhang et al., 2010)). Then, it is possible that the hollow fiber expanded, resulting in an increase in DCMD flux. If such an expansion did not take place, the flux could decrease with an increase in p_p as the model predicted. The model predicts a slight increase in flux as feed pressure rises, a condition where $p_f - p_p$ is maintained constant, as depicted in Figure 10. The concept of the liquid intrusion length (δ_l) serves as an indicator of partial pore wetting. Larger values of δ_l suggest more pronounced pore wetting. Although, there has been no direct measurement of δ_l under various DCMD operating conditions to date, it is reasonable to speculate that the likelihood of wetting along the entire pore length increases as δ_l becomes larger.

The model simulation, on the other hand, predicts that δ_l increases with an increase in p_f , when the pore size is as large as $1 \mu\text{m}$ (Figure 8). Thus, the model prediction agrees with 1) of the above experimental results. However, δ_l tends to decrease with an increase in the feed pressure when the pore size is as small as $0.1 \mu\text{m}$

(Figure 7). It would be interesting to test this prediction experimentally. δ_l decreases with an increase in p_p (Figure 9). This agrees with 2) of the above experimental results.

5 Conclusion

We developed a simulation model to investigate flux and partial pore wetting in DCMD while considering the influence of capillary pressure at the liquid–gas interface. In this context, we assumed that the contact angle inside the pore was less than 90° due to the high pressure in the gas phase or potential alterations in chemistry at the pore wall. The model predicts that the weight flow rate increases with an increase in the pore radius, rises with higher feed temperature, decreases with an increase in permeate temperature, and increases with an increase in the contact angle. These trends have already been experimentally confirmed by numerous authors.

Regarding the effect of feed pressure (p_f), the model predicts a decrease in the permeation rate as feed pressure increases while keeping the permeate pressure constant. This prediction generally aligns with experimental results, except in the case of hollow fibers, which are considered incompressible. Additionally, the model forecasts a decrease in permeation rate with increasing feed pressure while maintaining a constant pressure difference between the feed and permeate, a trend that contradicts certain experimental findings. However, these instances of disagreement can be attributed to the potential expansion of the pore during DCMD experiments.

Furthermore, the model suggests that partial pore wetting is enhanced with an increase in feed pressure when the pore size is as large as $1\ \mu\text{m}$, which is consistent with experimental results obtained from membranes with an average pore size of $0.67\ \mu\text{m}$. Conversely, the model predicts an opposite trend when the pore size is as small as $0.1\ \mu\text{m}$. This prediction warrants further experimental testing to validate its accuracy. According to the model, partial pore wetting diminishes as permeate pressure increases, a trend supported by experimental observations of pore wetting. These findings provide valuable insights into the complex interplay of feed and permeate pressure in the context of DCMD and its potential applications.

These insights deepen our comprehension of the nuanced dynamics within DCMD, shedding light on potential applications. Future research should prioritize rigorous experimental validation and refine the model to encompass diverse membrane characteristics and operating conditions, enhancing its predictive accuracy.

Data availability statement

The raw data supporting the conclusion of this article will be made available by the authors, without undue reservation.

References

- Alklaibi, A. M., and Lior, N. (2005). Membrane-distillation desalination: status and potential. *Desalination* 171, 111–131. doi:10.1016/j.desal.2004.03.024
- Ashoor, B. B., Mansour, S., Giwa, A., Dufour, V., and Hasan, S. W. (2016). Principles and applications of direct contact membrane distillation (DCMD): a comprehensive review. *Desalination* 398, 222–246. doi:10.1016/j.desal.2016.07.043
- Back, J. O., Brandstätter, R., Spruck, M., Koch, M., Penner, S., and Rupprich, M. (2019). Parameter screening of PVDF/PVP multi-channel capillary membranes. *Polym. (Basel)* 11, 463. doi:10.3390/polym11030463
- Baghbanzadeh, M., Rana, D., Lan, C. Q., and Matsuura, T. (2016). Effects of hydrophilic silica nanoparticles and backing material in improving the structure and

Author contributions

SA: visualization, and writing–original draft. TM: conceptualization, data curation, formal analysis, funding acquisition, investigation, methodology, resources, supervision, validation, visualization, writing–original draft, and writing–review and editing. JJ: conceptualization, funding acquisition, investigation, methodology, project administration, supervision, validation, visualization, writing–review and editing, and data curation. LJ: validation and writing–review and editing. AI: validation and writing–review and editing. MO: validation and writing–review and editing. MA: validation and writing–review and editing.

Funding

The author(s) declare that financial support was received for the research, authorship, and/or publication of this article from the Ministry of Higher Education, Malaysia under HICoE grant, R.J090301.7851.4J433 and from Universiti Teknologi Malaysia under Hi-Tech (F4) grant Q.J130000.4609.00Q14.

Acknowledgments

The authors would like to express gratitude to the Ministry of Higher Education, Malaysia for funding under HICoE grant, R.J090301.7851.4J433 and to Universiti Teknologi Malaysia for the financial funding under Hi-Tech (F4) grant Q.J130000.4609.00Q14.

Conflict of interest

The authors declare that the research was conducted in the absence of any commercial or financial relationships that could be construed as a potential conflict of interest.

The handling editor MK declared a past co-authorship with the author TM.

The author(s) declared that they were an editorial board member of Frontiers, at the time of submission. This had no impact on the peer review process and the final decision.

Publisher's note

All claims expressed in this article are solely those of the authors and do not necessarily represent those of their affiliated organizations, or those of the publisher, the editors, and the reviewers. Any product that may be evaluated in this article, or claim that may be made by its manufacturer, is not guaranteed or endorsed by the publisher.

performance of VMD PVDF membranes. *Sep. Purif. Technol.* 157, 60–71. doi:10.1016/j.seppur.2015.11.029

Biswas, D., and Kartha, S. A. (2019). Conceptual modeling of temperature effects on capillary pressure in dead-end pores. *Sādhanā* 44, 117. doi:10.1007/s12046-019-1108-y

Bolz, R. E. (1973). *CRC handbook of tables for applied engineering science*. Boca Raton, Florida, United States: CRC Press. doi:10.1201/9781315214092

Camacho, L. M., Dumée, L., Zhang, J., Li, J., Duke, M., Gomez, J., et al. (2013). Advances in membrane distillation for water desalination and purification applications. *Water* 5, 94–196. doi:10.3390/w5010094

Chesworth, W., Camps Arbestain, M., Macías, F., Spaargaren, O., and Mualem, Y. (2015). Capillary pressure BT - encyclopedia of soil science. in, ed. W. Chesworth (Dordrecht: Springer Netherlands), 81–91. doi:10.1007/978-1-4020-3995-9_87

Chamani, H., Matsuura, T., Rana, D., and Lan, C. Q. (2019). Modeling of pore wetting in vacuum membrane distillation. *J. Memb. Sci.* 572, 332–342. doi:10.1016/j.memsci.2018.11.018

Danish, M. (2020). *Contact angle studies of hydrophobic and hydrophilic surfaces BT - handbook of magnetic hybrid nanoalloys and their nanocomposites*. Cham: Springer International Publishing, 1–22. doi:10.1007/978-3-030-34007-0_24-1

Eljaddi, T., and Cabassud, C. (2022). Wetting of photoplasmonic PVDF/silver membranes in photothermal membrane distillation: identification of wetting mechanisms and comparison of wetting dynamics. *Desalination* 540, 116019. doi:10.1016/j.desal.2022.116019

Feng, X., Jiang, L. Y., Matsuura, T., and Wu, P. (2017). Fabrication of hydrophobic/hydrophilic composite hollow fibers for DCMD: influence of dope formulation and external coagulant. *Desalination* 401, 53–63. doi:10.1016/j.desal.2016.07.026

Gryta, M. (2005). Long-term performance of membrane distillation process. *J. Memb. Sci.* 265, 153–159. doi:10.1016/j.memsci.2005.04.049

Gryta, M. (2007). Influence of polypropylene membrane surface porosity on the performance of membrane distillation process. *J. Memb. Sci.* 287, 67–78. doi:10.1016/j.memsci.2006.10.011

Gryta, M. (2020). Mitigation of membrane wetting by applying a low temperature membrane distillation. *Membr. (Basel)* 10, 158. doi:10.3390/membranes10070158

Guillen-Burrieza, E., Thomas, R., Mansoor, B., Johnson, D., Hilal, N., and Arafat, H. (2013). Effect of dry-out on the fouling of PVDF and PTFE membranes under conditions simulating intermittent seawater membrane distillation (SWMD). *J. Memb. Sci.* 438, 126–139. doi:10.1016/j.memsci.2013.03.014

He, F., Gilron, J., Lee, H., Song, L., and Sirkar, K. K. (2008). Potential for scaling by sparingly soluble salts in crossflow DCMD. *J. Memb. Sci.* 311, 68–80. doi:10.1016/j.memsci.2007.11.056

Hou, C., Pang, Z., Xie, S., Hing Wong, N., Sunarso, J., and Peng, Y. (2023). Enhanced permeability and stability of PVDF hollow fiber membrane in DCMD via heat-stretching treatment. *Sep. Purif. Technol.* 304, 122325. doi:10.1016/j.seppur.2022.122325

Ibrar, I., Yadav, S., Naji, O., Alanezi, A. A., Ghaffour, N., Déon, S., et al. (2022). Development in forward Osmosis-Membrane distillation hybrid system for wastewater treatment. *Sep. Purif. Technol.* 286, 120498. doi:10.1016/j.seppur.2022.120498

Jacob, P., Laborie, S., and Cabassud, C. (2018). Visualizing and evaluating wetting in membrane distillation: new methodology and indicators based on Detection of Dissolved Tracer Intrusion (DDTI). *Desalination* 443, 307–322. doi:10.1016/j.desal.2018.06.006

Karakulski, K., and Gryta, M. (2005). Water demineralisation by NF/MD integrated processes. *Desalination* 177, 109–119. doi:10.1016/j.desal.2004.11.018

Khayet, M., and Matsuura, T. (2011). *Membrane distillation principles and applications*. Amsterdam: Elsevier. doi:10.1016/B978-0-444-53126-1.10017-X

Liu, Y., Horseman, T., Wang, Z., Arafat, H. A., Yin, H., Lin, S., et al. (2022). Negative pressure membrane distillation for excellent gypsum scaling resistance and flux enhancement. *Environ. Sci. Technol.* 56, 1405–1412. doi:10.1021/acs.est.1c07144

Naidu, L. D., Saravanan, S., Chidambaram, M., Goel, M., Das, A., and Babu, J. S. C. (2015). Nanofiltration in transforming surface water into healthy water: comparison with reverse osmosis. *J. Chem.* 2015, 1–6. doi:10.1155/2015/326869

Pangarkar, B. L., Sane, M. G., Parjane, S. B., and Guddad, M. (2011). Vacuum membrane distillation for desalination of ground water by using flat sheet membrane. <https://zenodo.org/records/1070211>.

Park, S.-M., and Lee, S. (2019). Influence of hydraulic pressure on performance deterioration of direct contact membrane distillation (DCMD) process. *Membr. (Basel)* 9, 37. doi:10.3390/membranes9030037

Peña, L., de Zárate, J. M. O., and Mengual, J. I. (1993). Steady states in membrane distillation: influence of membrane wetting. *J. Chem. Soc. Faraday Trans.* 89, 4333–4338. doi:10.1039/FT9938904333

Peng, P., Fane, A. G., and Li, X. (2005). Desalination by membrane distillation adopting a hydrophilic membrane. *Desalination* 173, 45–54. doi:10.1016/j.desal.2004.06.208

Peng, Y., Dong, Y., Fan, H., Chen, P., Li, Z., and Jiang, Q. (2013). Preparation of polysulfone membranes via vapor-induced phase separation and simulation of direct-contact membrane distillation by measuring hydrophobic layer thickness. *Desalination* 316, 53–66. doi:10.1016/j.desal.2013.01.021

Pfeiffer, A. M., Finnegan, N. J., and Willenbring, J. K. (2017). Sediment supply controls equilibrium channel geometry in gravel rivers. *Proc. Natl. Acad. Sci.* 114, 3346–3351. doi:10.1073/pnas.1612907114

Qtaishat, M., Khayet, M., and Matsuura, T. (2009). Novel porous composite hydrophobic/hydrophilic polysulfone membranes for desalination by direct contact membrane distillation. *J. Memb. Sci.* 341, 139–148. doi:10.1016/j.memsci.2009.05.053

Rácz, G., Kerker, S., Kovács, Z., Vatai, G. N., Ebrahimi, M., and Czermak, P. (2014). Theoretical and experimental approaches of liquid entry pressure determination in membrane distillation processes. *Period. Polytech. Chem. Eng.* 58, 81–91. doi:10.3311/PPCH.2179

Rezaei, M., and Samhaber, W. (2016). Wetting behaviour of superhydrophobic membranes coated with nanoparticles in membrane distillation. *Chem. Eng. Trans.* 47, 373–378. SE-Research Articles. doi:10.3303/CET1647063

Rezaei, M., Warsinger, D. M., Lienhard V, J. H., Duke, M. C., Matsuura, T., and Samhaber, W. M. (2018). Wetting phenomena in membrane distillation: mechanisms, reversal, and prevention. *Water Res.* 139, 329–352. doi:10.1016/j.watres.2018.03.058

Ritter, M. E. (2022). 18.2: channel Geometry and flow characteristics. *Univ. Wisconsin-Stevens Point. Libr.*, Available at: <https://geo.libretexts.org/@go/page/16641> (Accessed March 9, 2024).

Rouquerol, J., Baron, G., Denoyel, R., Giesche, H., Groen, J., Klobes, P., et al. (2011). Liquid intrusion and alternative methods for the characterization of macroporous materials (IUPAC Technical Report). *IUPAC Tech. Rep.* 84, 107–136. doi:10.1351/PAC-REP-10-11-19

Saffarini, R. B., Mansoor, B., Thomas, R., and Arafat, H. A. (2013). Effect of temperature-dependent microstructure evolution on pore wetting in PTFE membranes under membrane distillation conditions. *J. Memb. Sci.* 429, 282–294. doi:10.1016/j.memsci.2012.11.049

Shin, Y., Choi, J., Lee, T., Sohn, J., and Lee, S. (2016). Optimization of dewetting conditions for hollow fiber membranes in vacuum membrane distillation. *Desal. Water Treat.* 57, 7582–7592. doi:10.1080/19443994.2015.1044266

Sipahutar, W. S., Maulana, S., Augustina, S., Murda, R. A., and Bindar, Y. (2021). Effects of heat treatment on the wettability and color properties of betung bamboo (*dendrocalamus asper*) strand. *IOP Conf. Ser. Earth Environ. Sci.* 830, 012071. doi:10.1088/1755-1315/830/1/012071

Stewart, M. I. (2014). *Chapter nine - gas sweetening*. Boston: Gulf Professional Publishing, 433–539. doi:10.1016/B978-0-12-382207-9.00009-3

Taetz, S., John, T., Bröcker, M., and Spandler, C. (2016). Fluid-rock interaction and evolution of a high-pressure/low-temperature vein system in eclogite from New Caledonia: insights into intraslab fluid flow processes. *Contrib. Mineral. Petrol.* 171, 90. doi:10.1007/s00410-016-1295-z

Tun, C. M., Fane, A. G., Matheickal, J. T., and Sheikholeslami, R. (2005). Membrane distillation crystallization of concentrated salts—flux and crystal formation. *J. Memb. Sci.* 257, 144–155. doi:10.1016/j.memsci.2004.09.051

Warsinger, D. M., Servi, A., Connors, G. B., Mavukkandy, M. O., Arafat, H. A., Gleason, K. K., et al. (2017). Reversing membrane wetting in membrane distillation: comparing dryout to backwashing with pressurized air. *Environ. Sci. Water Res. Technol.* 3, 930–939. doi:10.1039/C7EW00085E

Yazgan-Birgi, P., Hassan Ali, M. I., and Arafat, H. A. (2018). Estimation of liquid entry pressure in hydrophobic membranes using CFD tools. *J. Memb. Sci.* 552, 68–76. doi:10.1016/j.memsci.2018.01.061

Zhang, J., Li, J.-D., Duke, M., Xie, Z., and Gray, S. (2010). Performance of asymmetric hollow fibre membranes in membrane distillation under various configurations and vacuum enhancement. *J. Memb. Sci.* 362, 517–528. doi:10.1016/j.memsci.2010.07.004

Zhang, J., Li, J.-D., and Gray, S. (2011). Effect of applied pressure on performance of PTFE membrane in DCMD. *J. Memb. Sci.* 369, 514–525. doi:10.1016/j.memsci.2010.12.033

Zhu, J., Jiang, L., Matsuura, T., Zhang, J., Du, R., Ni, J., et al. (2015). New insights into fabrication of hydrophobic/hydrophilic composite hollow fibers for direct contact membrane distillation. *Chem. Eng. Sci.* 137, 79–90. doi:10.1016/j.ces.2015.05.064



OPEN ACCESS

EDITED BY

Yunxia Hu,
Tianjin Polytechnic University, China

REVIEWED BY

Xiaobin Yang,
Harbin Institute of Technology, China
Chuanjie Fang,
Zhejiang University, China

*CORRESPONDENCE

Shoujian Gao,
✉ sjgao2012@sinano.ac.cn
Jian Jin,
✉ jjin@suda.edu.cn

RECEIVED 14 December 2023

ACCEPTED 23 January 2024

PUBLISHED 06 February 2024

CITATION

Gao S, Liu P and Jin J (2024), *In-situ* ionized construction of PVDF/sodium polyacrylate-grafted-PVDF blend ultrafiltration membrane with stable anti-oil-fouling ability for efficient oil-in-water emulsion separation.
Front. Membr. Sci. Technol. 3:1355773.
doi: 10.3389/fmst.2024.1355773

COPYRIGHT

© 2024 Gao, Liu and Jin. This is an open-access article distributed under the terms of the [Creative Commons Attribution License \(CC BY\)](https://creativecommons.org/licenses/by/4.0/). The use, distribution or reproduction in other forums is permitted, provided the original author(s) and the copyright owner(s) are credited and that the original publication in this journal is cited, in accordance with accepted academic practice. No use, distribution or reproduction is permitted which does not comply with these terms.

In-situ ionized construction of PVDF/sodium polyacrylate-grafted-PVDF blend ultrafiltration membrane with stable anti-oil-fouling ability for efficient oil-in-water emulsion separation

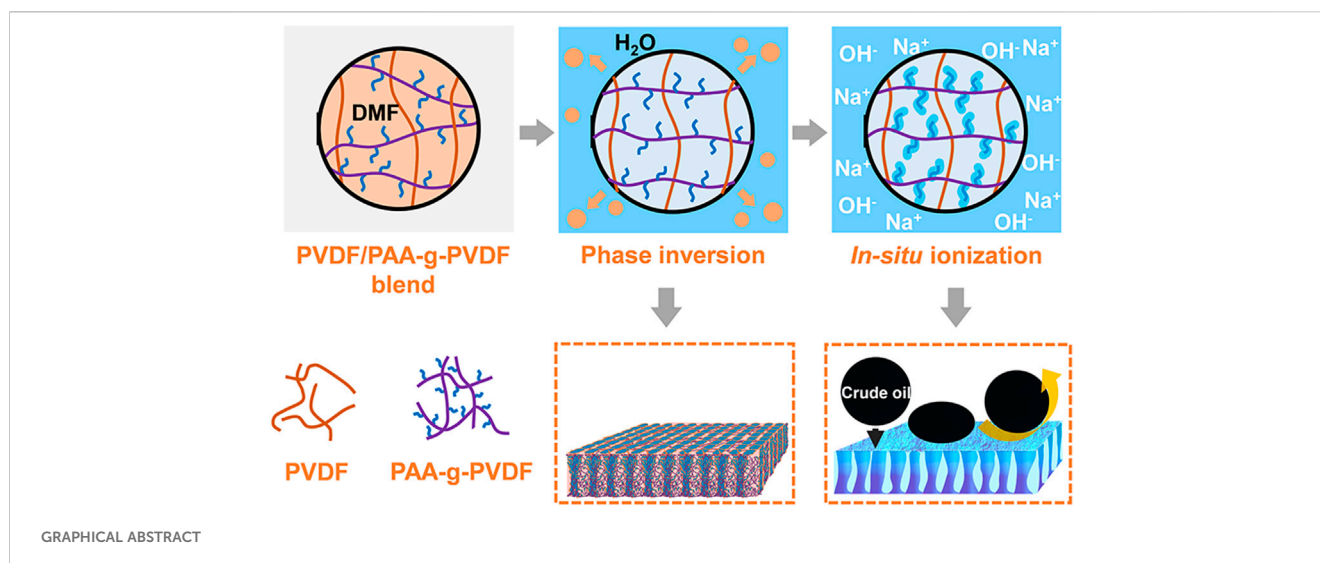
Shoujian Gao^{1*}, Pingping Liu² and Jian Jin^{3*}

¹i-Lab, CAS Key Laboratory of Nano-Bio Interface, Suzhou Institute of Nano-Tech and Nano-Bionics, Chinese Academy of Sciences, Suzhou, China, ²Nano Science and Technology Institute, University of Science and Technology of China, Suzhou, China, ³College of Chemistry, Chemical Engineering and Materials Science, Collaborative Innovation Center of Suzhou Nano Science and Technology, Soochow University, Suzhou, China

Traditional polymeric membranes usually suffer from serious oil fouling and quick decline of water flux when separating oil-in-water emulsions. In this work, we report the fabrication of the sodium polyacrylate (PAAS) blended polyvinylidene fluoride (PVDF) ultrafiltration membrane which behaves hydrophilicity, underwater low-oil-adhesive superoleophobicity and outstanding anti-oil-fouling ability even for viscous crude oil. The blend membrane was fabricated via a two-step method, including the nonsolvent-induced phase inversion of PVDF/polyacrylic acid-grafted-PVDF (PVDF/PAA-g-PVDF) blend membrane and the subsequent *in-situ* ionization of PAA into PAAS. The two-step method improves the affinity between the strong hydrophilic additive PAAS and the hydrophobic polymer matrix PVDF, thus endowing the blend membrane with long-term stable superwetting property for 1,100 days. The PVDF/PAAS-g-PVDF blend membrane can efficiently separate multiple emulsifier-stabilized oil-in-water emulsions with ultrahigh separation efficiency of 99.97% (the residual oil content in the filtrate is lower than 3 ppm after one-step separation) and high water flux of 350 L m⁻² h⁻¹ bar⁻¹. The blend membrane also shows good cycling performance, and can be easily cleaned by water washing during several separation cycles of the crude oil-in-water emulsion. This work inspires a feasible route of fabricating stable anti-oil-fouling membranes for separation of emulsified oily water.

KEYWORDS

blend membrane, anti-oil-fouling, *in-situ* ionization, oil/water separation, oil-inwater emulsion



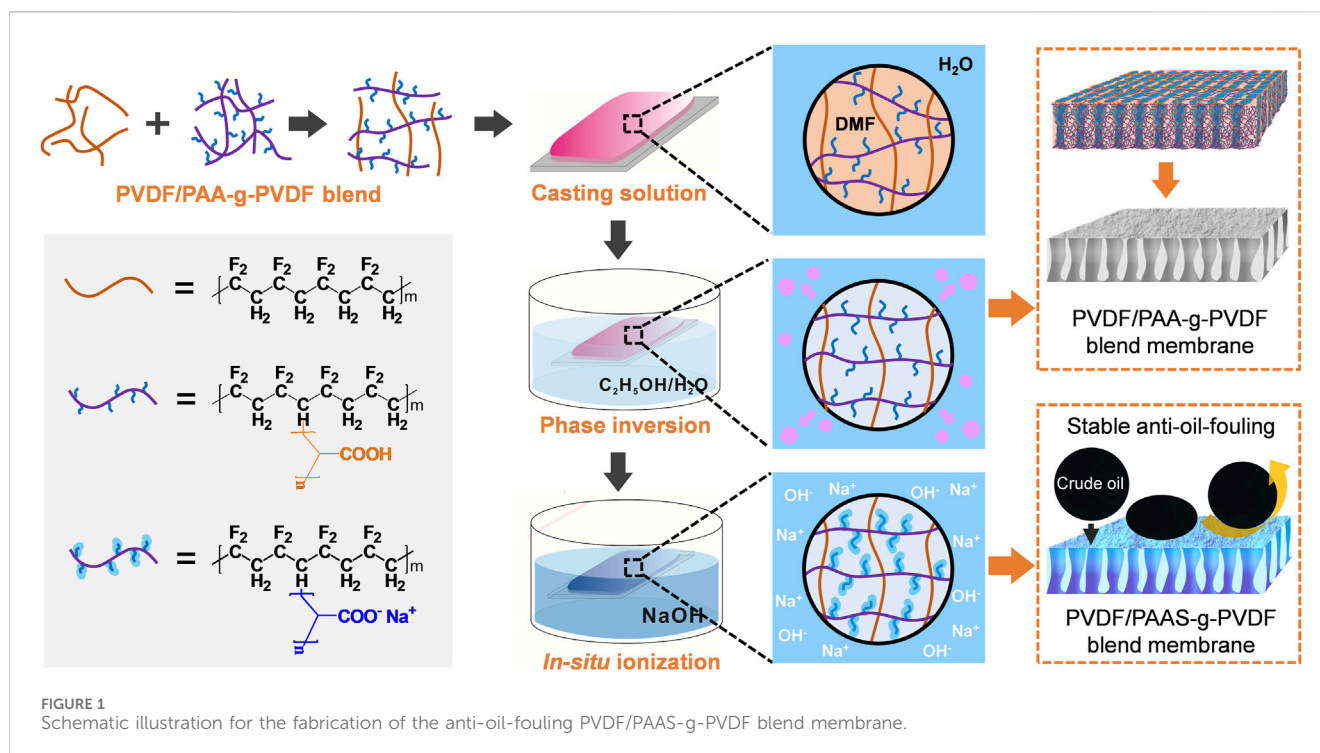
1 Introduction

Oily water generated from diverse oil-related activities such as oil recovery, petrochemical, metal finishing, food and leather industries has become a serious pollution problem around the world (Gao et al., 2015; Wang et al., 2023). It harms both the environment and human health (Oki and Kanae, 2006; Aurell and Gullett, 2010). Separating oil from oily water is recognized as a sustainable strategy, and has been extensively studied (Chu et al., 2015; Wang et al., 2015). However, long-term efficient separation of oil-in-water emulsions with the oil droplet size at a micro- or nanometer scale is still challenging. Membrane separation is an efficient technology for separating the oil-in-water emulsions due to its high efficiency, ease of operation and low energy consumption (Elimelech and Phillip, 2011; Chang et al., 2014). An obstacle of traditional membranes for separating oil-in-water emulsions is that the water flux declines quickly because of inevitable oil fouling on the membrane surfaces, which limits the separation capacity and long-term use of the membranes (Rana and Matsuura, 2010; Yang et al., 2022). The oil fouling is particularly serious during the separation of crude oil-in-water emulsion due to the high oil viscosity (Gao et al., 2022). So far, developing advanced membranes with an outstanding anti-oil-fouling property for efficient and long-term stable separation of oil-in-water emulsions remains highly desired.

Generally, hydrophilic membranes can form hydration layers on their surfaces in water and protect the membranes from oil fouling (Gao et al., 2015; Dong et al., 2022). Surface grafting and surface coating are effective techniques for fabricating the hydrophilic membranes, but they usually have the drawbacks of time consumption, harsh chemical environment requirement and coating layer instability. (Zhang et al., 2013a; Chen and Xu, 2013; Yang et al., 2014; Gao et al., 2015). Recently, the strategies for building biomimetic coatings with mild and versatile merits, as well as the atomic layers with precise and controllable features raise an exciting opportunity for fabricating the hydrophilic and anti-oil-fouling membranes (Yang et al., 2021; Geng et al., 2022; Yang et al., 2023). These approaches represent the state-of-the-art technologies in surface modification, but still have a long way to go

before industrialization. The interfacial energy and wettability difference of oil and water on solid surfaces provide another brand-new route for constructing the superhydrophilic and underwater superoleophobic membranes with high-surface-energy membrane materials and surface micro-/nanostructures (Zhang et al., 2013b; Tao et al., 2014; Zhang et al., 2014). But, it is difficult to construct micro-/nanostructures on polymeric membrane surfaces via common membrane-manufacturing methods. Blending hydrophilic additives like hydrophilic polymers, amphiphilic copolymers and inorganic nanoparticles, etc., In the traditional membrane matrixes like polyvinylidene fluoride (PVDF), polysulfone and polyether sulfone, etc., Through the phase inversion is widely adopted for fabricating the hydrophilic and anti-oil-fouling polymeric membranes (Shi et al., 2008; Liu et al., 2011; Kang and Cao, 2014; Chen et al., 2016). Compared with other techniques, blending modification is ease of operation and scaling up for industrialization. Nevertheless, the polarity difference and the weak interaction between the hydrophilic additives and the hydrophobic polymer matrixes often lead to the aggregation of the hydrophilic additives during the phase inversion. It finally brings about the non-uniform distribution and the easy release of the hydrophilic additives from the blend membranes (Choi et al., 2006; Zhu et al., 2014). Blending strong hydrophilic additives in traditional hydrophobic polymer matrixes to fabricate uniform and long-term stable membranes with hydrophilicity and superior anti-oil-fouling property is still a tough work.

Herein, we propose a two-step method to uniformly introduce a strong hydrophilic additive sodium polyacrylate (PAAS) in the hydrophobic PVDF and construct a hydrophilic, underwater superoleophobic and anti-oil-fouling blend membrane. PAAS is a well-known hydrogel material with underwater low-oil-adhesive superoleophobicity and superior anti-oil-fouling property even for viscous oils (Gao et al., 2016). But, it is difficult to directly blend PAAS with the hydrophobic polymer matrixes to obtain uniform and stable membranes. In our method, polyacrylic acid-grafted-PVDF (PAA-g-PVDF) was chosen as an additive precursor to blend with PVDF and form a PVDF/PAA-g-PVDF blend membrane via the nonsolvent-induced phase inversion (Figure 1). Then the PVDF/PAA-g-PVDF blend membrane was



treated by NaOH solution where PAA was *in situ* ionized to PAAS, and the PVDF/PAAS-PVDF blend membrane was fabricated. The two-step method improves the affinity between PAAS and PVDF, thus endowing the blend membrane with good uniformity and stable superwetting property. The wettability and water permeation flux of the PVDF/PAAS-g-PVDF blend membrane is controllable by regulating the mass ratio of PAA-g-PVDF and PVDF. The blend membrane can achieve efficient separation of multiple emulsifier-stabilized oil-in-water emulsions with ultrahigh separation efficiency of 99.97%, high water flux of $350 \text{ L m}^{-2} \text{ h}^{-1} \text{ bar}^{-1}$, as well as good cycling performance even for the crude oil-in-water emulsion.

2 Material and methods

2.1 Materials

PVDF powders (Solvay, Solef 1015, $M_n = 238000$) used in this work were purchased from Solvay Chemicals Company. PAA-g-PVDF powders with 8 wt% PAA graft ratio was synthesized via a pre-irradiation induced graft polymerization technique (45). Light crude oil (API Gravity $>20^\circ$) and heavy crude oil (API Gravity: 10° – 20°) were supplied by SINOPEC SABIC Tianjin Petrochemical Co., Ltd., China. Light crude oil was used for the separation of oil-in-water emulsion, and heavy crude oil was used for the measurement of oil contact angle (CA) and oil adhesive force. Diesel oil and soybean oil were commercial products from market. All other chemicals were commercially available from Shanghai Chemical Reagent Co. Ltd., and used as received without further purification. Deionized water was used throughout the experiments.

2.2 Preparation of the PVDF/PAAS-g-PVDF blend membrane

The PVDF/PAAS-g-PVDF blend membrane was prepared via the nonsolvent-induced phase inversion and the alkaline-induced *in-situ* ionization. PVDF/PAA-g-PVDF mixed powders with the PAA-g-PVDF: PVDF mass ratios of 3: 1, 2: 1, 1: 1, 1: 2 and 1: 3 were prepared, respectively. 3.6 g PVDF/PAA-g-PVDF mixed powders were dissolved in 32.4 g N, N'-dimethylformamide (DMF) to form the homogeneous solution under 85°C for 48 h. The solution was casted onto a flat glass plate by a casting knife with a gate height of 200 μm and then immersed in the water/ethanol (volume ratio = 1: 1) coagulation solution immediately. After 12 h, the PVDF/PAA-g-PVDF blend membrane was obtained. Then the PVDF/PAA-g-PVDF blend membrane was immersed in the 0.1 mol L^{-1} NaOH solution for 1 min. During this process, PAA reacted with NaOH and transformed into PAAS *in situ*. The PVDF/PAAS-g-PVDF blend membrane was thus obtained and then rinsed with water.

2.3 Separation of the oil-in-water emulsions

Three emulsifier-stabilized oil-in-water emulsions were prepared by mixing and stirring oil (soybean oil, diesel oil and crude oil) and water with an oil/water volume ratio of 1: 99, respectively. 0.1 mg mL^{-1} sodium dodecyl sulfate (SDS) was used as the emulsifier and added in water to prepare the oil-in-water emulsions. The soybean oil-in-water and diesel oil-in-water emulsions were prepared under stirring at a speed of 2000 rpm for 2 h. The crude oil-in-water emulsion was prepared under stirring at a speed of 8,000 rpm for 6 h. The PVDF/PAAS-g-PVDF blend membrane was fixed in a membrane cell with an effective filtration area of 7.06 cm^2 . The separation process was carried out under

a cross-flow filtration mode. The membrane was firstly compacted by pure water under a transmembrane pressure of 1 bar for 30 min. Then 50 mL SDS-stabilized oil-in-water emulsion was filtrated through the membrane under 1 bar. The filtrated water was collected, and the oil content in the filtrate was determined by a TOC analyzer. Water flux J ($\text{L m}^{-2} \text{h}^{-1} \text{bar}^{-1}$) of the membrane was calculated according to Eq. 1:

$$J = \frac{\Delta V}{A \Delta t} \quad (1)$$

where ΔV was the volume (L) of filtrated water through the membrane, Δt is the filtration time (h), and A is the effective filtration area (m^2).

Separation efficiency E (%) of the oil-in-water emulsion was calculated according to Eq. 2:

$$E = \left(1 - \frac{C_1}{C_0}\right) \times 100\% \quad (2)$$

where C_1 and C_0 was the oil content in the filtrate and the emulsion feed, respectively.

2.4 Evaluation of the antifouling and cycling performance

To evaluate the antifouling and cycling performance of the membrane, three separation cycles of the SDS-stabilized crude oil-in-water emulsion were carried out, and the water flux was monitored in real time. In each separation cycle, pure water was firstly filtrated through the membrane under 1 bar for 30 min, and the stabilized water flux was recorded as J_{w1} ($\text{L m}^{-2} \text{h}^{-1} \text{bar}^{-1}$). Then the SDS-stabilized crude oil-in-water emulsion was filtrated through the membrane under 1 bar for 60 min, and stabilized water flux was recorded as J_{p1} ($\text{L m}^{-2} \text{h}^{-1} \text{bar}^{-1}$). Then the membrane was washed by hydraulic flushing for 30 min to complete one cycle. After water washing, pure water flux of the membrane was re-measured and recorded as J_{w2} ($\text{L m}^{-2} \text{h}^{-1} \text{bar}^{-1}$). Flux decline ratio (DR , %) and flux recovery ratio (FRR , %) were calculated according to the following equations, respectively:

$$DR = \left(1 - \frac{J_p}{J_{w1}}\right) \times 100\% \quad (3)$$

$$FRR = \frac{J_{w2}}{J_{w1}} \times 100\% \quad (4)$$

Reversible fouling ratio (R_r , %) and irreversible fouling ratio (R_{ir} , %) were calculated according to the following equations, respectively:

$$R_r (\%) = \frac{J_{w2} - J_{p1}}{J_{w1}} \times 100\% \quad (5)$$

$$R_{ir} (\%) = \frac{J_{w1} - J_{w2}}{J_{w1}} \times 100\% \quad (6)$$

2.5 Evaluation of the long-term stability

Several PVDF/PAAS-g-PVDF blend membranes were cut into 100 pieces of square membranes with a size of $4 \text{ cm} \times 4 \text{ cm}$. The membranes were immersed in water with the pH of about 7. Every

15 days, a piece of the membrane was taken and washed by hydraulic cleaning for 30 min, then the measurements of water CA, underwater crude oil CA and underwater crude oil adhesive force were carried out on the membrane. Meanwhile, the water soaking the membranes was replaced with new water every 15 days. The water CA, underwater crude oil CA and underwater crude oil adhesive force of the membranes were recorded for 1,100 days.

2.6 Characterization

Scanning electron microscopy (SEM) images and energy dispersive x-ray (EDX) spectrum were obtained on a Quanta FEG 250 SEM (FEI, America). Attenuated total reflectance Fourier transform infrared spectroscopy (ATR-FTIR) was measured by a Nicolet 6700 FTIR spectrometer (Nicolet, America). Water CA and underwater oil CA were measured on an OCA20 machine (Data-physics, Germany). Underwater oil-adhesive force was measured by a DCAT11 high-sensitivity micro-electro-mechanical balance system (Data-Physics, Germany). Tensile strength was determined on an Instron 3,300 universal testing machine (Instron, America). Oil and polyethylene glycol (PEG) contents in water were determined by an Aurora 1030w total organic carbon (TOC) analyzer (O.I. Analytical, America).

3 Results and discussion

3.1 Fabrication and morphology characterization of the blend membrane

As shown in Figure 1, the PVDF/PAAS-g-PVDF blend membrane was fabricated via the nonsolvent-induced phase inversion of the PVDF/PAA-g-PVDF blend membrane and the subsequent *in-situ* ionization of PAA into PAAS. Compared with the strong hydrophilic PAAS, PAA-g-PVDF has better compatibility with the hydrophobic PVDF. Therefore, blending PAA-g-PVDF with PVDF can relieve the aggregation of the additive during the phase inversion and form a more homogeneous blend membrane than directly blending PAAS with PVDF. After PAA transformed into PAAS *in situ*, the PVDF/PAAS-g-PVDF blend membrane with a uniform distribution of PAAS was obtained. Meanwhile, PAAS-g-PVDF has relatively strong interaction with PVDF, thus reducing the release of the additive into water and endowing the PVDF/PAAS-g-PVDF blend membrane with high stability for long-term use. It is worth noting that the pure PAAS-g-PVDF membrane is hardly permeable despite the membrane behaves a hydrophilic and anti-oil-fouling property, because the easy hydrating and swelling feature of PAAS blocks the membrane pores.

Figure 2 reveals the morphology and chemical composition of the PVDF/PAAS-g-PVDF blend membrane which is fabricated with the PVDF: PAA-g-PVDF mass ratio of 2: 1. The top-view SEM image of the dry PVDF/PAAS-g-PVDF blend membrane displays a porous surface (Figure 2A). EDX imaging of the membrane (the inset in Figure 2A) shows the uniform distribution of Na element in the membrane, demonstrating the transformation of PAA into PAAS and the uniform distribution of PAAS in the membrane. The top-view environmental SEM image of the wet PVDF/PAAS-g-PVDF blend membrane exhibits a smooth surface without visible

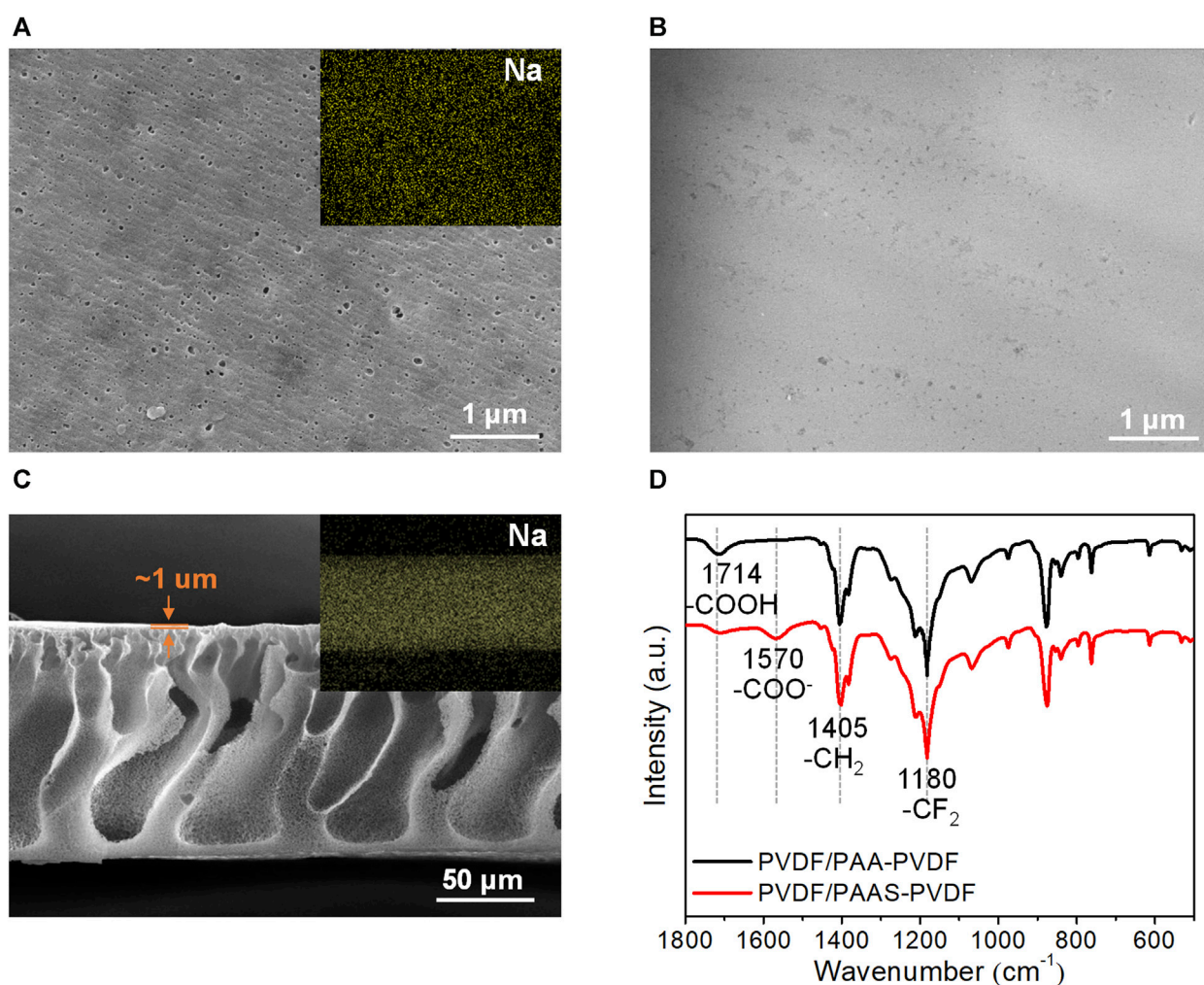


FIGURE 2 Morphology and chemical composition of the PVDF/PAAS-g-PVDF blend membrane. **(A)** Top-view SEM image of the membrane in a dry state and corresponding EDX imaging of Na element. **(B)** Top-view environmental SEM image of the membrane in a wet state. **(C)** Cross-sectional SEM image of the membrane in a dry state and corresponding EDX imaging of Na element. **(D)** ATR-FTIR spectra of the PVDF/PAA-g-PVDF blend membrane and the PVDF/PAAS-g-PVDF blend membrane.

pores (Figure 2B), which is ascribed to the hydration and swelling of PAAS. The cross-sectional SEM image of the dry PVDF/PAAS-g-PVDF blend membrane shows a finger-like pore structure of the membrane (Figure 2C). The thickness of the whole membrane is $\sim 120\ \mu\text{m}$, and the thickness of the skin layer is $\sim 1\ \mu\text{m}$. To further confirm the formation of PAAS in the blend membrane, the ATR-FTIR spectra of the PVDF/PAAS-g-PVDF blend membrane and the PVDF/PAA-g-PVDF blend membrane were measured (Figure 2D). In comparison with the PVDF/PAA-g-PVDF blend membrane, the absorption peak at $1714\ \text{cm}^{-1}$ which corresponds to the stretching vibration of COOH decreases, and an absorption peak at $1570\ \text{cm}^{-1}$ which corresponds to the stretching vibration of COO^- is observed in the PVDF/PAAS-g-PVDF blend membrane, demonstrating the *in-situ* ionization of PAA into PAAS. The absorption peaks at $1,180\ \text{cm}^{-1}$ and $1,405\ \text{cm}^{-1}$ are ascribed to the stretching vibration of CF_2 and CH_2 in PVDF, respectively. The atomic percentage of Na and O in the PVDF/PAAS-g-PVDF blend membrane is 0.33% and 1.03%, respectively (Supplementary Figure S1), indicating that $\sim 64\%$ PAA has been transformed into PAAS in the membrane.

3.2 Wettability and anti-oil-fouling property of the blend membrane

Underwater oil adhesive force is critical to evaluate the anti-oil-fouling property of a membrane. As shown in Figure 3, the real-time recorded force-distance curves were plotted according to the dynamic measurement of the underwater crude oil adhesive force of the PVDF/PAAS-g-PVDF blend membrane and the PVDF/PAA-g-PVDF blend membrane. During the measurement, a heavy crude oil droplet was used as the detecting probe to sufficiently contact the membrane surface and then lift up under water. There is no deformation of the crude oil droplet when lifting the oil droplet up from the PVDF/PAAS-g-PVDF blend membrane (Figure 3A). The detected underwater crude oil adhesive force of the PVDF/PAAS-g-PVDF blend membrane is only $1.8 \pm 0.1\ \mu\text{N}$, indicating an excellent anti-oil-adhesive property. In contrast, the crude oil droplet tightly adheres on the PVDF/PAA-g-PVDF blend membrane with obvious deformation when lifting the oil droplet up from the membrane (Figure 3B). The detected underwater crude

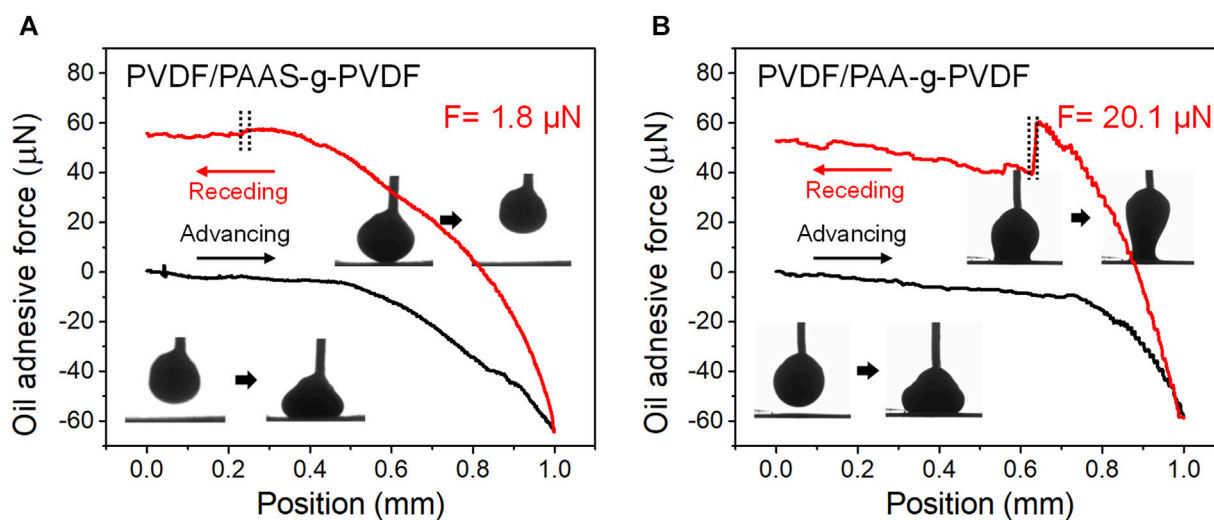


FIGURE 3
Real-time recorded force-distance curves during the dynamic measurements of underwater crude oil adhesive force on (A) the PVDF/PAAS-g-PVDF blend membrane and (B) the PVDF/PAA-g-PVDF blend membrane. A heavy crude oil droplet (3 μ L) was used as the detecting probe.

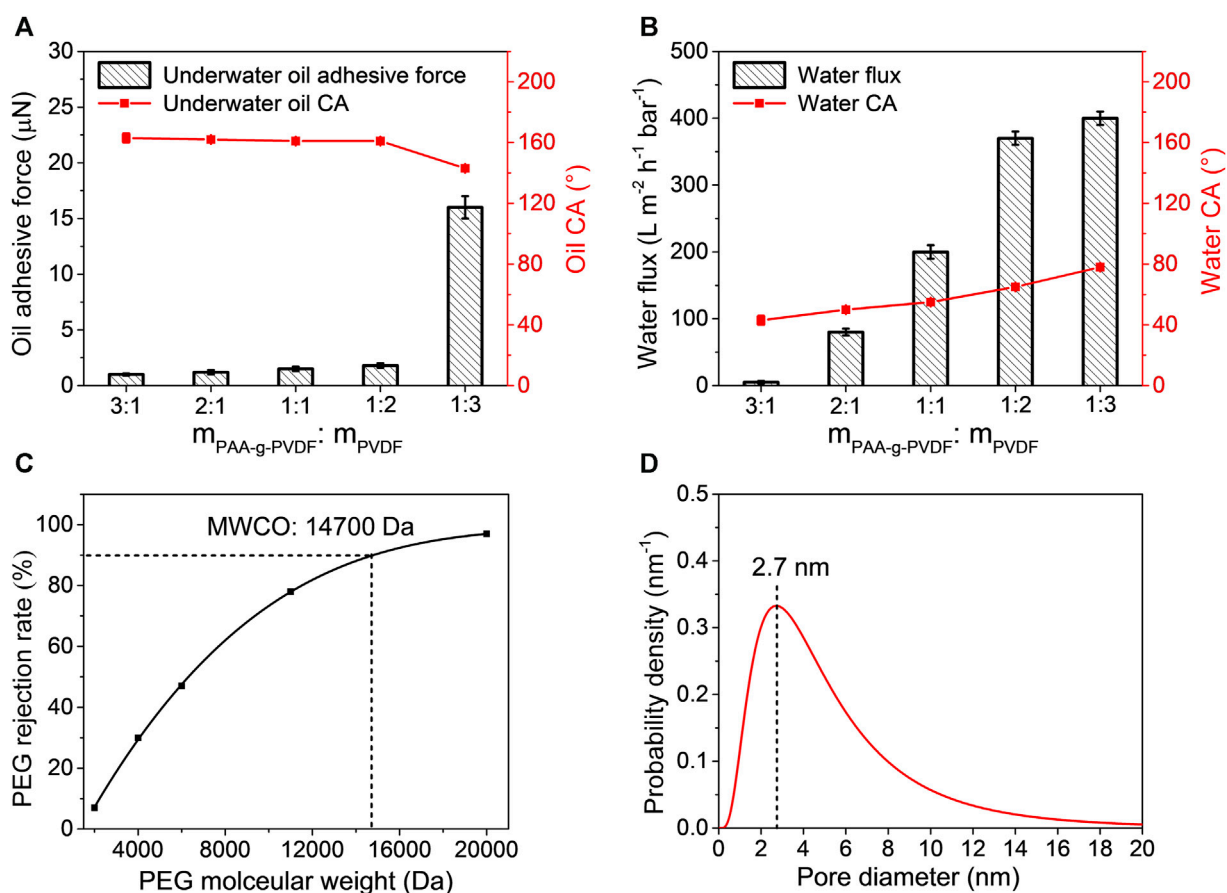


FIGURE 4
(A) Underwater crude oil adhesive force, underwater crude oil CA and (B) pure water flux, water CA of the PVDF/PAAS-g-PVDF blend membranes fabricated with different mass ratios of PAA-g-PVDF and PVDF. (C) PEG rejection curve and (D) pore size distribution of the PVDF/PAAS-g-PVDF blend membrane fabricated with $m_{\text{PAA-g-PVDF}} : m_{\text{PVDF}} = 1 : 2$.

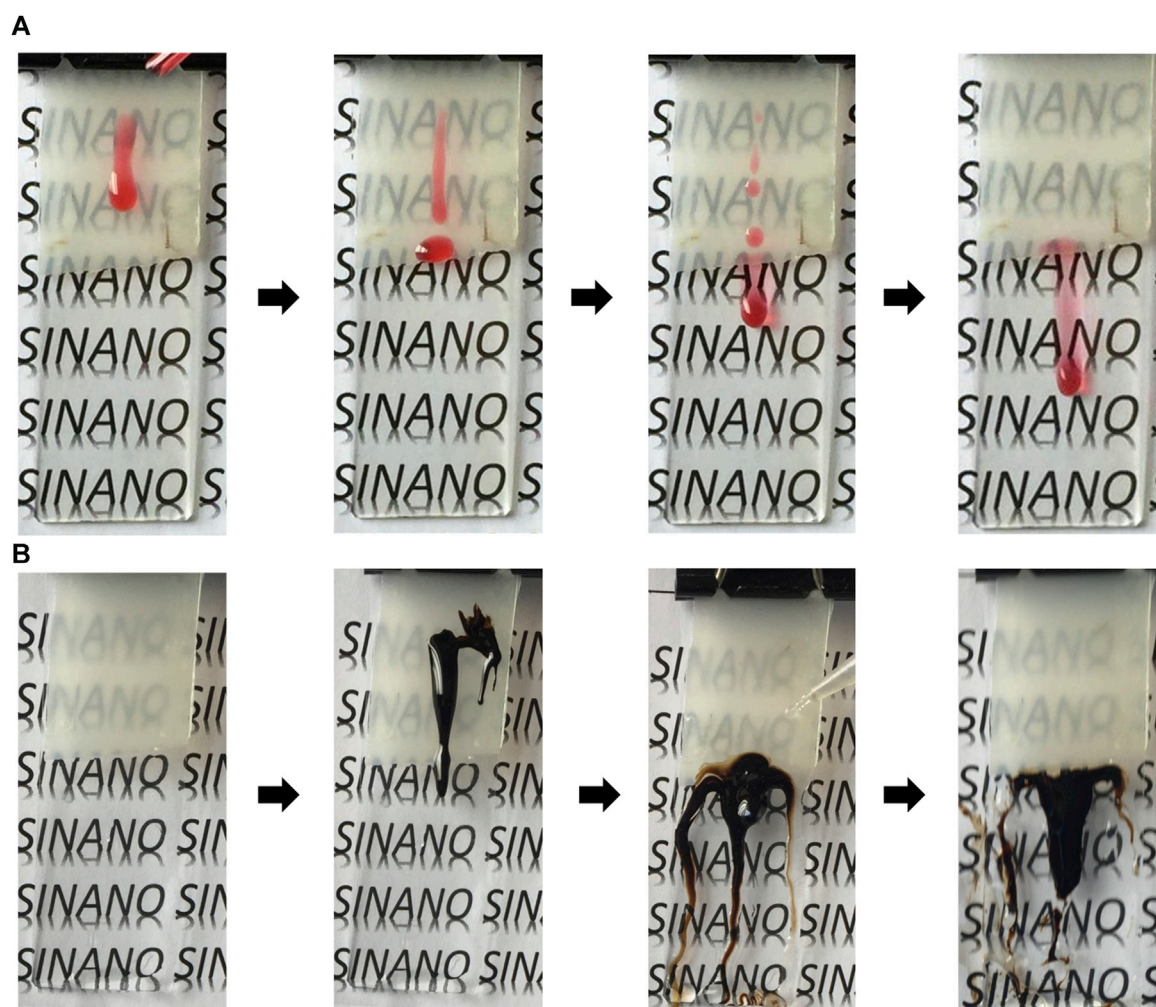


FIGURE 5 Photographs showing the anti-oil-fouling ability test of the PVDF/PAAS-g-PVDF blend membrane for (A) soybean oil (dyed red) and (B) crude oil.

oil adhesive force of the PVDF/PAA-g-PVDF membrane is as high as $20 \pm 0.5 \mu\text{N}$. Compared with the PVDF/PAA-g-PVDF blend membrane, the greatly decreased underwater oil adhesive force and superior anti-oil-adhesive property of the PVDF/PAAS-g-PVDF blend membrane is owing to the strong hydration ability of PAAS. The PVDF/PAAS-g-PVDF blend membrane can form a hydration layer on the membrane surface to prevent oil from contacting and adhering. Benefiting from the introduce of PAAS, the PVDF/PAAS-g-PVDF blend membrane also shows the hydrophilicity with the water CA of $65^\circ \pm 2^\circ$, as well as the underwater superoleophobicity with the crude oil CA of $161^\circ \pm 1^\circ$ and the soybean oil CA of $163^\circ \pm 2^\circ$ (Supplementary Figure S2).

As the easy hydrating and swelling feature of PAAS would result in pore blocking and extremely low water flux of the blend membrane, we investigated the effect of the PAAS content on the wettability and water flux of the PVDF/PAAS-g-PVDF blend membrane. A series of PVDF/PAAS-g-PVDF blend membranes were fabricated with the PAA-g-PVDF: PVDF mass ratios of 3: 1, 2: 1, 1: 1, 1: 2 and 1: 3. The PAAS content in the PVDF/PAAS-g-PVDF blend membrane increases with increasing the PAA-g-PVDF: PVDF mass ratio. As shown in Figure 4A, the underwater crude oil adhesive force of the PVDF/PAAS-g-PVDF

blend membrane increases slightly from 1 to $1.8 \mu\text{N}$, and the underwater crude oil CA decreases from 163° to 161° with increasing the PAA-g-PVDF: PVDF mass ratio from 3: 1 to 1: 2. Meanwhile, the water CA of the membrane increases from 43° to 65° , and the pure water flux increases from $5 \text{ L m}^{-2} \text{ h}^{-1} \text{ bar}^{-1}$ – $370 \text{ L m}^{-2} \text{ h}^{-1} \text{ bar}^{-1}$ (Figure 4B). When further increasing the PAA-g-PVDF: PVDF mass ratio to 1: 3, the PVDF/PAAS-g-PVDF blend membrane exhibits high underwater crude oil adhesive force of $16.2 \mu\text{N}$ and low underwater crude oil CA of 143° , although the membrane shows a pure water flux of $400 \text{ L m}^{-2} \text{ h}^{-1} \text{ bar}^{-1}$. Therefore, the PVDF/PAAS-g-PVDF blend membrane fabricated with the PAA-g-PVDF: PVDF mass ratios of 1: 2 is chosen for evaluating the anti-oil-fouling ability and oil/water separation performance in term of its outstanding anti-oil-adhesive property, underwater superoleophobicity, hydrophilicity and high water flux. Effective pore size of this PVDF/PAAS-g-PVDF blend membrane in water was studied according to the rejection rates of PEG with different molecular weights (Figure 4C). From the nonlinearly fitted PEG rejection curve, the molecular weight cut-off (MWCO) of the membrane is 14700 Da, which is defined as the molecular weight at the rejection rate of 90%. Based on a probability density function

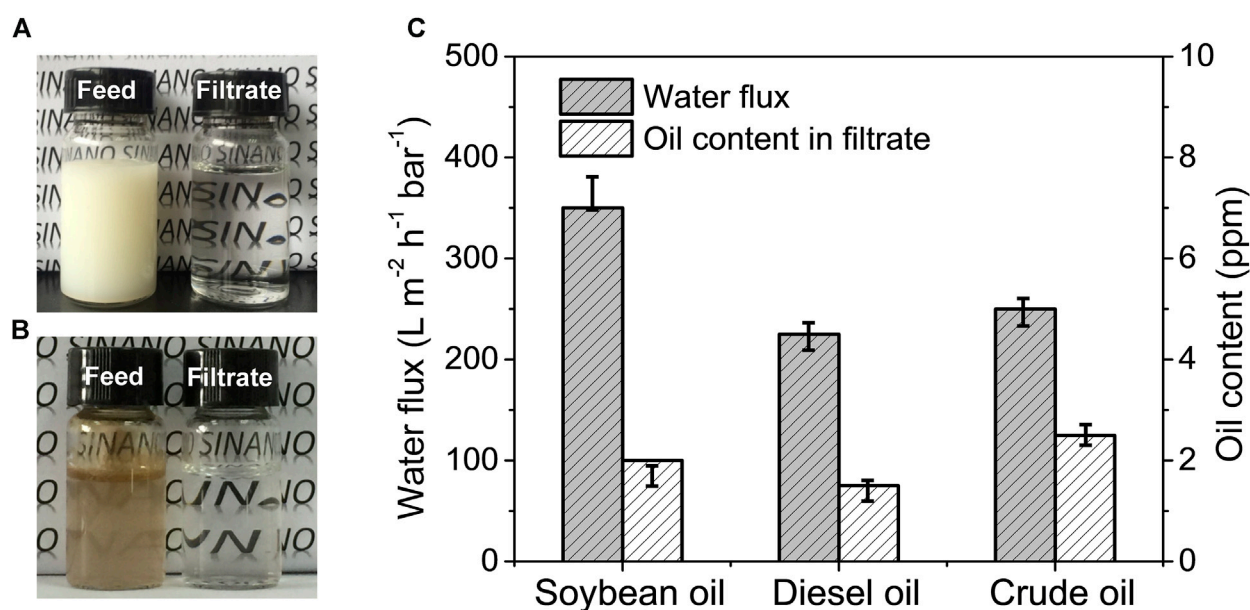


FIGURE 6 Photographs of the emulsion feed and the filtrated water of (A) the SDS-stabilized soybean oil-in-water emulsion and (B) the SDS-stabilized crude oil-in-water emulsion. (C) Water flux and oil content in the filtrate for the separation of the SDS-stabilized oil-in-water emulsions by the PVDF/PAAS-g-PVDF blend membrane.

between the rejection rate and Stokes radius (Lin et al., 2016; Jiang et al., 2018), the mean pore diameter of the membrane is calculated to be 2.7 nm, and the pore diameter distribution is shown in Figure 4D. The PVDF/PAAS-g-PVDF blend membrane is a typical ultrafiltration membrane.

The anti-oil-fouling property of the PVDF/PAAS-g-PVDF blend membrane was also tested. As shown in Figure 5, the half of a glass plate was covered by the wet PVDF/PAAS-g-PVDF blend membrane and vertically placed. The light oil like soybean oil and the viscous oil like heavy crude oil were chosen as the oil contaminants to foul the membrane, respectively. When the soybean oil was dropped on the membrane, the soybean oil slid off from the membrane spontaneously without leaving any trace (Figure 5A). When the heavy crude oil was used to foul the membrane, the crude oil shed off from the membrane immediately once the membrane was rinsed by a bunch of water (Figure 5B). These results demonstrate the outstanding oil-repellent and anti-oil-fouling property of the PVDF/PAAS-g-PVDF blend membrane for both the light oil and the viscous oil. The membrane can be easily cleaned by water washing when the membrane is fouled by oil.

3.3 Oil-in-water emulsion separation and cycling performance

A series of SDS-stabilized oil-in-water emulsions including soybean oil-, diesel oil- and crude oil-in-water emulsion were prepared and filtrated through the PVDF/PAAS-g-PVDF blend membrane under a transmembrane pressure of 1 bar to carry out the separation process, respectively. The optical images of the soybean oil-in-water emulsion and the crude oil-in-water emulsion before and after separation are shown in Figures 6A, B. The milky white soybean oil-in-water emulsion and the turbid

brown crude oil-in-water emulsion turn to be transparent clear after one-step separation by the PVDF/PAAS-g-PVDF blend membrane. All the oil contents in the filtrates are below 3 ppm for the three oil-in-water emulsions, which is equivalent to the separation efficiency above 99.97% (Figure 6C). These results indicate that the PVDF/PAAS-g-PVDF blend membrane can remove nearly all of the oil droplets from the oil-in-water emulsion, and owns ultrahigh separation efficiency. The high oil rejection of the PVDF/PAAS-g-PVDF blend membrane is benefited from its superior oil-repellent property and small effective pore size. The PVDF/PAAS-g-PVDF blend membrane also exhibits high water flux during the separation of the three oil-in-water emulsions: $350 \pm 30 \text{ L m}^{-2} \text{h}^{-1} \text{bar}^{-1}$ for soybean oil-in-water emulsion, $225 \pm 20 \text{ L m}^{-2} \text{h}^{-1} \text{bar}^{-1}$ for diesel oil-in-water emulsion, and $250 \pm 20 \text{ L m}^{-2} \text{h}^{-1} \text{bar}^{-1}$ for crude oil-in-water emulsion, respectively (Figure 6C).

To study the cycling performance of the PVDF/PAAS-g-PVDF blend membrane, the water flux during several separation cycles of the SDS-stabilized crude oil-in-water emulsion by the membrane was monitored. Same tests were carried out on the PVDF/PAA-g-PVDF blend membrane as a contrast. Figure 7A summarizes the alternating water flux of the membranes between filtrating pure water and filtrating the crude oil-in-water emulsion. In the first separation cycle, the PVDF/PAAS-g-PVDF blend membrane exhibits an initial pure water flux of $370 \pm 10 \text{ L m}^{-2} \text{h}^{-1} \text{bar}^{-1}$. When the crude oil-in-water emulsion is switched to be filtrated through the membrane, the water flux decreases and stabilizes at $250 \pm 20 \text{ L m}^{-2} \text{h}^{-1} \text{bar}^{-1}$ with a flux decline ratio *DR* of 32.4% (Figure 7B). After water washing, the pure water flux of the membrane recovers to $320 \pm 10 \text{ L m}^{-2} \text{h}^{-1} \text{bar}^{-1}$ in the second separation cycle with a flux recovery ratio *FRR* of 86.5%. It means that the water flux of the PVDF/PAA-g-PVDF blend membrane can be easily recovered by hydraulic flushing. Generally, membrane fouling can

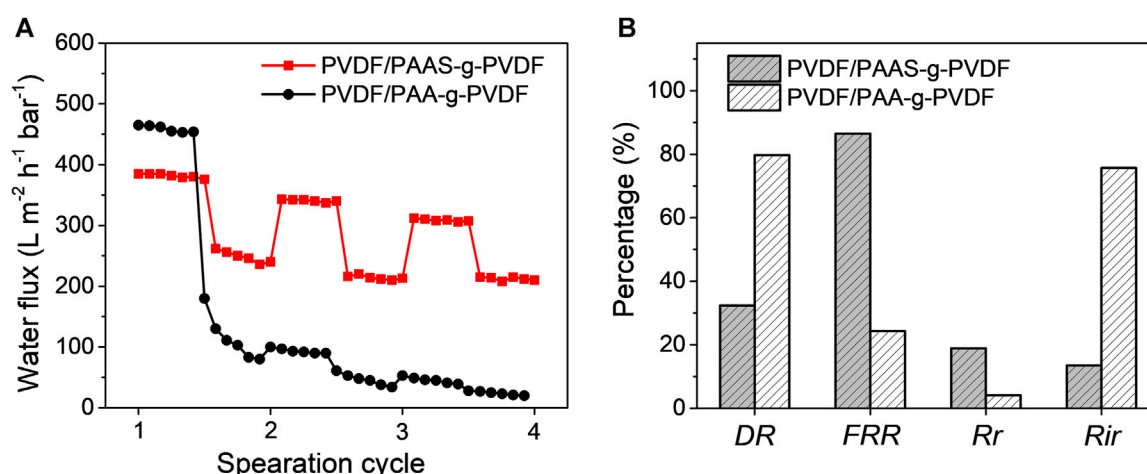


FIGURE 7 (A) Water flux variation of the PVDF/PAAS-g-PVDF blend membrane and the PVDF/PAA-g-PVDF blend membrane during three separation cycles of the SDS-stabilized crude oil-in-water emulsion. (B) Corresponding parameters for evaluating the antifouling ability of the membranes.

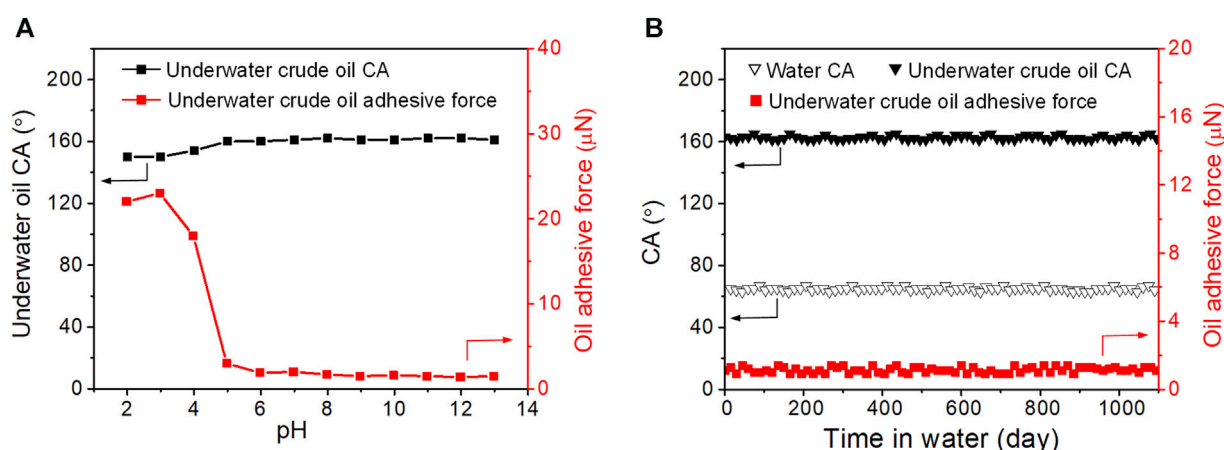


FIGURE 8 (A) Variation of underwater crude oil CA and underwater crude oil adhesive force of the PVDF/PAAS-g-PVDF blend membrane under different pH environments. (B) Variation of water CA, underwater crude oil CA and underwater crude oil adhesive force of the PVDF/PAAS-g-PVDF blend membrane in water (pH = 7) for 1,100 days.

be defined as reversible and irreversible fouling. Reversible fouling is caused by weak adhesion of the oil foulants which can be removed by hydraulic washing. Irreversible fouling corresponds to strong adhesion of the oil foulants or the oil foulants entrapped in the membrane pores which cannot be physically removed. The reversible fouling ratio *Rr* is 18.9%, and the irreversible fouling ratio *Rir* is 13.5% for the PVDF/PAAS-g-PVDF blend membrane according to the flux variation. As a contrast, the water flux of the PVDF/PAA-g-PVDF blend membrane decreases from $475 \pm 10 \text{ L m}^{-2} \text{ h}^{-1} \text{ bar}^{-1}$ to $75 \pm 5 \text{ L m}^{-2} \text{ h}^{-1} \text{ bar}^{-1}$ when filtrating the same crude oil-in-water emulsion. After the same water washing, the pure water flux can only recover to $90 \pm 5 \text{ L m}^{-2} \text{ h}^{-1} \text{ bar}^{-1}$ in the second separation cycle. The flux decline ratio *DR* is as high as 84.2%, the flux recovery ratio *FRR* is only 18.9%, the reversible fouling ratio *Rr* is 3.2%, and the irreversible fouling ratio *Rir* is 81.0% for the PVDF/PAA-g-PVDF blend membrane. What's more, the PVDF/PAA-

g-PVDF blend membrane exhibits the always decreased water flux to nearly zero when filtrating the crude oil-in-water emulsion in the second and the third separation cycle. These results demonstrate the excellent antifouling and cycling performance of the PVDF/PAAS-g-PVDF blend membrane, which is of vital importance to achieve long-term efficient separation of the oil-in-water emulsions.

3.4 Stability of the blend membrane

The mechanical strength of the PVDF/PAAS-g-PVDF blend membrane in the wet state was measured by a universal testing machine, and the same measurement was carried out on the PVDF/PAA-g-PVDF blend membrane as a contrast. As shown in [Supplementary Figure S3](#), the two membranes show the similar tensile

strength of ~ 1 MPa. The PVDF/PAAS-g-PVDF blend membrane exhibits the engineering strain of $\sim 82\%$ which is almost two times of the PVDF/PAA-g-PVDF blend membrane. It indicates that the PVDF/PAAS-g-PVDF blend membrane has better tensile breaking resistance than the PVDF/PAA-g-PVDF blend membrane owing to the good extensibility of the hydrated PAAS. In view of the easy deformation feature of PAAS under a high pressure, the pore size and separation performance of the PVDF/PAAS-g-PVDF blend membrane may be influenced by the transmembrane pressure. We investigated the performance stability of the PVDF/PAAS-g-PVDF blend membrane under different transmembrane pressures during the separation of the SDS-stabilized soybean oil-in-water emulsion. The membrane shows stable water flux of $335\text{--}350\text{ L m}^{-2}\text{ h}^{-1}\text{ bar}^{-1}$ under the transmembrane pressures of 1–3 bar ([Supplementary Figure S4](#)), revealing the well-maintained pore size. When further increasing the transmembrane pressure to 4 bar, the water flux decreases to $270\text{ L m}^{-2}\text{ h}^{-1}\text{ bar}^{-1}$ on account of the compressed membrane pores under such a high pressure. Under the transmembrane pressures of 1–4 bar, the oil content in the filtrate after separation was always below 3 ppm, indicating the stable separation efficiency of the membrane. The pH stability of the PVDF/PAAS-g-PVDF blend membrane was also evaluated by recording its underwater crude oil CA and underwater crude oil adhesive force after immersing the membrane in water with different pH from 2 to 13 for 10 days, respectively. Under the pH from 5 to 12, the membrane exhibits stable low-oil-adhesive underwater superoleophobicity with the underwater crude oil CA above 160° and crude oil adhesive force below $2\text{ }\mu\text{N}$ ([Figure 8A](#)). When the pH is below 4, the underwater crude oil CA decreases to 153° , and the crude oil adhesive force increases sharply to $20\text{ }\mu\text{N}$. This is ascribed to the transformation of PAAS to PAA in the acidic environment, as the acid dissociation constant of PAA is 4.2–4.5. Therefore, the PVDF/PAAS-g-PVDF blend membrane can maintain the outstanding anti-oil-fouling ability under a wide pH range of 5–12.

Restraining the release of the hydrophilic additives from the membranes to water, and endowing the membranes with high stability for long-term use is critically important for developing the blend membranes. In order to evaluate the long-term stability of the PVDF/PAAS-g-PVDF blend membrane, the water CA, underwater crude oil CA and underwater crude oil adhesive force of the membrane were continuously monitored for 1,100 days. During the test, the membrane was immersed in water with the pH of about 7, and the wettability parameters were recorded every 15 days. As shown in [Figure 8B](#), the PVDF/PAAS-g-PVDF blend membrane maintains the hydrophilicity with water CA below 70° , and the underwater superoleophobicity with crude oil CA above 160° , as well as the low-oil-adhesive property with underwater crude oil adhesive force below $2\text{ }\mu\text{N}$ during the whole test period. After the test, the surface morphology and chemical composition of the PVDF/PAAS-g-PVDF blend membrane was nearly unchanged ([Supplementary Figure S5](#)), indicating that the hydrophilic PAAS is stably blended in the membrane without obvious release. It is because of the strong interaction between the PAAS-g-PVDF additive and the PVDF matrix. These results indicate the high stability of the PVDF/PAAS-g-PVDF blend membrane for long-term use.

4 Conclusion

In this work, we proposed a facile method to introduce the strong hydrophilic PAAS in PVDF to fabricate the hydrophilic, underwater low-oil-adhesive superoleophobic and anti-oil-fouling blend ultrafiltration membrane. PAA-g-PVDF was used as the additive precursor to blend with the PVDF matrix to form the uniform PVDF/PAA-g-PVDF blend membrane via the nonsolvent-induced phase inversion. Then PAA in the blend membrane was *in situ* ionized to PAAS to endow the final PVDF/PAAS-g-PVDF blend membrane with strong hydration ability and superior anti-oil-fouling property. The wettability and water permeation flux of the PVDF/PAAS-g-PVDF blend membrane were optimized by regulating the mass ratio of PVDF and PAA-g-PVDF. The PVDF/PAAS-g-PVDF blend membrane achieved efficient separation of multiple emulsifier-stabilized oil-in-water emulsions even including the viscous crude oil-in-water emulsion, with ultrahigh separation efficiency of 99.97%, high water flux of $350\text{ L m}^{-2}\text{ h}^{-1}\text{ bar}^{-1}$, as well as good cycling performance. The blend membrane also exhibited long-term stability lasting for 1,100 days due to the strong interaction between the PAAS-g-PVDF additive and the PVDF matrix. The blend membrane with the outstanding anti-oil-fouling property had a great potential for prolonged separation of real emulsified oily wastewater in a large scale.

Data availability statement

The original contributions presented in the study are included in the article/[Supplementary Material](#), further inquiries can be directed to the corresponding authors.

Author contributions

SG: Conceptualization, Data curation, Formal Analysis, Funding acquisition, Investigation, Methodology, Writing—original draft, Supervision. PL: Data curation, Formal Analysis, Methodology, Writing—original draft. JJ: Conceptualization, Funding acquisition, Supervision, Writing—review and editing.

Funding

The author(s) declare financial support was received for the research, authorship, and/or publication of this article. This work was financially supported by the National Natural Science Foundation of China (21988102, 22105219), the National Key Research and Development Program of China (2022YFB3804901, 2022YFB3804900, 2019YFA0705800), the Natural Science Foundation of Jiangsu Province (BK20210132), the Key Research and Development Plan of Jiangsu Province (BE2022056), the Gusu's Young Leading Talent Program (ZXL2022461) and the Doctoral

Program of Innovation and Entrepreneurship in Jiangsu Province (JSSCBS20211415).

Acknowledgments

We acknowledge the kind support of the PAA-g-PVDF powders by Prof. Jingye Li from Shanghai Normal University.

Conflict of interest

The authors declare that the research was conducted in the absence of any commercial or financial relationships that could be construed as a potential conflict of interest.

References

- Aurell, J., and Gullett, B. K. (2010). Aerostat sampling of PCDD/PCDF emissions from the Gulf oil spill *in situ* burns. *Environ. Sci. Technol.* 44, 9431–9437. doi:10.1021/es103554y
- Chang, Q., Zhou, J.-E., Wang, Y., Liang, J., Zhang, X., Cerneaux, S., et al. (2014). Application of ceramic microfiltration membrane modified by nano-TiO₂ coating in separation of a stable oil-in-water emulsion. *J. Membr. Sci.* 456, 128–133. doi:10.1016/j.memsci.2014.01.029
- Chen, P., and Xu, Z. (2013). Mineral-coated polymer membranes with superhydrophilicity and underwater superoleophobicity for effective oil/water separation. *Sci. Rep.* 3, 2776. doi:10.1038/srep02776
- Chen, Y., Wei, M., and Wang, Y. (2016). Upgrading polysulfone ultrafiltration membranes by blending with amphiphilic block copolymers: beyond surface segregation. *J. Membr. Sci.* 505, 53–60. doi:10.1016/j.memsci.2016.01.030
- Choi, J.-H., Jegal, J., and Kim, W.-N. (2006). Fabrication and characterization of multi-walled carbon nanotubes/polymer blend membranes. *J. Membr. Sci.* 284, 406–415. doi:10.1016/j.memsci.2006.08.013
- Chu, Z., Feng, Y., and Seeger, S. (2015). Oil/water separation with selective superantifouling/superwetting surface materials. *Angew. Chem. Int. Ed.* 54, 2328–2338. doi:10.1002/anie.201405785
- Dong, D., Zhu, Y., Fang, W., Ji, M., Wang, A., Gao, S., et al. (2022). Double-defense design of super-anti-fouling membranes for oil/water emulsion separation. *Adv. Funct. Mater.* 32, 2113247. doi:10.1002/adfm.202113247
- Elimelech, M., and Phillip, W. A. (2011). The future of seawater desalination: energy, technology, and the environment. *Science* 333, 712–717. doi:10.1126/science.1200488
- Gao, S., Chen, J., Zheng, Y., Wang, A., Dong, D., Zhu, Y., et al. (2022). Gradient adhesive hydrogel decorated superhydrophilic membranes for ultra-stable oil/water separation. *Adv. Funct. Mater.* 32, 2205990. doi:10.1002/adfm.202205990
- Gao, S., Sun, J., Liu, P., Zhang, F., Zhang, W., Yuan, S., et al. (2016). A robust polyionized hydrogel with an unprecedented underwater anti-crude-oil-adhesion property. *Adv. Mater.* 28, 5307–5314. doi:10.1002/adma.201600417
- Gao, S., Zhu, Y., Zhang, F., and Jin, J. (2015). Superwetting polymer-decorated SWCNT composite ultrathin films for ultrafast separation of oil-in-water nanoemulsions. *J. Mater. Chem. A* 3, 2895–2902. doi:10.1039/C4TA05624H
- Geng, H., Zhong, Q.-Z., Li, J., Lin, Z., Cui, J., Caruso, F., et al. (2022). Metal ion-directed functional metal-phenolic materials. *Chem. Rev.* 122, 11432–11473. doi:10.1021/acs.chemrev.1c01042
- Jiang, G., Zhang, S., Zhu, Y., Gao, S., Jin, H., Luo, L., et al. (2018). Hydrogel-embedded tight ultrafiltration membrane with superior anti-dye-fouling property for low-pressure driven molecule separation. *J. Mater. Chem. A* 6, 2927–2934. doi:10.1039/C7TA09898G
- Kang, G., and Cao, Y. (2014). Application and modification of poly(vinylidene fluoride)(PVDF) membranes-a review. *J. Membr. Sci.* 463, 145–165. doi:10.1016/j.memsci.2014.03.055
- Lin, J., Ye, W., Baltaru, M. C., Tang, Y. P., Bernstein, N. J., Gao, P., et al. (2016). Tight ultrafiltration membranes for enhanced separation of dyes and Na₂SO₄ during textile wastewater treatment. *J. Membr. Sci.* 514, 217–228. doi:10.1016/j.memsci.2016.04.057
- Liu, F., Hashim, N. A., Liu, Y., Abed, M. R. M., and Li, K. (2011). Progress in the production and modification of PVDF membranes. *J. Membr. Sci.* 375, 1–27. doi:10.1016/j.memsci.2011.03.014
- Oki, T., and Kanae, S. (2006). Global hydrological cycles and world water resources. *Science* 313, 1068–1072. doi:10.1126/science.1128845
- Rana, D., and Matsuura, T. (2010). Surface modifications for antifouling membranes. *Chem. Rev.* 110, 2448–2471. doi:10.1021/cr800208y
- Shi, Q., Su, Y., Zhao, W., Li, C., Hu, Y., Jiang, Z., et al. (2008). Zwitterionic polyethersulfone ultrafiltration membrane with superior antifouling property. *J. Membr. Sci.* 319, 271–278. doi:10.1016/j.memsci.2008.03.047
- Tao, M., Xue, L., Liu, F., and Jiang, L. (2014). An intelligent superwetting PVDF membrane showing switchable transport performance for oil/water separation. *Adv. Mater.* 26, 2943–2948. doi:10.1002/adma.201305112
- Wang, A., Zhu, Y., Fang, W., Gao, S., and Jin, J. (2023). Zero-oil-fouling membrane with high coverage of grafted zwitterionic polymer for separation of oil-in-water emulsions. *Small Methods*, 2300247. doi:10.1002/smt.202300247
- Wang, B., Liang, W., Guo, Z., and Liu, W. (2015). Biomimetic super-lyophobic and super-lyophilic materials applied for oil/water separation: a new strategy beyond nature. *Chem. Soc. Rev.* 44, 336–361. doi:10.1039/C4CS00220B
- Yang, C., Long, M., Ding, C., Zhang, R., Zhang, S., Yuan, J., et al. (2022). Antifouling graphene oxide membranes for oil-water separation via hydrophobic chain engineering. *Nat. Commun.* 13, 7334. doi:10.1038/s41467-022-35105-8
- Yang, H., Pi, J., Liao, K., Huang, H., Wu, Q., Huang, X., et al. (2014). Silica-decorated polypropylene microfiltration membranes with a mussel-inspired intermediate layer for oil-in-water emulsion separation. *ACS Appl. Mater. Interfaces* 6, 12566–12572. doi:10.1021/am502490j
- Yang, X., Martinson, A., Elam, J. W., Shao, L., and Darling, S. (2021). Water treatment based on atomically engineered materials: atomic layer deposition and beyond. *Matter* 4, 3515–3548. doi:10.1016/j.matt.2021.09.005
- Yang, X., Wen, Y., Li, Y., Yan, L., Tang, C., Ma, J., et al. (2023). Engineering *in situ* catalytic cleaning membrane via prebiotic-chemistry-inspired mineralization. *Adv. Mater.* 35, 2306626. doi:10.1002/adma.202306626
- Zhang, F., Zhang, W., Shi, Z., Wang, D., Jin, J., and Jiang, L. (2013b). Nanowire-haired inorganic membranes with superhydrophilicity and underwater ultralow adhesive superoleophobicity for high-efficiency oil/water separation. *Adv. Mater.* 25, 4192–4198. doi:10.1002/adma.201301480
- Zhang, L., Zhong, Y., Cha, D., and Wang, P. (2013a). A self-cleaning underwater superoleophobic mesh for oil-water separation. *Sci. Rep.* 3, 2326. doi:10.1038/srep02326
- Zhang, W., Zhu, Y., Liu, X., Wang, D., Li, J., Jiang, L., et al. (2014). Salt-induced fabrication of superhydrophilic and underwater superoleophobic PAA-g-PVDF membranes for effective separation of oil-in-water emulsions. *Angew. Chem. Int. Ed.* 53, 856–860. doi:10.1002/anie.201308183
- Zhu, Y., Wang, D., Jiang, L., and Jin, J. (2014). Recent progress in developing advanced membranes for emulsified oil/water separation. *NPG Asia Mater* 6, e101. doi:10.1038/am.2014.23

Publisher's note

All claims expressed in this article are solely those of the authors and do not necessarily represent those of their affiliated organizations, or those of the publisher, the editors and the reviewers. Any product that may be evaluated in this article, or claim that may be made by its manufacturer, is not guaranteed or endorsed by the publisher.

Supplementary material

The Supplementary Material for this article can be found online at: <https://www.frontiersin.org/articles/10.3389/frmst.2024.1355773/full#supplementary-material>



OPEN ACCESS

EDITED BY

Nalan Kabay,
Ege University, Türkiye

REVIEWED BY

Isabel Coelho,
NOVA University of Lisbon, Portugal
Marek Bryjak,
Wrocław University of Technology, Poland

*CORRESPONDENCE

Sacide Alsoy Altinkaya,
✉ sacidealsoy@iyte.edu.tr

RECEIVED 04 February 2024

ACCEPTED 15 March 2024

PUBLISHED 09 April 2024

CITATION

Alsoy Altinkaya S (2024), A perspective on cellulose dissolution with deep eutectic solvents.
Front. Membr. Sci. Technol. 3:1382054.
doi: 10.3389/frmst.2024.1382054

COPYRIGHT

© 2024 Alsoy Altinkaya. This is an open-access article distributed under the terms of the [Creative Commons Attribution License \(CC BY\)](https://creativecommons.org/licenses/by/4.0/). The use, distribution or reproduction in other forums is permitted, provided the original author(s) and the copyright owner(s) are credited and that the original publication in this journal is cited, in accordance with accepted academic practice. No use, distribution or reproduction is permitted which does not comply with these terms.

A perspective on cellulose dissolution with deep eutectic solvents

Sacide Alsoy Altinkaya*

Department of Chemical Engineering, Izmir Institute of Technology, Izmir, Türkiye

Currently, membrane manufacturing relies heavily on fossil-based solvents and polymers, resulting in significant negative impacts on human health and the environment. Thus, there is an urgent need for eco-friendly, low-toxicity, and sustainable solvents and polymers to comply with the United Nations' sustainable development goals. Cellulose, as a green, natural, and abundant polymer, offers a sustainable source for membrane manufacturing. However, a significant challenge exists in dissolving cellulose due to strong intermolecular and intramolecular hydrogen bonds within cellulose molecules. Deep eutectic solvents (DESs), which contain both hydrogen bond donor and acceptor groups, have received significant attention as alternative solvents for cellulose dissolution owing to their low cost, low toxicity, environmentally friendly nature, ease of synthesis, and versatility. This review examines experimental studies, and theoretical approaches, highlighting key findings and factors influencing cellulose dissolution in deep eutectic solvents.

KEYWORDS

deep eutectic solvents, cellulose, polymer membranes, COSMO-RS aided deep eutectic solvent design, green solvent, basic deep eutectic solvent

1 Introduction

Membrane technology has been considered a green technology. However, the green membrane manufacturing process has just recently become a concern. Membrane production requires a large amount of fossil-based solvents and polymers. Polyethylene, polypropylene, polysulfone, poly(vinylidene fluoride), polyimide), and poly(benzimidazole) are commonly used petroleum derived polymers to fabricate membranes. Conventional solvents used for dissolving these polymers, such as N-methyl pyrrolidone (NMP), N, N-dimethylformamide (DMF), and dimethylacetamide (DMAc) (Heinze and Koschella, 2005), are also derived from fossil raw materials causing negative impact on the environment and human health. Bio-solvents have been alternatively produced from bio-based feedstock such as carbohydrates, carbohydrate polymers, proteins, alkaloids, plant oils, and animal fats. However, purification of these solvents, usually with extraction, requires toxic chemicals and high-energy input and generates a waste stream (Jin et al., 2017). Therefore, the adoption of greener membrane fabrication methods is currently being considered to align with the United Nations Sustainable Development Goals. In this regard, transitioning from fossil-based polymers to natural polymers is crucial, with cellulose emerging as a significant and abundant renewable biopolymer among them. Composed of repeating D-glucose monomers, each with three hydroxyl groups, cellulose offers a favorable structure for chemical modification. However, its strong intermolecular hydrogen bonds make this semicrystalline polymer insoluble in most organic solvents (Chen et al., 2019), thus, presenting a challenge for cellulose membrane

fabrication using conventional methods like phase inversion. Traditional solvents like N-methylmorpholine-N-oxide (Rosenau et al., 2002), lithium chloride/N,N-dimethylacetamide (DMAc) (Zhang et al., 2014), alkali/urea, or alkali/thiourea aqueous solutions (Xiong et al., 2014), used for dissolving cellulose, are not considered environmentally friendly due to their negative impact on the environment. High-temperature pretreatment or solvent exchange is necessary before dissolving cellulose in DMAc (Raus et al., 2012), while the alkali-urea aqueous system can only dissolve low molecular weight cellulose below -12°C (Egal et al., 2008). Newer, more popular ionic liquids (ILs) have been suggested as sustainable alternatives for cellulose dissolution (Swatloski et al., 2002; Zhao et al., 2009; Velioglu et al., 2014; Zhang et al., 2017). The low vapor pressure of ILs is an appealing feature for reducing air pollution. However, their relatively high solubilities in water and poor biodegradability (Jordana and Gathergood, 2015) cause toxicity in water (Flieger and Flieger, 2020), and their dissolution requires high energy consumption (Chundawat et al., 2020). Additionally, their synthesis is not environmentally friendly.

Deep eutectic solvents (DESs) are also recognized as green solvents and can be easily prepared by combining hydrogen bond donors (HBD) and acceptors (HBA) in a stoichiometric ratio (Cardellini et al., 2015). Similar to ILs, DESs exhibit low vapor pressure but with lower toxicity profiles, particularly when derived from natural compounds such as amino acids, sugars, and carboxylic acids (Hayyan et al., 2016). Furthermore, their synthesis does not require any solvent or extensive purification, making it a more cost-effective option. Like ILs, DESs have the potential to dissolve cellulose due to the hydrogen bonding interaction of hydrogen bond donor (HBD) and hydrogen bond acceptor (HBA). DESs are considered “designer” solvents of a new generation; changing the type and molar ratio of HBA and HBDs can finely adjust their physicochemical properties. This adaptability presents a challenge in selecting the appropriate DES for cellulose dissolution. The multitude of HBA and HBD combinations in various molar ratios increase the potential number of DES candidates for exploration. Consequently, developing predictive tools for designing DESs to enhance cellulose solubility is crucial for greener membrane fabrication. This mini-review aims to offer insights into cellulose dissolution in DESs and investigate the synergies between experimental and theoretical approaches to advance our current understanding of cellulose dissolution in designer DESs.

2 Recent progress in cellulose dissolution using deep eutectic solvents

The research on cellulose dissolution with DESs started in 2012 by testing 26 different DESs to evaluate their capability to dissolve lignin, starch, and cellulose (Francisco et al., 2012). Even though the tested DESs dissolved up to 14.9 wt% of lignin, they demonstrated a limited dissolution capacity for cellulose. The highest cellulose solubility (0.78 wt%) was observed with the DES composed of malic acid and proline in a 1:3 ratio, while the DES consisting of malic acid (HBD) and alanine (HBA) in a 1:1 ratio showed the lowest solubility (0.11 wt%). Sharma et al. (2013) tried

different cellulose dissolution methods, including heating at 100°C for 10 h, ultrasonication followed by heating at 80°C for 1 h, and microwave irradiation at 80°C for 2 h. They achieved an 8 wt% cellulose solubility using the choline chloride and urea (1:2 ratio) combination by keeping the dissolution temperature at 100°C . Surprisingly, microwave irradiation did not significantly enhance cellulose solubility.

Pan et al. (2017) observed that while choline chloride/urea effectively dissolved amorphous cellulose in rice straw, it was not efficient for the solubility of α -cellulose. Tenhunen et al. (2017) similarly reported that choline chloride/urea (molar ratio 1:2) failed to modify cellulose fibers. Hertel et al. (2012) noted the importance of temperature on cellulose dissolution. They found that microcrystalline cellulose (MCC) did not dissolve in DESs containing urea/choline chloride (2:1), oxalic acid/choline chloride, malonic acid/choline chloride (1:1), and formamide/ammonium formate (2:1) at 45°C . Increasing the temperature to 80°C slightly improved the dissolution in malonic acid/choline chloride and formamide/ammonium formate. While the acidic environment for urea/choline chloride and oxalic acid/choline chloride did not enhance cellulose dissolution, a basic medium (pH 14) did enhance it. Ren et al. (2016a) first activated the cellulose using ultrasound-assisted saturated calcium chloride solution. Their data demonstrated that cellulose solubility increased from 1.43 wt% in a choline chloride and urea mixture to 2.48 wt% when imidazole replaced urea. Malaek et al. (2018) reported a maximum solubility of 6.1 wt% in choline chloride and resorcinol through the use of ultrasound irradiation. Zhong et al. (2022) claimed that in contrast to the data reported in the literature, most choline chloride-based DESs cannot effectively dissolve cellulose. They introduced a novel DES by combining urea (Ur) with choline hydroxide (ChOH), which dissolved 9.5 wt% cellulose with a degree of polymerization (DP) of 926 (from cotton litter pulp). The ChOH/Ur system contained approximately 11 wt% water, and complete dissolution was achieved within 30 min at 70°C . The highest reported cellulose solubility in deep eutectic solvents (DESs) thus far is 15%, as documented by Sirvio and Heiskanen (2020), Sharma et al. (2021), and Tong et al. (2021; 2022). Sirvio and Heiskanen (2020) formulated DESs using tetraethylammonium hydroxide (TEAOH) combined with urea, N-methylurea, N-ethylurea, and 1,3-dimethylurea, achieving the best dissolution performance (15%) with the TEAOH:Water:Urea DES in a ratio of 1:15:2. Sharma and colleagues synthesized 22 zwitterion-based DESs by mixing four types of zwitterions with four saccharides at varying ratios. Two DES formulations, involving zwitterion C15 and 5 wt% sucrose and fructose, respectively, dissolved 15% and 10% cellulose at 120°C . Tong et al. (2021) combined zinc chloride (ZnCl_2), water, and phosphoric acid, achieving 15 wt% cellulose dissolution at room temperature in this DES with a molar ratio of 1:3:0.6. In a subsequent study, Tong et al. (2022) developed DESs using ZnCl_2 , water, and formic acid combinations, achieving the highest solubility of 15% for microcrystalline cellulose in a molar ratio of 1:1:4. The dissolution process occurred under relatively mild conditions with minimal heat energy usage, effectively dissolving various cellulose types, including cotton with high crystallinity and degree of polymerization (DP). Table 1 provides a summary of cellulose solubility in different DESs as reported in the literature.

TABLE 1 Solubilities of the cellulose in different DESs.

Hydrogen bond acceptor (HBA)	Hydrogen bond donor (HBD)	Molar ratio (HBA: HBD)	Dissolution Technique	Dissolution time	Solubility (wt%)	References
Alanine	Malic acid	1:1	Heating at 100°C		0.11	Francisco et al. (2012)
Proline	Malic acid	3:1	Heating at 100°C		0.78	Francisco et al. (2012)
Choline Chloride	Urea	1:2	Heating at 100°C	10 h	8	Sharma et al. (2013)
Choline Chloride	Urea	1:2	Ultrasonication and heating at 80°C	1 h	6	Sharma et al. (2013)
Choline Chloride	Urea	1:2	Microwave irradiation at 80°C	2 h	1.5	Sharma et al. (2013)
Choline Bromide	Urea	1:2	Heating at 100°C	10 h	5	Sharma et al. (2013)
Choline Bromide	Urea	1:2	Ultrasonication and heating at 80°C	1 h	6	Sharma et al. (2013)
Choline Bromide	Urea	1:2	Microwave irradiation at 80°C	2 h	6	Sharma et al. (2013)
Choline Chloride	Urea	1:2	Heating at 100°C	10 h	5	Sharma et al. (2013)
Choline Chloride	Urea	1:2	Ultrasonication and heating at 80°C	1 h	5	Sharma et al. (2013)
Choline Chloride Bromide	Urea	1:2	Microwave irradiation at 80°C	2 h	3	Sharma et al. (2013)
Betaine Hydrochloride	Urea	1:4	Heating at 100°C	10 h	2.5	Sharma et al. (2013)
Betaine Hydrochloride	Urea	1:4	Ultrasonication and heating at 80°C	1 h	2.5	Sharma et al. (2013)
Choline Chloride	Ethylene Glycol	1:2	Heating at 100°C	10 h	Non	Sharma et al. (2013)
Choline Chloride	Ethylene Glycol	1:2	Ultrasonication and heating at 80°C	1 h	Non	Sharma et al. (2013)
Choline Chloride	Ethylene Glycol	1:2	Microwave irradiation at 80°C	2 h	Non	Sharma et al. (2013)
Choline Chloride	Glycerol	1:2	Heating at 100°C	10 h	3	Sharma et al. (2013)
Choline Chloride	Glycerol	1:2	Ultrasonication and heating at 80°C	1 h	2.5	Sharma et al. (2013)
Choline Chloride	Glycerol	1:2	Microwave irradiation at 80°C	2 h	3.5	Sharma et al. (2013)
Choline Chloride	Imidazole	3:7	Heating from 20 to 120°C at a rate of 10°C intervals	1.5 h	2.48	Ren et al. (2016a)
Choline Chloride	Urea	1:2	Heating from 20 to 120°C at a rate of 10°C intervals	2 h	1.43	Ren et al. (2016a)
Choline Chloride	Ammonium thiocyanate	1:1	Heating from 20 to 120°C at a rate of 10°C intervals	3 h	0.85	Ren et al. (2016a)
Choline Chloride	Caprolactam	1:1	Heating from 20 to 120°C at a rate of 10°C intervals	4 h	0.16	Ren et al. (2016a)
Choline Chloride	Acetamide	1:2	Heating from 20 to 120°C at a rate of 10°C intervals	24 h	0.22	Ren et al. (2016a)
Allyl triethyl ammonium Chloride	Oxalic acid	1:1	Heating at 110°C		6.48	Ren et al. (2016b)
Choline Chloride	Oxalic acid	2:1	Heating at 110°C		0.8	Ren et al. (2016b)

(Continued on following page)

TABLE 1 (Continued) Solubilities of the cellulose in different DESs.

Hydrogen bond acceptor (HBA)	Hydrogen bond donor (HBD)	Molar ratio (HBA: HBD)	Dissolution Technique	Dissolution time	Solubility (wt%)	References
Choline Chloride	Phenol	2:1	Heating at 75°C and 20 min ultrasonic irradiation	24 h	4.7	Malaek et al. (2018)
Choline Chloride	α -naphthol	1:1	Heating at 75°C and 20 min ultrasonic irradiation	24 h	3.39	Malaek et al. (2018)
Choline Chloride	Resorcinol	1:1	Heating at 75°C and 20 min ultrasonic irradiation	24 h	6.1	Malaek et al. (2018)
Choline Chloride	Maleic acid	1:1	Heating at 75°C and 20 min ultrasonic irradiation	24 h	2.57	Malaek et al. (2018)
Choline Chloride	Ethylene Glycol	1:2	Stirring (500 rpm) at 25°C	1 week	1.3×10^{-4} *	Hakkinen and Abbott (2019)
Choline Chloride	1,5-pentanediol	1:3.5	Stirring (500 rpm) at 25°C	1 week	2.3×10^{-5} *	Hakkinen and Abbott (2019)
Choline Chloride	Glycerol	1:2	Stirring (500 rpm) at 25°C	1 week	1.9×10^{-5} *	Hakkinen and Abbott (2019)
Choline Chloride	Urea	1:2	Stirring (500 rpm) at 25°C	1 week	1.7×10^{-5} *	Hakkinen and Abbott (2019)
Choline Chloride	Oxalic acid dihydrate	1:1	Stirring (500 rpm) at 25°C	1 week	6.8×10^{-5} *	Hakkinen and Abbott (2019)
Choline Chloride	Formic acid	2:1	Heating at 60°C		<1	Lynam et al. (2017)
Choline Chloride	Lactic acid	10:1	Heating at 60°C		<3	Lynam et al. (2017)
Choline Chloride	Acetic acid	2:1	Heating at 60°C		<1	Lynam et al. (2017)
Choline Chloride	Lactic acid	2:1	Heating at 60°C		<1	Lynam et al. (2017)
Choline Chloride	Lactic acid	3.3:1	Heating at 60°C		<1	Lynam et al. (2017)
Tetraethylammonium hydroxide/water	Urea	1:15:2	Room temperature		15	Sirvio and Heiskanen (2020)
Tetraethylammonium hydroxide/water	Urea	1:16:3	Room temperature		10	Sirvio and Heiskanen (2020)
Tetraethylammonium hydroxide/water	Urea	1:15:4	Room temperature		10	Sirvio and Heiskanen (2020)
Tetraethylammonium hydroxide/water	Urea	1:16:5	Room temperature		7.5	Sirvio and Heiskanen (2020)
Tetraethylammonium hydroxide/water	Urea	1:15:6	Room temperature		7.5	Sirvio and Heiskanen (2020)
Tetraethylammonium hydroxide/water	Methylurea	1:15:2	Room temperature		12.5	Sirvio and Heiskanen (2020)
Tetraethylammonium hydroxide/water	Methylurea	1:16:3	Room temperature		5	Sirvio and Heiskanen (2020)
Tetraethylammonium hydroxide/water	Methylurea	1:15:4	Room temperature		5	Sirvio and Heiskanen (2020)
Tetraethylammonium hydroxide/water	Methylurea	1:16:5	Room temperature		5	Sirvio and Heiskanen (2020)
Tetraethylammonium hydroxide/water	Methylurea	1:15:6	Room temperature		5	Sirvio and Heiskanen (2020)

(Continued on following page)

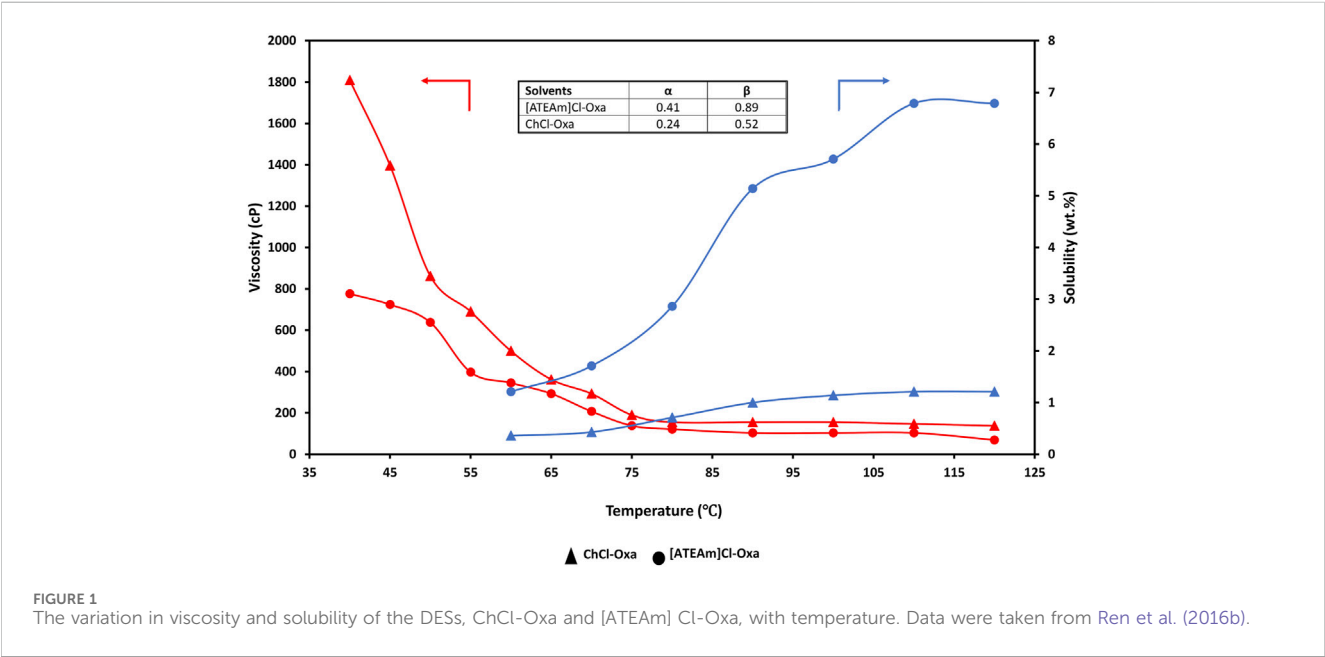
TABLE 1 (Continued) Solubilities of the cellulose in different DESs.

Hydrogen bond acceptor (HBA)	Hydrogen bond donor (HBD)	Molar ratio (HBA: HBD)	Dissolution Technique	Dissolution time	Solubility (wt%)	References
Tetraethylammonium hydroxide/water	Methylurea	1:15:7	Room temperature		5	Sirvio and Heiskanen (2020)
Tetraethylammonium hydroxide/water	Ethylurea	1:16:2	Room temperature		12.5	Sirvio and Heiskanen (2020)
Tetraethylammonium hydroxide/water	Ethylurea	1:16:3	Room temperature		Non	Sirvio and Heiskanen (2020)
Tetraethylammonium hydroxide/water	Ethylurea	1:15:4	Room temperature		Non	Sirvio and Heiskanen (2020)
Tetraethylammonium hydroxide/water	Ethylurea	1:15:5	Room temperature		Non	Sirvio and Heiskanen (2020)
Tetraethylammonium hydroxide/water	1,3 Dimethylurea	1:16:2	Room temperature		7.5	Sirvio and Heiskanen (2020)
Tetraethylammonium hydroxide/water	1,3 Dimethylurea	1:16:3	Room temperature		5	Sirvio and Heiskanen (2020)
Tetraethylammonium hydroxide/water	1,3 Dimethylurea	1:15:4	Room temperature		5	Sirvio and Heiskanen (2020)
Tetraethylammonium hydroxide/water	1,3 Dimethylurea	1:15:5	Room temperature		5	Sirvio and Heiskanen (2020)
Tetraethylammonium hydroxide/water	1,3 Dimethylurea	1:16:6	Room temperature		5	Sirvio and Heiskanen (2020)
Tetraethylammonium hydroxide/water	1,3 Dimethylurea	1:14:7	Room temperature		Non	Sirvio and Heiskanen (2020)
Tetraethylammonium hydroxide/water	1,3 Dimethylurea	1:15:2	Room temperature		10	Sirvio and Heiskanen (2020)
Tetraethylammonium hydroxide/water	1,3 Dimethylurea	1:15:3	Room temperature		Non	Sirvio and Heiskanen (2020)
Zinc Chloride/Water	Phosphoric acid	1:3:0.6	Room temperature		15	Tong et al. (2021)
Zinc Chloride/Water	Formic acid	1:1:4	Room temperature	1.6 h	15	Tong et al. (2022)
Zinc Chloride/Water	Formic acid	1:2:4	Room temperature	6 h	12.5	Tong et al. (2022)
Zinc Chloride/Water	Formic acid	1:3:4	Room temperature	7 h	9	Tong et al. (2022)
Zinc Chloride/Water	Formic acid	1:4:4	Room temperature	13.5 h	8	Tong et al. (2022)
Choline Chloride	Urea	2:1	Heating at 100°C	3 h	1.03	Zhang et al. (2020)
Choline Chloride	Citric acid	2:1	Heating at 100°C	2 h	1.94	Zhang et al. (2020)
Choline Chloride	Oxalic acid	2:1	Heating at 100°C	1.5 h	2.54	Zhang et al. (2020)
Choline Chloride	Glycerol	2:1	Heating at 100°C	12 h	0.6	Zhang et al. (2020)
Choline	L-lysine	1:2	Ultrasound (600 W) 40 min and heating at 90°C	24 h	~5	Wang et al. (2020)
Choline Chloride	Urea	1:2	Heating at 100°C	24 h	Non	Zhong et al. (2022)
Choline Chloride	Thiourea	1:2	Heating at 100°C	24 h	Non	Zhong et al. (2022)
Choline Chloride	Resorcinol	1:1	Heating at 100°C	24 h	Non	Zhong et al. (2022)
Choline Chloride	Imidazole	3:7	Heating at 100°C	24 h	Non	Zhong et al. (2022)
Choline Chloride	Acetic acid	1:1	Heating at 60°C	24 h	Non	Zhong et al. (2022)
Choline Hydroxide	Urea	1:2	Heating at 70°C	20 min	9.51	Zhong et al. (2022)

(Continued on following page)

TABLE 1 (Continued) Solubilities of the cellulose in different DESs.

Hydrogen bond acceptor (HBA)	Hydrogen bond donor (HBD)	Molar ratio (HBA: HBD)	Dissolution Technique	Dissolution time	Solubility (wt%)	References
Choline Hydroxide	Thiourea	1:2	Heating at 70°C	2 h	Non	Zhong et al. (2022)
Choline Hydroxide	Resorcinol	1:1	Heating at 100°C	2 h	Non	Zhong et al. (2022)
Choline Hydroxide	Imidazole	3:7	Heating at 100°C	2 h	Non	Zhong et al. (2022)
Choline Hydroxide	L-Histidine	1:1	Heating at 100°C	2 h	Non	Zhong et al. (2022)
Choline Hydroxide	Serine	1:1	Heating at 100°C	2 h	Non	Zhong et al. (2022)
Tetramethylammonium Chloride	Formic acid	1:3	Heating at 90°C	2 h	<0.49	Zhang et al. (2023)
Tetramethylammonium Chloride	Glycolic acid	1:2	Heating at 90°C	2 h	<0.54	Zhang et al. (2023)
Tetramethylammonium Chloride	Ethylene glycol	1:2	Heating at 90°C	2 h	<0.66	Zhang et al. (2023)
Choline Chloride	Oxalic acid	1:2	Heating at 90°C	2 h	<0.58	Zhang et al. (2023)
Choline Chloride	Oxalic acid	1:1	Heating at 90°C	2 h	<0.62	Zhang et al. (2023)



3 Exploration of key factors for cellulose dissolution in deep eutectic solvents

Literature studies indicate that the hydrogen bond acceptor strength (β) of a deep eutectic solvent (DES) is the primary factor influencing its ability to dissolve cellulose. Ren et al (2016a) reported the highest cellulose solubility of 2.48% for the DES, choline chloride/imidazole, with the highest basicity ($\beta = 0.864$). The order of solubility of DES correlated with the order of basicity values: Choline chloride/imidazole (2.48 wt%, $\beta = 0.864$) > choline chloride/urease (1.45 wt%, $\beta = 0.821$) > choline

chloride/ammonium thiocyanate (0.83 wt%, $\beta = 0.81$). Similarly, the data reported by Zhong et al. (2022) show that the higher cellulose solubility in choline hydroxide/urea ($\beta = 1.88$) than in choline chloride/urea ($\beta = 0.49$) is directly related to the basicities of the DESs.

Viscosity of the DES is another important parameter controlling its dissolution power. The solvents with lower viscosity penetrate the polymer matrix more readily, enhancing polymer chain mobility, leading to faster dissolution rates. Ren et al. (2016b) noted that the DES composed of allyl triethyl ammonium chloride ([ATEAm]Cl) and oxalic acid (Oxa) demonstrated greater cellulose dissolution compared to choline chloride (ChCl) and Oxa. This difference was

attributed to its lower viscosity, as illustrated in Figure 1. A lower activation energy for [ATEAm]Cl-Oxa (44.56 kJ mol⁻¹), compared to ChCl-Oxa (57.82 kJ mol⁻¹) suggests weaker hydrogen bonding between chloride and Oxa in [ATEAm]Cl-Oxa, leading to increased interaction with cellulose molecules and a higher cellulose dissolution capacity. In another study, the same research group reported the highest cellulose solubility at 2.48% in choline chloride/imidazole, which exhibited the lowest viscosity among the investigated DESs (Ren et al., 2016a). Fan et al. (2021) found that the viscosity of the natural deep eutectic solvents (NADES) correlates with the hydrogen-bond number and lifetime. Among five terpene-based natural deep eutectic solvents (NADES) including camphor/formic acid, menthol/acetic acid, menthol/ β -citronellol, menthol/lactic acid, and thymol/ β -citronellol, terpene-acid-based NADES with single sites exhibited the lowest viscosity due to their weak and unstable hydrogen bonding. Conversely, NADES based on multi-site terpene acids had comparatively higher viscosity. Based on their results, the DES with the lowest binding energy also demonstrated the lowest viscosity. Ghaedi et al. (2017) reported that the higher molecular weight of the DES resulted in the higher viscosity and surface tension.

The intrinsic viscosity (η_{sp}) of a DES/cellulose solution serves as another reference standard for solvation capacity of the DESs and can be calculated by Eqs 1, 2.

$$\eta = \left(\frac{\eta_{sp}}{C} \right)_{C \rightarrow 0} \quad (1)$$

$$\eta_{sp} = C[\eta] + K_H(C[\eta])^2 + A(C[\eta])^n \quad (2)$$

where K_H represents the Huggins constant, and solutes are considered dissolved in solvents when K_H is less than 0.5 (Kulicke and Kniewsker, 1984). Tong et al. (2022) reported that the K_H values, and consequently the viscosity of the cellulose solution increased with the degree of polymerization of cellulose, leading to a lower level of cellulose dissolution.

Theoretically, cellulose dissolution takes place when Gibbs free energy change ($\Delta G < 0$) is negative. Considering that $\Delta G = \Delta H - T\Delta S$, then, if the dissolution is endothermic ($\Delta H > 0$), the entropic contribution, $T\Delta S$, may not be sufficient to counterbalance the ΔH , thus the dissolution process will not be spontaneous. Tong et al. (2022) observed enhanced cellulose solubility with the increased exothermic heat of mixing for DESs formulated using combinations of ZnCl₂, water, and formic acid. Additionally, they noted that the DESs that induce more exothermic dissolution, leading to lower ΔG values, consequently, an exponential increase in the equilibrium constant shortened the dissolution time. Conversely, DESs that exhibited increased cellulose solubility with temperature, suggesting endothermic dissolution, dissolved cellulose at lower levels (Figure 1).

The presence of excessive water molecules is another factor affecting the dissolution power of DES. An increased water content in the DES formulation resulted in a reduction of the dissolved cellulose amount. (Tong et al., 2022; Zhong et al., 2022). Furthermore, the addition of the hydrophilic compound PEG in the DES formulation played a crucial role in disrupting the strong intermolecular hydrogen bonds between cellulose molecules. Ren et al. (2016a) reported improved cellulose solubility in choline chloride/imidazole-coupled PEG.

4 Computational tools for predicting the cellulose solubility in deep eutectic solvents

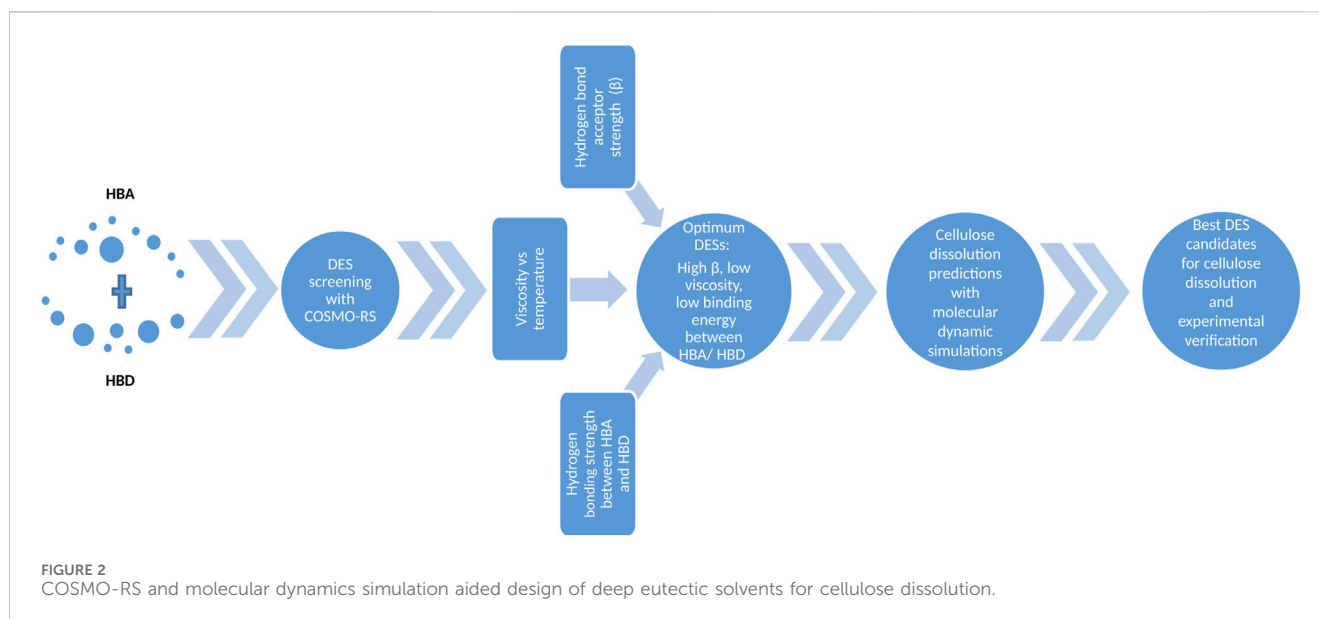
Generally, the solubility parameter (or Hildebrand parameter) is the most commonly used criterion in choosing a suitable solvent for dissolving a polymer based on the principle of “like dissolves like” (Hildebrand et al., 1962; Hansen et al., 2007). The small value of Flory-Huggins interaction parameter, ($\chi < 0.5$), which is proportional to polymer (δ_p) and solvent (δ_s) Hildebrand solubility parameters, $\chi \approx \frac{(\delta_p - \delta_s)^2}{RT}$ indicates complete dissolution of polymer by the selected solvent (Miller-Chou and Koenig, 2003). However, recent reports showed that solubility parameters cannot be a guideline for predicting polymer solubilities in DES and ILs (Winterton et al., 2006; Ueki and Watanabe, 2012; Ismail et al., 2022). For example, Ismail et al. (2022) calculated the solubility parameters from the group contribution method for three types of non-ionic DES and polyvinylidene fluoride (PVDF). According to their results, PVDF was not expected to be soluble in any of the DES, but indeed, PVDF was dissolved in all three DES.

Recent experimental studies have shown that the HBA strength, β values, can be a valuable indicator for evaluating the DES's cellulose dissolving power. β values and the other 2 Kamlet-Taft (KAT) polarity parameters can be experimentally measured using solvatochromic dyes (Zhong et al., 2022). However, considering the large number of HBA and HBD combinations for DES formulation, experimental screening of all formulations is expensive and impractical. A quantum chemical (QC) based conductor-like screening model real solvent (COSMO-RS) approach is a practical tool for predicting the KAT parameters of the DESs. In this method, the COSMO file is generated through independent optimization of the geometries of the HBAs and HBDs by QC calculation. Next, hydrogen bonding energy (EHB), misfit energy (EMF), van der Waals energy, and non-bonded interactions of DES are estimated using the COSMO-RS model. The H-bond acidity and basicity values are then calculated using the three specific interactions by Eqs 3, 4.

$$\alpha = A_\alpha \frac{E_{HB}}{\sum_n E_{HB}} + B_\alpha \frac{E_{MF}}{\sum_n E_{MF}} + C_\alpha \frac{E_{VDW}}{\sum_n E_{VDW}} + D_\alpha \quad (3)$$

$$\beta = A_\beta \frac{E_{HB}}{\sum_n E_{HB}} + B_\beta \frac{E_{MF}}{\sum_n E_{MF}} + C_\beta \frac{E_{VDW}}{\sum_n E_{VDW}} + D_\beta \quad (4)$$

The constants A_α , B_α , C_α , and D_α as well as A_β , B_β , C_β , and D_β , are determined by fitting the interaction energies of a specific subclass of DES to the experimentally determined KAT parameters. The subclasses are constructed based on the hydrophilicity/hydrophobicity of the DESs. Within each hydrophilic or hydrophobic group, the subgroups are then generated based on HBA and HBD types. Kundu et al. (2020) analyzed experimental data on 88 types of DESs. Among these, 26 fall into the hydrophilic class while the remaining belong to the hydrophobic class. The hydrophilic class comprises 19 ChCl-based DESs, 3 other choline cation-based DESs, 3 betaine DESs, and 1 ethyl (2-hydroxyethyl) dimethylammonium DES. The hydrophobic class is further divided into 34 tetraalkylammonium salt-based DESs (including chloride and bromide anions), 11 menthol-based DESs, and 17 thymol-based DESs. They predicted α and β parameters for these 88 DESs, yielding deviations of less than 2.25% and 3.14%, respectively. Subsequently, these models were applied to predict α and β values for novel hydrophilic and hydrophobic DESs formulated with new HBA and HBD. Based on



their predictions, tetraalkylammonium-based hydrophobic deep eutectic solvents (DESs) containing tetraheptylammonium chloride octanoic acid ([N7777]Cl/OctA) and tetraoctylammonium chloride octanoic acid ([N8888]Cl/OctA) show potential for high cellulose dissolution capacity, attributed to their relatively high β values. These estimations align with the experimental data reported by [Sirvio and Heiskanen \(2020\)](#) for tetraethylammonium hydroxide/water, which dissolved 15% cellulose at room temperature.

The KAT parameters were also predicted with the molecular dynamics (MD) and Monte Carlo (MC) approaches based on interactions with solvatochromic dye. However, developing reliable force fields for the DESs is still challenging. Consequently, the accuracy of predicted datasets remains questionable when employing the MD approach. Moreover, both approaches are computationally expensive, and given the ever-growing number of DES, constructing a comprehensive database using these approaches would be time consuming. Therefore, these methods are not suitable for a fast priori prediction.

5 Future directions and conclusion

Knowing the hydrogen bond acceptor strength (β) and viscosity of the DESs can provide insight into their capacity for dissolving cellulose. However, the experimental measurement of these quantities is a significant challenge and practically unfeasible task due to numerous alternative HBA and HBD couples that can be used in DES formulation. At this stage, computational tools can serve as a valuable resource for fast screening alternative DES formulations ([Figure 2](#)).

The COSMO-RS-aided design proves helpful in attaining this objective, as it can predict KAT parameters, viscosity, and hydrogen bonding strength between HBA and HBD groups in DES. Screening numerous DES formulations to identify those with high hydrogen bond basicity (β), low viscosity, low activation energy, and weak hydrogen-bonding strength saves time and resources. As a result, this approach enhances the chances of discovering promising DESs. The subsequent step involves implementing molecular dynamic

simulations to predict cellulose dissolution with optimal DES formulations, followed by experimental verification of the predictions. Utilizing computational power and experimental tools is believed to advance our current understanding of cellulose dissolution in DESs. The accuracy of COSMO-RS predictions is significantly dependent on the precise theoretical representation of interaction energies within the framework. As a result, further improvement of the predicted and extended scale database should be achieved by incorporating various interaction parameters available in the literature. Moreover, the emergence of artificial intelligence (AI)-based methodologies provides a novel avenue for establishing correlations between structure and material properties.

Cellulose dissolution occurs only when the dissolved state has lower energy compared to the solid state, indicating a balance between the enthalpy of mixing and the entropy term. From this perspective, designing DESs with excellent interaction with cellulose, thereby overcoming the low entropy gain, and providing an exothermic heat of mixing will enhance cellulose dissolution. Given that cellulose has both hydrophilic (equatorial OH-groups) and hydrophobic (axial CH groups) features, DES formulations should incorporate both a hydrogen bonding component and a hydrophobic segment to achieve high dissolution capacity for cellulose. Additionally, the experimental findings suggest that the HBA and HBD couples for DES design should feature short chains and single sites for binding. This design choice leads to DESs with lower molecular weights, resulting in reduced viscosity and weaker hydrogen bonding.

The exploration of industrial applications for DESs is still in its early stages of development. Future research in this area should focus on developing tailored DESs with low viscosity, high thermal stability, long lifetime, and the ability to provide efficient dissolution at room temperature within a short timeframe.

Author contributions

SA: Conceptualization, Data curation, Formal Analysis, Investigation, Writing—original draft, Writing—review and editing.

Funding

The author(s) declare that no financial support was received for the research, authorship, and/or publication of this article.

Conflict of interest

The author declares that the research was conducted in the absence of any commercial or financial relationships that could be construed as a potential conflict of interest.

References

- Cardellini, F., Germani, R., Cardinali, G., Corte, L., Roscini, L., Spreti, N., et al. (2015). Room temperature deep eutectic solvents of (1S)-(+)-10-camphorsulfonic acid and sulfobetaines: hydrogen bond-based mixtures with low ionicity and structure-dependent toxicity. *RSC Adv.* 5, 31772–31786. doi:10.1039/c5ra03932k
- Chen, Y.-L., Zhang, X., You, T.-T., and Xu, F. (2019). Deep eutectic solvents (DESs) for cellulose dissolution: a mini-review. *Cellulose* 26, 205–213. doi:10.1007/s10570-018-2130-7
- Chundawat, S. P. S., Sousa, L. D., Roy, S., Yang, Z., Gupta, S., Pal, R., et al. (2020). Ammonia-salt solvent promotes cellulosic biomass deconstruction under ambient pretreatment conditions to enable rapid soluble sugar production at ultra-low enzyme loadings. *Green Chem.* 22, 204–218. doi:10.1039/c9gc03524a
- Egal, M., Budtova, T., and Navard, P. (2008). The dissolution of microcrystalline cellulose in sodium hydroxide-urea aqueous solutions. *Cellulose* 15, 361–370. doi:10.1007/s10570-007-9185-1
- Fan, C., Liu, Y., Sebbah, T., and Cao, X. L. (2021). A theoretical study on terpene-based natural deep eutectic solvent: relationship between viscosity and hydrogen-bonding interactions. *Glob. Challenges* 5, 2000103. doi:10.1002/gch2.202000103
- Flieger, J., and Flieger, M. (2020). Ionic liquids toxicity—benefits and threats. *Int. J. Mol. Sci.* 21, 6267. doi:10.3390/ijms21176267
- Francisco, M., van den Bruinhorst, A., and Kroon, M. C. (2012). New natural and renewable low transition temperature mixtures (LTMs): screening as solvents for lignocellulosic biomass processing. *Green Chem.* 14, 2153–2157. doi:10.1039/c2gc35660k
- Ghaedi, H., Ayoub, M., Sufian, S., Shariff, A. M., and Lal, B. (2017). The study on temperature dependence of viscosity and surface tension of several Phosphonium-based deep eutectic solvents. *J. Mol. Liq.* 241, 500–510. doi:10.1016/j.molliq.2017.06.024
- Hakkinen, R., and Abbott, A. (2019). Solvation of carbohydrates in five choline chloride-based deep eutectic solvents and the implication for cellulose solubility. *Green Chem.* 21, 4673–4682. doi:10.1039/c9gc00559e
- Hansen, C. M. (2007). *Hansen solubility parameters: a user's handbook*. Boca Raton, FL: CRC Press.
- Hayyan, M., Mbous, Y. P., Looi, C. Y., Wong, W. F., Hayyan, A., Salleh, Z., et al. (2016). Natural deep eutectic solvents: cytotoxic profile. *SpringerPlus* 5, 913. doi:10.1186/s40064-016-2575-9
- Heinze, T., and Koschella, A. (2005). Solvents applied in the field of cellulose chemistry: a mini review. *Polímeros* 15, 84–90. doi:10.1590/s0104-14282005000200005
- Hertel, M., Bommarious, A., Realf, M., and Kang, Y. (2012). Deep eutectic solvent systems and methods. *Patent*. WO2012/145522.
- Hildebrand, J. H., and Scott, R. L. (1962). *Regular solutions*. Prentice Hall. Englewood Cliffs, N. J.
- Ismail, N., Pan, J., Rahmati, M., Wang, Q., Bouyer, D., Khayet, M., et al. (2022). Non-ionic deep eutectic solvents for membrane formation. *J. Membr. Sci.* 646, 120238. doi:10.1016/j.memsci.2021.120238
- Jin, S., Byrne, F., McElroy, C. R., Sherwood, J., Clark, J. H., and Hun, A. J. (2017). Challenges in the development of bio-based solvents: a case study on methyl(2,2-dimethyl-1,3-dioxolan-4-yl)methyl carbonate as an alternative aprotic solvent. *Faraday Discuss.* 202, 157–173. doi:10.1039/c7fd00049a
- Jordana, A., and Gathergood, N. (2015). Biodegradation of ionic liquids – a critical review. *Chem. Soc. Rev.* 44, 8200–8237. doi:10.1039/c5cs00444f
- Kulicke, M., and Kniewsker, R. (1984). The shear viscosity dependence on concentration, molecular weight, and shear rate of polystyrene solutions. *Rheol. Acta* 23, 75–83. doi:10.1007/bf01333878
- Kundu, D., Rao, P. S., and Banerjee, T. (2020). First-principles prediction of Kamlet–Taft solvatochromic parameters of deep eutectic solvent using the COSMO-RS model. *Industrial Eng. Chem. Res.* 59, 11329–11339. doi:10.1021/acs.iecr.0c00574
- Lynam, J. G., Kumar, N., and Wong, M. J. (2017). Deep eutectic solvents' ability to solubilize lignin, cellulose, and hemicellulose; thermal stability; and density. *Bioresour. Technol.* 238, 684–689. doi:10.1016/j.biortech.2017.04.079
- Malaeke, H., Housaindokht, M. R., Monhemi, H., and Izadyar, M. (2018). Deep eutectic solvent as an efficient molecular liquid for lignin solubilization and wood delignification. *J. Mol. Liq.* 263, 193–199. doi:10.1016/j.molliq.2018.05.001
- Miller-Chou, B. A., and Koenig, J. L. (2003). A review of polymer dissolution. *Prog. Polym. Sci.* 28, 1223–1270. doi:10.1016/s0079-6700(03)00045-5
- Pan, M., Zhao, G., Ding, C., Wu, B., Lian, Z., and Lian, H. (2017). Physicochemical transformation of rice straw after pretreatment with a deep eutectic solvent of choline chloride/urea. *Carbohydr. Polym.* 176, 307–314. doi:10.1016/j.carbpol.2017.08.088
- Raus, V., Sturcova, A., Dybal, J., Slouf, M., Vackova, T., Salek, P., et al. (2012). Activation of cellulose by 1,4-dioxane for dissolution in N,N-dimethylacetamide/LiCl. *Cellulose* 19, 1893–1906. doi:10.1007/s10570-012-9779-0
- Ren, H., Chen, C., Guo, S., Zhao, D., and Wang, Q. (2016b). Synthesis of a novel allyl-functionalized deep eutectic solvent to promote dissolution of cellulose. *BioResources* 11 (4), 8457–8469. doi:10.15376/biores.11.4.8457-8469
- Ren, H. W., Chen, C. M., Wang, Q. H., Zhao, D. S., and Guo, S. H. (2016a). The properties of choline chloride-based deep eutectic solvents and their performance in the dissolution of cellulose. *BioResources* 11, 5435–5451. doi:10.15376/biores.11.2.5435-5451
- Rosenau, T., Potthast, A., Adorjan, I., Hofinger, A., Sixta, H., Firgo, H., et al. (2002). Cellulose solutions in N-methylmorpholine-N-oxide (NMMO)—degradation processes and stabilizers. *Cellulose* 9, 283–291. doi:10.1023/a:1021127423041
- Sharma, G., Takahashi, K., and Kuroda, K. (2021). Polar zwitterion/saccharide-based deep eutectic solvents for cellulose processing. *Carbohydr. Polym.* 267, 118171. doi:10.1016/j.carbpol.2021.118171
- Sharma, M., Mukesh, C., Mondal, D., and Prasad, K. (2013). Dissolution of α -chitin in deep eutectic solvents. *RSC Adv.* 3, 18149–18155. doi:10.1039/c3ra43404d
- Sirvio, J. A., and Heiskanen, J. P. (2020). Room-temperature dissolution and chemical modification of cellulose in aqueous tetraethylammonium hydroxide–carbamide solutions. *Cellulose* 27, 1933–1950. doi:10.1007/s10570-019-02907-x
- Swatloski, R. P., Spear, S. K., Holbrey, J. D., and Rogers, R. D. (2002). Dissolution of cellulose [correction of cellose] with ionic liquids. *J. Am. Chem. Soc.* 124 (18), 4974–4975. doi:10.1021/ja025790m
- Tenhunen, T.-M., Lewandowska, A. E., Orelma, H., Johansson, L.-S., Virtanen, T., Harlin, A., et al. (2017). Understanding the interactions of cellulose fibres and deep eutectic solvent of choline chloride and urea. *Cellulose* 25, 137–150. doi:10.1007/s10570-017-1587-0
- Tong, Z., Meng, J., Liu, S., Liu, Y., Zeng, S., Wang, L., et al. (2021). Room temperature dissolving cellulose with a metal salt hydrate-based deep eutectic solvent. *Carbohydr. Polym.* 272, 118473. doi:10.1016/j.carbpol.2021.118473
- Tong, Z., Wang, W., Zeng, S., Sun, Y., Meng, J., Liu, Y., et al. (2022). Hydrogen bond reconstruction strategy for eutectic solvents that realizes room-temperature dissolution of cellulose. *Green Chem.* 24, 8760–8769. doi:10.1039/d2gc03372k
- Ueki, T., and Watanabe, M. (2012). Polymers in ionic liquids: dawn of neoteric solvents and innovative materials. *Bull. Chem. Soc. Jpn.* 85, 33–50. doi:10.1246/bcsj.20110225
- Velioglu, S., Yao, X., Devémy, J., Ahunbay, M. G., Tantekin-Ersolmaz, S. B., Dequidt, A., et al. (2014). Solvation of a cellulose microfibril in imidazolium acetate ionic liquids: effect of a cosolvent. *J. Phys. Chem. B* 118, 14860–14869. doi:10.1021/jp508113a
- Wang, J., Wang, Y., Ma, Z., and Yan, L. (2020). Dissolution of highly molecular weight cellulose isolated from wheat straw in deep eutectic solvent of Choline/L-Lysine hydrochloride. *Green Energy & Environ.* 5, 232–239. doi:10.1016/j.gee.2020.03.010

- Winterton, N. (2006). Solubilization of polymers by ionic liquids. *J. Mater. Chem.* 16, 4281–4293. doi:10.1039/b610143g
- Xiong, P., Zhao, K., Hu, L., Zhang, L., and Cheng, G. (2014). Dissolution of cellulose in aqueous NaOH/urea solution: role of urea. *Cellulose* 21, 1183–1192. doi:10.1007/s10570-014-0221-7
- Zhang, C., Liu, R., Xiang, J., Kang, H., Liu, Z., and Huang, Y. (2014). Dissolution mechanism of cellulose in N,N-dimethylacetamide/lithium chloride: revisiting through molecular interactions. *J. Phys. Chem. B* 118, 9507–9514. doi:10.1021/jp506013c
- Zhang, H., Lang, J., Lan, P., Yang, H., Lu, J., and Wang, Z. (2020). Study on the dissolution mechanism of cellulose by ChCl-based deep eutectic solvents. *Materials* 13, 278. doi:10.3390/ma13020278
- Zhang, J., Wu, J., Yu, J., Zhang, X., He, J., and Zhang, J. (2017). Application of ionic liquids for dissolving cellulose and fabricating cellulose-based materials: state of the art and future trends. *Mater. Chem. Front.* 1, 1273–1290. doi:10.1039/c6qm00348f
- Zhang, L., Yu, H., Liu, S., Wang, Y., Mu, T., and Xue, Z. (2023). Kamlet–Taft parameters of deep eutectic solvents and their relationship with dissolution of main lignocellulosic components. *Ind. Eng. Chem. Res.* 62, 11723–11734. doi:10.1021/acs.iecr.3c01309
- Zhao, H., Jones, C. L., Baker, G. A., Xia, S., Olubajo, O., and Person, V. N. (2009). Regenerating cellulose from ionic liquids for an accelerated enzymatic hydrolysis. *J. Biotechnol.* 139, 47–54. doi:10.1016/j.jbiotec.2008.08.009
- Zhong, Y., Wu, J., Kang, H., and Liu, R. (2022). Choline hydroxide based deep eutectic solvent for dissolving cellulose. *Green Chem.* 24, 2464–2475. doi:10.1039/d1gc04130d



OPEN ACCESS

EDITED BY

Johannes Carolus (John) Jansen, Istituto per la Tecnologia delle Membrane, Consiglio Nazionale delle Ricerche, Italy

REVIEWED BY

Maria Giovanna Buonomenna, Ordine dei Chimici e Fisici della Campania and MIUR, Italy
Mariagiulia Longo, National Research Council (CNR), Italy
Pavel Izak, Institute of Chemical Process Fundamentals (ASCR), Czechia

*CORRESPONDENCE

Bernardo Castro-Dominguez,
✉ bcd28@bath.ac.uk

RECEIVED 23 February 2024

ACCEPTED 16 April 2024

PUBLISHED 09 May 2024

CITATION

Alkandari SH and Castro-Dominguez B (2024), Advanced and sustainable manufacturing methods of polymer-based membranes for gas separation: a review. *Front. Membr. Sci. Technol.* 3:1390599. doi: 10.3389/frmst.2024.1390599

COPYRIGHT

© 2024 Alkandari and Castro-Dominguez. This is an open-access article distributed under the terms of the [Creative Commons Attribution License \(CC BY\)](#). The use, distribution or reproduction in other forums is permitted, provided the original author(s) and the copyright owner(s) are credited and that the original publication in this journal is cited, in accordance with accepted academic practice. No use, distribution or reproduction is permitted which does not comply with these terms.

Advanced and sustainable manufacturing methods of polymer-based membranes for gas separation: a review

Sharifah H. Alkandari¹ and Bernardo Castro-Dominguez^{1,2*}

¹Department of Chemical Engineering, University of Bath, Bath, United Kingdom, ²Centre for Digital Manufacturing and Design (dMaDe), University of Bath, Bath, United Kingdom

The fabrication of membranes for gas separation presents challenges that hinder their deployment as a truly sustainable technology. This review systematically explores the evolution and advancements in materials and manufacturing methods of polymer-based membranes, with a keen emphasis on sustainability and efficiency. The review delineates a broad spectrum of manufacturing techniques, ranging from traditional methods to cutting-edge approaches such as layer-by-layer assembly, and green synthesis, highlighting their implications for environmental sustainability, performance enhancement, scalability, and economic viability. Key findings indicate a significant shift towards greener solvents, bio-based polymers and processes that reduce waste and costs. Critical analysis uncovers a growing focus on understanding the life cycle of membranes and developing strategies for end-of-life such as recycling and the use of biodegradable materials, underscoring the commitment of the community to minimizing environmental footprints.

KEYWORDS

membrane manufacturing, sustainability, polymeric membranes, gas separation membranes, recyclability

1 Introduction

Over the past few decades, growing public awareness and concern for climate change and health issues have spurred significant advancements in environmental engineering technologies (Figuerola et al., 2008; Pipitone and Bolland, 2009). A notable area of progress is in membrane technology for gas separation, particularly the separation of natural gas from impurities, such as carbon dioxide (Hosseini and Chung, 2009; Scholes et al., 2012; Sholl and Lively, 2016; Žák et al., 2018; Wojnarova et al., 2023). This development is rooted in the fact that carbon dioxide not only corrodes pipelines but also diminishes the heating value of natural gas. Similarly, the flue gases emitted by industries and power plants, which are a mixture of CO₂, SO₂, and NO_x present an environmental challenge that necessitate the capture and utilization of CO₂ for compliance purposes (Du et al., 2011; Dolejš et al., 2014; Pasichnyk et al., 2023). Globally, carbon dioxide emissions from fossil fuels and industry totalled 37.15 billion metric tons (GtCO₂) in 2022 and projected to have risen 1.1 percent in 2023 to reach a record high of 37.55 GtCO₂. In fact, since 1990, global CO₂ emissions have increased by more than 60 percent (Tiseo, 2023). Echoing these concerns, in September 2021, the New England Journal of Medicine and other global health journals jointly published an article, urging immediate action to reduce GHG emissions to protect human

health (Atwoli et al., 2021). All of this reports significantly amplifies the demand for and efficient and cost-effective gas separation technologies.

Traditional separation methods, such as distillation and absorption, are effective for separating gas and vapor mixtures. However, they are characterized by high energy demands, accounting for 10%–15% of global energy consumption, significant economic costs, and the production of pollutants (Sholl and Lively, 2016). In the United States, separations account for a significant energy expenditure, consuming about 4500 trillion Btu annually. This represents roughly 22% of all energy used within industrial plants (USDOE, 2005). A substantial portion of this energy is used in distillation processes. With over 40,000 distillation columns operating across the U.S. for more than 200 distinct separations, distillation represents nearly half (49%) of the energy used in industrial separations (USDOE, 2005). These backdrops set the stage for the advent of membrane technology. Membranes stand out due to their high efficiency, cost-effectiveness, environmental sustainability, minimal footprint, and capability for continuous operation, making them a promising alternative to conventional methods. Compared to conventional distillation methods, membrane-based processes have the potential to reduce energy consumption by approximately 90% (Baker, 2002; Sholl and Lively, 2016).

The evolution of membrane technology has been remarkable since the first commercial membrane for gas separation was introduced, for the separation of H₂ from N₂, argon and CH₄ in 1980 (Henis and Tripodi, 1980). In fact, the market response to the gas separation membrane techniques has been overwhelmingly positive, with significant growth observed over the past few decades. A recent market analyst report published by Market Research Future[®], reveals that the gas separation membrane industry is projected to grow from USD 2.45 billion in 2023 to USD 4.68 billion by 2030, exhibiting a compound annual growth rate of 10.2% during the forecast period (2023–2030) (Chitranshi Jaiswal, 2024). The growth of the gas separation membrane market is primarily driven by two key factors: firstly, the increasing number of governmental regulations and laws regarding GHG emissions, with specific restrictions on carbon dioxide emissions across various industrial sectors; and secondly, the expansion of industrial processes such as natural gas treatment, hydrogen purification, and hydrocarbon separation, all of which require gas separation membranes (Chitranshi Jaiswal, 2024).

Although market projections for gas separation membranes are impressive, selecting the right materials for gas membrane fabrication is crucial to fully maximizing the economics and efficiency of the technology. Conventionally, membranes are classified based on the material used for its fabrication, the structure, and intended application of the membrane as well as on the mechanism of membrane action (Asad et al., 2020). Depending on the nature of material used, gas separation membranes are classified as organic (polymeric), inorganic/metallic and composite/hybrid membranes. Inorganic/metallic membranes made of metals, ceramic, zeolites, carbon nanotubes, carbon molecular sieves, and mesoporous are very suitable where harsh thermal and chemical conditions are expected, and some of them indicates a high gas flux and selectivity, but they are difficult to

process and usually expensive and difficult to fabricate and use at industrial scale because of its brittleness (Chung et al., 2007; Mantzalis et al., 2011; Kosinov et al., 2016; Garcia-Fayos et al., 2020). Hence, polymeric membranes are widely preferred and utilized in gas separation, due to their advantageous mechanical strength, consistent performance, ease of shaping into various modules, and cost-efficiency in processing (Xu et al., 2006; Wang et al., 2007). The versatility and tailorability of polymeric materials further enhance their appeal, allowing for customization to meet diverse industrial needs, including acid gas treatment, nitrogen enrichment, ammonia purge gas recovery, refinery gas purification, syngas ratio adjustment, dehydration, air purification and carbon capture (Sanders et al., 2013; Castel et al., 2021). In addition, the ease of installation and scalability of polymeric membranes significantly benefits their integration into various systems and their adaptation from laboratory research to industrial-scale applications.

Nevertheless, recently, there has been growing concern, particularly regarding the manufacturing techniques and material sustainability of currently used commercial polymeric gas separation membranes, many of which are derived from non-renewable sources. Although widely used synthetic polymers such as polyamides, polysulfones, polyethersulfone, polyacrylonitrile, polyvinylidene fluoride, polypropylene, polysiloxanes or silicone rubber, and polyethylene oxide have demonstrated desirable properties like permeability, selectivity, mechanical strength, and chemical stability (Purkait et al., 2018), the ecological impact of their fabrication and non-recyclability poses significant challenges. This is particularly concerning if membranes dominate the gas separation market, as membrane modules in industrial applications are typically replaced every three to 5 years. This leads to considerable plastic waste, with these non-biodegradable materials often ending up in landfills or natural ecosystems. Likewise, some of the common solvents used in these polymeric membrane fabrication includes N,N-dimethylformamide (DMF), N,N-dimethylacetamide (DMAc), N-methyl-2-pyrrolidone (NMP), dichloromethane (DCM), chloroform, and tetrahydrofuran (THF), many of which are organic and pose environmental and health hazards. The percentage of solvent in the polymer solution can vary widely, depending on the desired thickness and porosity of the membrane, as well as the specific polymer-solvent interaction. Typically, the polymer concentration in the dope solution, which includes the solvent, ranges from 1% to 20% by weight (Figoli et al., 2014).

Consequently, research interest in polymer-based gas membranes is steering towards improving the membrane properties and to go Net-zero by applying advanced and sustainable manufacturing techniques (Jiang and Ladewig, 2020; Bridge et al., 2022). The imperative to shift towards the development of advanced and sustainable polymeric gas separation membranes is underscored by a confluence of factors, including separation efficiency, durability, environmental impact, and economic considerations. This review focuses on reviewing advanced and sustainable manufacturing techniques currently employed for polymeric gas separation membranes. It will highlight study-based evidence of the latest technological advancements, sustainable practices, and potential improvements in gas membrane separation efficiency.

2 Commercial polymer membrane manufacturing

The manufacturing of commercial polymer membranes for gas separation is a crucial process in the field of industrial separation and purification, playing a key role across various sectors, including the petrochemical, environmental, and energy industries. This process typically involves the use of a range of synthetic polymers, semi-synthetic polymers, organic solvents, and established techniques. Over the years, these methods have formed the backbone of membrane manufacturing, driving numerous industrial applications by creating membranes specifically designed for separating different gas mixtures.

2.1 Commercial materials

Since the discovery of membrane technology, several polymers have been used for the development of gas separation membranes, including polyacetylenes, polyaniline, poly (arylene ether)s, polyarylates, polycarbonates, polyetherimides, poly (ethylene oxide), polyimides, poly (phenylene oxide)s, poly (pyrrolone)s, polysulfones and others (Amooghin et al., 2016). Cellulose acetate (Hu et al., 2022), polysulfone (Mohamed et al., 2023), and polyimide (Ma and Yang, 2018; Ohya et al., 2022) stand out in industrial gas separation for their excellent selectivity and permeability. Specifically, cellulose acetate's critical role is exemplified by its use in Pakistan's largest gas separation plant, which utilizes CA membranes for CO₂ extraction from natural gas, highlighting its stability and scalability (Hu et al., 2022). Polysulfone gained prominence with the establishment of the first plant using Polysulfone's hollow fiber membranes for H₂/N₂ separation in 1980 by Permea, demonstrating Polysulfone's notable mechanical strength, resistance to compaction, and thermal stability (Mohamad et al., 2016). Similarly, the inaugural deployment of polyimide membranes by Du Pont Co. (United States) and Ube Industries (Japan) marked a significant advancement in H₂ separation (Ma and Yang, 2018; Ohya et al., 2022), with polyimides acclaimed for their chemical resistance, thermal endurance, and mechanical durability (Xiao et al., 2009; Bryant, 2014). Their wide use in the membrane industry is also attributed to their ease of processing and ability to be tailored to specific separation needs through modifications and treatments. Most of these polymers are synthetic or semi-synthetic, and their applicability poses several challenges, including the effects of thermal and pressure conditioning, physical and chemical aging, plasticization, and permeation hysteresis. Likewise, the effectiveness of polymeric gas separation membrane is often gauged against the Robeson upper bound, a benchmark that delineates the trade-off between permeability and selectivity (Robeson, 2008). Therefore, to overcome the limitations of both polymeric membranes, mixed matrix membranes (MMMs) have been identified to provide a solution to go beyond the upper-bound trade-off limit of the polymeric membranes, by incorporating innovative material into the polymer matrix (Khorshidi et al., 2019; Xu et al., 2021b; Hu et al., 2022).

Furthermore, factors such as the choice of casting solvent and the impact of impurities or trace contaminants add further

complexities in conventional polymeric membrane fabrication and have garnered considerable research interest (Amooghin et al., 2016; Tekin and Çulfaz-Emecen, 2023). The solvents used in fabricating polymeric gas separation membranes play a pivotal role in determining the characteristics and performance of the final product. Often, these solvents are selected based on the type of polymer being used and the desired properties of the membrane. However, the challenge lies in the influence of solvent properties, such as viscosity, dielectric constant, polarity, and boiling point, on the membrane final features and the essential requirement of dissolving the selected polymer (at room or high temperature, depending on the technique) (Anbukarasu et al., 2021). Thus, one of the most challenging yet intriguing tasks for membrane scientists is replacing these conventional solvents. Table 1 shows a list of solvents and polymers traditionally used in membrane preparation and their respective Hansen solubility parameters. Solubility parameters are fundamental in predicting solvent-polymer compatibility, which directly influences membrane structure, performance, and sustainable manufacturability. Most membrane fabrication techniques require dissolving the polymer in a solvent to enable shaping the material in 2-dimensional films. Hansen solubility parameters (HSPs) serve as an indicator of whether a solvent will dissolve a specific polymer. This can be accomplished by calculating the distance (R_a) of the polymer-solvent system (Eq 1); and its ratio with respect to the interaction radius (R_0), known as the relative energy distance (RED) (Eq 2). When $RED \leq 1$, then the polymer will dissolve in the given solvent (Hansen, 2007; Jirsáková et al., 2021). This theory considers three components: δ_h , which accounts for the energy arising from hydrogen bonding between molecules; δ_p , which corresponds to the energy contribution from dipolar intermolecular forces; and δ_d , representing the energy associated with dispersion forces; $\delta = (\delta_h)^2 + (\delta_d)^2 + (\delta_p)^2$.

$$Ra^2 = 4 * (\delta_{d_solvent} - \delta_{d_polymer})^2 + (\delta_{p_solvent} - \delta_{p_polymer})^2 + (\delta_{h_solvent} - \delta_{h_polymer})^2 \quad (1)$$

$$RED = \frac{Ra}{Ro} \quad (2)$$

2.2 Commercial manufacturing techniques

The manufacturing technique used to fabricate polymeric or composite membranes plays a fundamental role and depends on the nature of the material and the desired morphology of the membrane. Over the years, various techniques have been used to synthesize polymeric membranes for gas separation. These include solution casting, phase inversion (Loeb and Sourirajan, 1963), interfacial polymerization (Jimenez-Solomon et al., 2016; Zhang et al., 2022), roll to roll coating (Chen et al., 2020), kiss coating (Dibrov et al., 2014), and track etching (Nailwal et al., 2023). Table 2 shows a concise summary of the various techniques. Among them, solution casting, phase inversion, interfacial polymerization, dip coating, roll to roll coating and kiss coating are the most notable, hence is concisely discussed.

TABLE 1 Conventional membrane fabrication solvents and polymers and their Hansen solubility parameters.

Solvent or polymer	δ_h (MPa) ^{1/2}	δ_d (MPa) ^{1/2}	δ_p (MPa) ^{1/2}	δ (MPa) ^{1/2}	R ₀
N,N-Dimethylformamide (DMF)	11.3	17.4	13.7	24.8	-
N,N-Dimethylacetamide (DMA)	11.8	17.8	14.1	22.7	-
N-Methyl-2-pyrrolidone (NMP)	7.2	18.4	12.3	22.9	-
Tetrahydrofuran (THF)	3.7	19.0	10.2	22.5	-
Dibutyl-phthalate (DBP)	4.1	17.8	8.6	20.2	-
Diocetyl-phthalate (DOP)	3.1	16.6	7.0	16.8	-
Acetone	6.9	15.5	10.4	19.9	-
Chloroform	5.5	17.8	3.1	19.0	-
1,4-Dioxane	8.0	16.8	5.7	18.5	-
Toluene	2.0	18.0	1.4	18.2	-
Methyl salicylate	12.3	16.0	8.0	21.7	-
Diphenyl ether	5.8	19.5	3.4	20.6	-
Cellulose acetate	9.4	17.1	13.1	23.5	10.6
Polysulfone	7	18.5	8.5	21.5	9.4
Polyetherimide	6.4	17.7	6	19.8	4.8
PVDF	10.2	17	12.1	23.2	4.1

2.2.1 Solution casting

The solution casting technique is a fundamental and widely utilized method in the fabrication of polymeric membranes for gas separation. This process begins with dissolving a polymer in a suitable solvent to form a homogeneous solution. Once the polymer solution is prepared, it is spread uniformly on a flat surface or a casting substrate and allowed to evaporate under controlled conditions, leading to the formation of a thin polymeric film (Zou and Zhu, 2020; Alkandari and Castro-Dominguez, 2023). The rate of solvent evaporation is a key factor in this process, as it influences the structure and morphology of the membrane. Slow evaporation under controlled environmental conditions can lead to more uniform membrane structures, whereas rapid evaporation might result in membranes with defects or non-uniformity (Yamasaki et al., 1999). One of the primary advantages of the solution casting technique is its simplicity and the ability to produce membranes with uniform thickness and smooth surfaces. Moreover, it allows for the incorporation of various additives into the polymer solution, providing a way to tailor the properties of the membrane, such as, permeability, and selectivity (Clarizia et al., 2019). However, the choice of solvent is critical in solution casting, as it must not only dissolve the polymer effectively but also be safe and environmentally benign. The disposal of used solvents and the environmental impact of the process are considerations that have led to ongoing research into greener and more sustainable solvent options.

2.2.2 Phase inversion

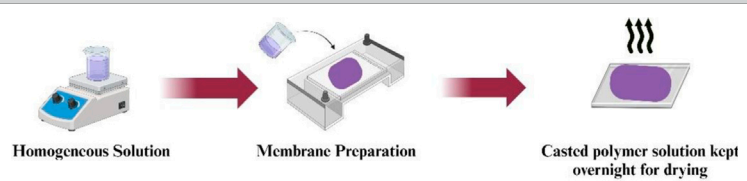
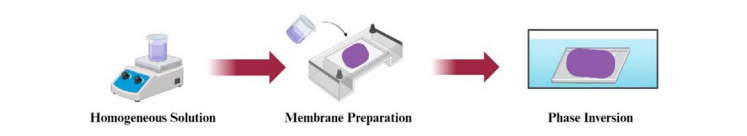
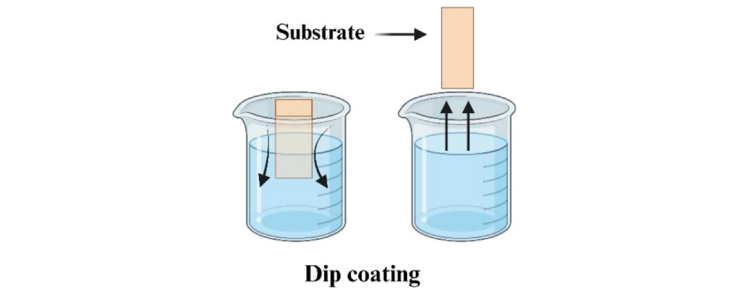
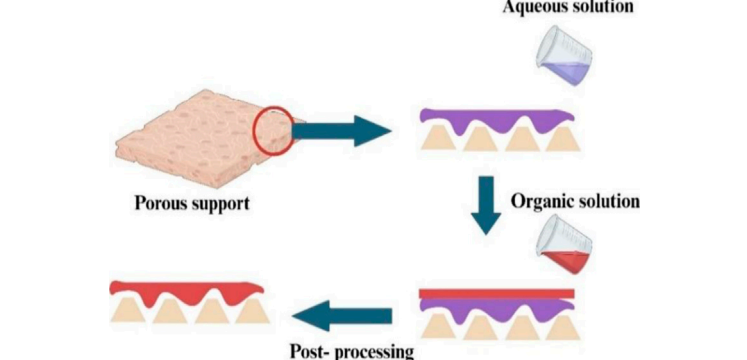
The phase inversion method, initially developed by Loeb and Sourirajan (Loeb and Sourirajan, 1963) for preparing cellulose acetate desalination membranes, later became prevalent in the

fabrication of polymeric membranes for gas separation because of its simplicity, economic feasibility, and the ability to create thin membranes (Scholes et al., 2012; Martínez-Izquierdo et al., 2021). The technique involves dissolving a water-insoluble polymer in a high-boiling point solvent to form a viscous polymer dope. This solution is then degassed and spread onto a support using a casting knife (Martínez-Izquierdo et al., 2021), followed by immersion in a coagulation bath of water or solvent, resulting in an asymmetric membrane with a dense top layer and a porous bottom layer. The formation of these distinct layers is influenced by factors like the solution composition, coagulation temperature, and additives (Alam et al., 2012). Three main types of phase inversion techniques exist: thermal induced phase inversion (TIPS), non-solvent induced phase inversion (NIPS), and vapor-induced phase inversion (VIPS). Despite the simplicity and widespread use of phase inversion and solvent evaporation techniques, the multitude of challenges associated with them underscores a vital need for meticulous consideration and innovative approaches that will guide future research and development. A primary challenge in this context is the difficulty in producing defect-free membranes (Higashi et al., 2021; Cui et al., 2023).

2.2.3 Dip-coating

Dip coating involves immersing a substrate into a coating solution and then lifting it out at a consistent speed, allowing a thin film to form on the surface. Recognized as one of the most fundamental film deposition techniques (Madaeni et al., 2013), it is particularly beneficial for fabricating membranes used in gas separation, as it facilitates the creation of uniform, precise thin layers crucial for optimal membrane performance (Madaeni et al., 2013). The method is effectively utilized in developing membranes

TABLE 2 Summarized conventional gas membrane fabrication techniques.

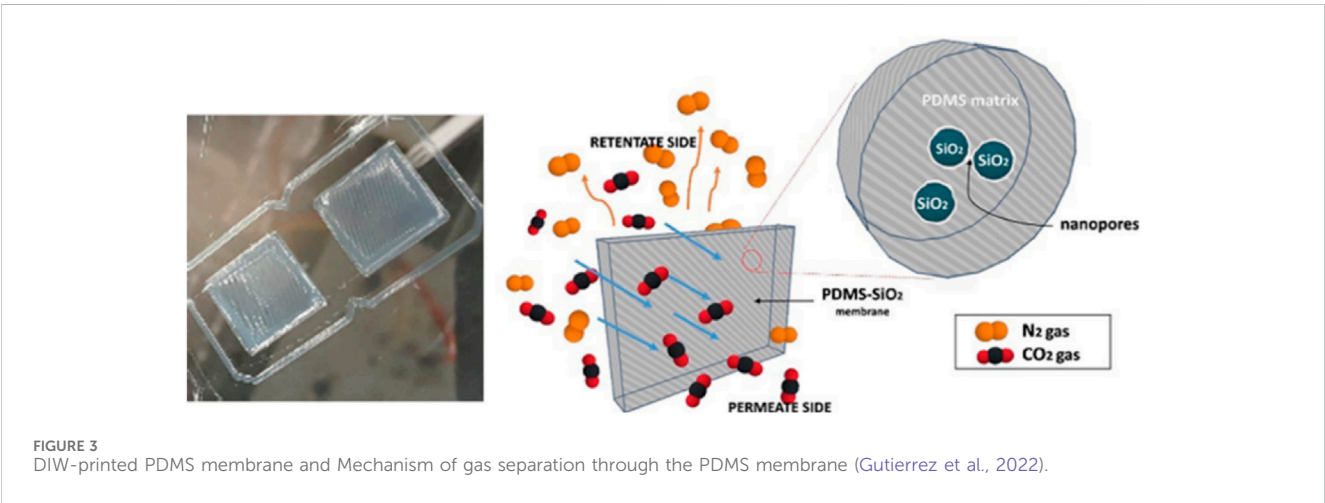
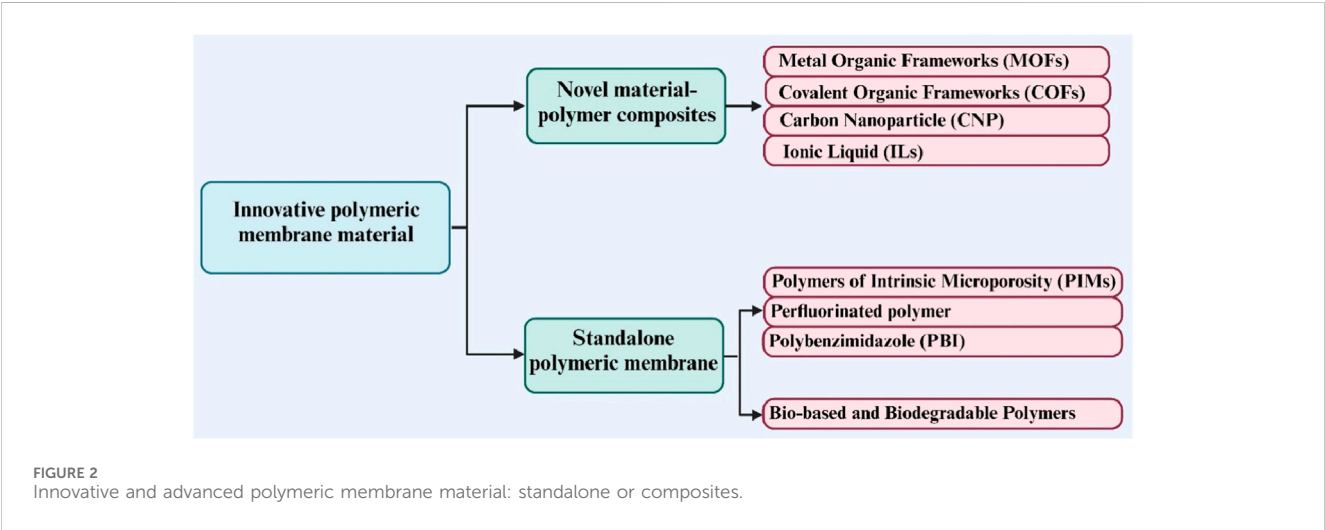
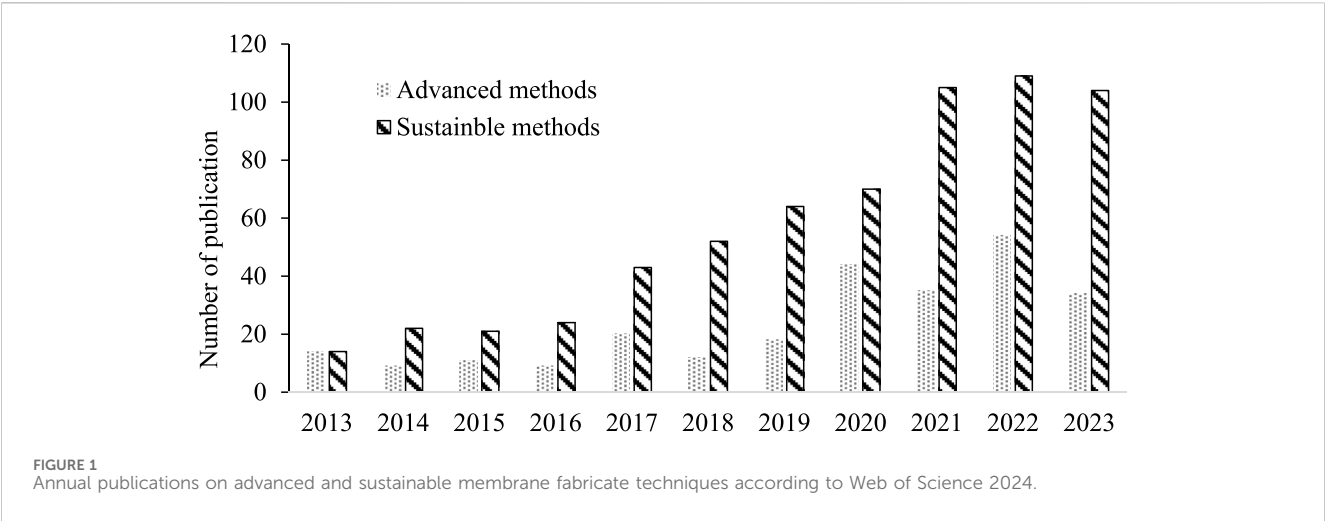
Name	Description	Schematic	Challenges
Commercial Scale Techniques			
Solution Casting	Involves dissolving polymer in a suitable solvent to form a homogeneous solution. It is spread cast uniformly on a flat surface and allowed to evaporate under controlled conditions, leading to the formation of thin polymeric film Clarizia et al. (2019) , Alkandari and Castro-Dominguez (2023)		<ul style="list-style-type: none">• Choice of solvent is critical as it must dissolve the polymer• Difficult to produce defect-free membranes• Environmental impact of the process
Phase Inversion	The method entails dissolving a water-insoluble polymer in a solvent to create a viscous mixture, which is then spread onto a support and immersed in a coagulation bath, forming an asymmetric membrane with a dense top and porous bottom, influenced by solution composition, temperature, and additives Martínez-Izquierdo et al. (2021)		<ul style="list-style-type: none">• Choice of solvent is critical as it must dissolve the polymer• Difficult to produce defect-free membranes
Dip-Coating	Is a method for applying a thin film to a substrate by immersing it in a liquid solution, then withdrawing it at a controlled speed. Madaeni et al. (2013)		<ul style="list-style-type: none">• Complicated chemical and physical variables used in the dip-coating process
Interfacial Polymerization (IP)	This process, also called polycondensation, involves polymerization at the interface of two non-mixing phases, where reactive monomers in each phase react on a porous membrane's surface to create an ultrathin layer on substrates Yang et al. (2021)		<ul style="list-style-type: none">• Low reproducibility• Hard to monitor the IP reaction• Hard to control the monomer uniformity
Roll to Roll (R2R) Coating	Is a manufacturing process used for large scale production to produce continuous sheets of material by unrolling a flexible substrate from one roll through various		<ul style="list-style-type: none">• Difficult to control over process• Difficult to maintain the substrate extremely

(Continued on following page)

TABLE 2 (Continued) Summarized conventional gas membrane fabrication techniques.

Name	Description	Schematic	Challenges
	processing stations and then rewinding it onto another roll Chen et al. (2020a)		flat during the process
Kiss Coating	Is a technique for applying thin material layers onto a substrate, where a wheel or roller lightly contacts the substrate surface, transferring a controlled, thin layer of material Dibrov et al. (2014)		<ul style="list-style-type: none">• Solvent is required to be safe and environmentally friendly• Difficult to control the solvent evaporation in the casting solution during the process• Limited material compatibility
Laboratory/Research Scale Techniques			
Track Etching	This process involves irradiating a thin polymer film with high-energy particles, such as ions or neutrons, which create latent tracks or damage trails in the material. These tracks are then selectively etched in either an acidic or basic solution, resulting in uniform and cylindrical pores across the membrane Ma et al. (2020)		<ul style="list-style-type: none">• High cost• Lower particle flux stability• Requires specialized equipment• Complicated process
Coating	In the spin coating process, the porous support is set to rotate around its vertical axis, and concurrently, the film-forming solution is uniformly dispersed over a surface, which is aligned perpendicularly to the support's surface as it spins Sokolov et al. (2021) In the spray coating technique, a fine mist of the film-forming solution is projected onto the substrate's surface, which is held stationary or moved to ensure even coverage Jiang et al. (2021)		<ul style="list-style-type: none">• Low reproducibility

for various gas separations like CO₂/N₂ ([Li et al., 2021](#)), CO₂/CH₄ ([Suleman et al., 2018](#)), H₂ ([Farjoo and Kuznicki, 2016](#)) and, O₂/N₂ ([Sazali et al., 2020](#)). The optimum concentration of the casting solution and the temperature were identified as key factors in achieving a uniform membrane ([Li et al., 2020](#)). Research has demonstrated that parameters such as the concentration of the coating solution ([Jamil et al., 2020](#)), withdrawal speed, and the number of coatings applied ([Shankar and Kandasamy, 2019](#)) are vital in tuning the membrane's gas separation characteristics, highlighting the importance of process control in achieving the



desired membrane functionality. Furthermore, the dip-coating technique has proven to be highly effective in fabricating composite membranes without defects for gas separation,

underscoring the method's adaptability and efficiency (Tan et al., 2019). However, this technique also has several limitations that can constrain its applicability and complicate its scalability. Initially, this

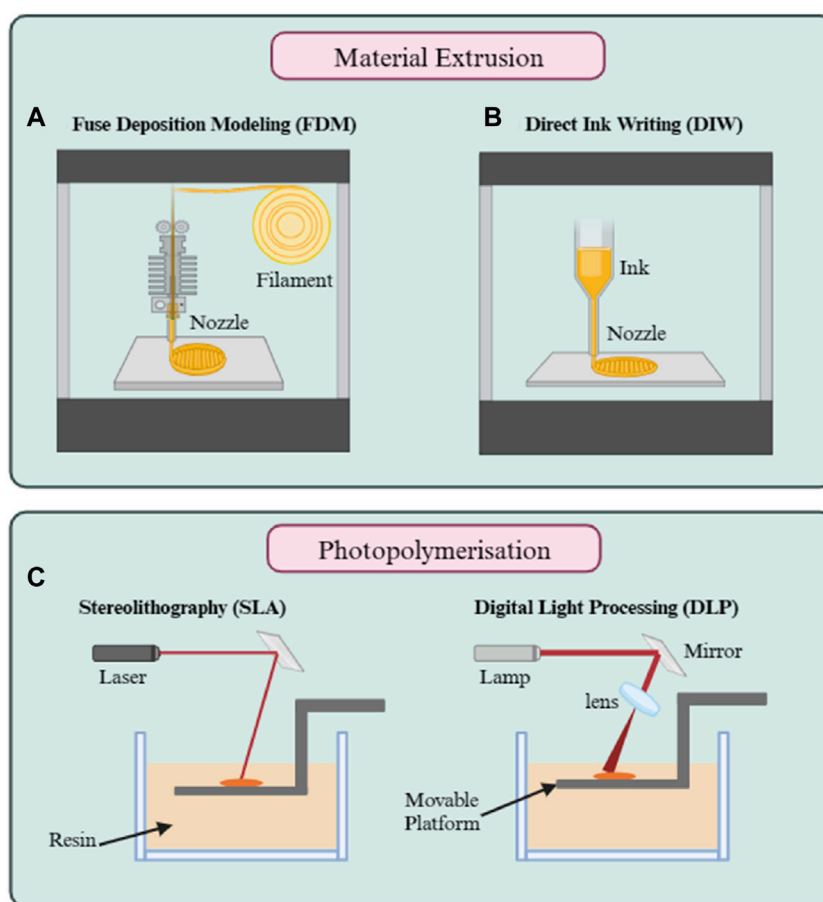


FIGURE 4
Approaches for 3D printing of membranes: (A) Fuse deposition (FDM); (B) Direct ink writing; and (C) Photopolymerization.

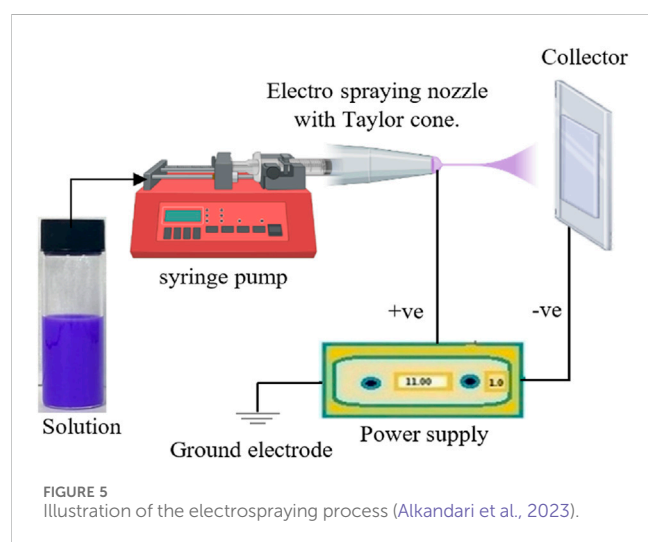


FIGURE 5
Illustration of the electrospinning process (Alkandari et al., 2023).

technique may not be ideal for applications requiring coating on only one side of a substrate, as the solution tends to envelop the entire immersed surface. Additionally, it is requiring a significant amount of precursor solution to occupy the coating container, introducing considerable challenges (Ceratti et al., 2015). For

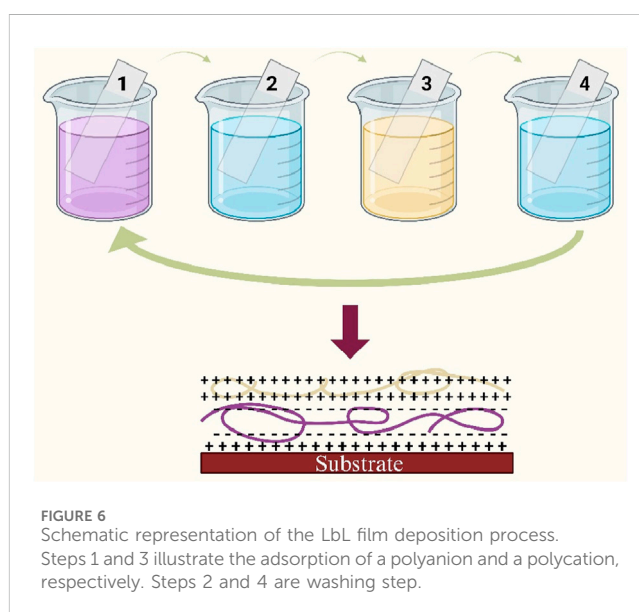


FIGURE 6
Schematic representation of the LbL film deposition process. Steps 1 and 3 illustrate the adsorption of a polyanion and a polycation, respectively. Steps 2 and 4 are washing step.

instance, managing large quantities of the solution can be hazardous, potentially impacting the environment adversely, and such constraints hold up scalability.

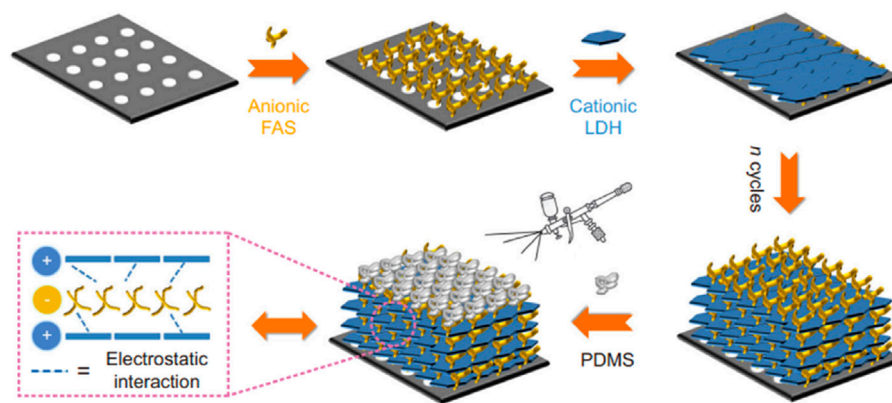


FIGURE 7
Schematic representation for the fabrication of (LDH/FAS)_n-PDMS membranes (Xu et al., 2021).

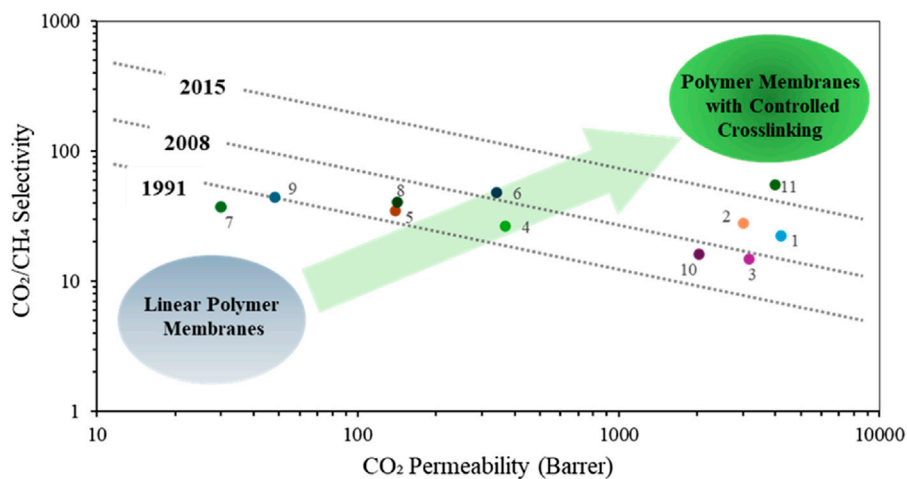


FIGURE 8
Upper bound plot for selected cross-linked membranes of CO₂/CH₄. Polymers are labelled as follows: (1) PPM-Y-CD-425 (Askari et al., 2012), (2) BMPI-60%-450 (Xu et al., 2021a), (3) 75%-X-PI (An et al., 2018), (4) 6FDA-DAT/DATCA-450 (Tian et al., 2018), (5) 6FDA-DAT1-450-3h (Yerzhankyy et al., 2022), (6) PI-Im-COOH-450-1 (Shi et al., 2022), (7) FDA-DAPI-DABA-40min (Dose et al., 2019), (8) PIM-BM-70(250C-10h) (Chen et al., 2020), (9) PIM-BM-70(300C-5h) (Chen et al., 2020), (10) 50%-X-PI (An et al., 2018), (11) PIM-300-2d (Li et al., 2012). Adapted from (Liu et al., 2023).

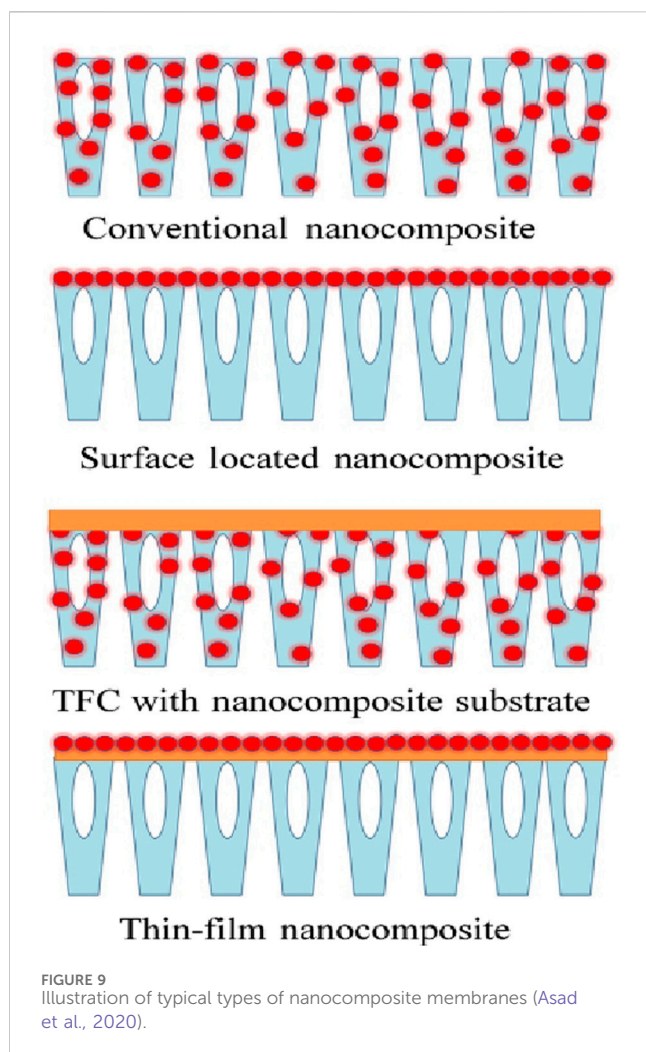
2.2.4 Interfacial polymerization

Interfacial Polymerization (IP) is another technique widely used in the fabrication of polymeric membranes, particularly effective for thin-film composite (TFC) and nanofiltration (NF) membranes (Jimenez-Solomon et al., 2016; Zhang et al., 2022). This technique involves a reaction between two monomers, each dissolved in different, immiscible solvents, typically water and solvents. The IP procedure typically consists of two steps: firstly, soaking the porous support in a solution with the first monomers until saturated, then removing excess solution; secondly, immersing the support in another solution with the second monomers for a reaction, followed by removing all solutions and further processing to form a dense polymer skin layer (Sridhar et al., 2007). Key advantages of the IP technique include its ability to produce extremely thin, highly selective, and scalable layers, which are particularly important in gas separation membranes efficiency, as demonstrated by several authors in the context of CO₂/CH₄, H₂/CO

and CO₂/N₂ gas pair separations (Li et al., 2012; Wang et al., 2013; Choi et al., 2015). Moreover, the properties of the resulting membrane, such as permeability and selectivity, can be finely tuned by adjusting factors like the type and concentration of monomers, reaction time, and temperature (Sridhar et al., 2007). However, challenges in this method include controlling the uniformity of the film and managing the interfacial reactions to prevent defects.

2.2.5 Roll-to-roll (R2R) coating

Roll-to-roll coating techniques represent a pivotal advancement in the fabrication of membranes, offering a scalable and efficient method for producing thin-film composite membranes. This continuous process involves the deposition of selective layers on a flexible substrate, which is then wound through various coating and drying stages. The technique's adaptability allows for the application of multiple layers, each contributing to the membrane's overall separation performance and mechanical



stability. R2R coating encompasses two distinct methods: direct roll coating and reverse roll coating. With direct roll coating, the applicator roll, and the substrate move in the same direction. Conversely, in reverse roll coating, the applicator roll turns against the direction of the substrate's movement (Makhlouf, 2011; Chen et al., 2020). Vakharia et al., 2018 employed a pilot-scale R2R coating method to manufacture thin polymer membranes on porous supports, aimed at CO₂ separation from flue gases. This study highlights the critical role of various parameters, including coating speed, solution viscosity, and the rate at which the coating solution is applied, in determining the final membrane properties. The R2R technique is noted for its efficiency and cost-effectiveness, which are essential for scaling up to industrial levels. However, the method presents challenges, notably in maintaining consistent process conditions to achieve uniform, defect-free membrane coatings. Ensuring the substrate remains perfectly flat during the coating is particularly challenging (Vakharia et al., 2018), as any deviations can introduce defects. Also, R2R direct coating of the membrane presents a challenge because a large amount of coated solution is applied to the substrate at once. Therefore, the interaction time between the dispersion media and the membrane is lengthier than it is for spray coating, which may result in increased absorption and swelling of the membrane (Park et al., 2020). Future research is

anticipated to enhance process controls, broaden the range of compatible materials, and incorporate advanced functional materials for R2R coated membranes in gas separation. These improvements aim to boost the efficacy and broaden the use of R2R-coated membranes in gas separation.

2.2.6 Kiss coating

The kiss-coating technique is a modified version of the dip-coating procedure. The kiss-coating technique offers an approach for fabricating thin-film composite (TFC) polymeric membranes for gas separation and the approach provides a one-sided contact between the surface of the porous support and the casting solution (Dibrov et al., 2014). Typically, the method involves the delicate application of a polymer solution onto a substrate, where the coating applicator barely “kisses” the surface, hence the name. This approach allows for precise control over the thickness and uniformity of the membrane layer, which are critical factors in determining the membrane's gas separation performance. Studies have shown that coating methods significantly impact gas separation efficiency. For instance, Bazhenov et al. created composite gas separation membranes with high permeance, aimed at capturing post-combustion CO₂, utilizing kiss-coating techniques. These membranes demonstrated favorable CO₂ permeance and CO₂/N₂ selectivity. The high-permeance thin-film composite (TFC) membranes were considered as promising bases for subsequent enhancements through the addition of layers that further improve CO₂ selectivity (Bazhenov et al., 2016). Another study Dibrov et al. has development of robust and stable in time poly [1-(trimethylsilyl)-1-propyne] (PTMSP) thin-film composite (TFC) membranes with high CO₂ permeance for its application in high pressure/temperature gas-liquid membrane contactors used for amine-based solvents regeneration (Dibrov et al., 2014). Also, Kiss coating enables the precise deposition of a uniform and defect-free selective layer on porous supports, leading to enhanced aging behavior and improved permeance-selectivity balance in thin-film composite membranes for gas separation applications (Foster et al., 2021). Despite these advantages, optimizing the Kiss Coating process for gas separation membrane fabrication requires careful consideration of several parameters, including the viscosity of the polymer solution, the speed of the substrate movement, and the distance between the applicator and the substrate (Bazhenov et al., 2016; Foster et al., 2021). In addition, the technique may be limited by the viscosity and drying rate of the coating solution, which can restrict the type of materials that can be effectively applied. Fine-tuning these parameters ensures the formation of a membrane layer with the desired thickness and material properties, crucial for achieving high separation efficiency.

3 Advanced membrane manufacturing

Over the past decade, the number of publications associated with advanced and sustainable manufacturing techniques has increased considerably as seen in Figure 1. By leveraging novel materials, intricate nanostructures, and sophisticated manufacturing processes, these techniques have opened new possibilities for enhancing membrane performance, durability, and specificity,

TABLE 3 List of commercial membranes and their characteristics.

Company/Membrane	Configuration/Target gas	Membrane material	Scale	Reference
Evonik - SEPURAN®	Hollow Fibre	polyimide	72 m³/h	Evonik (2024)
	Air, N ₂ , CO ₂ and H ₂			
Air Liquide MEDAL™	Hollow Fibre	polyimide		Air Liquide (2024)
	Air, N ₂ , CO ₂ and H ₂			
Air Liquide POROGEN	Hollow Fibre	polyether ether ketone		Air Liquide (2024)
	Air, N ₂ , CO ₂ and H ₂			
Honeywell PolySep	Hollow Fibre and Spiral wound membrane	N/A		Honeywell (2024)
	H ₂			
MTR- Polaris™	Spiral wound membrane	N/A	2,500 m³/h	MTR (2024)
	CO ₂ and H ₂			
SLB, Cynara™	Hollow Fibre	cellulose triacetate		SLB (2024)
	H ₂ S and CO ₂			
AirRane	N ₂ , O ₂	N/A	100–1200 m³/h	AirRane (2024)
Air Products PRISM®	Hollow Fibre	polysulfone	0.07 m³/h	Air Products (2024)
	N ₂ , H ₂			
BASF - Ultrason®	Hollow Fibre	polyphenylenesulfone		Basf (2024)

TABLE 4 Comprehensive overview of bio-based polymers used in membrane production.

Polymer	Origin	Advantage	Disadvantage
Cellulose	Cellulose is primarily sourced from lignocellulosic biomass, which also contains lignin and hemicellulose components	<ul style="list-style-type: none">• Easy to process• Good mechanical strength• Good gas selectivity• Film forming ability	Limited thermal stability
Chitosan (CS)	CS is derived from the outer shell of crustaceans	<ul style="list-style-type: none">• Film forming ability• Nontoxic Torre-Celeizabal et al. (2023)• Biocompatible Xu and Wang (2008), Zargar et al. (2015)	<ul style="list-style-type: none">• Poor solubility Shenvi et al. (2013), Shenvi et al. (2014)• Poor mechanical and barrier properties Yan et al. (2016)
Polylactic acid (PLA)	PLA derivation from biomass	<ul style="list-style-type: none">• Cost effective Kuruppalil (2011)• Good moisture resistance Kuruppalil (2011)• Good solubility in many non-polar organic solvents Phaechamud and Chitrattha (2016)• Wide processing possibilities Peelman et al. (2013)	<ul style="list-style-type: none">• Low temperature resistance Kuruppalil (2011)• Brittleness Kuruppalil (2011)
Polyhydroxyalkanoates (PHA)	PHA production through fermentation using different substrates as carbon sources	<ul style="list-style-type: none">• Tunable Properties Marcano et al. (2017)	<ul style="list-style-type: none">• Poor solubility Larsson et al. (2016)• Brittleness Larsson et al. (2016)• Poor thermal stability Larsson et al. (2016)• Expensive Marcano et al. (2017)

thereby addressing some of the most pressing challenges in sustainable technology and resource management.

3.1 Advanced membrane materials

In addition to conventional polymeric materials predominantly used in most commercial membrane manufacturing, several novel

materials are gaining prominence in the field of polymeric membrane fabrication. These materials are particularly noted for their enhanced performance in specific applications such as gas separation and carbon capture. They exhibit key characteristics that render them suitable for a range of advanced applications, providing tailored solutions for specific separation challenges across various industries (Jeon et al., 2017; Ulbricht, 2019; Widakdo et al., 2022). These characteristics include: 1) high selectivity and permeability, 2)

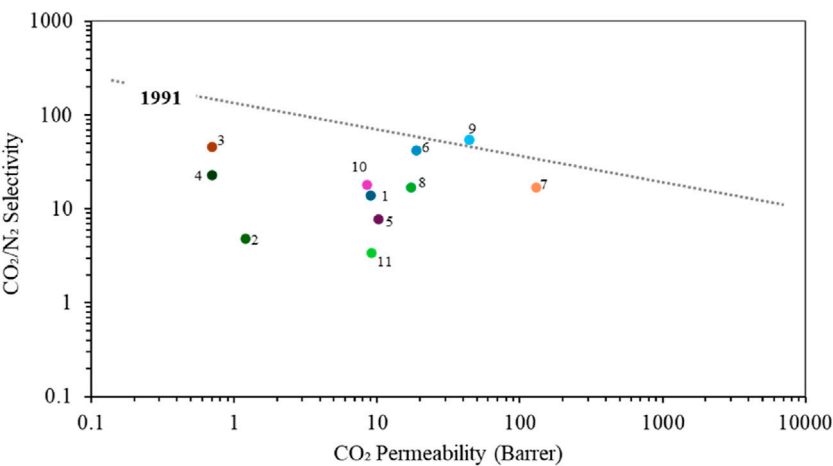


FIGURE 10 Upper bound plot for selected bio-based membranes of CO₂/N₂. Polymers are labelled as follows: (1) PHB (Follain et al., 2014), (2) PHB3V (Follain et al., 2014), (3) PHBV-DMC (Papchenko et al., 2022), (4) PHBV-CHCl₃(Papchenko et al., 2022), (5) PLA(Lehermeier et al., 2001), (6) CTA+[EMIM][BF₄] (Lam et al., 2016), (7) PVTCS/73 (Kunalan et al., 2022), (8) CA-ZIF67 (B*) (Alkandari et al., 2023), (9) CA-IL40-e (Alkandari and Castro-Dominguez, 2023), (10) CA (Alkandari and Castro-Dominguez, 2023), (11) PHB (Siracusa et al., 2017).

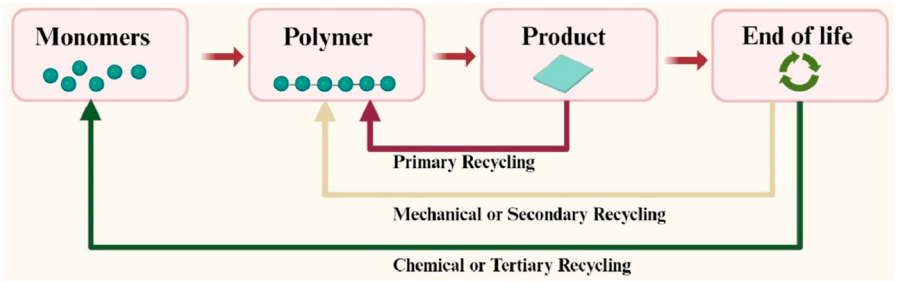


FIGURE 11 Polymer recycling techniques.

TABLE 5 Pillars of sustainable polymeric gas separation membrane manufacturing.

Materials	Techniques	Green manufacturing
Sustainable materials for polymeric gas separation membranes should be	Sustainable manufacturing techniques focus on reducing environmental impact, conserving energy, while maintaining or improving the performance of the membranes	The concept of green membrane manufacturing encompasses several key aspects
• Engineered to achieve a fine balance between selectivity and permeability	• Solvent-free 3D printing	• Biodegradable, recyclable, or derived from renewable sources to minimize environmental impact
• Designed to withstand harsh chemical environments and elevated temperatures	• Using bio-based or biodegradable materials in 3D printing/additive manufacturing	• Engineered to operate with reduced energy consumption
• Enhanced mechanical properties, such as tensile strength and resistance to tearing	• Using water as a solvent and bio-based polyelectrolytes in Layer-by-layer (LbL) assembly	• Minimizes the use of harmful chemicals in the membrane fabrication process
• Controlled pore size and distribution can be precisely controlled (tailored pore structure)	• Cross-linking strategies that do not rely on hazardous chemicals	• Sustainable fabrication, using less energy, using renewable energy sources, and generating fewer emissions
• Adapted to incorporate chemical functional group		• Implementing recycling and waste reduction measures in manufacturing facilities
• Designed to resist fouling and degradation		

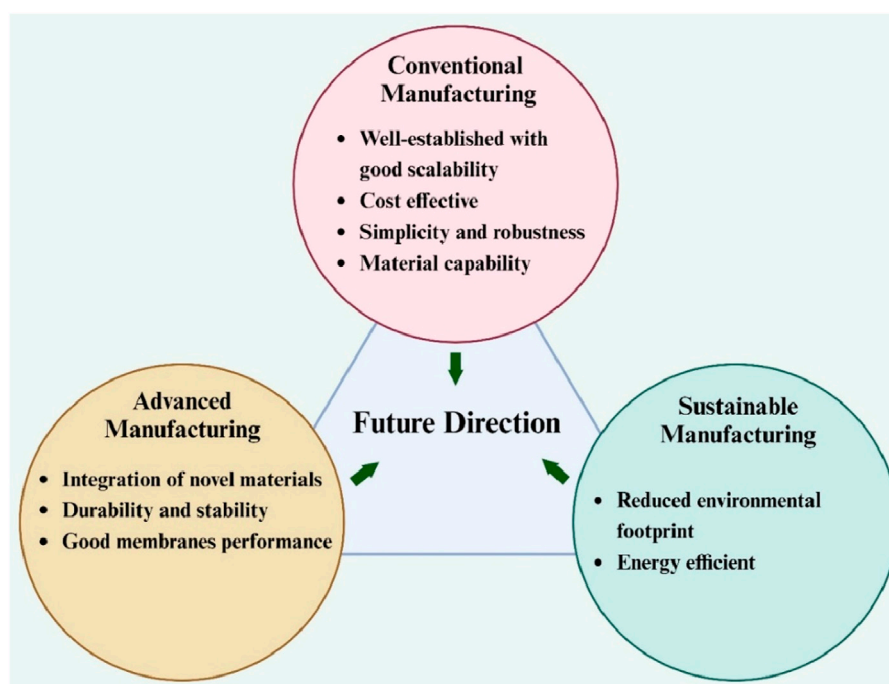


FIGURE 12
Schematic that illustrates future directions of gas separation membranes research.

chemical and thermal stability, 3) mechanical strength, 4) tailored pore structures, and 5) tunable functionalities. These innovative materials are broadly used to either fabricate standalone or composite polymeric membranes, as illustrated in Figure 2. Although many of these advanced materials provide enhanced separation performance; they are not further discussed in this review as their sustainability and scalability traits are yet to be demonstrated.

3.2 Advanced membrane manufacturing

3.2.1 Additive manufacturing—3D printing

There has been a significant shift in research towards environmentally friendly and solvent-free manufacturing practices. 3D printing, a technique used to fabricate items by layering of materials in a 3D printer, stands out as a key technology in this shift, particularly in the fabrication of membranes (Lee et al., 2016; Low et al., 2017). 3D printing, developed in 1986 by Hull (1986), has been the subject of intensive research over the past 2 decades. While its use in creating membranes for water treatment has been extensively studied, there is also a growing trend in applying this technology to gas separation membranes (Li et al., 2019; Gutierrez et al., 2021; Gutierrez et al., 2022). The appeal for 3D printing lies in its straightforwardness, eco-friendly nature, efficient design process, and the ability to create intricate shapes (Miramontes et al., 2020; Gutierrez et al., 2021). Additionally, 3D printing is cost-effective, reducing the need for solvents and other manufacturing materials (Gutierrez et al., 2021). It also offers the advantage of customizing surface areas to improve interaction with gases (Miramontes et al.,

2020; Gutierrez et al., 2021) and the pore size can be adjusted to optimize gas separation efficiency (Low et al., 2017). Various techniques exist for 3D printing membranes, with material extrusion and photopolymerization being particularly effective methods for creating gas separation membranes (Ligon et al., 2017; Herzberger et al., 2019). Material extrusion is one of the most common forms of 3D printing. It involves extruding a material, typically a thermoplastic filament, through a heated nozzle. The material is deposited layer by layer to build the desired shape (Thiam et al., 2022). The ability to use a variety of materials, including polymers and composites, makes it a versatile choice. For example, Thakkar et al., fabricated zeolite-embedded poly (amide-imide) monoliths using the material extrusion technique, and the resulting 3D-printed membranes displayed CO₂ capture capacities proportional to the zeolite loading, while exhibiting high compressive strengths and overall satisfactory mechanical stability (Thakkar et al., 2018).

One of the significant processes in 3D printing is direct ink writing (DIW). It typically involves extruding a paste-like ink, which can be a viscous solution, suspension, or composite material, and allows for the creation of more complex extruded materials (Gutierrez et al., 2023). Gutierrez et al., 2022, studied the fabrication of polydimethylsiloxane (PDMS)-based membranes for CO₂/N₂ gas separation using DIW 3D printing. To enable printability, silica particles were incorporated into the PDMS ink to introduce thixotropy. This ink was 3D printed into membranes, which displayed smooth surfaces and good silica dispersion as shown in Figure 3. Gas permeation testing showed the printed membranes had a CO₂ permeability over 1000 Barrer. A CO₂/N₂ selectivity around 10 was achieved and the membranes display high thermal and mechanical stability, with a good surface properties.

Nguyen et al. developed polymer composite inks, which were 3D printed to create innovative reactor designs aimed at capturing CO₂. These inks consisted of sodium carbonate particles embedded in uncured silicone and were applied through DIW. Once printed, the silicone underwent curing, and the structures were then hydrated, resulting in the formation of aqueous sodium carbonate domains that facilitated efficient CO₂ absorption (Nguyen et al., 2019).

Unlike the material extrusion technique, photopolymerization involves the transformation of monomers or oligomers from their liquid state into a solid polymer through radical or cationic polymerization. This process is triggered by exposing these materials to light, which can vary in wavelength, in the presence of a photo-initiator (Bagheri and Jin, 2019). This method uses light, typically in the form of ultraviolet (UV) rays, to cure and solidify a photosensitive resin (Low et al., 2017). It is a process known as Stereolithography or Digital Light Processing (DLP) (Figure 4). This technique involves using a laser to trace and instantaneously cure a liquid resin printed cross-section, while the rest of the resin stays liquid (Ligon et al., 2017; Herzberger et al., 2019). The process is carried out layer by layer, repeating the tracing and curing steps until both the 3D printing and curing processes are complete (Low et al., 2017). Gillono et al. developed azobenzene chromophore membranes using DLP. The 3D printed membrane exhibited light-triggered changes in CO₂ permeability, with up to a 70% increase under 532 nm laser irradiation due to azobenzene photoisomerization. The permeability increase was tunable based on laser intensity. This outcome highlights the technique's ability to finely adjust the permeation characteristics of membranes through controlled light exposure (Gillono et al., 2020). This technique, known for its high resolution and accuracy, is the preferred method for creating polymeric membranes, particularly effective in liquid and gas separation membrane fabrication. However, a profound challenge is the typically low mechanical integrity of the printed products (Ligon et al., 2017). Therefore, there is an ongoing exploration of other materials compatible with 3D printing photopolymerization to achieve the necessary characteristics and performance for such applications.

Despite these advancements, a critical evaluation reveals that 3D printing, while innovative, faces significant challenges when compared to methods traditionally employed in membrane production. Firstly, 3D printing is not a cost-effective method for conventional membrane fabrication as the scale and speed of production falls short when compared with conventional methods such as casting. Even so, 3D printing is a good alternative for generating membrane for niche applications (Low et al., 2017). Another issue of this technology is its current inability to consistently produce membranes with the sub-micron thickness required for optimal gas separation without encountering defects. This shortfall makes it challenging for 3D-printed membranes to match the performance and efficiency of their conventional counterparts, which rely on such thin films for enhanced selectivity and permeability. Specifically, FDM technique face limitations in producing membranes at the micro-to nanoscale thickness due to comparatively weak interlayer adhesion. This weakness can lead to structural flaws or voids that compromise the membrane's integrity, allowing gases to permeate undesirably and detract from the separation process's efficiency (Gutierrez et al., 2022).

3.2.2 Electrohydrodynamic emission—Electrospinning and electrospraying

Electrohydrodynamic emission, also known as Electrospinning/Electrospraying (shown in Figure 5), is a relatively novel technique that has garnered considerable interest for creating nanofibrous membranes with high porosity from various polymers and for its diverse applications, including tissue engineering, energy storage, and notably, gas separations (Wu et al., 2014; Tan and Rodrigue, 2019; Asad et al., 2020; Hosseini and Valipouri, 2023). These electrospun nanofibrous membranes (ENMs) exhibit several beneficial characteristics, including a network of interconnected pores, extensive porosity, and pore sizes that range from a few micrometers to several tens of nanometers, alongside a substantial surface-area-to-volume ratio (Hosseini and Valipouri, 2023). Particularly in membrane contactors, the EHD technique proves beneficial due to its promotion of high hydrophobicity, tortuosity, and surface porosity (Li et al., 2011; Li and Wang, 2013). The process of forming these fibrous structures is driven by the uniaxial expansion of a viscoelastic polymer solution (Sun et al., 2022). Although the electrospun membranes are majorly used in liquid separation due to challenges in creating dense membranes, recently, the modification of nanofibers has been applied widely to give them improved properties, as such, it is witnessing a growing use in gas application, particularly in carbon capture, air purification including the removal of NO_x, CO, CO₂, H₂S, VOCs, and SO₂ pollutants from air due to its advantageous characteristics (Olivieri et al., 2018; Zhang et al., 2018; Azzam et al., 2019; Huang et al., 2020; Sun et al., 2022). For instance, Huang et al. fabricated an electrospun polystyrene (PS)/polyethylenimine (PEI) fiber membrane to capture CO₂ from ambient air before the air is admitted into a Zinc-air batteries (ZABs) to enhance battery performance (Huang et al., 2020). Likewise, Alkandari et al. employed electrohydrodynamic emission and solution casting as a hybrid membrane manufacturing method, to produce ZIF-67/cellulose acetate asymmetric membranes with improved gas permeability and selectivity for CO₂/N₂, CO₂/CH₄, and O₂/N₂ (Alkandari et al., 2023). Also, Elsaidi et al. employed the EHD method to produce thin film MMMs for CO₂/N₂ separation, resulting in improved CO₂ permeance (Elsaidi et al., 2021). Similarly, Katepalli et al., 2011 developed multi-scale ACF-PANS nanofiber structures through electrospinning, which demonstrated high efficiency in the removal of atmospheric pollutants such as toluene, CO₂, SO₄, and NO. In addition, Electrospun nanofibers have emerged as a cutting-edge solution for fabricating supports for thin-film composite (TFC) membranes. The support layer of TFC membranes has been underappreciated and the main focused with TFC membranes was directed to the gutter layer and selective layer (Kattula et al., 2015; Yoo et al., 2018). This oversight is partly due to treating TFC supports as mere mechanical support, and not considering their potential impact on the selectivity and permeability of gases. Recent studies have highlighted that modifications to the morphology of the support layer can significantly improve the overall performance of the membranes. For instance, Fan et al., 2023 proposed a facile and versatile support layer modification strategy and they achieved high-performance TFCs with high selectivity and permeance, where the support layer is the porous electrospun nanofiber substrate. Electrospun support layers for TFC membranes, with their porous structure of

nanofibers, stand out for their potential in gas separation technologies. They embody a promising direction for the future of TFC membranes by enabling high selectivity and permeance. This is achieved through a facile and adaptable strategy for modifying the support layer, making use of the porous electrospun nanofiber substrate to enhance performance (Fan et al., 2023). The disadvantages of EHD include low throughput, high energy intensive as it operates at high voltages (5 to >20 kV). These factors raise concerns regarding its environmental impact and overall sustainability.

3.2.3 Functionalization and surface engineering

Functionalization and surface engineering are critical strategies in membrane fabrication to tailor the properties of membranes for specific applications, such as improving selectivity, permeability, and chemical stability (Ma et al., 2022). These modifications can significantly enhance the performance of membranes in various separation processes, including water treatment, and gas separation. Outlined below are several pivotal methods and strategies deployed in the realm of functionalization and surface engineering tailored for the development of membranes.

3.2.3.1 Layer-by-layer Assembly

The layer-by-layer (LbL) assembly method is an attractive technique for the fabrication of ultra-thin, defect-free films with tailored composition and tuneable properties. At its core, this method utilizes electrostatic interactions between materials of opposing charges. It involves the alternate, sequential layering of positively and negatively charged polyelectrolytes on a charged surface. Each layering step is interspersed with a rinsing phase to eliminate loosely bound polymer chains (Zhao et al., 2019), as demonstrated in Figure 6. To achieve enhanced membrane selectivity, particularly on microporous substrates, a substantial number of anion/cation polyelectrolyte depositions may be required (Ismail et al., 2015). One of the outstanding benefits of the LbL method is the precise control it offers over film thickness at the nanometer scale (Heo et al., 2020). This precision is meticulously adjustable through the number of sequential adsorption steps. The LbL technique is highly versatile, finding applications across various domains of membrane science. It plays a pivotal role in developing membranes for water purification (Dong et al., 2022) and gas separation (Heo et al., 2020). Beyond membrane technology, this technique is involved in biosensors (Correia et al., 2021), drug delivery (Alkekhia et al., 2020), and other nanotechnology applications.

The LbL assembly method is renowned for its simplicity and adaptability in producing extremely thin polyelectrolyte multilayers, making it highly effective in membrane separation applications. Unlike conventional membrane fabrication methods, LbL facilitates thorough control over the thickness and structure of membranes, down to the nanometer scale. This is exemplified in studies like those conducted by Heo et al., 2017, where LbL was utilized to construct nanoscale graphene oxide (GO) membranes with controlled structure and thickness by spray assisted LbL assembly to separate CO₂. This design enabled the membrane to block N₂ and enhance CO₂ permeance by controlling the number of GO layers. The study achieved an extraordinary balance of selectivity and permeability. The integration of the LbL technique with other

manufacturing methods significantly bolsters its utility in improving membrane separation efficiency. A compelling example of this synergy is found in the work of Li et al., where they combined LbL assembly with a PDMS spraying method to address defects in P84 gas separation membranes initially created through phase inversion. The fabricated membrane significantly improved gas separation performance, with H₂/CH₄ selectivity increasing by 270% compared to the original P84 membrane (Li et al., 2022). Moreover, Xu et al. drew inspiration from the LbL concept to fabricate 2D membranes with a meticulously ordered superlattice structure. This was achieved through an alternating Layer-by-Layer (LbL) assembly of MgAl-LDH nanosheets and formamidinium sulfonic acid (FAS), followed by coating with a thin layer of PDMS as seen in Figure 7. The alternating stacking of LDH and FAS leads to highly ordered sub-nanometre channels just 0.34 nm high between layers, allowing for effective molecular sieving. The combination of LDH's affinity for CO₂ and FAS reversible CO₂ binding enhanced CO₂ permeation selectively. This approach not only allows for precise control of the membrane separation capabilities but also offers a scalable, cost-effective solution for high-performance CO₂ separation (Xu et al., 2021). The thickness of individual layers in LbL assemblies can vary significantly, ranging from a few angstroms to hundreds of nanometers. This thickness is a tunable aspect, adjustable by modifying various characteristics of the deposition mixture. Key factors influencing layer thickness include the pH (Mendelsohn et al., 2000; Heo et al., 2017), deposition time (Tousley et al., 2016), the ionic strength and counter-ions (Scheepers et al., 2021; Scheepers et al., 2023), and the temperature of the mixture. Additionally, the molecular weight of the deposition species (Wong et al., 2009) the relative humidity in the fabrication environment are critical parameters that can significantly impact the individual layer thicknesses (Daio et al., 2015).

3.2.3.2 Cross-linking

Cross-linking techniques have become a pivotal approach in the fabrication of polymeric membranes for gas separation, offering enhanced stability and performance (Wright and Paul, 1997; Kelman, 2008). These techniques involve the formation of chemical bonds between polymer chains, creating a network structure that significantly improves the membrane mechanical strength and chemical resistance (Liu et al., 2023). Some profound benefits of cross-linked polymeric membranes in gas separation are their enhanced selectivity and permeability, as illustrated in (Figure 8). Cross-linking can reduce the free volume within the polymer matrix, thereby allowing for more selective gas transport. This is particularly beneficial for applications requiring high purity levels, such as in the separation of carbon dioxide from methane in natural gas processing (Hong et al., 2015; Liu et al., 2023). Additionally, cross-linked membranes exhibit improved resistance to swelling, CO₂ induced plasticization and chemical degradation, particularly in harsh environments (Wind et al., 2002; Begni et al., 2021). This increased stability extends the membranes operational lifespan and reduces the need for frequent replacements, thus offering economic advantages (Hunger et al., 2012). Various methods can be employed to crosslink polymer membranes for gas separation, such as ionic crosslinking (Schmeling et al., 2010), thermal crosslinking

(Alghunaimi, 2013), and photocrosslinking (Decker and Bianchi, 2003; Decker et al., 2004). However, the choice of approach depends on the polymer functional groups and the expected separation attributes of the membrane (Wind et al., 2002; Bolto et al., 2009; Esteban et al., 2022).

Hunger et al., 2012 demonstrated that copolyimide membranes which are crosslinked exhibit increased resistance to plasticization and maintain their selectivity, showing no notable decline compared to non-crosslinked membranes when subjected to CO₂/CH₄ or toluene/cyclohexane mixtures. Furthermore, it was found that membranes crosslinked covalently tend to have enhanced separation efficiency compared to those crosslinked ionically. Schmelting et al. investigated the advantages of using 6FDA (4,4'-hexafluoroisopropylidene diphthalic anhydride)-copolyimides with carboxy groups. Their research assessed a range of membrane materials, including non-cross-linked, ionically crosslinked, and covalently crosslinked variants, focusing on their effectiveness in separating CO₂/CH₄ gas and other liquid mixtures. The study also provided insights into the efficiency and suitability of these membranes for such applications (Schmelting et al., 2010). Zhang et al., 2023 developed a range of cross-linkable Polyimides (PIs) with varying degrees of polymer chain orientation, aimed at improving CO₂/CH₄ separation efficiency. Unlike traditional PIs, they achieved a 2.3-fold increase in CO₂ permeability by precisely controlling the polymer chain orientation, without negatively impacting the membrane resistance to plasticization.

However, the process of cross-linking must be carefully controlled. Over-cross-linking can lead to membranes that are too rigid, reducing their gas permeability (Hong et al., 2015). The choice of cross-linking agents and the conditions under which cross-linking is carried out (such as temperature and time) are critical factors that determine the final properties of the membrane (Wind et al., 2002; Tashvigh et al., 2019).

Recent advancements in cross-linking techniques include the use of UV radiation, thermal treatments, and the incorporation of nanoparticles to initiate or enhance the cross-linking process. These methods offer more precise control over the extent and nature of cross-linking, leading to membranes with tailored properties for specific gas separation tasks (Wright and Paul, 1997; Ismail and Aziz, 2012).

3.2.3.3 Nanocomposite membranes

Polymeric membranes, commonly utilized in membrane separation processes, encounter two primary challenges: 1) a trade-off between permeability and selectivity, and limited thermal stability. Notably, these issues are rooted in the materials properties rather than the fabrication methods of the membranes. To address these limitations, a novel class of membranes emerged in the 1970s, incorporating nanomaterials into cellulose acetate (CA) membranes to enhance their resistance to compaction. This innovative approach soon gained considerable attention as a means to adjust and improve membrane performance (Takahashi and Paul, 2006; Khorshidi et al., 2016b; Khorshidi et al., 2016a). For instance, prevalent polymers in membrane technology, such as polyethersulfone (PES), polyvinylidene fluoride (PVDF), polypropylene (PP), and polytetrafluoroethylene (PTFE), typically exhibit hydrophobic characteristics. The integration of hydrophilic nanomaterials into these membranes can transform their nature

from hydrophobic to hydrophilic (Yang et al., 2016; Khorshidi et al., 2019). Nanocomposite membranes can be categorized into four distinct types, depending on the placement of the nanomaterials and the membrane structure: 1) conventional nanocomposite, 2) surface-located nanocomposite, 3) thin-film nanocomposite (TFN), and 4) thin-film composite (TFC) with a nanocomposite substrate. Figure 9 provides a schematic representation of these four varieties of nanocomposite membranes. Each category offers specific advantages over the others, highlighting the diversity and adaptability of nanocomposite membranes in enhancing membrane technology (Takahashi and Paul, 2006; Rafiq et al., 2012). Sadeghi et al. investigated the impact of silica nanoparticles on the permeability of CO₂, CH₄, and N₂ gases in polybenzimidazole (PBI) membranes. Their result showed that increasing the silica content in the polymer matrix led to higher solubility but lower diffusivity of gases in the membranes. Consequently, the permeability of CO₂ and CH₄ was increased, while that of N₂ significantly declined as silica content increased (Sadeghi et al., 2009). Song et al. developed a defect-free composite membrane by integrating ZIF-8 nanoparticles into Matrimid 5218 by solution mixing. They found that the addition of ZIF-8 enhanced the membrane's structure, creating more space within the polymer. This change, coupled with the natural ability of gases to move through ZIF-8 unique structure, significantly improved the membrane's permeability to gases such as CO₂, CH₄, O₂, N₂, and H₂ (Song et al., 2012). Rafiq et al. explored the development of mixed matrix membranes (MMMs) by integrating inorganic silica nanoparticles into polysulfone/polyimide (PSF/PI) asymmetric membranes for gas separation, utilizing the phase inversion technique. They observed that the addition of 5.2 wt% silica into a PSF/PI-20% blend significantly enhanced CO₂ permeance, and the improvement was proportional to the increase in silica content (Rafiq et al., 2012).

3.3 Cost considerations and scalability

Gas separation membranes still face manufacturing challenges that need to be addressed to exploit their tremendous potential. As presented by Beuscher et al., 2022 "research in membrane separation has focused on developing better membrane materials, yet very few of these materials are being used in commercial applications". In fact, since 1976 only 10% of all papers containing "polymer," "material," "module," or "process" as keywords have focused on modules and process research. Moreover, currently, prominent players in gas separation membrane manufacturing, including Air Liquide, Air Products, AirRane, Evonik, MTR, and Honeywell UOP, cater to various separation needs such as oxygen/nitrogen generation and carbon dioxide/hydrogen purification. The prevalent commercial membrane materials encompass polyimide, cellulose, and polysulfone, fashioned into hollow fiber or occasionally spiral-wound modules, albeit specific costs remain undisclosed by suppliers, complicating the cost analysis landscape.

The scalability of membrane manufacturing hinges on achieving simplicity, robustness, and replicability to accommodate the diverse spectrum of module sizes dictated by different applications, as shown in Table 3. Furthermore, sustainability imperatives mandate that fabrication processes minimize waste, employ

renewable feedstocks, and utilize green solvents. Sustainable manufacturing, therefore, not only prioritizes scalability and waste reduction but also emphasizes energy efficiency and favorable economic attributes.

A comprehensive literature search, querying “polymer membrane technology for gas separation” and “manufacturing costs” via Web of Science, yielded 176 entries, comprising both articles and patents. Cost estimations for polymer membranes, ranging from \$10 to \$50 per square meter, have been reported for diverse applications including CO₂ capture, oxygen-nitrogen separation, and propylene/propane separation (Zarca et al., 2018; Adhikari et al., 2021; Lee et al., 2022). Remarkably, this cost range has remained unchanged since 1992 (Van Der Sluis et al., 1992). The authors advocate for technoeconomic analysis encompassing capital and operating costs (e.g., electricity, raw materials, land, labor) to update contemporary membrane cost profiles and validate economic viability during scale-up processes. Furthermore, in conjunction with technoeconomic assessments, a holistic understanding of the environmental life cycle of membranes is indispensable for developing truly sustainable membrane processes. Such insights will inform decisions throughout the design, fabrication, and deployment stages, ensuring that environmental considerations are integrated into the fabric of gas separation membrane technology.

4 Sustainable membrane manufacturing

Traditional polymeric membranes, made from synthetic polymers such as polyamide, polysulfone, polyethersulfone, polyvinylidene fluoride, and others, have been predominant in the industry due to their strong mechanical properties, chemical resistance, and flexibility (Cui et al., 2010; Purkait et al., 2018). However, the environmental impact of their production, including the need for greener processes and effective waste management, presents a significant challenge. In light of these environmental concerns, biodegradable polymeric membranes are gaining attention as a more sustainable alternative, offering a reduced ecological footprint (Galiano et al., 2018; Lasseuguette and Ferrari, 2020). Biodegradable polymer is a type of polymer that can break down into water, carbon dioxide, biomass, and other natural substances under the action of naturally occurring microorganisms such as bacteria, fungi, and algae, within a specific period of time and under environmental conditions (Jami'an et al., 2015; Bandehali et al., 2021). These polymers can be derived from renewable bio-based resources or from synthetic sources that are engineered to degrade (e.g., polycaprolactone (PCL), polybutylene adipate terephthalate (PBAT)).

Likewise, the development of these bio-based membranes involves considerations like choosing appropriate green solvents and optimizing waste management during production. Additionally, factors like reusability, cost-effectiveness, and post-use disposal strategies are crucial for their success in industrial applications (Figoli et al., 2016). Overall, the goal is to achieve membranes with high permeability, selectivity, mechanical and thermal resistance, but at a lower manufacturing cost, addressing the environmental and efficiency challenges in membrane technology.

4.1 Eco-friendly polymer feedstock

Eco-friendly polymers, those derived from biological sources, or recycled substances such as cellulose, chitosan (CS), polylactic acid (PLA), polyhydroxyalkanoates (PHA), and others, are attracting significant interest from researchers in the field of polymeric membrane fabrication. This interest is driven by the desire to align industrial practices with environmental conservation and resource management (Zhu et al., 2020; Iulianelli et al., 2022; Torre-Celeizabal et al., 2023). Table 4 presents a summary of the most common bio-based polymers used in membrane production outlining their advantages and disadvantages.

4.1.1 Cellulose

Cellulose biopolymers are plant-based polysaccharide, made up of long macromolecular chains of 1-4- β -glycosidic linked D-glucose units. Among the derivatives of cellulose, the application and performance of cellulose acetate (CA) and cellulose triacetate (CTA) in gas membrane fabrication have been investigated extensively due to its unique properties including easy processability, versatility and eco-friendliness (Wu and Yuan, 2002; Lam et al., 2016; Nikolaeva et al., 2018; Gopi et al., 2019; Raza et al., 2021; Regmi et al., 2021; Alkandari et al., 2023). However, CA is susceptible to plasticization when exposed to CO₂. The adsorption of CO₂ into the polymer matrix at elevated pressures can lead to an increased free volume and enhanced mobility of the polymer chains, resulting in the plasticization of the material (Donohue et al., 1989; Houde et al., 1996).

4.1.2 Chitosan

Chitosan (CS), a naturally abundant biopolymer produced from the deacetylation of chitin and recognized for its biocompatibility, biodegradability, hydrophilic, and non-toxicity, has been used to fabricate several membranes (de Alvarenga, 2011). CS membranes have proven to be effective in various gas separation applications (Xiao et al., 2007; Torre-Celeizabal et al., 2023). The molecular formation of chitosan is rich in amino and hydroxyl groups, a feature that greatly boosts its capacity to capture CO₂, a polar molecule. This absorption capability is particularly enhanced when the membrane is swollen with water or when specialized fillers are incorporated into mixed matrix membranes (MMM). (Ito et al., 2003; Xiao et al., 2007; Li et al., 2022; Torre-Celeizabal et al., 2023). In addition, incorporating small amounts of three-dimensional and two-dimensional particle fillers can enhance both the CO₂ capturing ability and the mechanical strength of chitosan (Torre-Celeizabal et al., 2023).

4.1.3 Polylactic acid

PLA, which are synthesised by a direct polycondensation of hydroxyl acid or ring-opening polymerization of lactide are regarded as exceptional biopolymer for membrane fabrication. Notable for its excellent processability, solubility in a variety of organic solvents, water resistance, and a melting point and glass transition temperature (T_g) ranging from 170°C to 80°C and 50°C–65°C, respectively. The T_g of PLA varies with crystallinity and biopolymer structure, while the crystallinity itself is a function of the proportion of D-lactide acid, which typically ranges from highly crystalline to amorphous (Castro-Aguirre et al., 2018; Galiano et al.,

2018). Iulianelli et al. fabricated dense symmetric PLA Easy Fil™ white membranes and tested the gas permeability and ideal selectivity of H₂, CH₄, CO₂, and He at room temperature with transmembrane pressures ranging from 100 to 1200 KPa. They discovered that CO₂ permeability reached approximately 70 Barrer, surpassing Robeson's upper bound for CO₂/CH₄ separation and achieved a selectivity of 285 (Iulianelli et al., 2019). Additionally, they reported a selectivity of 26.5 for H₂/CO₂ at room temperature and 1 bar (Iulianelli et al., 2017), making these membranes notably suitable for biogas separation applications. However, several authors have reported that PLA faces a significant limitation due to its susceptibility to hydrolytic degradation when exposed to water, bacteria, or UV radiation. This degradation of its ester bonds occurs under specific conditions such as temperature, humidity, and pH, which can influence its stability and, correspondingly, its practical applications (Moon et al., 2016; Li et al., 2017).

4.1.4 Polyhydroxyalkanoates

PHA, derived from microbial fermentation of various renewable sources, and their derivatives, poly (3-hydroxybutyrate) (PHB) and polyhydroxyvalerate (PHV), are characterized by desirable properties such as hydrophobicity, optical purity, high processability, and biocompatibility. These features make them suitable for a range of applications, including gas membrane fabrication, as well as packaging and the biomedical industry (Follain et al., 2014; Siracusa et al., 2017; Papchenko et al., 2022). Follain et al., 2014 investigated the application of PHB membranes for pervaporation and gas separation by evaluating the diffusion and gas permeation. They employed two different approaches for homopolymer PHB and copolymer PHBV preparation: 1) a classic film casting using chloroform as a solvent and 2) a compressing preparation technique at elevated temperature. A remarkable selectivity range of 1.5–6.7 for CO₂/O₂ and 4.8 to 19 for CO₂/N₂ in PHB and PHBV (3 mol% 3-HV units) were obtained. Siracusa, et al. observed selectivity values ranging from 1.7 to 2.5 for CO₂/O₂ and 2.2 to 3.4 for CO₂/N₂ in PHB films (Siracusa et al., 2017). Huh et al., 2017 investigated H₂ permeability and selectivity in PHBV (12 mol% 3-HV units) and composite membranes incorporating multiwall carbon nanotubes.

In addition to the characteristics listed in Table 4, it is critical to acknowledge the inherent challenge associated with the permeability and selectivity of bio-based polymers. Due to their semi-crystalline nature (Lam et al., 2016), these polymers generally exhibit low permeability coupled with moderate selectivity, which hinders their applicability as membrane for gas separation. This is clearly shown in Figure 10, where most bio-based polymers are below the 1991 upper bound line. However, it is possible to improve these properties through various synthetic modifications. These include chemically altering the polymer structure, mixing the polymer with plasticizers to make them less brittle or blending them with other polymers (Papchenko et al., 2022), and incorporating additives such as ionic liquids (Lam et al., 2016; Nikolaeva et al., 2018; Alkandari and Castro-Dominguez, 2023). Such enhancements are crucial because one of the main challenges with low-permeability materials is the need to make very thin membranes to maximize gas flux, and thus efficiency (Shen and Lua, 2010). Similarity, methods such as surface modification and the use of

nanocomposite membranes have been shown to further improve membrane performance (Mafirad et al., 2018; Dai et al., 2019; Zargar et al., 2019).

4.2 Green solvents and additives for membranes

The evolution of membrane fabrication has increasingly focused on the integration of green solvents and additives, reflecting a growing commitment to environmental sustainability and safer manufacturing practices (Ajari et al., 2019; Sing Soh et al., 2023). Green solvents, characterized by their low toxicity, biodegradability, and minimal environmental impact, are pivotal in this paradigm shift (Capello et al., 2007; Figoli et al., 2014; Marino et al., 2018). These solvents, including substances like γ -valerolactone (GVL), acetyl tributyl citrate (ATBC), and cyrene, offer safer alternatives to traditional, often hazardous solvents used in membrane production, such as N-Methyl-2-pyrrolidone (NMP) (Gu and Jérôme, 2013; Sherwood et al., 2014).

Rasool and Vankelecom, 2019 experimented with GVL and glycerol derivatives to create porous membranes using the NIPS method with common polymers like PI, PES, polysulfone (PSU), cellulose acetate (CA), and cellulose triacetate (CTA), aiming to explore bio-based green solvents in membrane fabrication. Similarly, Sherwood et al., 2014 demonstrated that Cyrene could be efficiently produced from biomass in two simple steps, minimizing environmental impacts. Figoli et al., 2017 applied Cyrene in fabricating PES and PVDF membranes using both VIPS and NIPS techniques, highlighting Cyrene versatility as a solvent for common membrane polymers. And also Bridge et al., 2022 applied the same solvent (Cyrene) in PSF to prepare defect-free asymmetric gas separation membrane via dry/wet NIPS. In addition to solvents, the incorporation of eco-friendly additives has been instrumental in enhancing the performance and sustainability of membranes. These additives can improve membrane properties like mechanical strength, without adding significant environmental burdens (Clarke et al., 2018). Examples include the use of natural polymers, bio-based nanomaterials, and other non-toxic compounds that complement the green solvents (Randová et al., 2016; Fu et al., 2019; Nasar et al., 2019). The synergy of green solvents and additives in membrane fabrication not only aligns with environmental regulations but also sets a new standard for the industry in terms of sustainability and safety. By reducing the reliance on harmful chemicals, this approach significantly diminishes the ecological footprint of membrane production processes. Moreover, it opens up new possibilities for innovative membrane applications in various sectors, including water treatment, gas separation, and biomedical applications, while ensuring compliance with stringent environmental and health standards (Clark and Tavener, 2007; Figoli et al., 2014). The ongoing research and development in this area are poised to yield membranes with improved performance characteristics, such as enhanced permeability, selectivity, and durability, in an environmentally responsible manner. Thus, the use of green solvents and additives represents a crucial step towards more sustainable and eco-friendly membrane technology.

4.3 Membrane reusability and recycling

Reusing and recycling of polymer membrane materials are becoming increasingly important in addressing environmental concerns associated with membrane technology. As the demand for membrane-based separation processes grows, so does the need for sustainable practices that minimize waste and reduce the ecological footprint of these technologies (El-Khair and Ali, 2013; Ignatyev et al., 2014; Al-Shaeli et al., 2022). Recycling of polymeric membranes involves the recovery and reprocessing of membrane materials at the end of their useful life. This can be achieved through mechanical recycling, where membranes are ground and remoulded into new products, or chemical recycling, where the polymer is broken down into its monomers or other valuable chemicals as shown in Figure 11. Recycling helps to conserve resources and reduce landfill waste (Achilias and Karayannidis, 2004; Karayannidis and Achilias, 2007; Jiun et al., 2016; Wang et al., 2017). On the other hand, Reusability focuses on designing membranes that can be cleaned and reused multiple times without significant loss of performance. This approach extends the lifespan of membranes, decreasing the frequency of replacement and the associated environmental impact. Strategies for enhancing reusability include developing fouling-resistant membranes or designing membranes that can be easily regenerated through simple cleaning procedures (Patel et al., 2022). Research efforts have primarily focused on recycling end-of-life (EoL) polymeric membranes, especially those used in water treatment processes. For example, Wang et al., who employed N-methyl-2-pyrrolidone (NMP) and DMF to dissolve EoL hollow fiber and flat sheet PVDF membranes used in microfiltration/ultrafiltration (MF/UF). These dissolved membranes were then reformed via phase inversion, resulting in recycled PVDF membranes for potential use as substrates in nanofiltration/reverse osmosis (NF/RO) applications (Wang et al., 2017). However, a notable deficiency remains in the area of recycling strategies for gas separation membranes at the end of their service life, underscoring a critical area for future research and development.

5 Membrane manufacturing challenges

The use of gas separation membranes in commercial settings has been established for decades, with the industry significantly expanding from the 1980s through the early 2000s. Although existing membranes are not appropriate for every gas separation application, they have proven to be highly effective when used appropriately (including suitable feedstock, scale, and purity requirements) and outperforms other separation techniques (IDTechEx, 2023). Currently, the gas separation membrane industry is experiencing a phase growth, driven by key market drivers, particularly the push towards renewable energy and decarbonization initiatives, along with technological innovations aimed at meeting these emerging demands. However, there are prevailing challenges to overcome, which is discussed in the sub-section.

5.1 Membrane material and manufacturing

The innovation in membrane materials and sustainable manufacturing techniques presents a significant opportunity for promoting a sustainable and eco-friendly future. The evolving field of polymeric membrane production is marked by a promising convergence of creativity, environmental sustainability, and improved operational efficiency. With the increasing global need for separation technologies, particularly for gas separation, the advancement of eco-friendly polymeric membranes is becoming more crucial. The process of creating polymeric membranes faces the complex task of balancing material characteristics with membrane efficiency, environmental sustainability, and affordability. It is essential to choose the right biodegradable polymer, one that provides an ideal mix of selectivity, permeability, and resistance to chemicals, tailored for specific uses. However, many biodegradable materials lack mechanical stability and degrade under harsh operational conditions. Consequently, polymers derived from fossil fuels are prevalently utilized. To address this, there is a strategy to develop hybrid polymers by blending biodegradable substances with a small quantity of novel materials (such as MOFs, COFs, CNPs, etc.) to bolster mechanical strength while minimally affecting biodegradability. This approach aims to improve the membranes mechanical robustness and stability. Additionally, the application of cross-linking techniques can reinforce the structural stability of biodegradable polymers. Chemical cross-linking can boost the mechanical strength and chemical resistance of membranes, rendering them more adaptable to rigorous uses.

Moreover, The integration of smart materials capable of responding to environmental stimuli (pH, temperature, electric field, etc.) (Ulbricht, 2019; Widakdo et al., 2022), and the incorporation of artificial intelligence and machine learning in polymeric gas membrane material discovery, selection, design and property testing, including degradability, tensile strength and resistance to tearing could revolutionize advanced membrane manufacturing, enabling the optimization of membrane performance and rapid prototyping (Yang et al., 2022). There is potential to compile both experimental and simulated data on membranes made with innovative materials into a vast database for functionality- and performance-based screening. This approach aims to expedite the thoughtful design and selection of membrane materials through machine learning, addressing the challenges posed by the limited nature and difficult-to-control degradability of biodegradable materials, alongside exploring advanced material options.

5.2 Scalability and reproducibility

In the realm of membrane technology research, the initial discovery of new materials with promising selectivity and permeability marks only the beginning of a journey toward practical application. The true challenges, and the source of most difficulties, lie in ensuring membrane stability under operational conditions, scaling up the production of defect-free membranes, and integrating these membranes into functional modules. Despite the

variety of materials investigated, industrial-scale applications predominantly utilize a limited array of polymers, such as cellulose acetate, polysulfone, and polyimide highlighting the gap between material discovery and application readiness. Moreover, discovering scalable methods to fabricate thin, impeccable membrane layers that fully utilize a material's capabilities often presents a greater challenge than merely identifying new materials with enhanced flux and selectivity. This discrepancy highlights a significant research gap: while the quest for superior membrane materials has intensified, the translation of these advancements into commercially viable solutions remains limited. A more concerted effort is necessary to advance beyond material discovery towards the development of reproducible, economically feasible membrane systems. This includes rigorous assessments of cost and scalability to meet industrial demands. Furthermore, it is notable that the cost range for membranes has not shifted significantly since 1992, remaining between \$10 to \$50 per square meter (Van Der Sluus et al., 1992). Nonetheless, designing membranes must also take economic constraints into account. Achieving this necessitates comprehensive technoeconomic assessments to ascertain the upper limits for polymer/composite costs, alongside the capital and operational expenses tied to the production methods.

Moreover, environmental sustainability of membrane technologies is critical, necessitating a deep understanding of their environmental life cycle. Scalability issues often hinder the adoption of advanced techniques, which, despite their potential, are challenged by the simplicity and cost-effectiveness of conventional methods. Scaling up these advanced techniques involves overcoming numerous obstacles, including high costs of sophisticated equipment and materials, the complexity of maintaining precise control over production parameters, and ensuring consistent quality and performance. Addressing these cost-effectiveness and comprehensive approach: investing in research and development to discover scalable processes, conducting extensive pilot testing, collaborating with material suppliers for availability and cost-effectiveness, and adopting modular scaling strategies. Additionally, focusing on reducing manufacturing costs and waste through strategies like material recycling can make advanced membranes more economically viable. Overcoming these hurdles is crucial for the commercial adoption of advanced gas separation membrane technologies, potentially revolutionizing their use across various industries (Sheng et al., 2021; Swaby et al., 2021).

6 Conclusion and future directions

This review highlights the growing emphasis on innovative and sustainable manufacturing techniques, emphasising the adoption of eco-friendly materials, advanced methodologies, and efforts to minimize waste and cost. The review comprehensively covers a wide array of manufacturing techniques, from conventional methods to advanced approaches, including green synthesis. It underscores the impact of these techniques on environmental sustainability, performance improvement, scalability, and economic feasibility. The exploration into sustainable membrane manufacturing reveals a pressing need for renewable material sources, minimizing or substituting toxic organic solvents, and implementing advanced techniques, such as surface modification and functionalization, in the industry to enhance

membrane performance. Despite the potential of advanced manufacturing techniques to yield high-performing membranes, their complexity and cost pose barriers to extensive application compared to conventional techniques such as casting. In addition, a critical analysis within this review examines the potential of bio-based polymers as viable alternatives to fossil fuel-derived polymers, emphasizing the importance of selecting biodegradable polymers that balance selectivity, permeability, and chemical resistance, suitable for specific applications. However, the challenge remains with many biodegradable materials lacking in mechanical stability and performance under harsh conditions, thus maintaining the dominance of fossil fuel-based polymers. To circumvent these limitations, the review discussed several methods to overcome this limitation, for example, the development of hybrid polymers, blending biodegradable materials with innovative substances to enhance mechanical strength and permeability without compromising biodegradability. As the search of advanced membrane materials increases in response to material challenges, the conversion of these innovations into practical, market-ready solutions is still constrained. A more concerted effort is necessary to advance, beyond material discovery, the development of reproducible, economically feasible membrane systems. This process demands thorough evaluation of affordability and scalability by comprehensive technoeconomic assessments to satisfy the requirements of industrial applications.

In light of the challenges identified in this review, it is imperative to undertake innovative measures to advance the development of sustainable gas separation membranes, focusing on the following key aspects:

- (1) Advancing material innovation: There is a critical need to develop advanced materials in a sustainable and cost-effective manner. Bio-based and environmentally friendly materials, along with nanomaterials such as metal-organic frameworks and carbon structures, have shown remarkable potential in enhancing membrane performance. However, their widespread industrial adoption is hindered by challenges related to cost and scalability of production. Innovative approaches such as mechanochemical synthesis offer promising avenues for manufacturing these materials at scale, eliminating the use of solvents and reducing production costs. Indeed, leveraging techniques like reactive extrusion and mechanochemistry holds significant promise in overcoming these challenges.
- (2) Intelligent membranes for eco-friendly disposal: Developing membranes that react to external triggers could pave the way for sustainable disposal methods at their life cycle's end. Currently, the predominant approaches to dispose of membranes at the end of their usefulness mirror those of plastic waste, primarily landfilling or burning. However, the introduction of smart membranes designed to break down in response to specific stimuli can help bypass these environmentally damaging disposal practices, thus enhancing the eco-sustainability of membrane technologies.
- (3) Incorporating life cycle and economic evaluations in membrane innovation. Traditionally, the emphasis in membrane research has been on improving selectivity and permeability. Yet, it's critical to balance these improvements with considerations of cost and environmental impact. New materials should be developed with an eye toward the entire process, including

raw materials, fabrication methods and other factors critical for scaling and deploying the technology effectively.

- (4) Embracing digital technologies and modelling. The use of digital tools, including artificial intelligence, can expedite the search for new membrane materials by evaluating multiple optimization goals, such as permeability, selectivity, affordability, and carbon footprint. Additionally, incorporating process analytical technologies within membrane systems allows for real-time monitoring, potentially improving maintenance strategies and extending the lifespan of membranes.

In general, future research endeavors should embrace a holistic strategy, as outlined in Table 5, covering the selection of materials, improvement of fabrication processes, and embedding biodegradable features into the creation of sustainable polymeric gas separation membranes. In conclusion, the evolution of membrane technology is poised at a promising juncture, driven by collaborative efforts across disciplines. By dedicating research to overcome current challenges and unlocking new possibilities for eco-friendly gas separation technologies, the field sets a new benchmark for performance and environmental responsibility in industrial applications. The collective endeavor towards sustainable manufacturing and the development of reproducible, economically viable membrane systems underscores the bright future of membrane technologies (Figure 12), promising not only enhanced performance but also a significant reduction in the ecological impact of gas separation processes.

Author contributions

SA: Data curation, Formal Analysis, Investigation, Software, Visualization, Writing—original draft, Conceptualization, Methodology. BC-D: Supervision, Writing—review and editing, Conceptualization.

References

- Achillas, D. S., and Karayannidis, G. P. (2004). The chemical recycling of PET in the framework of sustainable development. *Water, Air, & Soil Pollut. Focus* 4, 385–396. doi:10.1023/B:WAFO.0000044812.47185.0f
- Adhikari, B., Orme, C. J., Klahn, J. R., and Stewart, F. F. (2021). Technoeconomic analysis of oxygen-nitrogen separation for oxygen enrichment using membranes. *Sep. Purif. Technol.* 268, 118703. doi:10.1016/j.seppur.2021.118703
- Air Liquide (2024). Membrane technology. Available at: <https://advancedseparations.airliquide.com/about/membrane-technology> (Accessed March 25, 2024).
- Air Products (2024). Prism® membranes. Available at: <https://www.airproducts.com/equipment/prism-membranes> (Accessed March 25, 2024).
- AirRane (2024). Gas separation membrane technology. Available at: https://en.airrane.com/membrane_technology_principle (Accessed March 25, 2024).
- Ajari, H., Chaouachi, B., Galiano, F., Marino, T., Russo, F., and Figoli, A. (2019). A novel approach for dissolving crystalline LDPE using non-toxic solvents for membranes preparation. *Int. J. Environ. Sci. Technol.* 16, 5375–5386. doi:10.1007/s13762-018-2123-y
- Alam, J., Dass, L. A., Alhoshan, M. S., Ghasemi, M., and Mohammad, A. W. (2012). Development of polyaniline-modified polysulfone nanocomposite membrane. *Appl. Water Sci.* 2, 37–46. doi:10.1007/s13201-011-0021-2
- Alghunaimi, F. (2013). The performance of a thermally cross-linked polymer of intrinsic microporosity (PIM-1) for gas separation. *Saudi Arab KAUST Res. Repos.* doi:10.25781/KAUST-F5936
- Alkandari, S. H., and Castro-Dominguez, B. (2023). Electro-casting for superior gas separation membrane performance and manufacturing. *ACS Appl. Mater. Interfaces* 15, 56600–56611. doi:10.1021/acsami.3c14742
- Alkandari, S. H., Lightfoot, J., and Castro-Dominguez, B. (2023). Asymmetric membranes for gas separation: interfacial insights and manufacturing. *RSC Adv.* 13, 14198–14209. doi:10.1039/D3RA00995E
- Alkekhaia, D., Hammond, P. T., and Shukla, A. (2020). Layer-by-Layer biomaterials for drug delivery. *Annu. Rev. Biomed. Eng.* 22, 1–24. doi:10.1146/annurev-bioeng-060418-052350
- Al-Shaeli, M., Al-Juboori, R. A., Al Aani, S., Ladewig, B. P., and Hilal, N. (2022). Natural and recycled materials for sustainable membrane modification: recent trends and prospects. *Sci. Total Environ.* 838, 156014. doi:10.1016/j.scitotenv.2022.156014
- Amooghini, A. E., Sanaeepur, H., Pedram, M. Z., Omidkhah, M., and Kargari, A. (2016). New advances in polymeric membranes for CO₂ separation. *Polym. Sci. Res. Adv. Pract. Appl. Educ. aspects*, 354–368.
- An, H., Lee, A. S., Kammakakam, L., Sang Hwang, S., Kim, J.-H., Lee, J.-H., et al. (2018). Bromination/debromination-induced thermal crosslinking of 6FDA-Durene for aggressive gas separations. *J. Memb. Sci.* 545, 358–366. doi:10.1016/j.memsci.2017.09.083
- Anbukarasu, P., Sauvageau, D., and Elias, A. (2021). The effects of solvent casting temperature and physical aging on polyhydroxybutyrate-graphene nanoplatelet composites. *Polym. Compos.* 42, 1451–1461. doi:10.1002/pc.25915
- Asad, A., Sameoto, D., and Sadzadeh, M. (2020). “Overview of membrane technology,” in *Nanocomposite membranes for water and gas separation* (Amsterdam, Netherlands: Elsevier), 1–28. doi:10.1016/B978-0-12-816710-6.00001-8
- Askari, M., Xiao, Y., Li, P., and Chung, T.-S. (2012). Natural gas purification and olefin/paraffin separation using cross-linkable 6FDA-Durene/DABA co-polyimides grafted with α , β , and γ -cyclodextrin. *J. Memb. Sci.* 390 (391), 141–151. doi:10.1016/j.memsci.2011.11.030

Funding

The author(s) declare that no financial support was received for the research, authorship, and/or publication of this article.

Acknowledgments

The authors express their gratitude to the Kuwait Institute for Scientific Research (KISR) for providing financial support for SA's PhD studies.

Conflict of interest

The authors declare that the research was conducted in the absence of any commercial or financial relationships that could be construed as a potential conflict of interest.

Publisher's note

All claims expressed in this article are solely those of the authors and do not necessarily represent those of their affiliated organizations, or those of the publisher, the editors and the reviewers. Any product that may be evaluated in this article, or claim that may be made by its manufacturer, is not guaranteed or endorsed by the publisher.

Supplementary material

The Supplementary Material for this article can be found online at: <https://www.frontiersin.org/articles/10.3389/frmst.2024.1390599/full#supplementary-material>

- Atwoli, L., Baqui, A. H., Benfield, T., Bosurgi, R., Godlee, F., Hancocks, S., et al. (2021). Call for emergency action to limit global temperature increases, restore biodiversity, and protect health. *N. Engl. J. Med.* 385, 1134–1137. doi:10.1056/NEJMe2113200
- Azzam, S. A., Alshafei, F. H., López-Ausens, T., Ghosh, R., Biswas, A. N., Sautet, P., et al. (2019). Effects of morphology and surface properties of copper oxide on the removal of hydrogen sulfide from gaseous streams. *Ind. Eng. Chem. Res.* 58, 18836–18847. doi:10.1021/acs.iecr.9b03975
- Bagheri, A., and Jin, J. (2019). Photopolymerization in 3D printing. *ACS Appl. Polym. Mater* 1, 593–611. doi:10.1021/acsapm.8b00165
- Baker, R. W. (2002). Future directions of membrane gas separation technology. *Ind. Eng. Chem. Res.* 41, 1393–1411. doi:10.1021/ie0108088
- Bandehali, S., Sanaeepour, H., Ebadi Amooghin, A., Shirazian, S., and Ramakrishna, S. (2021). Biodegradable polymers for membrane separation. *Sep. Purif. Technol.* 269, 118731. doi:10.1016/j.seppur.2021.118731
- Basf, S. E. (2024) *Ultrason® – a versatile material for the production of tailor-made membranes – brochure, English.*
- Bazhenov, S. D., Borisov, I. L., Bakhtin, D. S., Rybakova, A. N., Khotimskiy, V. S., Molchanov, S. P., et al. (2016). High-permeance crosslinked PTMSP thin-film composite membranes as supports for CO₂ selective layer formation. *Green Energy & Environ.* 1, 235–245. doi:10.1016/j.gee.2016.10.002
- Begni, F., Lasseuguette, E., Paul, G., Bisio, C., Marchese, L., Gatti, G., et al. (2021). Hyper cross-linked polymers as additives for preventing aging of PIM-1 membranes. *Membr. (Basel)* 11, 463. doi:10.3390/membranes11070463
- Beuscher, U., Kappert, E. J., and Wijmans, J. G. (2022). Membrane research beyond materials science. *J. Memb. Sci.* 643, 119902. doi:10.1016/j.memsci.2021.119902
- Bolto, B., Tran, T., Hoang, M., and Xie, Z. (2009). Crosslinked poly(vinyl alcohol) membranes. *Prog. Polym. Sci.* 34, 969–981. doi:10.1016/j.progpolymsci.2009.05.003
- Bridge, A. T., Pedretti, B. J., Brennecke, J. F., and Freeman, B. D. (2022). Preparation of defect-free asymmetric gas separation membranes with dihydrolevoglucosenone (Cyrene™) as a greener polar aprotic solvent. *J. Memb. Sci.* 644, 120173. doi:10.1016/j.memsci.2021.120173
- Bryant, R. G. (2014). “Polyimides,” in *Ullmann's encyclopedia of industrial chemistry* (Weinheim, Germany: Wiley-VCH Verlag GmbH & Co. KGaA), 1–27. doi:10.1002/14356007.a21_253.pub2
- Capello, C., Fischer, U., and Hungerbühler, K. (2007). What is a green solvent? A comprehensive framework for the environmental assessment of solvents. *Green Chem.* 9, 927. doi:10.1039/b617536h
- Castel, C., Bounaceur, R., and Favre, E. (2021). Membrane processes for direct carbon dioxide capture from air: possibilities and limitations. *Front. Chem. Eng.* 3. doi:10.3389/feeng.2021.668867
- Castro-Aguirre, E., Auras, R., Selke, S., Rubino, M., and Marsh, T. (2018). Enhancing the biodegradation rate of poly(lactic acid) films and PLA bio-nanocomposites in simulated composting through bioaugmentation. *Polym. Degrad. Stab.* 154, 46–54. doi:10.1016/j.polymdegradstab.2018.05.017
- Ceratti, D. R., Louis, B., Paquez, X., Faustini, M., and Grosso, D. (2015). A new dip coating method to obtain large-surface coatings with a minimum of solution. *Adv. Mater.* 27, 4958–4962. doi:10.1002/adma.201502518
- Chen, J., Jiang, X., Tang, W., Ma, L., Li, Y., Huang, Y., et al. (2020a). Roll-to-roll stack and lamination of gas diffusion layer in multilayer structured membrane electrode assembly. *Proc. Inst. Mech. Eng. B J. Eng. Manuf.* 234, 66–74. doi:10.1177/0954405419862090
- Chen, X., Zhang, Z., Wu, L., Liu, X., Xu, S., Efome, J. E., et al. (2020b). Polymers of intrinsic microporosity having bulky substitutes and cross-linking for gas separation membranes. *ACS Appl. Polym. Mater* 2, 987–995. doi:10.1021/acsapm.9b01193
- Chitranshi Jaiswal (2024) *Global gas separation membrane market overview*. New York, USA: Spherical Insights.
- Choi, W., Ingole, P. G., Park, J.-S., Lee, D.-W., Kim, J.-H., and Lee, H.-K. (2015). H₂/CO mixture gas separation using composite hollow fiber membranes prepared by interfacial polymerization method. *Chem. Eng. Res. Des.* 102, 297–306. doi:10.1016/j.cherd.2015.06.037
- Chung, T.-S., Jiang, L. Y., Li, Y., and Kulprathipanja, S. (2007). Mixed matrix membranes (MMMs) comprising organic polymers with dispersed inorganic fillers for gas separation. *Prog. Polym. Sci.* 32, 483–507. doi:10.1016/j.progpolymsci.2007.01.008
- Clarizia, G., Tasselli, F., Simari, C., Nicotera, I., and Bernardo, P. (2019). Solution casting blending: an effective way for tailoring gas transport and mechanical properties of poly(vinyl butyral) and Pebax2533. *J. Phys. Chem. C* 123, 11264–11272. doi:10.1021/acs.jpcc.9b01459
- Clark, J. H., and Tavener, S. J. (2007). Alternative solvents: shades of green. *Org. Process Res. Dev.* 11, 149–155. doi:10.1021/op060160g
- Clarke, C. J., Tu, W.-C., Levers, O., Bröhl, A., and Hallett, J. P. (2018). Green and sustainable solvents in chemical processes. *Chem. Rev.* 118, 747–800. doi:10.1021/acs.chemrev.7b00571
- Correia, A. R., Sampaio, I., Comparetti, E. J., Vieira, N. C. S., and Zucolotto, V. (2021). Detecting cancer cells with a highly sensitive LbL-based biosensor. *Talanta* 233, 122506. doi:10.1016/j.talanta.2021.122506
- Cui, Y., Li, G., Wu, H., Pang, S., Zhuang, Y., Si, Z., et al. (2023). Preparation and characterization of asymmetric Kapton membranes for gas separation. *React. Funct. Polym.* 191, 105667. doi:10.1016/j.reactfunctpolym.2023.105667
- Cui, Z. F., Jiang, Y., and Field, R. W. (2010). “Fundamentals of pressure-driven membrane separation processes,” in *Membrane technology* (Amsterdam, Netherlands: Elsevier), 1–18. doi:10.1016/B978-1-85617-632-3.00001-X
- Dai, Z., Deng, J., Yu, Q., Helberg, R. M. L., Janakiram, S., Ansaloni, L., et al. (2019). Fabrication and evaluation of bio-based nanocomposite TFC hollow fiber membranes for enhanced CO₂ capture. *ACS Appl. Mater Interfaces* 11, 10874–10882. doi:10.1021/acsami.8b19651
- Daio, T., Bayer, T., Ikuta, T., Nishiyama, T., Takahashi, K., Takata, Y., et al. (2015). In-Situ ESEM and EELS observation of water uptake and ice formation in multilayer graphene oxide. *Sci. Rep.* 5, 11807. doi:10.1038/srep11807
- de Alvarenga, E. S. (2011). “Characterization and properties of chitosan,” in *Biotechnology of biopolymers* (InTech). doi:10.5772/17020
- Decker, C., and Bianchi, C. (2003). Photocrosslinking of a maleimide functionalized polymethacrylate. *Polym. Int.* 52, 722–732. doi:10.1002/pi.1119
- Decker, C., Bianchi, C., and Jönsson, S. (2004). Light-induced crosslinking polymerization of a novel N-substituted bis-maleimide monomer. *Polym. Guildf.* 45, 5803–5811. doi:10.1016/j.polymer.2004.06.047
- Dibrov, G. A., Volkov, V. V., Vasilevsky, V. P., Shutova, A. A., Bazhenov, S. D., Khotimsky, V. S., et al. (2014). Robust high-permeance PTMSP composite membranes for CO₂ membrane gas desorption at elevated temperatures and pressures. *J. Memb. Sci.* 470, 439–450. doi:10.1016/j.memsci.2014.07.056
- Dolejš, P., Poštulka, V., Sedláková, Z., Jandová, V., Vejražka, J., Esposito, E., et al. (2014). Simultaneous hydrogen sulphide and carbon dioxide removal from biogas by water-swollen reverse osmosis membrane. *Sep. Purif. Technol.* 131, 108–116. doi:10.1016/j.seppur.2014.04.041
- Dong, C., He, R., Xu, S., He, H., Chen, H., Zhang, Y.-B., et al. (2022). Layer-by-layer (LBL) hollow fiber nanofiltration membranes for seawater treatment: ion rejection. *Desalination* 534, 115793. doi:10.1016/j.desal.2022.115793
- Donohue, M. D., Minhas, B. S., and Lee, S. Y. (1989). Permeation behavior of carbon dioxide-methane mixtures in cellulose acetate membranes. *J. Memb. Sci.* 42, 197–214. doi:10.1016/S0376-7388(00)82376-5
- Dose, M. E., Chwatko, M., Hubacek, I., Lynd, N. A., Paul, D. R., and Freeman, B. D. (2019). Thermally cross-linked diaminophenylindane (DAPI) containing polyimides for membrane based gas separations. *Polym. Guildf.* 161, 16–26. doi:10.1016/j.polymer.2018.11.050
- Du, N., Park, H. B., Robertson, G. P., Dal-Cin, M. M., Visser, T., Scoles, L., et al. (2011). Polymer nanosieve membranes for CO₂-capture applications. *Nat. Mater* 10, 372–375. doi:10.1038/nmat2989
- El-Khair, A., and Ali, A. A. (2013). The mechanical behaviour of recycled high density polyethylene. *Int. J. Mod. Eng. Res. (IJMER)* 3.
- Elsaidi, S. K., Ostwal, M., Zhu, L., Sekizkardes, A., Mohamed, M. H., Gipple, M., et al. (2021). 3D printed MOF-based mixed matrix thin-film composite membranes. *RSC Adv.* 11, 25658–25663. doi:10.1039/D1RA03124D
- Esteban, N., Juan-y-Seva, M., Aguilar-Lugo, C., Miguel, J. A., Staudt, C., de la Campa, J. G., et al. (2022). Aromatic polyimide membranes with tert-butyl and carboxylic side groups for gas separation applications—covalent crosslinking study. *Polym. (Basel)* 14, 5517. doi:10.3390/polym14245517
- Evonik (2024). Efficient gas separation using hollow-fiber membranes. Available at: <https://www.membrane-separation.com/en/efficient-gas-separation-with-separan-by-evonik> (Accessed March 25, 2024).
- Fan, S.-T., Wang, J.-X., Liao, L.-G., Feng, J.-F., Li, B.-J., and Zhang, S. (2023). Enhanced selectivity in thin-film composite membrane for CO₂ capture through improvement to support layer. *Chem. Eng. J.* 468, 143645. doi:10.1016/j.cej.2023.143645
- Farjoo, A., and Kuznicki, S. M. (2016). H₂ separation using tubular stainless steel support type equation here. *Can. J. Chem. Eng.* 94, 2219–2224. doi:10.1002/cjce.22589
- Figoli, A., Marino, T., and Galiano, F. (2016). “Polymeric membranes in biorefinery,” in *Membrane technologies for biorefining* (Amsterdam, Netherlands: Elsevier), 29–59.
- Figoli, A., Marino, T., Galiano, F., Dorraji, S. S., Di Nicolò, E., and He, T. (2017). “Sustainable route in preparation of polymeric membranes,” in *Green chemistry and sustainable technology book series (GCST)* (Berlin, Germany: Springer), 97–120. doi:10.1007/978-981-10-5623-9_4
- Figoli, A., Marino, T., Simone, S., Di Nicolò, E., Li, X.-M., He, T., et al. (2014). Towards non-toxic solvents for membrane preparation: a review. *Green Chem.* 16, 4034–4059. doi:10.1039/C4GC00613E
- Figuerola, J. D., Fout, T., Plasynski, S., McIlvried, H., and Srivastava, R. D. (2008). Advances in CO₂ capture technology—the U.S. Department of energy's carbon sequestration program. *Int. J. Greenh. Gas Control* 2, 9–20. doi:10.1016/S1750-5836(07)00094-1
- Follain, N., Chappey, C., Dargent, E., Chivrac, F., Cretois, R., and Marais, S. (2014). Structure and barrier properties of biodegradable polyhydroxyalkanoate films. *J. Phys. Chem. C* 118, 6165–6177. doi:10.1021/jp408150k

- Foster, A. B., Beal, J. L., Tamaddondar, M., Luque-Alled, J. M., Robertson, B., Mathias, M., et al. (2021). Importance of small loops within PIM-1 topology on gas separation selectivity in thin-film composite membranes. *J. Mater. Chem. A Mater* 9, 21807–21823. doi:10.1039/D1TA03712A
- Fu, Y., Qin, L., Huang, D., Zeng, G., Lai, C., Li, B., et al. (2019). Chitosan functionalized activated coke for Au nanoparticles anchoring: green synthesis and catalytic activities in hydrogenation of nitrophenols and azo dyes. *Appl. Catal. B* 255, 117740. doi:10.1016/j.apcatb.2019.05.042
- Galiano, F., Briceño, K., Marino, T., Molino, A., Christensen, K. V., and Figoli, A. (2018). Advances in biopolymer-based membrane preparation and applications. *J. Memb. Sci.* 564, 562–586. doi:10.1016/j.memsci.2018.07.059
- Garcia-Fayos, J., Serra, J. M., Luiten-Olieman, M. W. J., and Meulenber, W. A. (2020). “Gas separation ceramic membranes,” in *Advanced ceramics for energy conversion and storage* (Amsterdam, Netherlands: Elsevier), 321–385. doi:10.1016/B978-0-08-102726-4.00008-9
- Gillono, M., Roppolo, I., Frascella, F., Scaltrito, L., Pirri, C. F., and Chiappone, A. (2020). CO₂ permeability control in 3D printed light responsive structures. *Appl. Mater Today* 18, 100470. doi:10.1016/j.apmt.2019.100470
- Gopi, S., Pius, A., Kargl, R., Kleinschek, K. S., and Thomas, S. (2019). Fabrication of cellulose acetate/chitosan blend films as efficient adsorbent for anionic water pollutants. *Polym. Bull.* 76, 1557–1571. doi:10.1007/s00289-018-2467-y
- Gu, Y., and Jérôme, F. (2013). Bio-based solvents: an emerging generation of fluids for the design of eco-efficient processes in catalysis and organic chemistry. *Chem. Soc. Rev.* 42, 9550–9570. doi:10.1039/c3cs60241a
- Gutierrez, D. B., Caldon, E. B., Espiritu, R. D., and Advincula, R. C. (2021). The potential of additively manufactured membranes for selective separation and capture of CO₂. *MRS Commun.* 11, 391–401. doi:10.1557/s43579-021-00062-8
- Gutierrez, D. B., Caldon, E. B., Yang, Z., Suo, X., Cheng, X., Dai, S., et al. (2022). 3D-printed PDMS-based membranes for CO₂ separation applications. *MRS Commun.* 12, 1174–1182. doi:10.1557/s43579-022-00287-1
- Gutierrez, D. B., Caldon, E. B., Yang, Z., Suo, X., Cheng, X., Dai, S., et al. (2023). PDMS-silica composite gas separation membranes by direct ink writing. *J. Appl. Polym. Sci.* 140. doi:10.1002/app.54277
- Hansen, C. M. (2007). “Hansen solubility parameters,” in *A user's handbook*. Editor C. M. Hansen (Boca Raton: CRC Press).
- Henis, J. M. S., and Tripodi, M. K. (1980). A novel approach to gas separations using composite hollow fiber membranes. *Sep. Sci. Technol.* 15, 1059–1068. doi:10.1080/01496398008076287
- Heo, J., Choi, M., Chang, J., Ji, D., Kang, S. W., and Hong, J. (2017). Highly permeable graphene oxide/polyelectrolytes hybrid thin films for enhanced CO₂/N₂ separation performance. *Sci. Rep.* 7, 456. doi:10.1038/s41598-017-00433-z
- Heo, J., Choi, M., Choi, D., Jeong, H., Kim, H. Y., Jeon, H., et al. (2020). Spray-assisted layer-by-layer self-assembly of tertiary-amine-stabilized gold nanoparticles and graphene oxide for efficient CO₂ capture. *J. Memb. Sci.* 601, 117905. doi:10.1016/j.memsci.2020.117905
- Herzberger, J., Sirrine, J. M., Williams, C. B., and Long, T. E. (2019). Polymer design for 3D printing elastomers: recent advances in structure, properties, and printing. *Prog. Polym. Sci.* 97, 101144. doi:10.1016/j.progpolymsci.2019.101144
- Higashi, S., Yamato, M., and Kawakami, H. (2021). Effect of phase separation due to solvent evaporation on particle aggregation in the skin layer of the gas separation membrane. *J. Photopolym. Sci. Technol.* 34, 449–456. doi:10.2494/photopolymer.34.449
- Honeywell (2024). Honeywell announces new technology for green hydrogen production. Available at: <https://pmt.honeywell.com/us/en/about-pmt/newsroom/press-release/2022/03/honeywell-announces-new-technology-for-green-hydrogen-production> (Accessed March 25, 2024).
- Hong, T., Niu, Z., Hu, X., Gmernicki, K., Cheng, S., Fan, F., et al. (2015). Effect of cross-link density on carbon dioxide separation in polydimethylsiloxane-norbornene membranes. *ChemSusChem* 8, 3595–3604. doi:10.1002/cssc.201500903
- Hosseini, S. S., and Chung, T. S. (2009). Carbon membranes from blends of PBI and polyimides for N₂/CH₄ and CO₂/CH₄ separation and hydrogen purification. *J. Memb. Sci.* 328, 174–185. doi:10.1016/j.memsci.2008.12.005
- Hosseini, S. S., and Valipouri, A. (2023). “Chapter 3 - electrospraying for membrane fabrication,” in *Electrospun and nanofibrous membranes*. Editors A. Kargari, T. Matsuura, and M. M. A. Shirazi (Amsterdam, Netherlands: Elsevier), 53–80. doi:10.1016/B978-0-12-823032-9.00024-6
- Houde, A. Y., Krishnakumar, B., Charati, S. G., and Stern, S. A. (1996). Permeability of dense (homogeneous) cellulose acetate membranes to methane, carbon dioxide, and their mixtures at elevated pressures. *J. Appl. Polym. Sci.* 62, 2181–2192. doi:10.1002/(SICI)1097-4628(19961226)62:13<2181::AID-APP1>3.0.CO;2-F
- Hu, Z., Zhang, H., Zhang, X.-F., Jia, M., and Yao, J. (2022). Polyethylenimine grafted ZIF-8/cellulose acetate membrane for enhanced gas separation. *J. Memb. Sci.* 662, 120996. doi:10.1016/j.memsci.2022.120996
- Huang, C.-L., Wang, P.-Y., and Li, Y.-Y. (2020). Fabrication of electrospun CO₂ adsorption membrane for zinc-air battery application. *Chem. Eng. J.* 395, 125031. doi:10.1016/j.cej.2020.125031
- Huh, M., Lee, H. M., Park, Y. S., and Yun, S. I. (2017). Biocomposite membranes based on poly(3-hydroxybutyrate-co-3-hydroxyvalerate) and multiwall carbon nanotubes for gas separation. *Carbon Lett.* 21, 116–121. doi:10.5714/CL.2017.21.116
- Hull, C. W. (1986). *Apparatus for production of three-dimensional objects by stereolithography*, 1–16.
- Hunger, K., Schmeling, N., Jeazet, H. B. T., Janiak, C., Staudt, C., and Kleinermmanns, K. (2012). Investigation of cross-linked and additive containing polymer materials for membranes with improved performance in pervaporation and gas separation. *Membr. (Basel)* 2, 727–763. doi:10.3390/membranes2040727
- IDTechEx (2023). *Gas separation membranes 2023-2033*. Cambridge, UK.
- Ignatyev, I. A., Thielemans, W., and Vander Beke, B. (2014). Recycling of polymers: a review. *ChemSusChem* 7, 1579–1593. doi:10.1002/cssc.201300898
- Ismail, A., and Aziz, F. (2012). “Chemical cross-linking modifications of polymeric membranes for gas separation applications,” in *Membrane modification* (Florida, United States: CRC Press), 363–384. doi:10.1201/b12160-12
- Ismail, A. F., Khulbe, K. C., and Matsuura, T. (2015). *Gas separation membranes*, 10. Switz.: Springer, 973–978. doi:10.1007/978-3-319-01095-3
- Ito, A., Sato, M., and Anma, T. (2003). Permeability of CO₂ through chitosan membrane swollen by water vapor in feed gas. *Die Angew. Makromol. Chem.* 248, 85–94. doi:10.1002/apmc.1997.052480105
- Iulianelli, A., Algieri, C., Donato, L., Garofalo, A., Galiano, F., Bagnato, G., et al. (2017). New PEEK-WC and PLA membranes for H₂ separation. *Int. J. Hydrogen Energy* 42, 22138–22148. doi:10.1016/j.ijhydene.2017.04.060
- Iulianelli, A., Russo, F., Galiano, F., Desiderio, G., Basile, A., and Figoli, A. (2019). PLA easy fil – white-based membranes for CO₂ separation. *Greenh. Gases Sci. Technol.* 9, 360–369. doi:10.1002/ghg.1853
- Iulianelli, A., Russo, F., Galiano, F., Manisco, M., and Figoli, A. (2022). Novel biopolymer based membranes for CO₂/CH₄ separation. *Int. J. Greenh. Gas Control* 117, 103657. doi:10.1016/j.ijggc.2022.103657
- Jami'an, W. N. R., Hasbullah, H., Mohamed, F., Wan Salleh, W. N., Ibrahim, N., and Ali, R. R. (2015). Biodegradable gas separation membrane preparation by manipulation of casting parameters. *Chem. Eng. Trans.* 43, 1105–1110. doi:10.3303/CET1543185
- Jamil, N., Othman, N. H., Shahrudin, M. Z., Mohd Razlan, M. R., Alias, N. H., Marpani, F., et al. (2020). Effects of pebax coating concentrations on CO₂/ch₄ separation of rgo/zif-8 pes membranes. *J. Teknol.* 82. doi:10.11113/jt.v82.13872
- Jeon, J. W., Kim, D.-G., Sohn, E., Yoo, Y., Kim, Y. S., Kim, B. G., et al. (2017). Highly carboxylate-functionalized polymers of intrinsic microporosity for CO₂-selective polymer membranes. *Macromolecules* 50, 8019–8027. doi:10.1021/acs.macromol.7b01332
- Jiang, S., and Ladewig, B. P. (2020). Green synthesis of polymeric membranes: recent advances and future prospects. *Curr. Opin. Green Sustain Chem.* 21, 1–8. doi:10.1016/j.cogsc.2019.07.002
- Jiang, X., Chuah, C. Y., Goh, K., and Wang, R. (2021). A facile direct spray-coating of Pebax® 1657: towards large-scale thin-film composite membranes for efficient CO₂/N₂ separation. *J. Memb. Sci.* 638, 119708. doi:10.1016/j.memsci.2021.119708
- Jimenez-Solomon, M. F., Song, Q., Jelfs, K. E., Munoz-Ibanez, M., and Livingston, A. G. (2016). Polymer nanofilms with enhanced microporosity by interfacial polymerization. *Nat. Mater* 15, 760–767. doi:10.1038/nmat4638
- Jiršáková, K., Stanovský, P., Dytrych, P., Morávková, L., Příbylová, K., Petrusová, Z., et al. (2021). Organic vapour permeation in amorphous and semi-crystalline rubbery membranes: experimental data versus prediction by solubility parameters. *J. Memb. Sci.* 627, 119211. doi:10.1016/j.memsci.2021.119211
- Jiun, Y. L., Tze, C. T., Moosa, U., and Tawawneh, M. A. A. (2016). Effects of recycling cycle on used thermoplastic polymer and thermoplastic elastomer polymer. *Polym. Compos.* 24, 735–740. doi:10.1177/096739111602400909
- Karayannidis, G. P., and Achillas, D. S. (2007). Chemical recycling of poly(ethylene terephthalate). *Macromol. Mat. Eng.* 292, 128–146. doi:10.1002/mame.200600341
- Katepalli, H., Bikshapathi, M., Sharma, C. S., Verma, N., and Sharma, A. (2011). Synthesis of hierarchical fabrics by electrospinning of PAN nanofibers on activated carbon microfibers for environmental remediation applications. *Chem. Eng. J.* 171, 1194–1200. doi:10.1016/j.cej.2011.05.025
- Kattula, M., Ponnuru, K., Zhu, L., Jia, W., Lin, H., and Furlani, E. P. (2015). Designing ultrathin film composite membranes: the impact of a gutter layer. *Sci. Rep.* 5, 15016. doi:10.1038/srep15016
- Kelman, S. (2008). *Crosslinking and stabilization of high fractional free volume polymers for the separation of organic vapors from permanent gases*.
- Khorshidi, B., Hajinasiri, J., Ma, G., Bhattacharjee, S., and Sadrzadeh, M. (2016a). Thermally resistant and electrically conductive PES/ITO nanocomposite membrane. *J. Memb. Sci.* 500, 151–160. doi:10.1016/j.memsci.2015.11.015
- Khorshidi, B., Hosseini, S. A., Ma, G., McGregor, M., and Sadrzadeh, M. (2019). Novel nanocomposite polyethersulfone-antimony tin oxide membrane with enhanced thermal, electrical and antifouling properties. *Polym. Guildf.* 163, 48–56. doi:10.1016/j.polymer.2018.12.058
- Khorshidi, B., Thundat, T., Fleck, B. A., and Sadrzadeh, M. (2016b). A novel approach toward fabrication of high performance thin-film composite polyamide membranes. *Sci. Rep.* 6, 22069. doi:10.1038/srep22069

- Kosinov, N., Gascon, J., Kapteijn, F., and Hensen, E. J. M. (2016). Recent developments in zeolite membranes for gas separation. *J. Memb. Sci.* 499, 65–79. doi:10.1016/j.memsci.2015.10.049
- Kunalan, S., Palanivelu, K., Sachin, E. K., Syrtsova, D. A., and Teplyakov, V. V. (2022). Thin-film hydrogel polymer layered polyvinyltrimethylsilane dual-layer flat-bed composite membrane for CO₂ gas separation. *J. Appl. Polym. Sci.* 139. doi:10.1002/app.52024
- Kuruppalil, Z. (2011). "Green plastics: an emerging alternative for petroleum based plastics," in IAJC-ASEE International Conference, April 29-30, 2011, 59–64.
- Lam, B., Wei, M., Zhu, L., Luo, S., Guo, R., Morisato, A., et al. (2016). Cellulose triacetate doped with ionic liquids for membrane gas separation. *Polym. Guildf.* 89, 1–11. doi:10.1016/j.polymer.2016.02.033
- Larsson, M., Markbo, O., and Jannasch, P. (2016). Melt processability and thermomechanical properties of blends based on polyhydroxyalkanoates and poly(butylene adipate-co-terephthalate). *RSC Adv.* 6, 44354–44363. doi:10.1039/C6RA06282B
- Lasseguette, E., and Ferrari, M.-C. (2020). "Polymer membranes for sustainable gas separation," in *Sustainable nanoscale engineering* (Amsterdam, Netherlands: Elsevier), 265–296. doi:10.1016/B978-0-12-814681-1.00010-2
- Lee, J.-Y., Tan, W. S., An, J., Chua, C. K., Tang, C. Y., Fane, A. G., et al. (2016). The potential to enhance membrane module design with 3D printing technology. *J. Memb. Sci.* 499, 480–490. doi:10.1016/j.memsci.2015.11.008
- Lee, T. H., Shin, M. G., Jung, J. G., Suh, E. H., Oh, J. G., Kang, J. H., et al. (2022). Facile suppression of intensified plasticization in glassy polymer thin films towards scalable composite membranes for propylene/propane separation. *J. Memb. Sci.* 645, 120215. doi:10.1016/j.memsci.2021.120215
- Lehermeier, H. J., Dorgan, J. R., and Way, J. D. (2001). Gas permeation properties of poly(lactic acid). *J. Memb. Sci.* 190, 243–251. doi:10.1016/S0376-7388(01)00446-X
- Li, F., Li, L., Liao, X., and Wang, Y. (2011). Precise pore size tuning and surface modifications of polymeric membranes using the atomic layer deposition technique. *J. Memb. Sci.* 385–386, 1–9. doi:10.1016/j.memsci.2011.06.042
- Li, F. Y., Xiao, Y., Chung, T.-S., and Kawi, S. (2012a). High-performance thermally self-cross-linked polymer of intrinsic microporosity (PIM-1) membranes for energy development. *Macromolecules* 45, 1427–1437. doi:10.1021/ma202667y
- Li, G., Knozowska, K., Kujawa, J., Tonkonogovas, A., Stankevičius, A., and Kujawski, W. (2021). Fabrication of polydimethylsiloxane (PDMS) dense layer on polyetherimide (PEI) hollow fiber support for the efficient CO₂/N₂ separation membranes. *Polym. (Basel)* 13, 756. doi:10.3390/polym13050756
- Li, G., Si, Z., Yang, S., Xue, T., Baeyens, J., and Qin, P. (2022a). Fast layer-by-layer assembly of PDMS for boosting the gas separation of P84 membranes. *Chem. Eng. Sci.* 253, 117588. doi:10.1016/j.ces.2022.117588
- Li, J., Cheng, P., Lin, M., Wey, M., and Tseng, H. (2020). Uniformity control and ultra-micropore development of tubular carbon membrane for light gas separation. *AIChE J.* 66. doi:10.1002/aic.16226
- Li, N., Wang, Z., and Wang, J. (2022b). Water-swollen carboxymethyl chitosan (CMC)/polyamide (PA) membranes with octopus-branched nanostructures for CO₂ capture. *J. Memb. Sci.* 642, 119946. doi:10.1016/j.memsci.2021.119946
- Li, R., Yuan, S., Zhang, W., Zheng, H., Zhu, W., Li, B., et al. (2019). 3D printing of mixed matrix films based on metal-organic frameworks and thermoplastic polyamide 12 by selective laser sintering for water applications. *ACS Appl. Mater. Interfaces* 11, 40564–40574. doi:10.1021/acsami.9b11840
- Li, S., Wang, Z., Yu, X., Wang, J., and Wang, S. (2012b). High-performance membranes with multi-permeability for CO₂ separation. *Adv. Mater.* 24, 3196–3200. doi:10.1002/adma.201200638
- Li, X., Chu, C., Wei, Y., Qi, C., Bai, J., Guo, C., et al. (2017). *In vitro* degradation kinetics of pure PLA and Mg/PLA composite: effects of immersion temperature and compression stress. *Acta Biomater.* 48, 468–478. doi:10.1016/j.actbio.2016.11.001
- Li, Z., and Wang, C. (2013). *One-Dimensional nanostructures*. 1st Edn. Berlin, Heidelberg: Springer Berlin Heidelberg. doi:10.1007/978-3-642-36427-3
- Ligon, S. C., Liska, R., Stampfl, J., Gurr, M., and Mülhaupt, R. (2017). Polymers for 3D printing and customized additive manufacturing. *Chem. Rev.* 117, 10212–10290. doi:10.1021/acs.chemrev.7b00074
- Liu, M., Seeger, A., and Guo, R. (2023). Cross-linked polymer membranes for energy-efficient gas separation: innovations and perspectives. *Macromolecules* 56, 7230–7246. doi:10.1021/acs.macromol.3c01196
- Loeb, S., and Sourirajan, S. (1963). Saline water conversion-II. *Adv. Chem. Ser.* 38, 117.
- Low, Z.-X., Chua, Y. T., Ray, B. M., Mattia, D., Metcalfe, I. S., and Patterson, D. A. (2017). Perspective on 3D printing of separation membranes and comparison to related unconventional fabrication techniques. *J. Memb. Sci.* 523, 596–613. doi:10.1016/j.memsci.2016.10.006
- Ma, T., Janot, J., and Balme, S. (2020). Track-Etched nanopore/membrane: from fundamental to applications. *Small Methods* 4. doi:10.1002/smtd.202000366
- Ma, X.-H., and Yang, S.-Y. (2018). "Polyimide gas separation membranes," in *Advanced polyimide materials* (Amsterdam, Netherlands: Elsevier), 257–322. doi:10.1016/B978-0-12-812640-0.00006-8
- Ma, Z.-Y., Xue, Y.-R., Yang, H.-C., Wu, J., and Xu, Z.-K. (2022). Surface and interface engineering of polymer membranes: where we are and where to go. *Macromolecules* 55, 3363–3383. doi:10.1021/acs.macromol.1c02647
- Madaeni, S. S., Badieh, M. M. S., and Vatanpour, V. (2013). Effect of coating method on gas separation by PDMS/PES membrane. *Polym. Eng. Sci.* 53, 1878–1885. doi:10.1002/pen.23456
- Mafirad, S., Mehrnia, M. R., Zahedi, P., and Hosseini, S. (2018). Chitosan-based nanocomposite membranes with improved properties: effect of cellulose acetate blending and TiO₂ nanoparticles incorporation. *Polym. Compos.* 39, 4452–4466. doi:10.1002/pc.24539
- Makhlouf, A. S. H. (2011). "Current and advanced coating technologies for industrial applications," in *Nanocoatings and ultra-thin films* (Amsterdam, Netherlands: Elsevier), 3–23. doi:10.1533/9780857094902.1.3
- Mantzalis, D., Asproulis, N., and Drikakis, D. (2011). *Gas separation through carbon nanotubes*.
- Marcano, A., Bou Haidar, N., Marais, S., Valletton, J.-M., and Duncan, A. C. (2017). Designing biodegradable PHA-based 3D scaffolds with antibiofilm properties for wound dressings: optimization of the microstructure/nanostructure. *ACS Biomater. Sci. Eng.* 3, 3654–3661. doi:10.1021/acsbomaterials.7b00552
- Marino, T., Blasi, E., Tornaghi, S., Di Nicolò, E., and Figoli, A. (2018). Polyethersulfone membranes prepared with Rhodiasolv®Polarclean as water soluble green solvent. *J. Memb. Sci.* 549, 192–204. doi:10.1016/j.memsci.2017.12.007
- Martinez-Izquierdo, L., Malankowska, M., Téllez, C., and Coronas, J. (2021). Phase inversion method for the preparation of Pebax® 3533 thin film membranes for CO₂/N₂ separation. *J. Environ. Chem. Eng.* 9, 105624. doi:10.1016/j.jece.2021.105624
- Mendelsohn, J. D., Barrett, C. J., Chan, V. V., Pal, A. J., Mayes, A. M., and Rubner, M. F. (2000). Fabrication of microporous thin films from polyelectrolyte multilayers. *Langmuir* 16, 5017–5023. doi:10.1021/la000075g
- Miramontes, E., Love, L. J., Lai, C., Sun, X., and Tsouris, C. (2020). Additively manufactured packed bed device for process intensification of CO₂ absorption and other chemical processes. *Chem. Eng. J.* 388, 124092. doi:10.1016/j.cej.2020.124092
- Mohamad, M. B., Fong, Y. Y., and Shariff, A. (2016). Gas separation of carbon dioxide from methane using polysulfone membrane incorporated with zeolite-T. *Procedia Eng.* 148, 621–629. doi:10.1016/j.proeng.2016.06.526
- Mohamed, A., Yousef, S., Tuckute, S., Tonkonogovas, A., and Stankevičius, A. (2023). Gas permeation and selectivity of polysulfone/carbon non-woven fabric membranes with sponge and finger-like structures. *Process Saf. Environ. Prot.* 171, 630–639. doi:10.1016/j.psep.2023.01.055
- Moon, J., Kim, M. Y., Kim, B. M., Lee, J. C., Choi, M.-C., and Kim, J. R. (2016). Estimation of the microbial degradation of biodegradable polymer, poly(lactic acid) (PLA) with a specific gas production rate. *Macromol. Res.* 24, 415–421. doi:10.1007/s13233-016-4060-2
- MTR (2024). A cleaner approach to carbon capture. Available at: <https://mtrccs.com/> (Accessed March 25, 2024).
- Nailwal, B. C., Goswami, N., Nair, J. P., Keshavkumar, B., Surendran, P., Gupta, A. K., et al. (2023). Polyethylene terephthalate track etched membrane for recovery of helium from helium-nitrogen system. *Express Polym. Lett.* 17, 596–609. doi:10.3144/expresspolymlett.2023.44
- Nasar, M. Q., Zohra, T., Khalil, A. T., Saqib, S., Ayaz, M., Ahmad, A., et al. (2019). *Seripheidium quetense* mediated green synthesis of biogenic silver nanoparticles and their theranostic applications. *Green Chem. Lett. Rev.* 12, 310–322. doi:10.1080/17518253.2019.1643929
- Nguyen, D., Murialdo, M., Hornbostel, K., Pang, S., Ye, C., Smith, W., et al. (2019). 3D printed polymer composites for CO₂ capture. *Ind. Eng. Chem. Res.* 58, 22015–22020. doi:10.1021/acs.iecr.9b04375
- Nikolaeva, D., Azcune, I., Tanczyk, M., Warmuzinski, K., Jaschik, M., Sandru, M., et al. (2018). The performance of affordable and stable cellulose-based poly-ionic membranes in CO₂/N₂ and CO₂/CH₄ gas separation. *J. Memb. Sci.* 564, 552–561. doi:10.1016/j.memsci.2018.07.057
- Ohya, H., Kudryavtsev, V. V., and Semenova, S. I. (2022). *Polyimide membranes*. London: Routledge. doi:10.1201/9780203742969
- Olivieri, L., Roso, M., De Angelis, M. G., and Lorenzetti, A. (2018). Evaluation of electrospun nanofibrous mats as materials for CO₂ capture: a feasibility study on functionalized poly(acrylonitrile) (PAN). *J. Memb. Sci.* 546, 128–138. doi:10.1016/j.memsci.2017.10.019
- Papchenko, K., Degli Esposti, M., Minelli, M., Fabbri, P., Morselli, D., and De Angelis, M. G. (2022). New sustainable routes for gas separation membranes: the properties of poly(hydroxybutyrate-co-hydroxyvalerate) cast from green solvents. *J. Memb. Sci.* 660, 120847. doi:10.1016/j.memsci.2022.120847
- Park, J., Kang, Z., Bender, G., Ulsh, M., and Mauger, S. A. (2020). Roll-to-roll production of catalyst coated membranes for low-temperature electrolyzers. *J. Power Sources* 479, 228819. doi:10.1016/j.jpowsour.2020.228819
- Pasichnyk, M., Stanovsky, P., Polezhaev, P., Zach, B., Šyc, M., Bobák, M., et al. (2023). Membrane technology for challenging separations: removal of CO₂,

- SO₂ and NO_x from flue and waste gases. *Sep. Purif. Technol.* 323, 124436. doi:10.1016/j.seppur.2023.124436
- Patel, R. V., Raj, G. B., Chaubey, S., and Yadav, A. (2022). Investigation on the feasibility of recycled polyvinylidene difluoride polymer from used membranes for removal of methylene blue: experimental and DFT studies. *Water Sci. Technol.* 86, 194–210. doi:10.2166/wst.2022.193
- Peelman, N., Ragaert, P., De Meulenaer, B., Adons, D., Peeters, R., Cardon, L., et al. (2013). Application of bioplastics for food packaging. *Trends Food Sci. Technol.* 32, 128–141. doi:10.1016/j.tifs.2013.06.003
- Phaechamud, T., and Chitrattha, S. (2016). Pore formation mechanism of porous poly(d,l-lactic acid) matrix membrane. *Mater. Sci. Eng. C* 61, 744–752. doi:10.1016/j.msec.2016.01.014
- Pipitone, G., and Bolland, O. (2009). Power generation with CO₂ capture: technology for CO₂ purification. *Int. J. Greenh. Gas Control* 3, 528–534. doi:10.1016/j.ijggc.2009.03.001
- Purkait, M. K., Sinha, M. K., Mondal, P., and Singh, R. (2018). "Introduction to membranes," in *Stimuli responsive polymeric membranes: smart polymeric membranes* (Cambridge, MA, USA: Academic Press), 1–37. doi:10.1016/B978-0-12-813961-5.00001-2
- Rafiq, S., Man, Z., Maulud, A., Muhammad, N., and Maitra, S. (2012). Separation of CO₂ from CH₄ using polysulfone/polyimide silica nanocomposite membranes. *Sep. Purif. Technol.* 90, 162–172. doi:10.1016/j.seppur.2012.02.031
- Randová, A., Bartovská, L., Morávek, P., Matějka, P., Novotná, M., Matějková, S., et al. (2016). A fundamental study of the physicochemical properties of Rhodiasolv®Polarclean: a promising alternative to common and hazardous solvents. *J. Mol. Liq.* 224, 1163–1171. doi:10.1016/j.molliq.2016.10.085
- Rasool, M. A., and Vankelecom, I. F. J. (2019). Use of γ -valerolactone and glycerol derivatives as bio-based renewable solvents for membrane preparation. *Green Chem.* 21, 1054–1064. doi:10.1039/C8GC03652G
- Raza, A., Farrukh, S., Hussain, A., Khan, I., Othman, M. H. D., and Ahsan, M. (2021). Performance analysis of blended membranes of cellulose acetate with variable degree of acetylation for CO₂/CH₄ separation. *Membr. (Basel)* 11, 245. doi:10.3390/membranes11040245
- Regmi, C., Ashtiani, S., Sofer, Z., and Friess, K. (2021). Improved CO₂/CH₄ separation properties of cellulose triacetate mixed-matrix membranes with CeO₂/GO hybrid fillers. *Membr. (Basel)* 11, 777. doi:10.3390/membranes11100777
- Robeson, L. M. (2008). The upper bound revisited. *J. Memb. Sci.* 320, 390–400. doi:10.1016/j.memsci.2008.04.030
- Sadeghi, M., Semsarzadeh, M. A., and Moadel, H. (2009). Enhancement of the gas separation properties of polybenzimidazole (PBI) membrane by incorporation of silica nano particles. *J. Memb. Sci.* 331, 21–30. doi:10.1016/j.memsci.2008.12.073
- Sanders, D. F., Smith, Z. P., Guo, R., Robeson, L. M., McGrath, J. E., Paul, D. R., et al. (2013). Energy-efficient polymeric gas separation membranes for a sustainable future: a review. *Polym. Guildf.* 54, 4729–4761. doi:10.1016/j.polymer.2013.05.075
- Sazali, N., Syafiq Sharip, M., Ibrahim, H., Shahir Jamaludin, A., and Norharyati Wan Salleh, W. (2020). Influence of dip-coating times towards oxygen separation performance. *IOP Conf. Ser. Mater. Sci. Eng.* 788, 012035. doi:10.1088/1757-899X/788/1/012035
- Scheepers, D., Casimiro, A., Borneman, Z., and Nijmeijer, K. (2023). Addressing specific (Poly)ion effects for layer-by-layer membranes. *ACS Appl. Polym. Mater.* 5, 2032–2042. doi:10.1021/acscpm.2c02078
- Scheepers, D., Chatillon, B., Borneman, Z., and Nijmeijer, K. (2021). Influence of charge density and ionic strength on diallyldimethylammonium chloride (DADMAC)-based polyelectrolyte multilayer membrane formation. *J. Memb. Sci.* 617, 118619. doi:10.1016/j.memsci.2020.118619
- Schmeling, N., Konietzny, R., Sieffert, D., Röling, P., and Staudt, C. (2010). Functionalized copolyimide membranes for the separation of gaseous and liquid mixtures. *Beilstein J. Org. Chem.* 6, 789–800. doi:10.3762/bjoc.6.86
- Scholes, C. A., Stevens, G. W., and Kentish, S. E. (2012). Membrane gas separation applications in natural gas processing. *Fuel* 96, 15–28. doi:10.1016/j.fuel.2011.12.074
- Shankar, K., and Kandasamy, P. (2019). Carbon dioxide separation using α -alumina ceramic tube supported cellulose triacetate-tributyl phosphate composite membrane. *Greenh. Gases Sci. Technol.* 9, 287–305. doi:10.1002/ghg.1845
- Shen, Y., and Lua, A. C. (2010). Effects of membrane thickness and heat treatment on the gas transport properties of membranes based on P84 polyimide. *J. Appl. Polym. Sci.* 116, 2906–2912. doi:10.1002/app.31810
- Sheng, M., Dong, S., Qiao, Z., Li, Q., Yuan, Y., Xing, G., et al. (2021). Large-scale preparation of multilayer composite membranes for post-combustion CO₂ capture. *J. Memb. Sci.* 636, 119595. doi:10.1016/j.memsci.2021.119595
- Shenvi, S., Ismail, A. F., and Isloor, A. M. (2014). Preparation and characterization study of PPEES/chitosan composite membrane crosslinked with tripolyphosphate. *Desalination* 344, 90–96. doi:10.1016/j.desal.2014.02.026
- Shenvi, S. S., Rashid, S. A., Ismail, A. F., Kassim, M. A., and Isloor, A. M. (2013). Preparation and characterization of PPEES/chitosan composite nanofiltration membrane. *Desalination* 315, 135–141. doi:10.1016/j.desal.2012.09.009
- Sherwood, J., De bruyn, M., Constantinou, A., Moity, L., McElroy, C. R., Farmer, T. J., et al. (2014). Dihydrolevoglucosenone (Cyrene) as a bio-based alternative for dipolar aprotic solvents. *Chem. Commun.* 50, 9650–9652. doi:10.1039/C4CC04133J
- Shi, Y., Wang, Z., Shi, Y., Zhu, S., Zhang, Y., and Jin, J. (2022). Synergistic design of enhanced π - π interaction and decarboxylation cross-linking of polyimide membranes for natural gas separation. *Macromolecules* 55, 2970–2982. doi:10.1021/acs.macromol.1c02573
- Sholl, D. S., and Lively, R. P. (2016). Seven chemical separations to change the world. *Nature* 532, 435–437. doi:10.1038/532435a
- Sing Soh, L., Uyini Hong, S., Zeng Liang, C., and Fen Yong, W. (2023). Green solvent-synthesized polyimide membranes for gas separation: coupling Hansen solubility parameters and synthesis optimization. *Chem. Eng. J.* 478, 147451. doi:10.1016/j.cej.2023.147451
- Siracusa, V., Ingrao, C., Karpova, S. G., Olkhov, A. A., and Iordanskii, A. L. (2017). Gas transport and characterization of poly(3 hydroxybutyrate) films. *Eur. Polym. J.* 91, 149–161. doi:10.1016/j.eurpolymj.2017.03.047
- SLB (2024). Cynara H2S and CO₂ separation membranes. Available at: <https://www.slb.com/products-and-services/innovating-in-oil-and-gas/well-production/processing-and-separation/gas-treatment/cynara-h2s-and-co2-separation-membranes> (Accessed March 25, 2024).
- Sokolov, S., Balynin, A., Bakhtin, D., and Borisov, I. (2021). Influence of spin coating parameters on gas transport properties of thin-film composite membranes. *Materials* 14, 5093. doi:10.3390/ma14175093
- Song, Q., Nataraj, S. K., Roussanova, M. V., Tan, J. C., Hughes, D. J., Li, W., et al. (2012). Zeolitic imidazolate framework (ZIF-8) based polymer nanocomposite membranes for gas separation. *Energy Environ. Sci.* 5, 8359. doi:10.1039/c2ee21996d
- Sridhar, S., Smitha, B., Mayor, S., Prathab, B., and Aminabhavi, T. M. (2007). Gas permeation properties of polyamide membrane prepared by interfacial polymerization. *J. Mater. Sci.* 42, 9392–9401. doi:10.1007/s10853-007-1813-5
- Suleman, M. S., Lau, K. K., and Yeong, Y. F. (2018). Enhanced gas separation performance of PSF membrane after modification to PSF/PDMS composite membrane in CO₂/CH₄ separation. *J. Appl. Polym. Sci.* 135, 201602/app.45650
- Sun, Y., Zhang, X., Zhang, M., Ge, M., Wang, J., Tang, Y., et al. (2022). Rational design of electrospun nanofibers for gas purification: principles, opportunities, and challenges. *Chem. Eng. J.* 446, 137099. doi:10.1016/j.cej.2022.137099
- Swaby, S., Ureña, N., Pérez-Prior, M. T., Várez, A., and Levenfeld, B. (2021). Synthesis and characterization of novel anion exchange membranes based on semi-interpenetrating networks of functionalized polysulfone: effect of ionic crosslinking. *Polym. (Basel)* 13, 958. doi:10.3390/polym13060958
- Takahashi, S., and Paul, D. R. (2006). Gas permeation in poly(ether imide) nanocomposite membranes based on surface-treated silica. Part I: without chemical coupling to matrix. *Polym. Guildf.* 47, 7519–7534. doi:10.1016/j.polymer.2006.08.029
- Tan, P. C., Ooi, B. S., Ahmad, A. L., and Low, S. C. (2019). Formation of a defect-free polyimide/zeolitic imidazolate framework-8 composite membrane for gas separation: in-depth analysis of organic-inorganic compatibility. *J. Chem. Technol. Biotechnol.* 94, 2792–2804. doi:10.1002/jctb.5908
- Tan, X., and Rodrigue, D. (2019). A review on porous polymeric membrane preparation. Part I: production techniques with polysulfone and poly (vinylidene fluoride). *Polym. (Basel)* 11, 1160. doi:10.3390/polym11071160
- Tashvigh, A. A., Feng, Y., Weber, M., Maletzko, C., and Chung, T.-S. (2019). 110th anniversary: selection of cross-linkers and cross-linking procedures for the fabrication of solvent-resistant nanofiltration membranes: a review. *Ind. Eng. Chem. Res.* 58, 10678–10691. doi:10.1021/acs.iecr.9b02408
- Tekin, F. S., and Çulfaz-Emecen, P. Z. (2023). Controlling cellulose membrane performance via solvent choice during precursor membrane formation. *ACS Appl. Polym. Mater.* 5, 2185–2194. doi:10.1021/acscpm.2c02185
- Thakkar, H., Lawson, S., Rownaghi, A. A., and Rezaei, F. (2018). Development of 3D-printed polymer-zeolite composite monoliths for gas separation. *Chem. Eng. J.* 348, 109–116. doi:10.1016/j.cej.2018.04.178
- Thiam, B. G., El Magri, A., Vanaci, H. R., and Vaudreuil, S. (2022). 3D printed and conventional membranes-A review. *Polym. (Basel)* 14, 1023. doi:10.3390/polym14051023
- Tian, Z., Cao, B., and Li, P. (2018). Effects of sub-Tg cross-linking of triptycene-based polyimides on gas permeation, plasticization resistance and physical aging properties. *J. Memb. Sci.* 560, 87–96. doi:10.1016/j.memsci.2018.05.018
- Tiseo, I. (2023). *Annual carbon dioxide (CO₂) emissions worldwide from 1940 to 2023*. Hamburg: Statista.
- Torre-Celeizabal, A., Casado-Coterillo, C., Gomis-Berenguer, A., Iniesta, J., and Garea, A. (2023). Chitosan-based mixed matrix composite membranes for CO₂/CH₄ mixed gas separation. Experimental characterization and performance validation. *Sep. Purif. Technol.* 325, 124535. doi:10.1016/j.seppur.2023.124535

- Tousley, M. E., Shaffer, D. L., Lee, J.-H., Osuji, C. O., and Elimelech, M. (2016). Effect of final monomer deposition steps on molecular layer-by-layer polyamide surface properties. *Langmuir* 32, 10815–10823. doi:10.1021/acs.langmuir.6b02746
- Ulbricht, M. (2019). “Smart polymeric membranes with magnetic nanoparticles for switchable separation,” in *Smart membranes* (London, United Kingdom: The Royal Society of Chemistry), 297–328. doi:10.1039/9781788016377-00297
- USDOE, D. (2005). Materials for separation technologies. Energy and emission reduction opportunities. *Energy Emiss. Reduct. Oppor.* doi:10.2172/1218755
- Vakharia, V., Salim, W., Wu, D., Han, Y., Chen, Y., Zhao, L., et al. (2018). Scale-up of amine-containing thin-film composite membranes for CO₂ capture from flue gas. *J. Memb. Sci.* 555, 379–387. doi:10.1016/j.memsci.2018.03.074
- Van Der Sluis, J. P., Hendriks, C. A., and Blok, K. (1992). Feasibility of polymer membranes for carbon dioxide recovery from flue gases. *Energy Convers. Manag.* 33, 429–436. doi:10.1016/0196-8904(92)90040-4
- Wang, L., Cao, Y., Zhou, M., Zhou, S. J., and Yuan, Q. (2007). Novel copolyimide membranes for gas separation. *J. Memb. Sci.* 305, 338–346. doi:10.1016/j.memsci.2007.08.024
- Wang, M., Wang, Z., Li, S., Zhang, C., Wang, J., and Wang, S. (2013). A high performance antioxidant and acid resistant membrane prepared by interfacial polymerization for CO₂ separation from flue gas. *Energy Environ. Sci.* 6, 539–551. doi:10.1039/c2ee23080a
- Wang, X., Xiao, C., Pan, J., Hu, X., and Huan, G. (2017). Recycled performance of waste polyvinylidene fluoride hollow fiber membrane. *Gaofenzi Cailiao Kexue Yu Gongcheng/Polymeric Mater. Sci. Eng.* 33, 107–113. doi:10.16865/j.cnki.1000-7555.2017.04.019
- Widakdo, J., Huang, T. J., Subrahmanya, T. M., Austria, H. F. M., Chou, H. L., Hung, W. S., et al. (2022). Bioinspired ionic liquid-graphene based smart membranes with electrical tunable channels for gas separation. *Appl. Mater. Today* 27, 101441. doi:10.1016/j.apmt.2022.101441
- Wind, J. D., Staudt-Bickel, C., Paul, D. R., and Koros, W. J. (2002). The effects of crosslinking chemistry on CO₂ plasticization of polyimide gas separation membranes. *Ind. Eng. Chem. Res.* 41, 6139–6148. doi:10.1021/ie0204639
- Wojnarova, P., Rusin, J., Basinas, P., Kostejn, M., Nemec, J., Stanovsky, P., et al. (2023). Unveiling the potential of composite water-swollen spiral wound membrane for design of low-cost raw biogas purification. *Sep. Purif. Technol.* 326, 124783. doi:10.1016/j.seppur.2023.124783
- Wong, J. E., Díez-Pascual, A. M., and Richtering, W. (2009). Layer-by-Layer assembly of polyelectrolyte multilayers on thermoresponsive P(NiPAM-co-maa) microgel: effect of ionic strength and molecular weight. *Macromolecules* 42, 1229–1238. doi:10.1021/ma802072c
- Wright, C. T., and Paul, D. R. (1997). Gas sorption and transport in UV-irradiated polyarylate copolymers based on tetramethyl bisphenol-A and dihydroxybenzophenone. *J. Memb. Sci.* 124, 161–174. doi:10.1016/S0376-7388(96)00215-3
- Wu, B., Li, X., An, D., Zhao, S., and Wang, Y. (2014). Electro-casting aligned MWCNTs/polystyrene composite membranes for enhanced gas separation performance. *J. Memb. Sci.* 462, 62–68. doi:10.1016/j.memsci.2014.03.015
- Wu, J., and Yuan, Q. (2002). Gas permeability of a novel cellulose membrane. *J. Memb. Sci.* 204, 185–194. doi:10.1016/S0376-7388(02)00037-6
- Xiao, S., Feng, X., and Huang, R. Y. M. (2007). Trimesoyl chloride crosslinked chitosan membranes for CO₂/N₂ separation and pervaporation dehydration of isopropanol. *J. Memb. Sci.* 306, 36–46. doi:10.1016/j.memsci.2007.08.021
- Xiao, Y., Low, B. T., Hosseini, S. S., Chung, T. S., and Paul, D. R. (2009). The strategies of molecular architecture and modification of polyimide-based membranes for CO₂ removal from natural gas—a review. *Prog. Polym. Sci.* 34, 561–580. doi:10.1016/j.progpolymsci.2008.12.004
- Xu, D., and Wang, K. (2008). Chitosan membrane in separation applications. *Mater. Sci. Technol.* 24, 1076–1087. doi:10.1179/174328408X341762
- Xu, S., Ren, X., Zhao, N., Wu, L., Zhang, Z., Fan, Y., et al. (2021a). Self-crosslinking of bromomethylated 6FDA-DAM polyimide for gas separations. *J. Memb. Sci.* 636, 119534. doi:10.1016/j.memsci.2021.119534
- Xu, S., Zhou, H., Jia, H., Xu, J., Liu, D., Zhang, M., et al. (2021b). Preparation and high CO₂/CH₄ selectivity of ZSM-5/Ethyl cellulose mixed matrix membranes. *Mater. Res. Express* 8, 026403. doi:10.1088/2053-1591/abe321
- Xu, X., Wang, J., Zhou, A., Dong, S., Shi, K., Li, B., et al. (2021c). High-efficiency CO₂ separation using hybrid LDH-polymer membranes. *Nat. Commun.* 12, 3069. doi:10.1038/s41467-021-23121-z
- Xu, Y., Chen, C., Zhang, P., Sun, B., and Li, J. (2006). Pervaporation properties of polyimide membranes for separation of ethanol + water mixtures. *J. Chem. Eng. Data* 51, 1841–1845. doi:10.1021/je060208l
- Yamasaki, A., Tyagi, R. K., Fouda, A. E., Matsuura, T., and Jonasson, K. (1999). Effect of solvent evaporation conditions on gas separation performance for asymmetric polysulfone membranes. *J. Appl. Polym. Sci.* 71, 1367–1374. doi:10.1002/(SICI)1097-4628(19990228)71:9<1367::AID-APP2>3.0.CO;2-H
- Yan, N., Capezzuto, F., Lavorgna, M., Buonocore, G. G., Tescione, F., Xia, H., et al. (2016). Borate cross-linked graphene oxide–chitosan as robust and high gas barrier films. *Nanoscale* 8, 10783–10791. doi:10.1039/C6NR00377J
- Yang, H.-C., Hou, J., Chen, V., and Xu, Z.-K. (2016). Surface and interface engineering for organic-inorganic composite membranes. *J. Mater. Chem. A Mater.* 4, 9716–9729. doi:10.1039/C6TA02844F
- Yang, J., Tao, L., He, J., McCutcheon, J. R., and Li, Y. (2022). Machine learning enables interpretable discovery of innovative polymers for gas separation membranes. *Sci. Adv.* 8, eabn9545. doi:10.1126/sciadv.abn9545
- Yang, T., Wan, C. F., Zhang, J., Gudipati, C., and Chung, T.-S. (2021). Optimization of interfacial polymerization to fabricate thin-film composite hollow fiber membranes in modules for brackish water reverse osmosis. *J. Memb. Sci.* 626, 119187. doi:10.1016/j.memsci.2021.119187
- Yerzhankyy, A., Wang, Y., Ghanem, B. S., Puspasari, T., and Pinna, I. (2022). Gas separation performance of solid-state in-situ thermally crosslinked 6FDA-based polyimides. *J. Memb. Sci.* 641, 119885. doi:10.1016/j.memsci.2021.119885
- Yoo, M. J., Kim, K. H., Lee, J. H., Kim, T. W., Chung, C. W., Cho, Y. H., et al. (2018). Ultrathin gutter layer for high-performance thin-film composite membranes for CO₂ separation. *J. Memb. Sci.* 566, 336–345. doi:10.1016/j.memsci.2018.09.017
- Žák, M., Bendová, H., Friess, K., Bara, J. E., and Izák, P. (2018). Single-step purification of raw biogas to biomethane quality by hollow fiber membranes without any pretreatment – an innovation in biogas upgrading. *Sep. Purif. Technol.* 203, 36–40. doi:10.1016/j.seppur.2018.04.024
- Zarca, G., Urtiaga, A., Biegler, L. T., and Ortiz, I. (2018). An optimization model for assessment of membrane-based post-combustion gas upcycling into hydrogen or syngas. *J. Memb. Sci.* 563, 83–92. doi:10.1016/j.memsci.2018.05.038
- Zargar, V., Asghari, M., and Afsari, M. (2019). Gas separation properties of swelled nanocomposite chitosan membranes cross-linked by 3-aminopropyltriethoxysilane. *Int. J. Environ. Sci. Technol.* 16, 37–46. doi:10.1007/s13762-017-1554-1
- Zargar, V., Asghari, M., and Dashti, A. (2015). A review on chitin and chitosan polymers: structure, chemistry, solubility, derivatives, and applications. *ChemBioEng Rev.* 2, 204–226. doi:10.1002/cben.201400025
- Zhang, S., Shen, L., Deng, H., Liu, Q., You, X., Yuan, J., et al. (2022). Ultrathin membranes for separations: a new era driven by advanced nanotechnology. *Adv. Mater.* 34, 2108457. doi:10.1002/adma.202108457
- Zhang, Y., Xin, J., Huo, G., Zhang, Z., Zhou, X., Bi, J., et al. (2023). Cross-linked PI membranes with simultaneously improved CO₂ permeability and plasticization resistance via tuning polymer precursor orientation degree. *J. Memb. Sci.* 687, 121994. doi:10.1016/j.memsci.2023.121994
- Zhang, Y., Zhang, Y., Wang, X., Yu, J., and Ding, B. (2018). Ultrahigh metal-organic framework loading and flexible nanofibrous membranes for efficient CO₂ capture with long-term, ultrastable recyclability. *ACS Appl. Mater. Interfaces* 10, 34802–34810. doi:10.1021/acsami.8b14197
- Zhao, S., Caruso, F., Dähne, L., Decher, G., De Geest, B. G., Fan, J., et al. (2019). The future of layer-by-layer assembly: a tribute to *acs nano* associate editor helmuth möhwal. *ACS Nano* 13, 6151–6169. doi:10.1021/acs.nano.9b03326
- Zhu, B., Jiang, X., He, S., Yang, X., Long, J., Zhang, Y., et al. (2020). Rational design of poly(ethylene oxide) based membranes for sustainable CO₂ capture. *J. Mater. Chem. A Mater.* 8, 24233–24252. doi:10.1039/D0TA08806D
- Zou, X., and Zhu, G. (2020). Microporous materials for separation membranes. *Chromatographia* 83, 1561–1562. doi:10.1007/s10337-020-03968-y



OPEN ACCESS

EDITED BY

Nalan Kabay,
Ege University, Türkiye

REVIEWED BY

Zhongyun Liu,
Georgia Institute of Technology, United States
Aydın Cihanoğlu,
Ege University, Türkiye
Enver Güler,
Atılım University, Türkiye

*CORRESPONDENCE

Anna Siekierka,
✉ anna.siekierka@pwr.edu.pl

RECEIVED 23 February 2024

ACCEPTED 08 April 2024

PUBLISHED 02 May 2024

CITATION

Muratow M, Yalcinkaya F, Bryjak M and
Siekierka A (2024), Surface-modified PVDF
membranes for separation of dye by
forward osmosis.
Front. Membr. Sci. Technol. 3:1390727.
doi: 10.3389/frmst.2024.1390727

COPYRIGHT

© 2024 Muratow, Yalcinkaya, Bryjak and
Siekierka. This is an open-access article
distributed under the terms of the [Creative
Commons Attribution License \(CC BY\)](#). The use,
distribution or reproduction in other forums is
permitted, provided the original author(s) and
the copyright owner(s) are credited and that the
original publication in this journal is cited, in
accordance with accepted academic practice.
No use, distribution or reproduction is
permitted which does not comply with these
terms.

Surface-modified PVDF membranes for separation of dye by forward osmosis

Marta Muratow¹, Fatma Yalcinkaya², Marek Bryjak¹ and
Anna Siekierka^{1*}

¹Wrocław University of Science and Technology, Faculty of Chemistry, Wrocław, Poland, ²Technical University of Liberec, Faculty of Mechatronics, Liberec, Czechia

Modification of membranes is widely used for altering their separation properties. In this study, the modification of PVDF nanofiber mat by deposition of polyamide layers was evaluated to improve dye recovery by means of forward osmosis process. The polyamide active layer was prepared by a reaction of cyclic aromatic amines, m-phenylenediamine, or piperazine, and trimesoylchloride. The modification progress was monitored by FTIR analysis, water uptake, nitrogen content, and grafting yields. Investigated membranes showed an excellent dye separation features with water flux and dye fluxes strongly related to type of applied amines and reaction time. The best obtained membrane demonstrated outstanding performance in forward osmosis; their water flux was 3.3 LMH and rejection rate of 97% for bromocresol green dye. The membrane allowed increase dye concentration by 50% after 24 h of the process.

KEYWORDS

PVDF, dye concentration, forward osmosis, piperazine, phenylenediamine

1 Introduction

Wastewaters from industrial sources, containing a combination of organic compounds and salts, pose ongoing challenges in meeting goals for minimal or zero liquid discharge, as well as resource recovery (Li et al., 2023). Treating such wastewater streams is significantly challenged by elevated content of organic compound, which can hinder the effectiveness of traditional methods like advanced oxidation processes, biological treatments, carbon adsorption, membrane separation, and UV ozonation (Lin et al., 2020). Among the mentioned methods, membrane separation is extensively utilized due to its straightforward operation, minimal chemical requirements, and comprehensive removal of pollutants across varying sizes. Nevertheless, the traditional pressure-driven membrane separation techniques rely on hydraulic pressure application, leading to drawbacks such as heightened fouling susceptibility, increased cleaning frequency, and shortened membrane lifespan. Hence, there is a critical need for the development of innovative membrane technologies to address these challenges (Zhao et al., 2015).

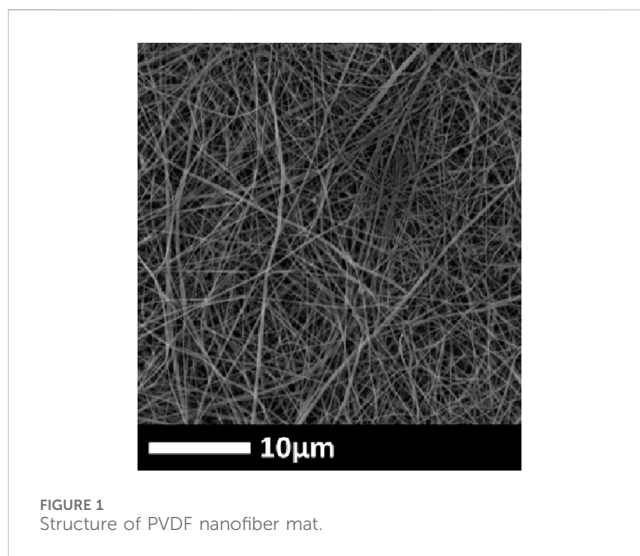
Forward osmosis (FO), a membrane process driven by osmotic forces, has emerged as a viable alternative for water and wastewater treatment. FO, unlike reverse osmosis, offers numerous potential advantages, including reduction of operating pressure and a decreasing of fouling phenomenon (Peng et al., 2020). Presently, thin film composite (TFC) polyamide membranes are widely utilized in forward osmosis applications (Fam et al., 2014; Huang and McCutcheon, 2015; Alihemati et al., 2020). Existing literature predominantly highlights their critical attribute of high salt rejection, particularly concerning NaCl. However, this

high salt rejection often accompanies reduced water permeability due to an inherent tradeoff. Moreover, the retention of salts from the feed solution can lead to their accumulation, thereby diminishing the osmotic driving force and subsequently lowering the FO water flux (Peng et al., 2020). While salt rejection remains a crucial parameter for desalination-focused applications, its significance may not be as pronounced for forward osmosis processes employed for non-desalination purposes. As an example, in the pretreatment stage of seawater desalination with forward osmosis, the primary objective should be the removal of algae and scalants (such as calcium and magnesium sulfates) to mitigate the potential risks of biofouling and scaling in the subsequent reverse osmosis process (Achilli et al., 2009). In an osmotically-driven membrane bioreactor, a high level of salt rejection could paradoxically diminish bioactivity, which is undesirable for the process. (Achilli et al., 2009; Xiao et al., 2011; Qiu and Ting, 2013). It is presumed that an ideal forward osmosis membrane should be tailored and fine-tuned to suit specific applications, allowing for the selective retention or recovery of valuable compounds.

Recent research has directed attention towards various polymer materials utilized in the fabrication of forward osmosis membranes. These materials include cellulose derivatives, polyamide, various polyelectrolyte, and polybenzimidazole (Alihemati et al., 2020). Cellulose derivatives like cellulose triacetate membranes are produced as flat sheets and hollow fibers using the phase inversion process followed by heat treatment. Nonetheless, the traditional thin film composite reverse osmosis membrane, featuring a hydrophobic phase-inversion polysulfone supporting layer and a thick nonwoven fabric backing layer, has consistently underperformed in forward osmosis trials due to significant mass transfer resistance near the interface of the selective thin film layer (Huang et al., 2016).

Electrospun nanofibers represent a category of material characterized by inherently high porosity and an interconnected pore structure (Yalcinkaya et al., 2017; Torres-Mendieta et al., 2020; Havelka et al., 2023). These distinctive attributes render nanofiber mats highly favorable as potential support materials for thin film composite forward osmosis (TFC-FO) membranes. A membrane material intended for forward osmosis applications should possess hydrophilic properties along with robust thermal and chemical resistance, as well as exceptional mechanical strength. The utilization of PVDF in the fabrication of TFC-FO membranes is advocated due to its outstanding thermal, mechanical, and chemical characteristics (Ndiaye et al., 2022).

In this study, the polyamide thin film composite PVDF membranes, received by reactions of TMC and MPDA, or TMC and PIP, were explored. The chemical and physical analyses of prepared membranes were done. They included the functional groups' analysis, water content, nitrogen content, or grafting yields. Systematic investigations of FO separation performance including water permeability, dye rejection, and dye concentration were performed. The



outcomes of the studies broaden the scope of applications for forward osmosis-based separation processes, particularly before desalination. They might stimulate the development of innovative membranes capable for highly selective rejection of target solutes tailored for some specific applications.

2 Materials and methods

2.1 Materials

Hexane, 97%, piperazine (PIP), 99%, 1,3,5-Benzenetricarbonyl chloride (Trimesoylchloride-TMC), 97%, m-phenylenediamine (MPDA) were delivered by Sigma- Aldrich. D-(+)- glucose and bromocresol green were delivered by POCH, Poland.

2.2 PVDF nanofibers preparation

The nanofibers were prepared through direct current (+55 kV, -15 kV) electrospinning of PVDF (13 wt%, Solef 1015) dissolved in N, N-dimethylformamide (DMF, Penta s. r.o.). The electrospinning process was performed using an electrospinning system (Nanospider, NS 8S1600U, Elmarco), and the produced nanofibers were collected over silicone paper. Secondly, the fibers were laminated over a spun-bond polyethylene terephthalate (PET) nonwoven fabric (100 g m⁻²) previously coated with a 12 g m⁻² co-polyamide adhesive web (Protechnic, Cernay, France). Finally, a heat press (HLV 150, Pracovní stroje Teplice s. r.o.) was employed to promote the lamination process at 130°C and 50 kN for 3 min, resulting in a proper union between the nanofiber net and the support. The SEM image of pristine PVDF is shown in Figure 1.

TABLE 1 Nitrogen content for investigated membranes.

Sample	PVDF	PVDF-PDA-1min	PVDF- PDA-2 min	PVDF-PIP-1 min	PVDF-PIP-2 min
Z _n [mmol/g]	0	0.13	0.25	0.19	0.22

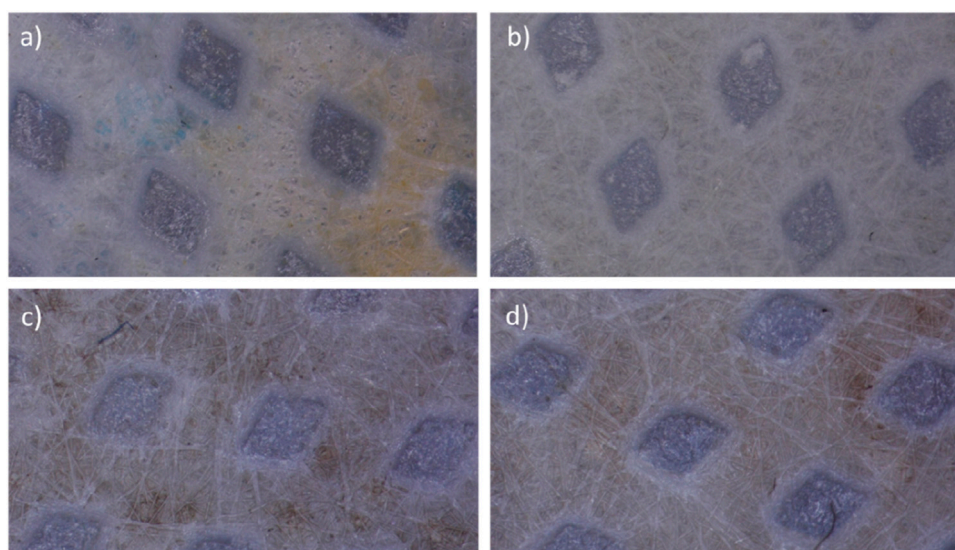


FIGURE 2
Modified membranes PVDF by PDA by (A) 1 min and (B) 2 min, by piperazine by (C) 1 min and (D) 2 min (x40 magnification).

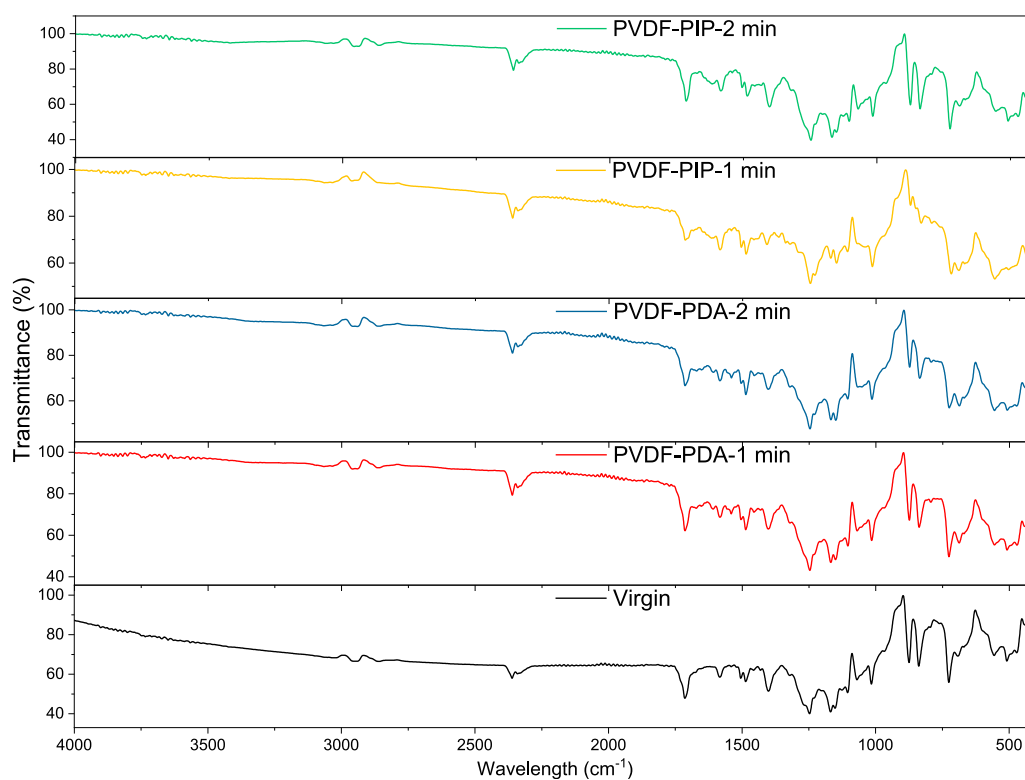


FIGURE 3
FTIR spectra from investigated membranes.

The previous findings demonstrated that laminated composite PVDF nanofiber membranes had a notable tensile strength of 133 N/5 cm in the machine direction and 107 N/5 cm in the counter direction (Islam et al., 2022). Moreover,

the membranes demonstrated enhanced chemical resistance when subjected to extreme acidic and basic conditions, as well as a range of chemical agents (Gul et al., 2022; Havelka et al., 2023).

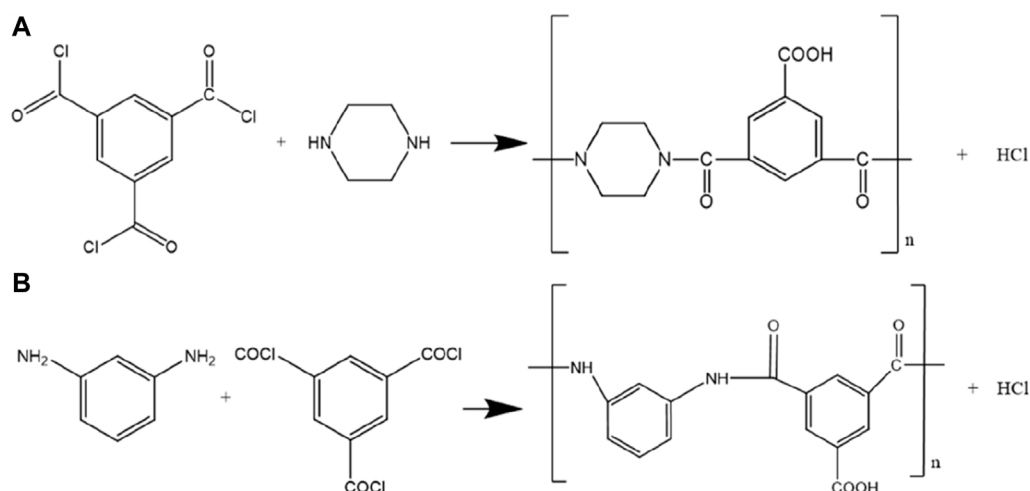


FIGURE 4
Reactions between TMC and (A) PIP, (B) MPDA.

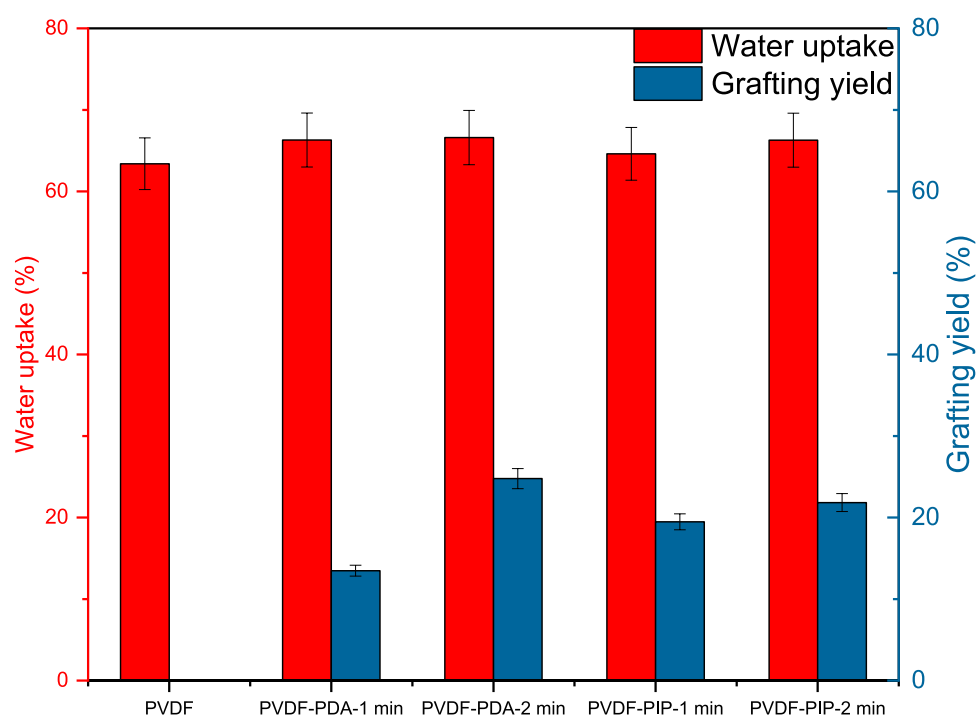


FIGURE 5
Water uptake and grafting yield of the investigated membranes.

2.3 FO membrane preparation

Laminated PVDF nanofibers were modified separately by PIP and MPDA. Firstly, The PVDF nanofibers were immersed in 4 wt% PIP or MPDA for 2 min. Then the soaked membranes were immersed in TMC (0.5% wt. in hexene) for 1 or 2 min. In the next step, membranes were put to an oven kept there for 8 min at 80°C. After that, four different membranes were obtained. They were encoded as PVDF-PIP-1, PVDF-PIP-2,

PVDF-MPDA-1, and PVDF-MPDA-2. Here, PIP-1, PIP-2, MPDA-1, and MPDA-2 describe used diamine and time of reaction.

2.4 FO process and calculations

The process of concentration was conducted in the flowing FO module. The peristaltic pump Jebao auto dosing pump was

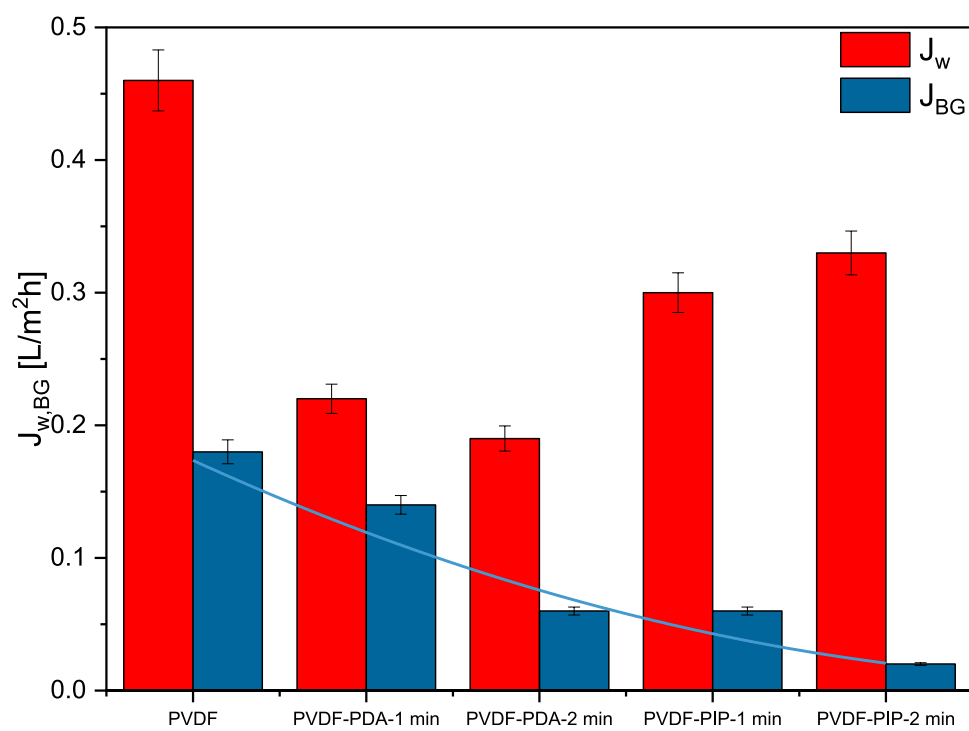


FIGURE 6
Intrinsic separation properties of TFC PVDF membranes: water flux and BG flux for investigated membranes.

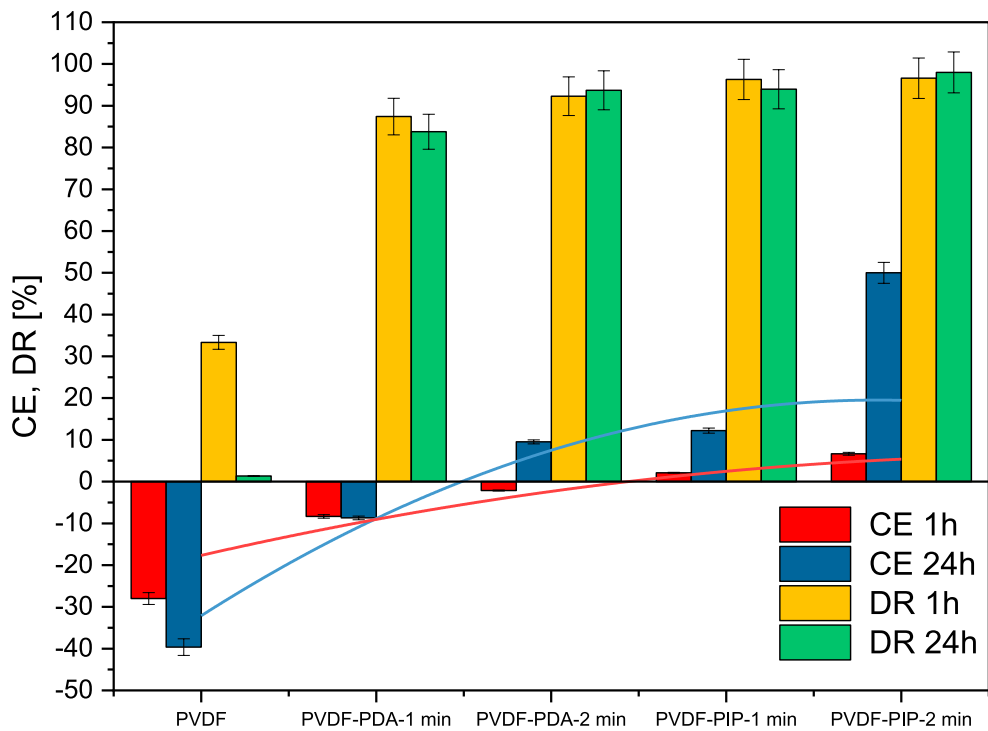


FIGURE 7
Concentration efficiency (CE) and dye rejection (DR) for investigated membrane at various time of FO process.

TABLE 2 FO performance benchmarks of TFC PVDF membranes with different modification paths.

Support	Active layer	Type of compound	Compound flux	Water flux	Ref.
			g/m ² h	L/m ² h	
PVDF/PAN	TMC + MPDA	NaCl	1.9	32.7	Ndiaye et al. (2022)
PVDF	TMC + MPDA	NaCl	8	33	Kallem et al. (2021)
PVDF/PAN	TMC + MPDA	NaCl	3.5	25	Park et al. (2018)
PVDF/GO/MWCNTs	TMC + MPDA	NaCl	1.1	0.34	Yu et al. (2020)
CA/PVDF	TMC + MPDA	NaCl	1.8	32	Shibuya et al. (2018)
PVDF	TMC + MPDA + PEI	MgCl ₂	0.03	1.27	Liu et al. (2017)
PVDF/PFSA	TMC + MPDA	NaCl	7.5	51	Zhang et al. (2017)
PVDF	TMC + MPDA	NaCl	2.33	3.15	Tian et al. (2013)
PVDF/Nylon 6,6	TMC + MPDA	NaCl	27	50	Huang et al. (2016)
PVDF/bentonite	TMC + MPDA	NaCl	5.22	40.64	Shah et al. (2020)
PVDF/SiO ₂ /MWCNTs	TMC + MPDA	NaCl	9	30	Zhang et al. (2018)
PVDF/PDA-PEI	TMC + MPDA	malachite green + NaCl	0.60	29.98	Hu et al. (2021)
PVDF/PMMA + PA-GQD	TMSCI + MDA	Methylene blue, Congo red, NaCl, Mg(NO ₃) ₂	-	170.00	Maiti et al. (2020)
PANI@PAN/PVDF	TMC + MPDA	acid red GR + NaCl	-	40.10	Zhou et al. (2023)
PVD	TMC + DA-PEI	Tannic acid + taurine	0.055	42.10	Li et al. (2022)
PVDF	TMC + MPDA-2min	Glucose	0.6	1.9	This work
PVDF	TMC + PIP-2min	Glucose	0.2	3.3	This work

employed for continuous move of draw and feed solutions with flow rate of 6L/h. As a draw solution, the 10% wt. glucose was applied, while the feed solution was 1% wt. of bromocresol green. The FO process was conducted according to Al-FS strategy, where the active site of prepared membranes is attached to the feed solution. The crucial parameters belonging to the FO are water flux (1), bromocresol green (BG) flux (2), and concentration efficiency (CE). They are given by the following equations:

$$J_w = \frac{\Delta V}{A_m \cdot t} \left[\frac{L}{m^2 \cdot h} \right]$$
(1)

$$J_{BG} = \frac{\Delta V_{BG}}{A_m \cdot t} \left[\frac{L}{m^2 \cdot h} \right],$$
(2)

$$CE = \frac{C_{BG}(t)}{C_{BG}(0)}$$
(3)

$$DR = \left(1 - \frac{C_{BG,drawn}}{C_{BG,feed}} \right) \cdot 100\%$$
(4)

ΔV –volume of water [cm³].
 ΔV_{BG} –volume of BG [cm³].
 A_m –active area of membranes, 13.5 cm².
 t –time [h].
 C_{BG} –concentration of BG in particular time [g/L].

2.5 Material analysis

2.5.1 Optical microscopy

A TECHREBAL stereo optical microscope was employed for microscopic analysis of the membrane surface. Images of the active layer were captured using the built-in camera within the device.

2.5.2 Fourier transform infrared spectroscopy (FTIR)

Fourier transform infrared spectroscopy (FTIR) in the 4000–400 cm^{−1} range was carried out using a Jasco 4700 spectrometer equipped with a horizontal attenuated total reflection (ATR) device to identify the functional groups in polymer films. Each analysis involved the accumulation of 64 scans.

2.5.3 Analytical section

Water uptake $W_{H_2O} \left[\frac{g_{H_2O}}{g} \right]$ was calculated according Eq. 5:

$$W_{H_2O} = \frac{(m_{wet} - m_{dry})}{m_{dry}}$$
(5)

where m_w is the weight of swollen membrane and m_d is the weight of the dry membrane.

Nitrogen content (Z_N) was determined by Kjeldahl's method after mineralization of the sample (about 200 mg) in concentrated sulphuric acid with copper and potassium sulfates (Table 1).

Grafting yields (G_y) was determined as a balance ration between dry membranes and those after modification, also in dry state. The G_y is express as follows:

$$G_y = \frac{m_{modif,dry} - m_{unmodif,dry}}{m_{unmodif,dry}} \cdot 100\% \quad (6)$$

Water contact angle (WCA) of the PVDF before modification has been taken by using The Krüss Drop Shape Analyser DS4 (Krüss GmbH, Hamburg, Germany) against distilled water (surface tension 72.0 mN m⁻¹). Following modification, the samples were maintained in a moist state to maintain the activity of functional groups. As a consequence, the WCA was not measured. The complete submersion of the samples in water demonstrates that the membranes are superhydrophilic.

3 Results and discussions

3.1 Physical and chemical characterization of membranes

The physical structure of membranes PVDF are presented at Figure 2. It could be noticed that after modification, the layer of polymerized TMC with MPDA or PIP are visible.

To confirm modification of PVDF nanofibers, the FTIR measurements were performed. The results are presented in Figure 3. The region exhibiting a peak at 875 cm⁻¹ represents the characteristic region for C-H bonds. Similarly, the region at 1015 cm⁻¹ corresponds to C-F bonds. Hence, those peaks confirm the presence of PVDF polymer (Casciola et al., 2005; Pereira et al., 2018).

According to the reactions between TMC with MPDA and PIP, the following specific groups should be found: NH (associated with the aromatic rings), -CNHO (amide groups), -C=O (ketone groups), and -COOH (carboxylic groups). The region displaying a peak at 726 cm⁻¹ is indicative of N-H bonds. At 875 cm⁻¹, the peak is attributed to C-H bonds. The region with a peak at 1015 cm⁻¹ corresponds to C-O bonds, at 1168 cm⁻¹ to C-N amino groups, at 1246 cm⁻¹ to R-COOH carboxyl groups. Furthermore, at a wavelength of 1401 cm⁻¹, the peak is associated with carbons in C-C aromatics while at region of 1650 cm⁻¹ with the amide groups (Sizeland et al., 2018; Ji et al., 2020). Finally, the region at 1713 cm⁻¹ attributes to ketone bond, C=O. Hence, the presented spectra confirm the reactions between the TMC and PDA, and between TMC and PIP, respectively. Figure 4 depicted the reaction between TMC with PIP and TMC with MPA.

The final parameters describing the performance of obtained membranes are water uptake and grafting yield (G_y). Initially, G_y reflects the effectiveness of modification and the accumulation of polyamide groups on the surface of pristine PVDF. Based on the obtained data, it should be noted t modification efficiency exceeded 10% in all cases. The highest G_y was observed for the reaction of TMC and MPDA for 2 min. Additionally, for PIP modification, a prolonged reaction time resulted in the highest G_y .

The next aspect to be considered is water uptake, a parameter intricately linked to the porosity of PVDF nanofibers. While incorporation of polyamide groups, along with their associated amine groups, may influence water uptake to some extent, the overall change is not so significant. The most notable change occurred for PVDF-PDA-2 min, resulting in a 3.3% increase in water uptake. This observation is directly attributed to the hydrophilic nature of MPDA and PIP, as depicted in Figure 5 (Yang, 2020).

The WCA of the pristine PVDF composite nanofiber membrane was measured to be 90.40° ± 3.40°, indicating that it is hydrophobic. PVDF nanofibers typically exhibit higher hydrophobicity since fluoropolymers usually exhibit low surface energy (Liao et al., 2013; Sethupathy et al., 2013; Rafael et al., 2022). The composite hydrophilicity was altered as a result of the utilisation of co-polyamide adhesives.

The final parameter associated with the analysis of the membranes is nitrogen content. The amount of nitrogen is directly linked to the chemical reaction between TMC and aromatic amines. After a 1-min modification in both cases, the Zn levels ranged from 0.13 to 0.19 mmol/g. Increasing the modification time to 2 min resulted in significantly higher Zn value. The successful modification of PVDF is confirmed by the nitrogen content in all investigated cases.

3.2 Forward osmosis investigations

3.2.1 Transport of water and dye by membranes

Water flux and salt rejection factors serve as the most valuable tools for characterizing the properties of TFC membranes. Figure 6 illustrates the impact of various amines and reaction times between them and TMC. It can be observed that water permeability decreased from 0.46 L/m²h for virgin PVDF to 0.19 L/m²h for PVDF-PIP-2min, while dye flux decreased from 0.18 L/m²h for virgin PVDF to 0.02 L/m²h for PVDF-PIP-2min.

Comparing the different types of amines, the nitrogen linked to the cyclic aromatic ring result in a denser layer, as seen in the case of PDA. This phenomenon is evident in the tendency for lower dye fluxes in PVDF-PIP compared to PVDF-PDA. Additionally, the water flux exhibits significantly higher values, with an increase of over 36% and 74% for PVDF-PIP-1min and PVDF-PIP-2min, respectively. The separation properties of the ultrathin polyamide film synthesized via interfacial polymerization are greatly affected by polymerization conditions, including the type of aromatic amines and reaction times. Variations in water flux can be attributed to the differences in structure, morphology, surface properties, and chemistry observed between membranes based on PDA and those based on PIP. Although membranes based on PDA may have reduced water flux as a result of their denser selective layer, membranes based on PIP generally exhibit enhanced water permeability owing to their porous structure.

3.2.2 Concentration of dye by investigated membranes

The forward osmosis performance of TFC PVDF membranes was investigated for its potential to concentrate bromocresol green (BG) dye in the feed solution. The results are presented in Figure 7. In the case of virgin PVDF, it is evident that there was no noticeable

concentration effect of BG. During the FO process, the solution became diluted due to the mixing of liquids. The dye rejection was observed only at the beginning of the process, while the effect disappeared later on. Such phenomenon was expected due to the high porosity of the PVDF nanofibers. In the case of TFC membranes, the dye rejection increased significantly from 33% for PVDF nanofibers to up to 96.6% for PVDF-PIP-2min. However, in the case of PVDF-MPDA-1min, the effect of concentrating BG was not observed. The system prevented BG penetration through the membranes; however, it was unable to extract water. By increasing the reaction time of TMC and MPDA one observed a concentration efficiency of 9.5%.

Replacing the cyclic amines from MPDA to PIP resulted in achieving a dye rejection (DR) of over 90% in all PVDF-PIP cases. The most significant differences were observed in the concentration efficiency (50% for PVDF-PIP-2min membrane. Additionally, dye rejection reached the value of at 98% for this membrane.

4 Comparison to other membranes

The modified PVDF-MPDA and PVDF-PIP membranes are compared with other lab-scale nanofiber PVDF FO membranes. As shown in Table 2, our TFC membrane exhibited comparable water flux and specific salt flux to other nanofiber-based TFC membranes. Interestingly, the modified PVDF-MPDA and PVDF-PIP membranes exhibited the lowest dye flux in the majority of comparable systems. Only PVDF modified by PEI also exhibited a low dye flux of 0.03 g/m²h. With increasing water flux, the salt and other compound flux also rise. This is a general tendency observed for TFC FO membranes. Here, the water flux is limited to only 3.3 L/m²h; however, this system can effectively block BG with a back flux of 0.2 g/m²h.

5 Conclusion

This study investigates the feasibility of using surface-modified hydrophobic PVDF nanofibers as the support for preparation of TFC-FO membrane. In this work, polyamide thin films were synthesized by a reaction between TMC and MPDA and PIP. The type of aromatic amines and time of reaction between them and TMC have a significantly impact on the modification paths and their FO performances. The modification reactions were confirmed by the visibility of characteristic groups at FTIR analysis. The chemical analysis confirmed the presence of nitrogen and grafting yields. The PVDF-PIP-2min exhibited excellent FO performance with water flux at 3.3 LMH and bromocresole green dye rejection at 97% with the possibility to 50% concentrate this dye after 24 h of operation.

References

- Achilli, A., Cath, T. Y., Marchand, E. A., and Childress, A. E. (2009). The forward osmosis membrane bioreactor: a low fouling alternative to MBR processes. *Desalination* 239, 10–21. doi:10.1016/j.desal.2008.02.022
- Alihemati, Z., Hashemifard, S. A., Matsuura, T., Ismail, A. F., and Hilal, N. (2020). Current status and challenges of fabricating thin film composite forward osmosis membrane: a comprehensive roadmap. *Desalination* 491, 114557. doi:10.1016/j.desal.2020.114557

Data availability statement

The raw data supporting the conclusions of this article will be made available by the authors, without undue reservation. The raw data will be made available upon request.

Author contributions

MM: Writing–original draft, Data curation, Investigation. FY: Investigation, Resources, Writing–original draft, Writing–review and editing. MB: Writing–original draft, Writing–review and editing. AS: Conceptualization, Formal Analysis, Methodology, Supervision, Visualization, Writing–original draft, Writing–review and editing.

Funding

The author(s) declare that financial support was received for the research, authorship, and/or publication of this article. AS supported by the Polish Ministry of Education and Science by the program for outstanding young scientists.

Acknowledgments

AS would like to thank the Department of Process Engineering and Technology of Polymeric and Carbon Materials, Wrocław University of Science and Technology, for financial support from the ministerial subsidy.

Conflict of interest

The authors declare that the research was conducted in the absence of any commercial or financial relationships that could be construed as a potential conflict of interest.

The author(s) declared that they were an editorial board member of Frontiers, at the time of submission. This had no impact on the peer review process and the final decision.

Publisher's note

All claims expressed in this article are solely those of the authors and do not necessarily represent those of their affiliated organizations, or those of the publisher, the editors and the reviewers. Any product that may be evaluated in this article, or claim that may be made by its manufacturer, is not guaranteed or endorsed by the publisher.

- Casciola, M., Donnadio, A., Pica, M., Valentini, V., and Piaggio, P. (2005). Characterization of Zr phosphate/PVDF nanocomposites by vibrational spectroscopy. *Macromol. Symp.* 230, 95–104. doi:10.1002/MASY.200551147

- Fam, W., Phuntsho, S., Lee, J. H., Cho, J., and Shon, H. K. (2014). Boron transport through polyamide-based thin film composite forward osmosis membranes. *Desalination* 340, 11–17. doi:10.1016/j.desal.2014.02.010

- Gul, A., Hruza, J., Dvorak, L., and Yalcinkaya, F. (2022). Chemical cleaning process of polymeric nanofibrous membranes. *Polymers* 14, 1102–1114. doi:10.3390/POLYM14061102
- Havelka, O., Yalcinkaya, F., Wacławek, S., Padil, V. V. T., Amendola, V., Černík, M., et al. (2023). Sustainable and scalable development of PVDF-OH Ag/TiO_x nanocomposites for simultaneous oil/water separation and pollutant degradation. *Environ. Sci. Nano* 10, 2359–2373. doi:10.1039/D3EN00335C
- Hu, Y. N., Li, Q. M., Guo, Y. F., Zhu, L. J., Zeng, Z. X., and Xiong, Z. (2021). Nanofiltration-like forward osmosis membranes on *in-situ* mussel-modified polyvinylidene fluoride porous substrate for efficient salt/dye separation. *J. Polym. Sci.* 59, 1065–1071. doi:10.1002/POL.20210138
- Huang, L., Arena, J. T., and McCutcheon, J. R. (2016). Surface modified PVDF nanofiber supported thin film composite membranes for forward osmosis. *J. Memb. Sci.* 499, 352–360. doi:10.1016/J.MEMSCI.2015.10.030
- Huang, L., and McCutcheon, J. R. (2015). Impact of support layer pore size on performance of thin film composite membranes for forward osmosis. *J. Memb. Sci.* 483, 25–33. doi:10.1016/J.MEMSCI.2015.01.025
- Islam, M. N., Yıldırım, B., Maryska, J., and Yalcinkaya, F. (2022). Multi-layered nanofiber membranes: preparation, characterization, and application in wastewater treatment. *J. Industrial Text.* 52, 152808372211274. doi:10.1177/15280837221127443
- Ji, Y., Yang, X., Ji, Z., Zhu, L., Ma, N., Chen, D., et al. (2020). DFT-calculated IR spectrum amide I, II, and III band contributions of N-methylacetamide fine components. *ACS Omega* 5, 8572–8578. doi:10.1021/acsomega.9b04421
- Kallem, P., Gaur, R., Pandey, R. P., Hasan, S. W., Choi, H., and Banat, F. (2021). Thin film composite forward osmosis membranes based on thermally treated PAN hydrophilized PVDF electrospun nanofiber substrates for improved performance. *J. Environ. Chem. Eng.* 9, 106240. doi:10.1016/J.JECE.2021.106240
- Li, K., Li, M., Zhang, W., Xue, Y., Wang, Z., and Zhang, X. (2023). A staged forward osmosis process for simultaneous desalination and concentration of textile wastewaters. *ACS ES T Water* 3, 1817–1825. doi:10.1021/acsestwater.2c00314
- Li, M., Yang, Y., Zhu, L., Wang, G., Zeng, Z., and Xue, L. (2022). Anti-fouling and highly permeable thin-film composite forward osmosis membranes based on the reactive polyvinylidene fluoride porous substrates. *Colloids Surf. A Physicochem Eng. Asp.* 654, 130144. doi:10.1016/J.COLSURFA.2022.130144
- Liao, Y., Wang, R., Tian, M., Qiu, C., and Fane, A. G. (2013). Fabrication of polyvinylidene fluoride (PVDF) nanofiber membranes by electro-spinning for direct contact membrane distillation. *J. Memb. Sci.* 425–426, 30–39. doi:10.1016/J.MEMSCI.2012.09.023
- Lin, C. S., Tung, K. L., Lin, Y. L., Di Dong, C., Chen, C. W., and Wu, C. H. (2020). Fabrication and modification of forward osmosis membranes by using graphene oxide for dye rejection and sludge concentration. *Process Saf. Environ. Prot.* 144, 225–235. doi:10.1016/J.PSEP.2020.07.007
- Liu, C., Lei, X., Wang, L., Jia, J., Liang, X., Zhao, X., et al. (2017). Investigation on the removal performances of heavy metal ions with the layer-by-layer assembled forward osmosis membranes. *Chem. Eng. J.* 327, 60–70. doi:10.1016/J.CEJ.2017.06.070
- Maiti, S., Samantaray, P. K., and Bose, S. (2020). *In situ* assembly of a graphene oxide quantum dot-based thin-film nanocomposite supported on de-mixed blends for desalination through forward osmosis. *Nanoscale Adv.* 2, 1993–2003. doi:10.1039/C9NA00688E
- Ndiaye, I., Chaoui, I., Eddouibi, J., Vaudreuil, S., and Bounahmidi, T. (2022). Synthesis of poly (vinylidene fluoride)/polyacrylonitrile electrospun substrate-based thin-film composite membranes for desalination by forward osmosis process. *Chem. Eng. Process. - Process Intensif.* 181, 109132. doi:10.1016/J.CEP.2022.109132
- Park, M. J., Gonzales, R. R., Abdel-Wahab, A., Phuntsho, S., and Shon, H. K. (2018). Hydrophilic polyvinyl alcohol coating on hydrophobic electrospun nanofiber membrane for high performance thin film composite forward osmosis membrane. *Desalination* 426, 50–59. doi:10.1016/J.DESAL.2017.10.042
- Peng, L. E., Yao, Z., Chen, J., Guo, H., and Tang, C. Y. (2020). Highly selective separation and resource recovery using forward osmosis membrane assembled by polyphenol network. *J. Memb. Sci.* 611, 118305. doi:10.1016/J.MEMSCI.2020.118305
- Pereira, E. L. M., Batista, A. de S. M., Alves, N., de Oliveira, A. H., Ribeiro, F. A. S., Santos, A. P., et al. (2018). Effects of the addition of MWCNT and ZrO₂ nanoparticles on the dosimetric properties of PVDF. *Appl. Radiat. Isotopes* 141, 275–281. doi:10.1016/J.APRADISO.2018.07.015
- Qiu, G., and Ting, Y. P. (2013). Osmotic membrane bioreactor for wastewater treatment and the effect of salt accumulation on system performance and microbial community dynamics. *Bioresour. Technol.* 150, 287–297. doi:10.1016/J.BIORTECH.2013.09.090
- Rafael, R., Rosas, R., Rosas, J. M., García-Mateos, F. J., Pisarenko, T., Papež, N., et al. (2022). Comprehensive characterization of PVDF nanofibers at macro- and nanolevel. *Polymers* 14, 593. doi:10.3390/POLYM14030593
- Sethupathy, M., Sethuraman, V., Manisankar, P., Sethupathy, M., Sethuraman, V., and Manisankar, P. (2013). Preparation of PVDF/SiO₂ and PVDF/PAA/SiO₂ composite nanofiber membrane using electrospinning for Polymer Electrolyte Analysis. *Soft Nanosci. Lett.* 3, 37–43. doi:10.4236/SNL.2013.32007
- Shah, A. A., Cho, Y. H., Nam, S. E., Park, A., Park, Y. I., and Park, H. (2020). High performance thin-film nanocomposite forward osmosis membrane based on PVDF/bentonite nanofiber support. *J. Industrial Eng. Chem.* 86, 90–99. doi:10.1016/J.JIEC.2020.02.016
- Shibuya, M., Park, M. J., Lim, S., Phuntsho, S., Matsuyama, H., and Shon, H. K. (2018). Novel CA/PVDF nanofiber supports strategically designed via coaxial electrospinning for high performance thin-film composite forward osmosis membranes for desalination. *Desalination* 445, 63–74. doi:10.1016/J.DESAL.2018.07.025
- Sizeland, K. H., Hofman, K. A., Hallett, I. C., Martin, D. E., Potgieter, J., Kirby, N. M., et al. (2018). Nanostructure of electrospun collagen: do electrospun collagen fibers form native structures? *Mater. (Oxf)* 3, 90–96. doi:10.1016/J.MTLA.2018.10.001
- Tian, M., Qiu, C., Liao, Y., Chou, S., and Wang, R. (2013). Preparation of polyamide thin film composite forward osmosis membranes using electrospun polyvinylidene fluoride (PVDF) nanofibers as substrates. *Sep. Purif. Technol.* 118, 727–736. doi:10.1016/J.SEPPUR.2013.08.021
- Torres-Mendieta, R., Yalcinkaya, F., Boyraz, E., Havelka, O., Wacławek, S., Maryska, J., et al. (2020). PVDF nanofibrous membranes modified via laser-synthesized Ag nanoparticles for a cleaner oily water separation. *Appl. Surf. Sci.* 526, 146575. doi:10.1016/J.APSUSC.2020.146575
- Xiao, D., Tang, C. Y., Zhang, J., Lay, W. C. L., Wang, R., and Fane, A. G. (2011). Modeling salt accumulation in osmotic membrane bioreactors: implications for FO membrane selection and system operation. *J. Memb. Sci.* 366, 314–324. doi:10.1016/J.MEMSCI.2010.10.023
- Yalcinkaya, F., Siekierka, A., and Bryjak, M. (2017). Surface modification of electrospun nanofibrous membranes for oily wastewater separation. *RSC Adv.* 7, 56704–56712. doi:10.1039/C7RA11904F
- Yang, X. (2020). Monitoring the interfacial polymerization of piperazine and trimethylol chloride with hydrophilic interlayer or macromolecular additive by *in situ* FT-IR spectroscopy. *Membranes* 10, 12–10. doi:10.3390/MEMBRANES10010012
- Yu, F., Shi, H., Shi, J., Teng, K., Xu, Z., and Qian, X. (2020). High-performance forward osmosis membrane with ultra-fast water transport channel and ultra-thin polyamide layer. *J. Memb. Sci.* 616, 118611. doi:10.1016/J.MEMSCI.2020.118611
- Zhang, X., Shen, L., Guan, C. Y., Liu, C. X., Lang, W. Z., and Wang, Y. (2018). Construction of SiO₂@MWNTs incorporated PVDF substrate for reducing internal concentration polarization in forward osmosis. *J. Memb. Sci.* 564, 328–341. doi:10.1016/J.MEMSCI.2018.07.043
- Zhang, X., Shen, L., Lang, W. Z., and Wang, Y. (2017). Improved performance of thin-film composite membrane with PVDF/PFSA substrate for forward osmosis process. *J. Memb. Sci.* 535, 188–199. doi:10.1016/J.MEMSCI.2017.04.038
- Zhao, P., Gao, B., Xu, S., Kong, J., Ma, D., Shon, H. K., et al. (2015). Polyelectrolyte-promoted forward osmosis process for dye wastewater treatment – exploring the feasibility of using polyacrylamide as draw solute. *Chem. Eng. J.* 264, 32–38. doi:10.1016/J.CEJ.2014.11.064
- Zhou, L., Yu, H., Yamin Hossain, M., Chen, F., Du, C., and Zhang, G. (2023). Fabrication of high-performance forward osmosis membrane based on asymmetric integrated nanofiber porous support induced by a new controlled photothermal induction method. *Chem. Eng. J.* 470, 144366. doi:10.1016/J.CEJ.2023.144366



OPEN ACCESS

EDITED BY

Nalan Kabay,
Ege University, Türkiye

REVIEWED BY

Marek Bryjak,
Wrocław University of Technology, Poland
Sacide Alsoy Altinkaya,
Izmir Institute of Technology, Türkiye

*CORRESPONDENCE

Glenn Lipscomb,
✉ parisa.safari@rockets.utoledo.edu

RECEIVED 24 March 2024

ACCEPTED 11 April 2024

PUBLISHED 29 April 2024

CITATION

Safari P, Rahnema H and Lipscomb G (2024),
Opportunities for membrane technology in
controlled environment agriculture.
Front. Membr. Sci. Technol. 3:1406326.
doi: 10.3389/frmst.2024.1406326

COPYRIGHT

© 2024 Safari, Rahnema and Lipscomb. This is
an open-access article distributed under the
terms of the [Creative Commons Attribution
License \(CC BY\)](#). The use, distribution or
reproduction in other forums is permitted,
provided the original author(s) and the
copyright owner(s) are credited and that the
original publication in this journal is cited, in
accordance with accepted academic practice.
No use, distribution or reproduction is
permitted which does not comply with these
terms.

Opportunities for membrane technology in controlled environment agriculture

Parisa Safari, Hamed Rahnema and Glenn Lipscomb*

Chemical Engineering, University of Toledo, Toledo, OH, United States

Controlled environment agriculture has the potential to enhance agriculture sustainability, a United Nations sustainable development goal. Enclosed agricultural facilities can be used in locations that cannot support field agriculture while reducing water usage and increasing productivity relative to open field agriculture. The primary challenges with operation arise from energy consumption to maintain the proper growth conditions. Membrane processes can reduce energy consumption by controlling temperature, humidity, and carbon dioxide concentration. Membrane processes also can minimize water consumption by enabling the use of non-conventional water resources and reducing wastewater production. The literature describing these applications is reviewed and opportunities for future innovation are discussed.

KEYWORDS

membrane gas separator, reverse osmosis, controlled environment agriculture (CEA), Dehumidication, membranes

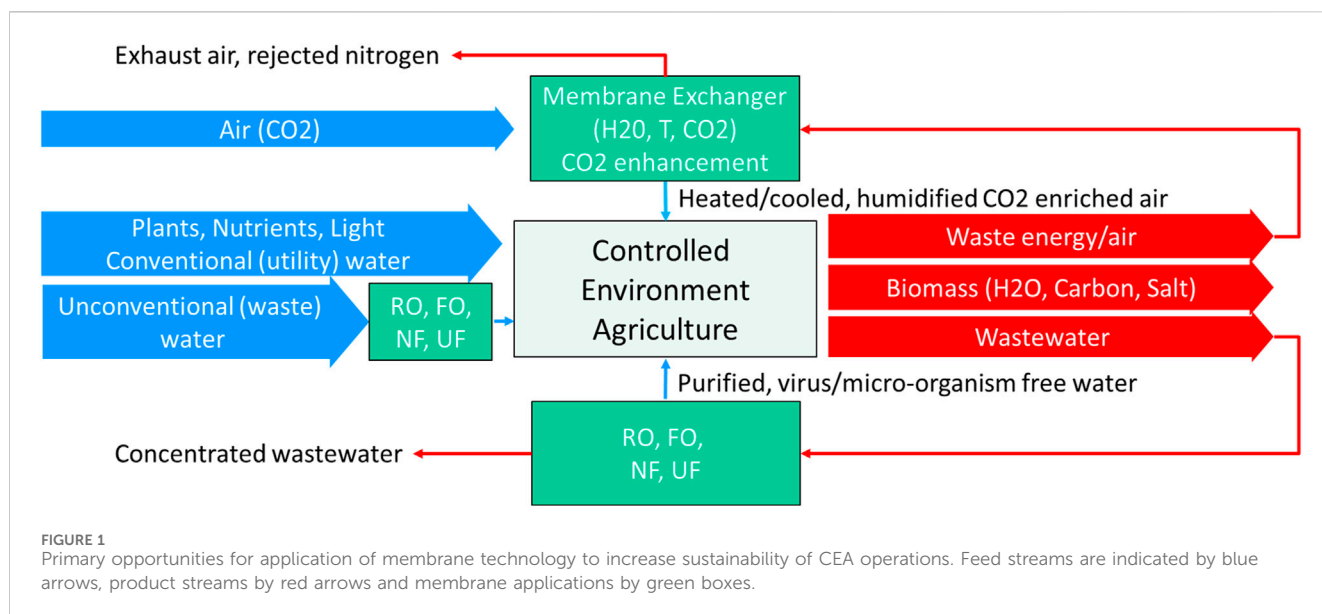
1 Introduction

Global food supply chains are under stress as the population surges past 8 billion, climate change reduces farm productivity, and agricultural land is repurposed or lost (Tilman et al., 2011). This stress is exacerbated by attempts to intensify traditional field cultivation through increased use of fertilizer that in turn leads to increased greenhouse gas emissions (Menegat et al., 2022), greater eutrophication of adjacent bodies of water (Liu et al., 2021), and loss of soil health (Krasilnikov et al., 2022).

Controlled environment agriculture (CEA) offers the potential to dramatically intensify agricultural operations while simultaneously enhancing sustainability and resiliency (McClements et al., 2020). CEA encompasses a spectrum of technologies that allow food production in facilities isolated from the external environment including traditional soil-based greenhouses, vertical farms, hydroponics, aeroponics, and aquaponics (Cowan et al., 2022).

The potential benefits of indoor food production are reduced water consumption through precision application and recycle, optimization of growth conditions, increased productivity through year-round growth, increased arable area through vertical farming, reduced transportation costs through farm placement closer to markets (especially near food deserts), and reduced exposure to pests and invasive plants (Benke and Tomkins, 2017). However, these benefits come at the cost of increased capital expenses for the production infrastructure, greater energy consumption for environmental control and lighting, and lack of ecosystem services such as pollination (Cowan et al., 2022).

Currently, food production with CEA systems is more expensive than field production. An analysis of landed costs for field-produced lettuce sent from California to New York and



Chicago indicated field lettuce costs were less than one-half of CEA lettuce costs. Moreover, energy usage and greenhouse gas emissions were higher (Nicholson et al., 2020). Despite these cost differences, sales of CEA produced crops have risen to \$600 million in 2019 (corrected to 2012 dollars) with production coming from nearly 3000 facilities (Dohlman et al., 2024). The top three sales crops were tomatoes, lettuce, and herbs.

To improve economics, energy consumption in CEA must be reduced (Engler and Krarti, 2021). A study of energy consumption in leafy green production indicated 70% was for lighting and 28% for HVAC (Zeidler and Vrakking, 2015). Membrane technology has the potential to reduce the HVAC contribution. Additionally, membrane technology has the potential to reduce water consumption, increase productivity, and improve resilience.

This review summarizes past work on the use of membrane technology in CEA. It emphasizes how membranes can improve sustainability. Finally, opportunities for future innovation are suggested.

Figure 1 illustrates the opportunities that exist. CEA facilities can be envisioned as biochemical reactors that transform feed streams into food products. Plant DNA (seeds or seedlings), carbon dioxide (CO_2), water, and nutrients are needed to produce the hydrocarbons constituting the food product. Continuous flows of CO_2 and water are required to provide carbon, hydrogen, and oxygen for photosynthesis and plant growth. Additional inputs include natural light for photosynthesis and energy for temperature control, equipment operation, and supplemental artificial lighting.

Three primary streams exit the bioreactor: 1) the desired food product and other biomass that accompanies its production such as roots, stems, and leaves, 2) a waste air stream from displacement of air in the facility by the incoming air stream, and 3) a wastewater stream to remove contaminants that build-up in the water supply system. The waste streams are valuable due to their water and energy content. Membrane processes offer the potential to recover both. Membranes also can be used to control humidity and CO_2 concentration within the facility. Additionally, membranes allow use of unconventional water sources when conventional water

sources are lacking or insufficient. Past work in these areas is reviewed here.

2 Water management

Global water scarcity and rising food demand necessitate innovation in water management for the entire agriculture industry (Greenlee et al., 2009). By 2025, half the global population will inhabit water-stressed regions (WHO, 2024) underscoring the importance of identifying unconventional sources and enhancing conservation. Agriculture currently utilizes ~70% of freshwater withdrawals globally, often unsustainably (Organization et al., 2012). Greenhouses, with their controlled environments, offer a viable solution to manage water more efficiently in agricultural areas (Al-Ismaili and Jayasuriya, 2016). Incorporation of membrane technology in CEA has the potential to lower agriculture's water demand relative to field cultivation.

2.1 Source water management

Greenhouses typically rely on municipal water, which can be costly and scarce in some regions. This has led to the use of groundwater instead. However, approximately 50% of global groundwater resources exhibit salinity levels ($0.5 \leq S \leq 5 \text{ g/kg}$) too high for agricultural use (Gleick, 2012). Therefore, there is a critical need for desalination to ensure sustainable and efficient crop cultivation (Pimentel et al., 1997).

Reverse osmosis (RO) offers a solution to water salinity control. RO, with its reduced energy consumption relative to traditional thermal desalination methods, is especially effective for treating brackish water, due to its low osmotic pressure (Fikana and Raafi u, 2023). Efforts from the large body of literature on membranes for desalination that focus on CEA applications are discussed here.

While RO effectively removes 99% of ions, resulting in a low concentration, it also eliminates essential nutrients for crop growth (Ukraine et al., 2020) which must be replaced either by adding fertilizers (increasing costs (Ben Gal et al., 2009)) or blending with brackish water; blending can have the detrimental effect of raising soil salinity and requiring extra water to flush out salts (Cohen et al., 2018). Fouling and scaling, common problems of RO systems, increase costs but can be controlled through pretreatment. Many pilot studies have shown that that MF, UF, and FO are effective pretreatment steps for RO, enhancing biofouling prevention and water quality while potentially lowering energy use (Zhang et al., 2006; Shaffer et al., 2012; Coday et al., 2014; Lew et al., 2020).

Recent studies highlight the advantages of integrating nanofiltration (NF) as a pretreatment for reverse osmosis (RO) in desalination. Hassan et al., 1998 and others (Uhlinger, 2001) have demonstrated that NF reduces divalent ions, lowers water production costs by 27%, and improves RO efficiency, despite higher complexity and initial costs. These findings suggest NF pretreatment can double RO recovery rates, reduce energy use by 40%, and cut water costs by 20%. Furthermore, the RO-NF process can lead to reduced investment costs and electricity usage compared to a two-stage RO process (Kurihara et al., 2001). Studies of ultrafiltration (UF) and forward osmosis (FO) with RO as an alternative pretreatment suggest potential for further efficiency gains (Pazouki et al., 2022). The key challenge is balancing the benefits of NF, UF, and FO pretreatments against their added complexity and costs for commercial-scale viability.

Monovalent selective electrodialysis (MSED) offers a tailored approach to water management, selectively separating beneficial divalent ions (Ca^{2+} , Mg^{2+} , SO_4^{2-}) from harmful monovalent ions (Na^+ , Cl^-) providing an effective alternative to RO. Although not yet commercialized for brackish water, research shows the potential for MSED cost savings by minimizing fertilizer usage. Rehman et al. (Rehman et al., 2021) modeled MSED for U.S. greenhouse irrigation, estimating \$4,991 per hectare savings in fertilizer costs by retaining nutrients. Kishor et al. (Nayar and V, 2020) found switching from RO to MSED saved \$15,000 annually in fertilizer for a 10-ha farm. The viability of MSED desalination for greenhouses depends on nutrient and water savings outweighing higher capital and operating costs than RO. Yvana et al. (Ahdab et al., 2021a) found SW-MSED 30% more expensive than SW-RO at current prices. However, SW-MSED matches SW-RO cost-effectiveness if electricity is under \$0.08/kWh.

Membrane distillation (MD) utilizes a membrane contactor for thermal separation by evaporation and shows promise for hypersaline water when combined with use of waste heat or solar energy (Lee et al., 2020). Studies have demonstrated the potential for MD in desalinating seawater and hypersaline water, especially when used alongside conventional desalination systems like ED, RO, and FO (Yadav et al., 2021). However, the limited water flux of MD has hindered scale-up (Hussain et al., 2022a).

While ED, Reverse ED and MD have been successfully piloted for agricultural projects (Chafidz et al., 2014), they presently lack the reliability and cost-effectiveness for widespread adoption. Further R&D focused on enhancing membrane performance and integration with renewable energy is needed to realize the potential of these technologies.

The use of concentrated aqueous fertilizer as a draw solution in FO has also been proposed to produce fertilized irrigation water (fertigation) from brackish water, desalination brine, and other non-potable water sources. Since the concept was first introduced in 2011 (Phuntsho et al., 2011), numerous investigators have studied stand-alone fertilizer-driven FO processes as well as hybrids with other water purification processes. Pourmovahed et al., 2022 summarize the literature and provide an analysis of the thermodynamic limits to the amount of water that can be recovered, relative to water irrigation requirements, as well as limitations imposed by maintaining sufficiently high-water fluxes to ensure economic viability.

2.2 Wastewater management

Fertigation, the addition of fertilizer including nitrogen as nitrate or ammonium to irrigation water, is used to enhance crop growth. However, excess fertilizer not used by crops leads to nutrient-rich wastewater. Due to stricter EU and US regulations on nitrate disposal, two main wastewater treatment methods have emerged: biological denitrification in large basins or artificial wetlands, which is land-intensive and offers limited control (Gruyer et al., 2013), and wastewater reuse for irrigation after disinfection to mitigate disease and biofilm growth in irrigation systems. Reusing wastewater for irrigation reduces source water demand but leads to challenges like sodium buildup which can damage crops. Operators must choose between discharging this water or using energy-intensive reverse osmosis (RO) that also removes beneficial minerals, necessitating extra fertilizer.

MSED technology has been demonstrated to outperform RO in greenhouse wastewater treatment for irrigation with selective ion removal with over 90% water recovery, less waste, and longer-lasting, fouling-resistant membranes (Strathmann, 2010) enhancing cost-effectiveness and efficiency. Additional studies by Ahdab et al. (Ahdab et al., 2021b) and Schücking (Schücking, 2020) have demonstrated MSED can treat greenhouse wastewater by removing sodium and nitrates. Despite this potential, MSED technology has not yet been adopted commercially for greenhouse wastewater treatment.

Additional challenges exist in separating potassium and sodium in sustainable greenhouse farming. Potassium (K^+) is vital for plant health, enhancing water uptake, enzyme activity, photosynthesis, nutrient transport, growth, and stress resilience (Ragel et al., 2019; Rawat et al., 2022). However, the K^+ and Na^+ separation is difficult with conventional MSED due to the similarity in ion exchange equilibrium coefficients and physicochemical characteristics (Zhang et al., 2021). B et al., 2022 investigate the development of sustainable K^+/Na^+ monovalent-selective membranes using a hot-pressed polyelectrolyte complex method. The resulting membrane demonstrates superior selectivity for K^+ over Na^+ . Moreover, Qian et al., 2022 examine sodium ion removal from greenhouse water using electrodialysis with a supported liquid membrane (SLM) and a cation-selective membrane (CIMS), achieving up to 96% potassium recovery and 80% for other ions. This method shows potential for improving water quality in greenhouse farming.

3 Air management

CEA systems offer the ability to produce food in geographical locations where field agriculture is not viable due to climatic conditions, most notably extreme temperature and humidity conditions. For example, CEA can enable food production in desert areas or other hot climates and be integrated with energy production via thermal solar or photovoltaics (Ghoulem et al., 2019; Lefers et al., 2020). Membrane processes offer alternatives to systems being considered for temperature (e.g., evaporative cooling (Cuce and Riffat, 2016) and humidity (e.g., heat pump (Cámara-Zapata et al., 2019)) control. Additionally, membranes offer the potential for CO₂ management.

3.1 Humidity management

Humidity control is critical for optimization of plant growth and prevention of physiological disorders. Traditional methods for humidity control include condensation, use of solid and liquid desiccants, and electrochemical techniques (Huang and Zhang, 2013; Lefers et al., 2016; Ali et al., 2017; Amani et al., 2020; Hussain et al., 2022b; Soussi et al., 2022).

Liquid desiccants can capture water vapor either directly or via a membrane contactor. The use of membrane contactors in liquid desiccant-based systems has been studied extensively (Abdel-Salam et al., 2013; Das and Jain, 2013; Zhang and Zhang, 2014; Zhang et al., 2016). Dehumidification utilizes a semi-permeable membrane barrier to facilitate contacting the process air with the liquid desiccant. The membrane allows water vapor transport across it but prevents desiccant flow; the direction and rate of water permeation determined by the water vapor chemical potential difference across the membrane (Qu et al., 2018). A membrane contactor allows use of smaller dehumidification systems and can provide more efficient performance.

System performance is controlled by the type of membrane used. Triethylene glycol (TEG) supported liquid membranes were used in early studies for indoor humidity control (Abdul-Wahab et al., 2004; Li and Ito, 2008; Li et al., 2011). Kneifel et al. (Kneifel et al., 2006) developed a coated polyetherimide hollow fiber membrane and evaluated the effect of the PDMS coating thickness on water vapor permeation using LiCl as the absorbent. Bergero et al. (Bergero and Chiari, 2010) demonstrated that a hybrid air-conditioning system combining vapor-compression with LiCl-based membrane dehumidification could reduce energy costs by 50% compared to conventional systems. Zhang, 2011 reported a hollow fiber membrane contactor model and its use in dehumidification process optimization. They noted the importance of preventing liquid desiccant crossover. Bettahalli et al., 2016 developed a dehumidification device using a calcium chloride desiccant with a PVDF triple-bore hollow fiber membrane that offered enhanced efficiency. They examined how the device could be used for energy-efficient humidity control in CEA systems located in Jeddah. Lefers et al., 2019 explored the use of magnesium chloride with PVDF membrane contactors and demonstrated its potential to maintain desired humidity levels. Pasqualin and Davies, 2022 examined the use of multi-stage nanofiltration for liquid desiccant regeneration in air conditioning, focusing on how salt

rejection in NF membranes is influenced by desiccant concentration and pressure. They tested four commercial NF membranes with LiCl, LiBr, and MgCl₂, finding that LiCl shows lower rejection but higher permeate flux. The study revealed the need for membranes capable of operation at higher pressures for effective water removal from used desiccant solutions (i.e., desalination where the desired product is the concentrated brine) and improved coefficient of performance.

Moussaddy et al., 2024 proposed using concentrated fertilizer solution as the desiccant in a membrane-based process. Using dense polydimethylsiloxane hollow fiber membranes, they demonstrated the ability to reduce humidity to ~40% with diverse fertilizer mixtures. Energy efficiencies as high as 0.24 Wh/g were observed which compare well with other technologies. Control of desiccant temperature was critical to optimizing dehumidification performance.

3.2 Thermal management

Temperature control is critical for CEA operations in areas with extreme ambient temperatures. Both cooling and heating may be required depending on the location and time of year.

The need for cooling in warm climates has motivated significant efforts to evaluate the technological options for maintenance, ease of use, and cost (Rabbi et al., 2019). Membrane-based systems using liquid desiccant air conditioning (LDAC) have attracted attention recently. Pasqualin and Davies, 2022 proposed a LDAC system using multi-stage nanofiltration (NF) for desiccant regeneration. Their system enabled closed air recirculation and a closed water cycle for both cooling and irrigation while keeping temperatures below 32°C with greater efficiency than conventional cooling. Future advancements could reduce complexity and cost. Lefers et al., 2016 explored a greenhouse cooling system using liquid desiccation and solar-powered MD with PVDF membranes. The system was designed for hot, humid climates and integrated dehumidification with freshwater generation. The study addressed challenges with efficient desiccant regeneration and managing thermal inputs through use of solar energy. Pilot systems are being developed to refine the technology.

Membrane enthalpy exchangers offer the potential for simultaneous temperature and humidity management. A relatively new concept (Zhang and Jiang, 1999; Zhang, 2012), these air-to-air heat exchangers used to contact building exhaust air with incoming air can exchange both enthalpy and humidity. Such systems have been studied extensively to improve efficiency of building HVAC systems (Li et al., 2022). However, studies of their application in CEA are limited.

3.3 CO₂ control

CO₂ concentration is a critical variable, along with temperature and humidity, in the optimization of CEA environment for plant growth (Pasgianos et al., 2003; Panwar et al., 2011). Increased CO₂ levels can enhance photosynthesis efficiency thereby leading to enhanced energy and water utilization (Thongbai et al., 2010; Zhang et al., 2014). Five primary sources of CO₂ enrichment

have been used in CEA: compost, exhaust gas from fossil fuels, exhaust gas from renewable energy, natural or forced ventilation, and pure liquefied CO₂ (Jin et al., 2009; Dion et al., 2011; Kuroyanagi et al., 2014; Roy et al., 2014). Membrane gas separation is a highly promising technology to concentrate CO₂ for use in CEA that offers reduced capture cost, smaller process footprints, and reduced process complexity relative to other processes (Yang et al., 2008; Brunetti et al., 2010; Dion et al., 2011; Khalilpour et al., 2015; Norahim et al., 2018).

Wang et al., 2014 proposed the use of an anion exchange membrane in a moisture swing adsorption process for direct air capture (DAC) and greenhouse agriculture. The membrane they evaluated had a capacity of 0.83 mol CO₂ per kilogram and adsorption was well described by a Langmuir isotherm model. Desorption studies indicated nearly 80% of the adsorbed CO₂ could be recovered and the impact on greenhouse energy consumption was evaluated.

Stacey et al., 2018 investigated the use of CO₂ enrichment to reduce water losses in CEA. Water is lost in the humid air displaced when outside air is circulated into a CEA facility to provide CO₂ for plant growth. Humidity losses were estimated to be 90% of overall water usage. Simulations of mass and energy flows indicated water losses could be reduced by 95% using a pressure-driven membrane gas separation process for CO₂ enrichment in the entering air. Changes in process energy requirements were evaluated, including compression for the membrane process and changes in greenhouse heating or cooling arising from use of CO₂ enriched air, but the impact on plant growth was not considered.

Shin et al., 2019 focused on repurposing CO₂ from biogas (a mixture of carbon dioxide and methane) for industrial and agricultural use. They evaluated a commercial hollow-fiber membrane module, made of polysulfone (PSf) coated with polydimethylsiloxane (PDMS). At the optimal operating conditions of 40°C and 7 bar, a 95.6% CO₂ product was produced with minimal CH₄ loss demonstrating the viability of CO₂ recovery from biogas.

Hu et al., 2022 prepared composite membranes consisting of polydimethylsiloxane (PDMS), polyethylene oxide (PEO) and polyether block amide copolymer (Pebax) supported by a porous polysulfone (PSf) layer on a nonwoven polyester fabric. The PDMS/PSf membranes possessed the highest CO₂ permeance and produced the most concentrated permeate. Optimum crosslinker concentration, UV/ozone treatment time (to produce a silica-like surface layer), and final heat treatment time were determined to achieve the desired CO₂ permeance and selectivity. Growth of *Glebionis coronaria* with the CO₂ enriched air led to increases in plant mass and height of 458% and 61%, respectively, after 4 weeks. Similar increases were observed for *bok choy*. Membrane performance was stable over an 80-day period demonstrating the potential of the process to enhance CEA productivity.

Yoo et al., 2023 studied a membrane-based system for indoor CO₂ management and utilization, featuring a commercial hollow fiber membrane module. Designed to maintain CO₂ levels below 300 ppm to ensure healthy indoor environments, the system also produced a CO₂ enriched permeate for enhancement of indoor plant growth. Such findings indicate the synergy that can exist by combining CO₂ capture with CEA utilization in urban environments.

4 Conclusion

Applications of membrane technology to increase sustainable CEA operation are reviewed. Membranes offer unique approaches to control water, air, and carbon dioxide flows to reduce energy consumption. The primary applications have been in source water management, wastewater management, humidity control, thermal management, and CO₂ enrichment.

Opportunities for further innovation are numerous. Continued improvement in membrane material properties and module design is expected to increase process efficiency, especially for use in water recycling and utilization of non-potable feed waters. Water management also would benefit significantly from improved monovalent selective electrodialysis membranes. Additionally, new materials for use in liquid desiccant air conditioning have the potential to reduce energy consumption and simultaneously control CEA facility humidity and temperature.

CO₂ enrichment strategies may benefit from integration of membrane technology with adsorption and absorption technology being developed for point source and direct air carbon capture. Co-location of CEA facilities with these carbon dioxide capture operations, including both fossil fuel power plants and enclosed environments such as office buildings (Sinha et al., 2018), would further improve economics. Furthermore, opportunities exist for hybrid processes that integrate membrane enthalpy exchanger technology with non-membrane technologies being developed to reduce energy consumption of HVAC systems.

Author contributions

PS: Investigation, Writing–original draft, Writing–review and editing. HR: Investigation, Writing–original draft, Writing–review and editing. GL: Conceptualization, Supervision, Visualization, Writing–original draft, Writing–review and editing.

Funding

The author(s) declare that no financial support was received for the research, authorship, and/or publication of this article.

Conflict of interest

The authors declare that the research was conducted in the absence of any commercial or financial relationships that could be construed as a potential conflict of interest.

Publisher's note

All claims expressed in this article are solely those of the authors and do not necessarily represent those of their affiliated organizations, or those of the publisher, the editors and the reviewers. Any product that may be evaluated in this article, or claim that may be made by its manufacturer, is not guaranteed or endorsed by the publisher.

References

- Abdel-Salam, A. H., Ge, G., and Simonson, C. J. (2013). Performance analysis of a membrane liquid desiccant air-conditioning system. *Energy Build.* 62, 559–569. doi:10.1016/j.enbuild.2013.03.028
- Abdul-Wahab, S. A., Zurigat, Y. H., and Abu-Arabi, M. K. (2004). Predictions of moisture removal rate and dehumidification effectiveness for structured liquid desiccant air dehumidifier. *Energy* 29, 19–34. doi:10.1016/j.energy.2003.08.001
- Ahdab, Y. D., Schücking, G., Rehman, D., and Lienhard, J. H. (2021a). Cost effectiveness of conventionally and solar powered monovalent selective electrodialysis for seawater desalination in greenhouses. *Appl. Energy* 301, 117425. doi:10.1016/j.apenergy.2021.117425
- Ahdab, Y. D., Schücking, G., Rehman, D., and Lienhard, J. H. (2021b). Treatment of greenhouse wastewater for reuse or disposal using monovalent selective electrodialysis. *Desalination* 507, 115037. doi:10.1016/j.desal.2021.115037
- Ali, A., Ishaque, K., Lashin, A., and Arifi, N. A. (2017). Modeling of a liquid desiccant dehumidification system for close type greenhouse cultivation. *Energy* 118, 578–589. doi:10.1016/j.energy.2016.10.069
- Al-Ismaili, A. M., and Jayasuriya, H. (2016). Seawater greenhouse in Oman: a sustainable technique for freshwater conservation and production. *Renew. Sustain. Energy Rev.* 54, 653–664. doi:10.1016/j.rser.2015.10.016
- Amani, M., Foroushani, S., Sultan, M., and Bahrami, M. (2020). Comprehensive review on dehumidification strategies for agricultural greenhouse applications. *Appl. Therm. Eng.* 181, 115979. doi:10.1016/j.applthermaleng.2020.115979
- B, A. K., Zwiinnenberg, H. J., Lindhoud, S., and Vos, W. M. de (2022). Sustainable K+/Na+ monovalent-selective membranes with hot-pressed PSS-PVA saloplastics. *J. Membr. Sci.* 652, 120463. doi:10.1016/j.memsci.2022.120463
- Ben Gal, A., Yermiyahu, U., and Cohen, S. (2009). Fertilization and blending alternatives for irrigation with desalinated water. *J. Environ. Qual.* 38, 529–536. doi:10.2134/jeq2008.0199
- Benke, K., and Tomkins, B. (2017). Future food-production systems: vertical farming and controlled-environment agriculture. *Sustain. Sci. Pr. Polic.* 13, 13–26. doi:10.1080/15487733.2017.1394054
- Bergero, S., and Chiari, A. (2010). Performance analysis of a liquid desiccant and membrane contactor hybrid air-conditioning system. *Energy Build.* 42, 1976–1986. doi:10.1016/j.enbuild.2010.06.003
- Bettahalli, N. M. S., Lefers, R., Fedoroff, N., Leiknes, T., and Nunes, S. P. (2016). Triple-bore hollow fiber membrane contactor for liquid desiccant based air dehumidification. *J. Membr. Sci.* 514, 135–142. doi:10.1016/j.memsci.2016.04.059
- Brunetti, A., Scura, F., Barbieri, G., and Drilo, E. (2010). Membrane technologies for CO2 separation. *J. Membr. Sci.* 359, 115–125. doi:10.1016/j.memsci.2009.11.040
- Cámara-Zapata, J. M., Sánchez-Molina, J. A., Rodríguez, F., and López, J. C. (2019). Evaluation of a dehumidifier in a mild weather greenhouse. *Appl. Therm. Eng.* 146, 92–103. doi:10.1016/j.applthermaleng.2018.09.107
- Chafidz, A., Al-Zahrani, S., Al-Otaibi, M. N., Hoong, C. F., Lai, T. F., and Prabu, M. (2014). Portable and integrated solar-driven desalination system using membrane distillation for arid remote areas in Saudi Arabia. *Desalination* 345, 36–49. doi:10.1016/j.desal.2014.04.017
- Coday, B. D., Yaffe, B. G. M., Xu, P., and Cath, T. Y. (2014). Rejection of trace organic compounds by forward osmosis membranes: a literature review. *Environ. Sci. Technol.* 48, 3612–3624. doi:10.1021/es4038676
- Cohen, B., Lazarovitch, N., and Gilron, J. (2018). Upgrading groundwater for irrigation using monovalent selective electrodialysis. *Desalination* 431, 126–139. doi:10.1016/j.desal.2017.10.030
- Cowan, N., Ferrier, L., Spears, B., Drewler, J., Reay, D., and Skiba, U. (2022). CEA systems: the means to achieve future food security and environmental sustainability? *Front. Sustain. Food Syst.* 6, 891256. doi:10.3389/fsufs.2022.891256
- Cuce, P. M., and Riffat, S. (2016). A state of the art review of evaporative cooling systems for building applications. *Renew. Sustain. Energy Rev.* 54, 1240–1249. doi:10.1016/j.rser.2015.10.066
- Das, R. S., and Jain, S. (2013). Experimental performance of indirect air-liquid membrane contactors for liquid desiccant cooling systems. *Energy* 57, 319–325. doi:10.1016/j.energy.2013.05.013
- Dion, L.-M., Lefsrud, M., and Orsat, V. (2011). Review of CO2 recovery methods from the exhaust gas of biomass heating systems for safe enrichment in greenhouses. *Biomass Bioenergy* 35, 3422–3432. doi:10.1016/j.biombioe.2011.06.013
- Dohlman, M. E., Davis, K., Husby, W. V., Bovay, M., Weber, J., and Lee, C. (2024). Yoonjung: trends, insights, and future prospects for production in controlled environment agriculture and agrivoltaics systems. *U S Dep. Agric. Econ. Res. Serv.*
- Engler, N., and Krarti, M. (2021). Review of energy efficiency in controlled environment agriculture. *Renew. Sustain. Energy Rev.* 141, 110786. doi:10.1016/j.rser.2021.110786
- Fikana, E. R., and Raafi u, B. (2023). Design of water treatment system to change Brackish water into fresh water using Reverse Osmosis method. *AIP Conf. Proc.* 2580, 040008. doi:10.1063/5.0124367
- Ghoulam, M., Moueddeb, K. E., Nehdi, E., Boukhanouf, R., and Calautit, J. K. (2019). Greenhouse design and cooling technologies for sustainable food cultivation in hot climates: review of current practice and future status. *Biosyst. Eng.* 183, 121–150. doi:10.1016/j.biosystemseng.2019.04.016
- Gleick (2012). *Gleick: the world's water volume 7: the biennial report on freshwater resources*. China: Island press.
- Greenlee, L. F., Lawler, D. F., Freeman, B. D., Marrot, B., and Moulin, P. (2009). Reverse osmosis desalination: water sources, technology, and today's challenges. *Water Res.* 43, 2317–2348. doi:10.1016/j.watres.2009.03.010
- Gruyer, N., Dorais, M., Alsanius, B. W., and Zagury, G. J. (2013). Simultaneous removal of nitrate and sulfate from greenhouse wastewater by constructed wetlands. *J. Environ. Qual.* 42, 1256–1266. doi:10.2134/jeq2012.0306
- Hassan, A. M., Al-Sofi, M. A. K., Al-Amoudi, A. S., Jamaluddin, A. T. M., Farooque, A. M., Rowaili, A., et al. (1998). A new approach to membrane and thermal seawater desalination processes using nanofiltration membranes (Part 1). *Desalination* 118, 35–51. doi:10.1016/s0011-9164(98)00079-4
- Hu, C.-C., Lin, C.-W., Hu, C.-P., Keshebo, D. L., Huang, S.-H., Hung, W.-S., et al. (2022). Carbon dioxide enrichment of PDMS/PSF composite membranes for solving the greenhouse effect and food crisis. *J. CO2 Util.* 61, 102011. doi:10.1016/j.jcou.2022.102011
- Huang, S.-M., and Zhang, L.-Z. (2013). Researches and trends in membrane-based liquid desiccant air dehumidification. *Renew. Sustain. Energy Rev.* 28, 425–440. doi:10.1016/j.rser.2013.08.005
- Hussain, A., Janson, A., Matar, J. M., and Adham, S. (2022a). Membrane distillation: recent technological developments and advancements in membrane materials. *Emergent Mater* 5, 347–367. doi:10.1007/s42247-020-00152-8
- Hussain, G., Aleem, M., Sultan, M., Sajjad, U., Ibrahim, S. M., Shamshiri, R. R., et al. (2022b). Evaluating evaporative cooling assisted solid desiccant dehumidification system for agricultural storage application. *Sustainability* 14, 1479. doi:10.3390/su14031479
- Jin, C., Du, S., Wang, Y., Condon, J., Lin, X., and Zhang, Y. (2009). Carbon dioxide enrichment by composting in greenhouses and its effect on vegetable production. *J. Plant Nutr. Soil Sci.* 172, 418–424. doi:10.1002/jpln.200700220
- Khalilpour, R., Mumford, K., Zhai, H., Abbas, A., Stevens, G., and Rubin, E. S. (2015). Membrane-based carbon capture from flue gas: a review. *J. Clean. Prod.* 103, 286–300. doi:10.1016/j.jclepro.2014.10.050
- Kneifel, K., Nowak, S., Albrecht, W., Hilke, R., Just, R., and Peinemann, K.-V. (2006). Hollow fiber membrane contactor for air humidity control: Modules and membranes. *J. Membr. Sci.* 276, 241–251. doi:10.1016/j.memsci.2005.09.052
- Krasilnikov, P., Taboada, M. A., and Amanullah, H. (2022). Amanullah: fertilizer use, soil health and agricultural sustainability. *Agriculture* 12, 462. doi:10.3390/agriculture12040462
- Kurihara, M., Yamamura, H., Nakanishi, T., and Jinno, S. (2001). Operation and reliability of very high-recovery seawater desalination technologies by brine conversion two-stage RO desalination system. *Desalination* 138, 191–199. doi:10.1016/s0011-9164(01)00264-8
- Kuroyanagi, T., Yasuba, K., Higashide, T., Iwasaki, Y., and Takaichi, M. (2014). Efficiency of carbon dioxide enrichment in an unventilated greenhouse. *Biosyst. Eng.* 119, 58–68. doi:10.1016/j.biosystemseng.2014.01.007
- Lee, W. J., Ng, Z. C., Hubadillah, S. K., Goh, P. S., Lau, W. J., Othman, M. H. D., et al. (2020). Fouling mitigation in forward osmosis and membrane distillation for desalination. *Desalination* 480, 114338. doi:10.1016/j.desal.2020.114338
- Lefers, R., Bettahalli, N. M. S., Nunes, S. P., Fedoroff, N., Davies, P. A., and Leiknes, T. (2016). Liquid desiccant dehumidification and regeneration process to meet cooling and freshwater needs of desert greenhouses. *Desalination Water Treat.* 57, 23430–23442. doi:10.1080/19443994.2016.1173383
- Lefers, R. M., Bettahalli, N. M. S., Fedoroff, N. V., Ghaffour, N., Davies, P. A., Nunes, S. P., et al. (2019). Hollow fibre membrane-based liquid desiccant humidity control for controlled environment agriculture. *Biosyst. Eng.* 183, 47–57. doi:10.1016/j.biosystemseng.2019.04.010
- Lefers, R. M., Tester, M., and Lauenstein, K. J. (2020). Emerging technologies to enable sustainable controlled environment agriculture in the extreme environments of Middle East-north africa coastal regions. *Front. Plant Sci.* 11, 801. doi:10.3389/fpls.2020.00801
- Lew, B., Tarnapolski, O., Afgin, Y., Portal, Y., Ignat, T., Yudachev, V., et al. (2020). Exploratory ranking analysis of brackish groundwater desalination for sustainable agricultural production: a case study of the Arava Valley in Israel. *J. Arid. Environ.* 174, 104078. doi:10.1016/j.jaridenv.2019.104078
- Li, J., and Ito, A. (2008). Dehumidification and humidification of air by surface-soaked liquid membrane module with triethylene glycol. *J. Membr. Sci.* 325, 1007–1012. doi:10.1016/j.memsci.2008.09.034
- Li, J., Shao, S., Wang, Z., Xie, G., Wang, Q., Xu, Z., et al. (2022). A review of air-to-air membrane energy recovery technology for building ventilation. *Energy Build.* 265, 112097. doi:10.1016/j.enbuild.2022.112097

- Li, J., Sui, G., Zuo, C., and Deng, Q. (2011). Air humidification by a liquid membrane of triethylene glycol. *Int. Conf. Remote Sens. Environ. Transp. Eng.*, 7357–7359. doi:10.1109/rsete.2011.5966068
- Liu, L., Zheng, X., Wei, X., Kai, Z., and Xu, Y. (2021). Excessive application of chemical fertilizer and organophosphorus pesticides induced total phosphorus loss from planting causing surface water eutrophication. *Sci. Rep.* 11, 23015. doi:10.1038/s41598-021-02521-7
- McClements, D. J., Barrangou, R., Hill, C., Kokini, J. L., Lila, M. A., Meyer, A. S., et al. (2020). Building a resilient, sustainable, and healthier food supply through innovation and technology. *Annu. Rev. Food Sci. Technol.* 12, 1–28. doi:10.1146/annurev-food-092220-030824
- Menegat, S., Ledo, A., and Tirado, R. (2022). Greenhouse gas emissions from global production and use of nitrogen synthetic fertilisers in agriculture. *Sci. Rep.* 12, 14490. doi:10.1038/s41598-022-18773-w
- Moussaddy, S., Aryal, S., and Maisonneuve, J. (2024). Specific energy analysis of using fertilizer-based liquid desiccants to dehumidify indoor plant environments. *Appl. Therm. Eng.* 238, 121849. doi:10.1016/j.applthermaleng.2023.121849
- Nayar, K. G., and V, J. H. L. (2020). Brackish water desalination for greenhouse agriculture: comparing the costs of RO, CCRO, EDR, and monovalent-selective EDR. *Desalination* 475, 114188. doi:10.1016/j.desal.2019.114188
- Nicholson, C. F., Harbick, K., Gómez, M. I., and Mattson, N. S.: An economic and environmental comparison of conventional and controlled environment agriculture (CEA) supply chains for leaf lettuce to US cities. 33–68. (2020). doi:10.1007/978-3-030-34065-0
- Norahim, N., Yaisanga, P., Faungnawakij, K., Charinpanitkul, T., and Klayson, C. (2018). Recent membrane developments for CO₂ separation and capture. *Chem. Eng. Technol.* 41, 211–223. doi:10.1002/ceat.201700406
- Organization, U. N. E., Balaji, R., Connor, R., Glennie, P., Gun, J. van der, Lloyd, G. J., et al. (2012). The united Nations world water development report 2012. *U. N. World Water Dev. Rep.* doi:10.18356/bd022534-en
- Panwar, N. L., Kaushik, S. C., and Kothari, S. (2011). Solar greenhouse an option for renewable and sustainable farming. *Renew. Sustain. Energy Rev.* 15, 3934–3945. doi:10.1016/j.rser.2011.07.030
- Pasgianos, G. D., Arvanitis, K. G., Polycarpou, P., and Sigrimis, N. (2003). A nonlinear feedback technique for greenhouse environmental control. *Comput. Electron. Agric.* 40, 153–177. doi:10.1016/s0168-1699(03)00018-8
- Pasqualin, P., and Davies, P. A. (2022). Concept design of a greenhouse cooling system using multi-stage nanofiltration for liquid desiccant regeneration. *Appl. Therm. Eng.* 216, 119057. doi:10.1016/j.applthermaleng.2022.119057
- Pazouki, P., Sidhu, J. P. S., Ipe, D. S., Pype, M. L., Wohlsen, T. D., Helfer, F., et al. (2022). Seawater dilution desalination with hybrid FO-RO and UF-RO: characterisation and assessment of pathogen removal efficacy. *Desalination* 525, 115509. doi:10.1016/j.desal.2021.115509
- Phuntsho, S., Shon, H. K., Hong, S., Lee, S., and Vigneswaran, S. (2011). A novel low energy fertilizer driven forward osmosis desalination for direct fertigation: evaluating the performance of fertilizer draw solutions. *J. Membr. Sci.* 375, 172–181. doi:10.1016/j.memsci.2011.03.038
- Pimentel, D., Houser, J., Preiss, E., White, O., Fang, H., Mesnick, L., et al. (1997). Water resources: agriculture, the environment, and society. *BioScience* 47, 97–106. doi:10.2307/1313020
- Pourmovahed, P., Lefsrud, M., and Maisonneuve, J. (2022). Thermodynamic limits of using fertilizer to produce clean fertigation solution from wastewater via forward osmosis. *J. Membr. Sci.* 647, 120168. doi:10.1016/j.memsci.2021.120168
- Qian, Z., Miedema, H., Pintossi, D., Ouma, M., and Sudhölter, E. J. R. (2022). Selective removal of sodium ions from greenhouse drainage water – a combined experimental and theoretical approach. *Desalination* 536, 115844. doi:10.1016/j.desal.2022.115844
- Qu, M., Abdelaziz, O., Gao, Z., and Yin, H. (2018). Isothermal membrane-based air dehumidification: a comprehensive review. *Renew. Sustain. Energy Rev.* 82, 4060–4069. doi:10.1016/j.rser.2017.10.067
- Rabbi, B., Chen, Z.-H., and Sethuvenkatraman, S. (2019). Protected cropping in warm climates: a review of humidity control and cooling methods. *Energies* 12, 2737. doi:10.3390/en12142737
- Ragel, P., Raddatz, N., Leidi, E. O., Quintero, F. J., and Pardo, J. M. (2019). Regulation of K⁺ nutrition in plants. *Front. Plant Sci.* 10, 281. doi:10.3389/fpls.2019.00281
- Rawat, J., Pandey, N., and Saxena, J. (2022). “Role of potassium in plant photosynthesis, transport, growth, and yield,” in *Role of potassium in abiotic stress*. Editors N. Iqbal and S. Umar (Singapore: Springer), 1–14. doi:10.1007/978-981-16-4461-0_1
- Rehman, D., Ahdab, Y. D., and Lienhard, J. H. (2021). Monovalent selective electrodialysis: modelling multi-ionic transport across selective membranes. *Water Res.* 199, 117171. doi:10.1016/j.watres.2021.117171
- Roy, Y., Lefsrud, M., Orsat, V., Filion, F., Bouchard, J., Nguyen, Q., et al. (2014). Biomass combustion for greenhouse carbon dioxide enrichment. *Biomass Bioenergy* 66, 186–196. doi:10.1016/j.biombioe.2014.03.001
- Schücking, G. (2020). *Monovalent selective electrodialysis in greenhouses*. Master Thesis: Lund University.
- Shaffer, D. L., Yip, N. Y., Gilron, J., and Elimelech, M. (2012). Seawater desalination for agriculture by integrated forward and reverse osmosis: improved product water quality for potentially less energy. *J. Membr. Sci.* 415, 1–8. doi:10.1016/j.memsci.2012.05.016
- Shin, M. S., Jung, K.-H., Kwag, J.-H., and Jeon, Y.-W. (2019). Biogas separation using a membrane gas separator: focus on CO₂ upgrading without CH₄ loss. *Process Saf. Environ. Prot.* 129, 348–358. doi:10.1016/j.psep.2019.07.020
- Sinha, A., Thakkar, H., Rezaei, F., Kawajiri, Y., and Realf, M. J. (2018). Direct air capture of CO₂ in enclosed environments: design under uncertainty and techno-economic analysis. *Comput. Aided Chem. Eng.* 44, 2179–2184. doi:10.1016/b978-0-444-64241-7.50358-x
- Soussi, M., Chaibi, M. T., Buchholz, M., and Saghrouni, Z. (2022). Comprehensive review on climate control and cooling systems in greenhouses under hot and arid conditions. *Agronomy* 12, 626. doi:10.3390/agronomy12030626
- Stacey, N., Fox, J., and Hildebrandt, D. (2018). Reduction in greenhouse water usage through inlet CO₂ enrichment. *AIChE J.* 64, 2324–2328. doi:10.1002/aic.16120
- Strathmann, H. (2010). Electrodialysis, a mature technology with a multitude of new applications. *Desalination* 264, 268–288. doi:10.1016/j.desal.2010.04.069
- Thongbai, P., Kozai, T., and Ohya, K. (2010). CO₂ and air circulation effects on photosynthesis and transpiration of tomato seedlings. *Sci. Hortic.* 126, 338–344. doi:10.1016/j.scienta.2010.07.018
- Tilman, D., Balzer, C., Hill, J., and Befort, B. L. (2011). Global food demand and the sustainable intensification of agriculture. *Proc. Natl. Acad. Sci.* 108, 20260–20264. doi:10.1073/pnas.1116437108
- Uhlir, A. R. (2001). *Desalination method and apparatus utilizing nanofiltration and reverse osmosis membranes*.
- Ukraine, U. N. U. of H., Hospodarenko, H. M., Prokopchuk, I. V., and Boiko, V. P. (2020). Soybean uptake of essential nutrients from soil and fertilizers. *Agrochem. Soil Sci.*, 63–70. doi:10.31073/acss89-07
- Wang, T., Huang, J., He, X., Wu, J., Fang, M., and Cheng, J. (2014). CO₂ fertilization system integrated with a low-cost direct air capture technology. *Energy Procedia* 63, 6842–6851. doi:10.1016/j.egypro.2014.11.718
- WHO (2024) WHO: WHO. World Health Organization—Water, *Fact. Sheet* 391.
- Yadav, A., Labhasetwar, P. K., and Shahi, V. K. (2021). Membrane distillation using low-grade energy for desalination: a review. *J. Environ. Chem. Eng.* 9, 105818. doi:10.1016/j.jece.2021.105818
- Yang, H., Xu, Z., Fan, M., Gupta, R., Slimane, R. B., Bland, A. E., et al. (2008). Progress in carbon dioxide separation and capture: a review. *J. Environ. Sci.* 20, 14–27. doi:10.1016/s1001-0742(08)60002-9
- Yoo, S. Y., Kim, Y. J., Lee, T. H., Lee, B. K., Kim, M. J., Han, S. H., et al. (2023). Membrane system for management and utilization of indoor CO₂. *J. Ind. Eng. Chem.* 122, 161–168. doi:10.1016/j.jiec.2023.02.018
- Zeidler, S. C., and Vrakking, D. and: Vertical farm 2.0: designing an economically feasible vertical farm - a combined European endeavor for sustainable urban agriculture. (2015)
- Zhang, J. D., Liu, Y. W., Gao, S. M., Li, C. Z., Zhang, F., Zen, H. M., et al. (2006). Pilot testing of outside-in UF pretreatment prior to RO for high turbidity seawater desalination. *Desalination* 189, 269–277. doi:10.1016/j.desal.2005.07.009
- Zhang, L.-Z. (2011). An analytical solution to heat and mass transfer in hollow fiber membrane contactors for liquid desiccant air dehumidification. *J. Heat. Transf.* 133, 092001. doi:10.1115/1.4003900
- Zhang, L.-Z. (2012). Progress on heat and moisture recovery with membranes: from fundamentals to engineering applications. *Energy Convers. Manag.* 63, 173–195. doi:10.1016/j.enconman.2011.11.033
- Zhang, L. Z., and Jiang, Y. (1999). Heat and mass transfer in a membrane-based energy recovery ventilator. *J. Membr. Sci.* 163, 29–38. doi:10.1016/s0376-7388(99)00150-7
- Zhang, L.-Z., and Zhang, N. (2014). A heat pump driven and hollow fiber membrane-based liquid desiccant air dehumidification system: modeling and experimental validation. *Energy* 65, 441–451. doi:10.1016/j.energy.2013.10.014
- Zhang, N., Yin, S.-Y., and Zhang, L.-Z. (2016). Performance study of a heat pump driven and hollow fiber membrane-based two-stage liquid desiccant air dehumidification system. *Appl. Energy*. 179, 727–737. doi:10.1016/j.apenergy.2016.07.037
- Zhang, S., Ou, R., Ma, H., Lu, J., Holl, M. M. B., and Wang, H. (2021). Thermally regenerable metal-organic framework with high monovalent metal ion selectivity. *Chem. Eng. J.* 405, 127037. doi:10.1016/j.cej.2020.127037
- Zhang, Z., Liu, L., Zhang, M., Zhang, Y., and Wang, Q. (2014). Effect of carbon dioxide enrichment on health-promoting compounds and organoleptic properties of tomato fruits grown in greenhouse. *Food Chem.* 153, 157–163. doi:10.1016/j.foodchem.2013.12.052



OPEN ACCESS

EDITED BY

Maria Giovanna Buonomenna,
Ordine dei Chimici e Fisici della Campania and
MIUR, Italy

REVIEWED BY

Yuan Liao,
Nankai University, China
Zhongyun Liu,
Georgia Institute of Technology, United States

*CORRESPONDENCE

Yunxia Hu,
✉ yunxiahu@tiangong.edu.cn

RECEIVED 27 March 2024

ACCEPTED 20 May 2024

PUBLISHED 28 June 2024

CITATION

Hao S, Zhang Z, Zhao X, An X and Hu Y (2024),
Investigation of multi-stage forward osmosis
membrane process for concentrating high-
osmotic acrylamide solution.
Front. Membr. Sci. Technol. 3:1407819.
doi: 10.3389/frmst.2024.1407819

COPYRIGHT

© 2024 Hao, Zhang, Zhao, An and Hu. This is an
open-access article distributed under the terms
of the [Creative Commons Attribution License](#)
(CC BY). The use, distribution or reproduction in
other forums is permitted, provided the original
author(s) and the copyright owner(s) are
credited and that the original publication in this
journal is cited, in accordance with accepted
academic practice. No use, distribution or
reproduction is permitted which does not
comply with these terms.

Investigation of multi-stage forward osmosis membrane process for concentrating high-osmotic acrylamide solution

Shuang Hao¹, Zhaoqian Zhang¹, Xin Zhao¹, Xiaochan An² and Yunxia Hu^{1*}

¹State Key Laboratory of Separation Membranes and Membrane Processes, School of Materials Science and Engineering, Tiangong University, Tianjin, China, ²Department of Municipal Engineering, College of Civil Engineering, Sichuan Agricultural University, Chengdu, China

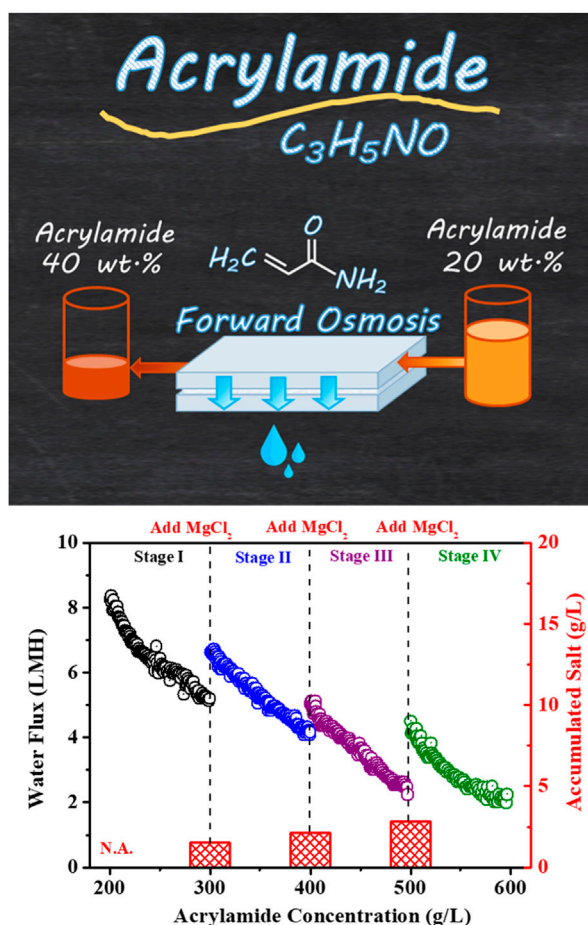
Acrylamide is an important chemical in great global demand for the synthesis of polyacrylamide. A facile and benign approach of concentrating high osmotic acrylamide aqueous solution at a low temperature is needed to replace the current energy-intensive and cost-expensive thermal flash evaporation process. For the first time, a multi-stage forward osmosis (FO) process has been developed to concentrate acrylamide solution from 200 g/L to 600 g/L. Thin-film composite (TFC) membrane was fabricated and used for the multi-stage FO process. Acrylamide feed solution (FS) with various concentrations was systematically characterized in terms of viscosity and osmotic pressure (OP). Draw solutes including NaCl and MgCl₂ were tested, and their reverse salt fluxes were measured with the quantification of their accumulative contents in the resultant concentrated acrylamide solution. Different operation modes including AL-FS (active layer facing FS) and AL-DS (active layer facing DS) were explored to optimize the system efficiency of the FO concentration process. Both single- and multi-stage FO operations were investigated, and their performances were quantified to assess the efficiency of the concentration of acrylamide solution. The results demonstrate that the multi-stage FO operation could dramatically improve the system efficiency for the concentration of acrylamide solution better than the single-stage FO process, and the draw concentration renewal at Stages II, III, and IV led to a water flux increase of 18.56%, 17.52%, and 18.43%, respectively. Moreover, the accumulated MgCl₂ in the final 600 g/L acrylamide solution was below 3.7 g/L, less than 0.62 wt% impurity in the product of acrylamide. Our work provides a practical insight into the viability and optimization of a multi-stage FO process for concentrating high osmotic chemicals.

KEYWORDS

forward osmosis, multi-stage, high osmotic pressure, acrylamide, concentration

Highlights

- The potential of multi-stage forward osmosis in concentrating acrylamide was demonstrated.
- The acrylamide solution could be concentrated from 200 to 600 g/L during the FO process.



GRAPHICAL ABSTRACT

- $MgCl_2$ was used as a more effective draw solute than NaCl with a very low reverse salt flux.
- The AL-FS mode was favored for concentrating acrylamide at a high concentration (> 200 g/L).
- The multi-stage FO operation could dramatically improve both water flux and concentration time.

1 Introduction

Acrylamide holds significant industrial importance; it is primarily utilized in creating polyacrylamide, which accounts for approximately 90% of its usage (Smith and Oehme, 1991; Braun et al., 2022). Polyacrylamide is extensively used as a coagulant or flocculant for water treatment, with growing demand being driven by increasingly stringent environmental regulations (Seybold, 2008; Nath and Pande, 2020). Polyacrylamide also works as a water-soluble thickener for enhanced oil recovery, shale strengthening, and shale gas extraction (Xudong et al., 2004; Li et al., 2017; Al-Kindi et al., 2022). Thanks to numerous applications of polyacrylamide, its global demand is expected to grow continuously (Xiong, Loss, Shields, et al., 2018). Currently, acrylamide is synthesized through acrylonitrile (ACN) hydrolysis with nitrile hydratase (Lee et al., 1991; Raj et al., 2006; Asano et al., 2014), and it needs

further concentration into a highly concentrated acrylamide solution for the synthesis of polyacrylamide. However, the present practical upper limit of produced acrylamide solution is only approximately 150 g/L–250 g/L (James Munch, 1975), and the high concentration of acrylamide severely decreases the stability and activity of the nitrile hydratase catalysts. It can especially cause a rapid catalyst deactivation when the acrylamide concentration is higher than 300 g/L (Watanabe, 1982; Nagasawa et al., 1993). Therefore, an enhanced concentration process for acrylamide product solution is imperative for meeting the necessary polymerization conditions required for polyacrylamide synthesis.

Thermal flash evaporation is a widely employed technique for concentrating acrylamide solution by removing water under the reduced-pressure of 1 bar at 50 °C–55 °C (Watanabe et al., 1989). However, this process is energy-intensive and is accompanied by high installation and maintenance expenses due to the complexity of the equipment (Wade, 1993; McGinnis and Elimelech, 2007). In addition, the relatively high operating temperature for the flash evaporation technique often causes the undesired free-radical polymerization of acrylamide, thereby inducing impurity (Ogata, 1960; Smith and Oehme, 1991). Therefore, a benign process of concentrating acrylamide aqueous solution at a low temperature is needed to improve purity, save energy, and reduce cost.

As an emerging concentration process, forward osmosis (FO) has been developed to concentrate high osmotic solution (Qi, Hu, Chai & Wang, 2019; An, Hu, Wang, Zhou & Liu, 2019; (Hu, 2023). During the FO process, osmosis drives water through a semipermeable membrane from feed to DS, thus concentrating a solute in the feed solution (FS) (Chekli et al., 2016; She et al., 2016). Therefore, selecting an appropriate draw solution (DS) with a higher osmotic pressure (OP) than that of the FS is key to sustaining the osmotic driving force through the FO membrane to concentrate the solute in FS (Zhao et al., 2012). In contrast, in counteracting the OP of FS, the pressure-driven membrane process of reverse osmosis has a limiting performance and does not work for concentrating high-osmotic FS (Rastogi, 2016). Meanwhile, FO membrane is also a core element in the FO system; recently, the gold standard for FO application has been thin-film composite (TFC) membrane, which exhibits relatively high permeability-selectivity far exceeding those cellulose-acetate-based FO membranes. Notably, the FO process provides the great advantage of membrane process of concentrating the high-osmotic FS at ambient conditions without extra pressure or heat (McGinnis and Elimelech, 2007; Zhao et al., 2012). Thus, with a high-performance membrane and suitable draw solutes, the FO process should have greater benefits than thermal concentration for concentrating acrylamide solution in terms of final product quality and energy demand. However, no work has been done to investigate the forward osmosis membrane process for concentrating high osmotic acrylamide solution.

The single-stage forward osmosis (FO) process requires a draw solution of initially higher concentration to generate an adequate driving force which can lead to inefficient resource utilization and higher reverse salt flux (Giagnorio et al., 2022; Truong and Chong, 2024). To overcome such limitations inherent in single-stage membrane processes, multi-stage membrane systems have been developed which have been theoretically proven to enhance the efficiency of separation or concentration operations (Zhu et al., 2009; Alshehri and Lai, 2014; Truong and Chong, 2024). Additionally, multi-stage membranes offer the advantage of maintaining a more uniform water flux across entire modules. This is achieved by adjusting the applied pressure at various stages to counteract the increasing osmotic pressure of the concentrated feed solution (Lin and Elimelech, 2015; Giagnorio et al., 2022). Therefore, multi-stage membrane processes have the potential to significantly reduce the overall economic costs of separation or concentration operations by reducing any unnecessary consumption of energy and resources. In this study, a multi-stage FO system is developed and evaluated for concentrating 200 g/L acrylamide solution with high OP (71.49 bar) for the first time. The current advanced TFC polyamide membrane is fabricated and evaluated in the FO process. Different concentrations of acrylamide solution are methodically studied for viscosity and OP and employed as FS. Draw solutes including representative monovalent salt sodium chloride (NaCl) and divalent salt magnesium chloride (MgCl_2) were tested for the concentration of acrylamide solution; their reverse salt fluxes were measured, and their accumulative contents were quantified in the resultant concentrated acrylamide solution. Different

operation modes including the AL-FS (active layer facing FS) and the AL-DS (active layer facing DS) were also studied to optimize the system efficiency of the FO concentration process. Both single- and multi-stage operations were then carried out, and their performances were quantified and compared to assess the efficiency of the FO process for the concentration of acrylamide solution. Our work provides a practical insight into the viability and optimization of multi-stage FO process for concentrating high-osmotic chemicals.

2 Materials and methods

2.1 Materials and chemicals

Polysulfone (PSf, M_n : 21,000 g/mol) was sourced from Solvay (Brussels, Belgium). M-phenylenediamine (MPD) and trimesoyl chloride (TMC) were obtained from Sigma-Aladdin (United States). Sodium chloride (NaCl), magnesium chloride (MgCl_2), acrylamide, N-methyl-2-pyrrolidinone (NMP), and n-hexane were purchased from Sinopharm (China). All chemicals were utilized in their received state without further modification.

2.2 Fabrication and characterization of the TFC FO membrane

TFC FO membrane was fabricated via a two-step method according to our previous work (Liu and Hu, 2016): preparation of PSf support membrane through non-solvent-induced phase separation and the fabrication of the top PA layer through interfacial polymerization (IP) (Hao et al., 2023a; Hao et al., 2023b). In brief, 12 wt% PSf/NMP casting solution was cast on an NMP-pretreated PET nonwoven fabric using a casting knife with a gap of 150 μm and was immersed in deionized (DI) water ($25 \pm 1^\circ\text{C}$) overnight to produce the PSf support. The PA layer was then prepared on top of the PSf support using 3.4 wt% MPD aqueous solution and 0.15 wt% TMC organic solution in hexane. The obtained TFC membrane was immersed in 90°C water bath for 120 s and then transferred in 4°C DI water for further use.

The morphologies of the TFC membranes were observed using a Hitachi scanning electron microscope (SEM, S-4800). The contact angle of polyamide surface was determined using the Data Physics optical instrument (OCA20, Germany) with a digital camera. The surface charge of the sample was determined through Anton Paar electrokinetic analyzer (SurPASSTM 2, Austria) with 1.0 mmol/L KCl buffer solution, with 3–10 pH. The FO performance (details in Supporting Information, S1) of the fabricated TFC membrane was measured via a cross-flow custom-designed FO system at $25.0^\circ\text{C} \pm 0.5^\circ\text{C}$ using a circulating cooling system (SDC-6, Scientz Biotechnology, China) (Supplementary Figure S1) according to Tiraferri et al. (2013). The effective surface area of the membrane cell was 38.52 cm^2 and the crossflow velocity of both feed and draw solution was maintained at 7 cm/s. The water flux and reverse salt flux were determined following our previous work (Liu and Hu, 2016) and tested under the AL-DS and AL-FS operation modes, respectively.

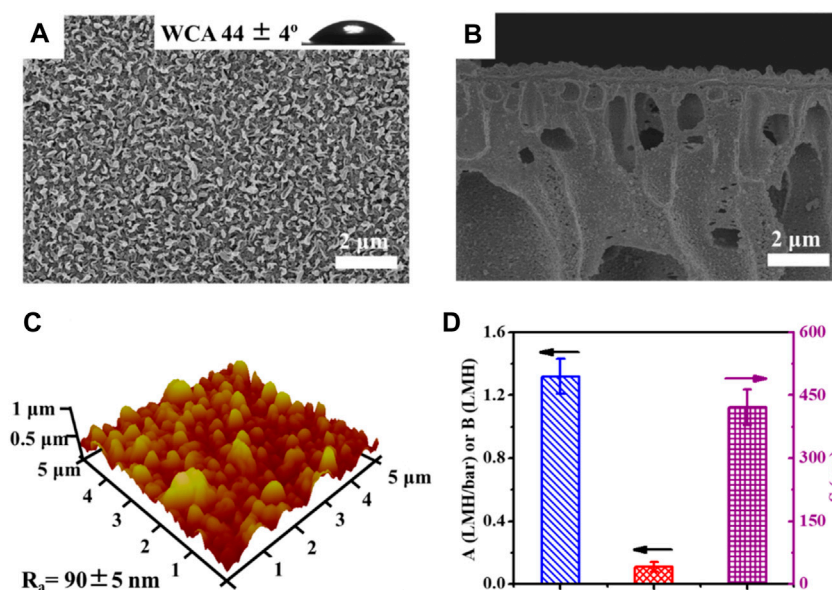


FIGURE 1

Surface and cross-section morphologies of the TFC membrane, including SEM images (A, B) and AFM image (C) of the TFC membrane; the insert in the SEM image A is a water drop on the membrane surface and its average water contact angle (WCA), and intrinsic transport parameters (A, B, S) of the TFC membrane (D).

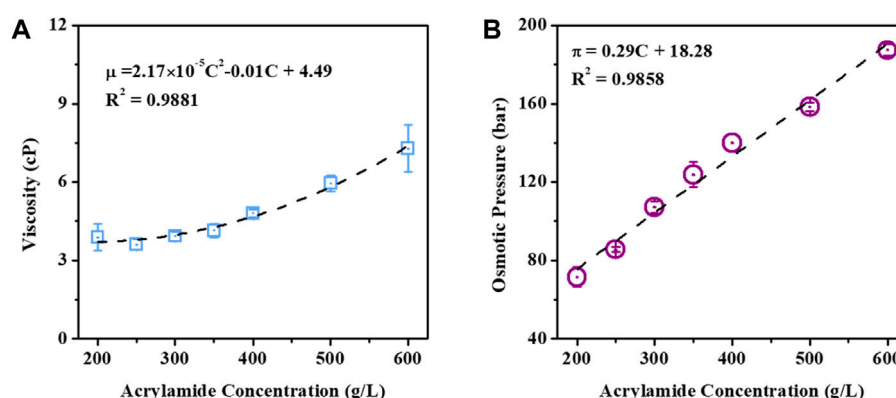


FIGURE 2

Viscosity (A) and OP (B) of acrylamide solution with various concentrations 200 g/L–600 g/L in water at 25 °C.

2.3 Characterization of acrylamide and draw solutions

OP of solutions was determined using a YASN freezing-point osmometer (Osmopro3250, United Kingdom). The viscosities of NaCl, MgCl₂, and acrylamide solutions with various concentrations were determined using a Brookfield viscometer (DVS+, United States) under 25 °C. The concentration of acrylamide solution was determined using Persee UV-Vis spectrometer (TU-1810, China) at 198 nm based on the calibration curve shown in Supplementary Figure S2.

2.4 The operation of the FO process for concentrating high-osmotic acrylamide solution

The concentration process of acrylamide solution was carried out in the above-mentioned crossflow FO system; draw solutions were 4 mol/L (M) and 5 M MgCl₂, respectively. For each run, the initial acrylamide and DSs were performed at a crossflow velocity of 0.7 cm/s and kept at a constant volume of 1 L. The continuous flux was monitored via a Mettler digital balance (ME104E, Switzerland) and a Eutech conductivity meter (CON2700, United States) according to our previous work (Liu and Hu, 2016).

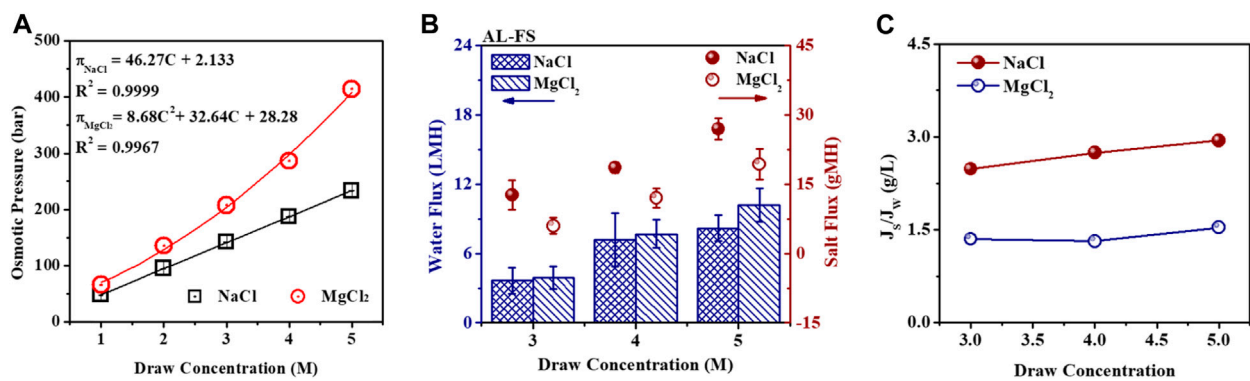


FIGURE 3
OPs (A) of NaCl and MgCl₂ solutions with various concentrations 1 M–5 M at 25 °C. Water flux (J_w), reverse salt flux (J_s) (B), and SRSF (J_s/J_w) (C) of the TFC polyamide membrane with different concentrations of NaCl and MgCl₂ solutions as DS, respectively, under the AL-FS mode. Here, 200 g/L acrylamide solution was used as the feed solution.

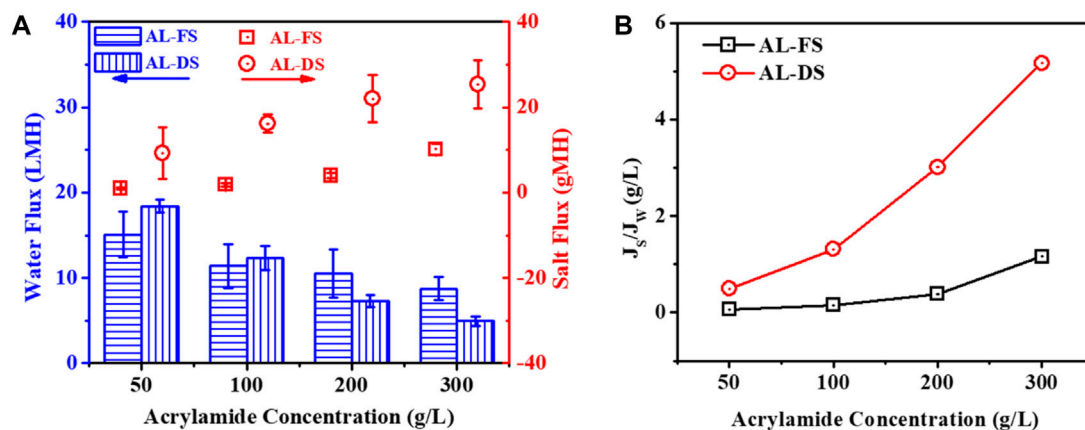


FIGURE 4
Water flux, reverse salt flux (A), and SRSF (J_s/J_w) (B) of the TFC polyamide membrane with different concentrations of acrylamide solutions as feed solution, respectively, under AL-FS and AL-DS modes. Here, 4 M MgCl₂ solution was used as draw.

3 Results and discussion

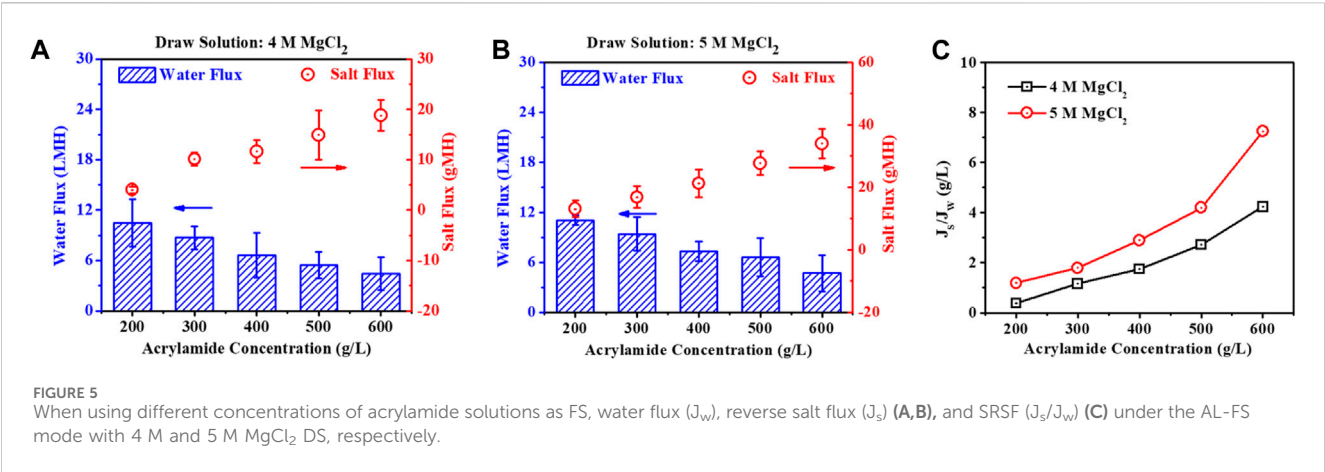
3.1 TFC polyamide membrane

The PA active layer of the TFC membrane was formed on a PSf support membrane via the IP method. As illustrated in Figure 1A, the polyamide surface of the TFC membrane presents a characteristic ridge and valley morphology and exhibits good hydrophilicity with a relative low water contact angle (WCA) of $44^\circ \pm 4^\circ$. The average surface roughness of the polyamide layer was measured by AFM to be 90 ± 5 nm (Figure 1C), comparable with other reported TFC membranes (Han et al., 2012; Tian et al., 2013; Sun et al., 2014). In addition, the morphology of the cross-sectional TFC FO membrane revealed a thin polyamide layer of approximately 300 nm, crafted atop the porous PSf support exhibiting a finger-like pore structure (Figure 1B); this is expected to have a much lower mass transport resistance and, thereby, a suppressed internal concentration polarization (ICP) effect (Yip et al., 2010). Furthermore, TFC polyamide membrane

exhibits a typical high water permeability coefficient (A) as 1.32 ± 0.11 LMH/bar, a very low solute permeability coefficient of NaCl (B) as 0.11 ± 0.08 LMH, and a characteristic structure parameter (S) of 421 ± 80 μ m (Figure 1D), close to those of the previous reported TFC FO membranes (Zhang et al., 2021; Ibraheem et al., 2023), but much higher water permeability and NaCl selectivity than the well-used commercial TFC membrane or cellulose triacetate membrane from HTI (Tiraferri et al., 2013; Long et al., 2016) (Supplementary Table S1).

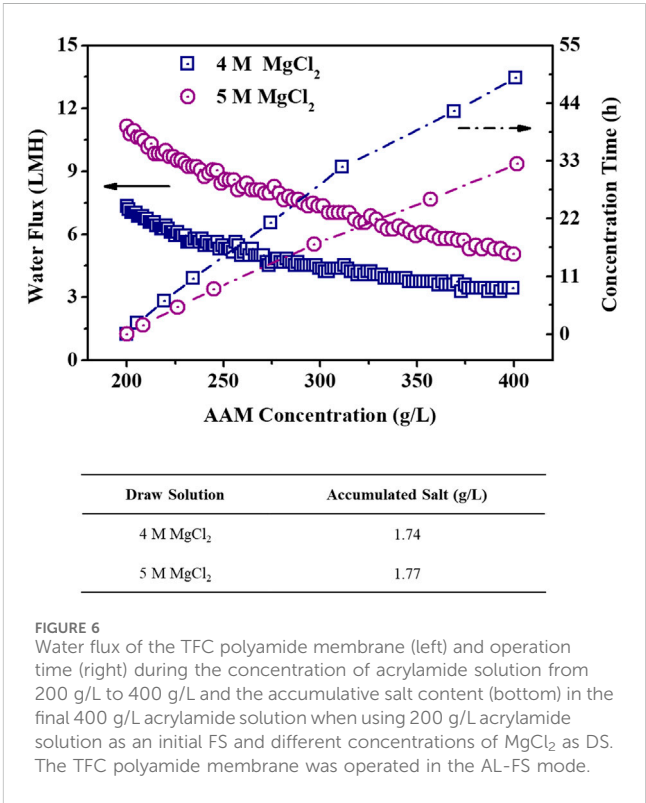
3.2 Acrylamide solution and draw solution

The viscosity and OP of acrylamide solution with various concentrations were measured since they may have significant impacts on the FO concentration process and determine the selection of DS. As shown in Figure 2A, acrylamide solution exhibits a slightly increased viscosity with its concentration but presents a relatively low viscosity below 10 cP, even at a high



concentration of 600 g/L. The increased viscosity often leads to a decreased solution diffusivity and subsequent intensified concentration polarization in FO. Compared to the viscosity of DI water (2.61 cP), results show that acrylamide solution has a comparably low viscosity. The OP of acrylamide solution with various concentrations exhibits a linear increase from 71.49 bar to 187.28 bar, with its concentration increasing from 200 g/L to 600 g/L (Figure 2B). Such a high OP of the acrylamide solution requires an appropriate DS with a much higher OP to concentrate the acrylamide solution in the FO process.

NaCl and MgCl₂ were selected as a typical monovalent and divalent draw solute owing to the popularity and high OP. As presented in Figure 3A, the OPs of NaCl and MgCl₂ solutions increase almost linearly with their concentrations following the Van 't Hoff law. The OP of 5 M MgCl₂ solution is 413.81 bar, dramatically higher than 232.86 bar of 5 M NaCl solution. Nonetheless, NaCl DS is selected for many FO studies due to its abundance, low cost, and high solubility. In addition, as the concentration of NaCl DS rises from 3 M to 5 M, the water flux escalates from 3.65 LMH to 7.20 LMH in the AL-DS mode. Simultaneously, the salt flux displays a significantly accelerated rising pattern, surging from 12.65 gMH to 26.95 gMH (Figure 3B). When MgCl₂ was selected as DS with the concentration increasing from 3 M to 5 M, the water flux increased rapidly from 3.88 LMH to 10.22 LMH in the AL-FS mode, which is greater than that with the NaCl DS owing to higher OP of MgCl₂ solution. Moreover, the reverse salt flux was higher when the MgCl₂ concentration increased and reached ~20 gMH when operated in AL-FS operation mode with 5 M MgCl₂, which was obviously lower than that when using the same NaCl draw concentration. Moreover, the special reverse salt flux (SRSF, J_s/J_w , g/L) was calculated to ascertain the mass loss of the draw solute, which diffused across the TFC polyamide membrane since little water permeates through the membrane, which is lower for higher performance of FO membrane with the better selectivity-permeability. Results in Figure 3C illustrate that the SRSF of the TFC membrane is obviously lower under MgCl₂ DS than under NaCl DS. For example, with the increasing MgCl₂ draw concentration from 3 M to 5 M, the corresponding SRSF of the TFC membrane changed from 1.32 g/L to 1.54 g/L in the AL-FS mode; however, with NaCl DS, it increased from 2.48 g/L to 2.94 g/L,



indicating a much less loss of MgCl₂ than NaCl in the FO process (Hancock and Cath, 2009).

Therefore, the MgCl₂ would be an appropriate draw solute for the concentration experiment of acrylamide solution during the FO process. The high concentration of MgCl₂ solutions from 4 M to 5 M would be appropriate DSs for providing high osmotic driving force for TFC membranes with a water flux higher than 5 LMH.

3.3 Effect of operation mode on FO performance

With 4 M MgCl₂ DS, the performance of the TFC membrane in terms of water and salt permeabilities was investigated using

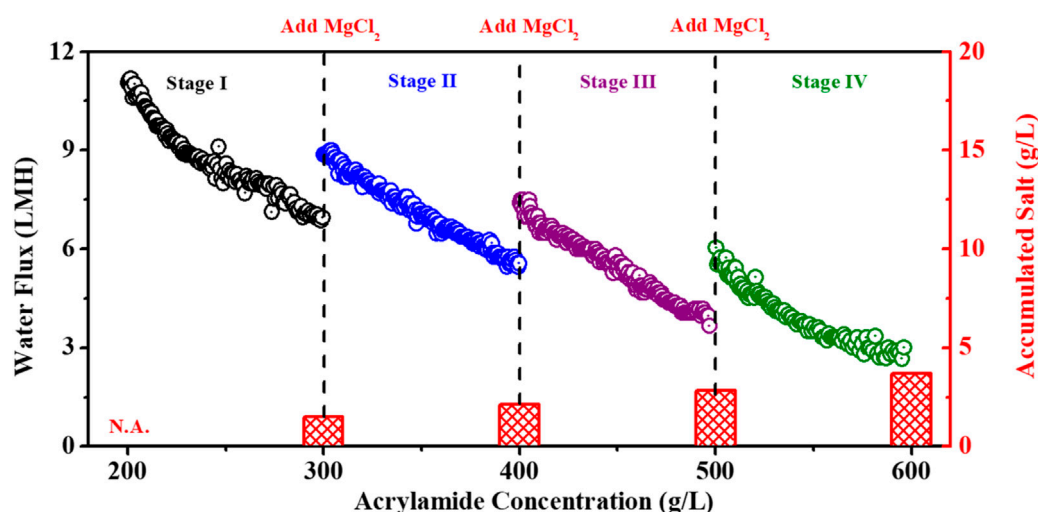


FIGURE 7
Water flux profile of the TFC polyamide membrane and accumulative salt content during the concentration of acrylamide solution from 200 g/L to 600 g/L when using 5 M MgCl_2 as the DS. The TFC polyamide membrane was operated in the AL-FS mode.

different feed solutions. The result in Figure 4A shows that the water flux of the TFC membrane was obviously lower in the AL-FS than that in the AL-DS mode when using 50 g/L and 100 g/L acrylamide solution as FS. For example, with 50 g/L acrylamide FS, the water fluxes of the TFC membrane were 15.06 LMH in AL-FS and 18.37 LMH in AL-DS, respectively, which is characteristic because there is less ICP of the TFC polyamide membrane in AL-DS than that in AL-FS mode (Tiraferri et al., 2013; Liu et al., 2017). However, when the acrylamide feed concentration was increased to 200 g/L, the water flux of the TFC membrane under the AL-DS mode was 7.29 LMH, which is lower than 10.49 LMH under the AL-FS mode. This is because of the severe ICP also occurring at the AL-DS operation mode when the support layer faced high concentration acrylamide solutions. In addition, with the increasing feed concentration from 50 g/L to 300 g/L, the corresponding SRSF of the TFC membrane increased slowly from 0.06 g/L to 1.16 g/L when operated under the AL-FS mode, but it increased rapidly from 0.50 g/L to 5.17 g/L when using the AL-DS as the operation mode, signifying considerably lesser and slower draw solute loss in the AL-FS mode than in the AL-DS mode (Figure 4B). This result suggests that AL-FS would be an appropriate operation orientation for the concentration experiment of acrylamide solution ($\text{Conc.} > 200$ g/L) during the FO process.

3.4 Impact of acrylamide feed concentration and MgCl_2 draw concentration on FO performance

The impact of the concentration of acrylamide feed solution was investigated on the membrane performance, and 4 M and 5 M MgCl_2 solutions were chosen as DS when operating the FO process in the AL-FS mode. Figure 5 shows the decrease of J_w and the increase of both J_s and the J_s/J_w with increasing

concentration of acrylamide FS using 4 M and 5 M MgCl_2 DS. For example, with 4 M MgCl_2 DS, J_w decreased rapidly from 10.49 LMH to 4.43 LMH, and J_s simultaneously increased from 4.00 gMH to 18.77 gMH with increasing acrylamide feed concentration from 200 to 600 g/L (Figure 5A). The same trend of J_w and J_s also occurred when 5 M MgCl_2 was used as a DS (Figure 5B), such as the decreasing J_w from 11.05 LMH to 4.68 LMH and the increasing J_s from 13.07 gMH to 33.97 gMH, with the concentration of acrylamide FS increasing from 200 to 600 g/L. This was because the OP of the FS dramatically increased from 71.49 bar to 187.28 bar with the increasing acrylamide FS from 200 to 600 g/L, and the resulting driving force of the OP difference between feed and draw solutions significantly decreased from 342.32 bar to 226.53 bar at the initial operation. Moreover, the high salt permeability at the high osmotic FS may be related to a weakened Donnan potential in the negatively charged polyamide surfaces (Bartels et al., 2005).

The SRSF (J_s/J_w) value presents an increasing trend with the increasing acrylamide FS and MgCl_2 DS (Figure 5C). For example, the SRSF (J_s/J_w) value obviously increased from 0.38 g/L to 4.24 g/L with the increasing acrylamide concentration from 200 to 600 g/L when employing 4 M MgCl_2 DS. In addition, with the same acrylamide FS, the SRSF (J_s/J_w) value was higher employing a 5 M MgCl_2 than that employing 4 M MgCl_2 as DS. These results illustrate that both the loss of draw solutes and the ICP of the AL-FS operation were aggravated with the increasing concentration of feed and draw solutions. This is due to the decreased diffusion rate of salt solutes and increased salt passage in the TFC membrane with the increasing concentrations of DS and FS (Bartels et al., 2005; Song et al., 2011).

All of these results demonstrate that the concentrations of both FS and DS significantly affect the water flux and reverse salt flux and thus impact the long-term FO operation efficiency and the quality of the concentrated acrylamide product.

TABLE 1 Evaluation of FO performances in multi- and single-stage acrylamide (AAM) concentrations.

Multi-stage				
AAM concentration (g/L)	200~300	300~400	400~500	500~600
Stage no.	1	2	3	4
Initial flux (LMH)	11.06	8.89	6.75	6.07
Final flux (LMH)	6.83	5.57	4.03	3.03
Flux decline ratio (%)	38.23	37.29	40.30	50.11
Average flux (LMH)	8.94	7.23	5.39	4.54
Concentration time (h)	18.58	11.59	9.28	7.45
Single-stage			Improvements	
AAM concentration (g/L)	200~300	300~400	(Multi/single, Stage II)	
Average flux (LMH)	9.04	5.99	Flux increment (%)	14.61
Concentration time (h)	18.36	14.03	Time decrement (%)	13.91

3.5 Long-term performance of the TFC membrane during the concentration of acrylamide solution

In order to more highly concentrate the acrylamide FS, the long-term FO process was operated and the long-term performance of FO membrane was investigated. Both 4 M and 5 M MgCl_2 draw solution were used to concentrate the acrylamide solution from 200 g/L to 400 g/L; the final accumulated salt concentration in the acrylamide solution and the operation time were measured as two important parameters to evaluate the FO performance during the concentration of acrylamide solution. Figure 6 shows that the water flux of the FO membrane decreased rapidly in the initial stage and then slowly when the acrylamide solution was concentrated gradually from 200 g/L to 400 g/L. Moreover, the membrane water flux was higher when using 5 M MgCl_2 DS than when using 4 M MgCl_2 solution, while the flux difference between using 5 M and 4 M MgCl_2 DSs became smaller with the increasing acrylamide solution during the concentration process. This is because of the greater dilution for higher concentration of DS when drawing the same amount of water, thus inducing the fast flux decline. In addition, higher concentrations of Mg^{2+} ions may also increase the scale on the membrane surface, possibly aggravating membrane fouling and causing a decrease in flux (Sun et al., 2016; Almoalimi and Liu, 2022). Importantly, it took 32.42 h to concentrate acrylamide solution from 200 g/L to 400 g/L with 5 M MgCl_2 DS, which is much shorter than 48.79 h with 4 M MgCl_2 DS (Figure 6). The accumulated salt in the acrylamide solution was 1.77 g/L when using 5 M MgCl_2 solution as the DS, which is slightly higher than that of 1.74 g/L when using 4 M MgCl_2 solution as the DS. Therefore, considering the FO process efficiency and the quality of concentrated product, 5 M MgCl_2 is a better selection as the DS.

3.6 Concentration of acrylamide solution when operating the FO process in stages

In order to improve the FO efficiency for the concentration of acrylamide solution, a multi-stage operation system was introduced to compensate for the dilution of DS and thus maintain the high flux. Here, the solute of MgCl_2 was supplemented in the DS to remain at 5 M at the end of each stage when the acrylamide concentration was increased by 100 g/L. The results shown in Figure 7 and Table 1 indicate that the concentration efficiency can be effectively improved via multi-stage operation. For example, at the end of Stage I, the declined water flux was 6.83 LMH. By updating the draw concentration to 5 M, the water flux at the beginning of Stage II was increased 18.56% to 8.89 LMH. Additionally, the increased percentages of water flux were 17.52% and 18.43% at the beginning of Stages III and IV, respectively, compared with the water fluxes at the end of Stages II and III. This improved performance was achieved by renewing the draw concentration, demonstrating the efficiency of multi-stage operation and highlighting its potential for real FO applications.

Moreover, the initial flux at each stage decreased gradually with the increase of the acrylamide concentration. For example, the initial water flux dropped significantly from 11.06 LMH (Stage I) to 6.07 LMH (Stage IV), while the initial concentration of acrylamide FS increased from 200 g/L (Stage I) to 500 g/L (Stage IV) and caused the decreased driving force of the FO process. Noticeably, the initial water fluxes at Stages II, III, and IV were very close to the membrane flux (Figure 5B) when operated at the same condition of the FO process but without the accumulative effect from the former stage. In addition, the flux decline percentage at each stage was also calculated to be 38.23% (Stage I), 37.29% (Stage II), 40.30% (Stage III), and 50.11% (Stage IV), respectively (Table 1). This observation further suggests that the flux decline accelerated at the later stage with the concentration increase of acrylamide FS because of the intensified ICP effect at the higher concentration of FS.

The accumulated salt in the final product was considered to be another critical factor for the concentration process of FO. As shown in Figure 7, the accumulated salt in the resultant acrylamide solution increased from 1.5 g/L to 3.7 g/L with an increase in the concentration factor from 1.5 to 3.0 when the acrylamide FS was concentrated from 300 g/L to 600 g/L. The concentration of MgCl_2 in the final concentrated acrylamide solution (600 g/L) was only 3.7 g/L, less than the 0.62 wt% impurity in the product of acrylamide. Additionally, our results also suggest that the concentration of acrylamide solution can be further increased to be higher than 600 g/L since there was approximately 4.69 LMH of flux when 600 g/L acrylamide was used as FS (Figure 5B).

Furthermore, we summarized the FO performances of single- and multi-stage FO processes in Table 1. The results illustrate that the multi-stage process helped increase the average flux and save the concentration time compared with the single-stage FO process during the concentration of acrylamide FS from 200 g/L to 400 g/L. The flux increment and time-saving percentages were up to 14.61% and 13.91%, respectively, relative to the single-stage process. In addition, it took less time for the later stage to increase the acrylamide concentration by 100 g/L because of the decreasing volume of the FS. All results indicate that the multi-stage FO process would be preferred for the chemicals' concentration because of high system efficiency, including high water flux and short operation time.

In comparison to the conventional multi-stage evaporation process (described in US patents US3887425A and US5922912A), the multi-stage FO process presents distinct advantages, including the elimination of high-temperature operations and enhanced concentration efficiency. According to these patents (Munch, 1975; Kambara et al., 1999), the conventional evaporation process typically requires operation at temperatures nearing 100 °C, accompanied by substantial energy consumption. In addition, high temperatures may cause acrylamide to polymerize to form insoluble polymers, reducing product quality. Furthermore, conventional evaporation methods typically achieve concentration limits of approximately 40–50 wt%. In contrast, our multi-stage FO process operates at a significantly lower temperature of 25 °C for the feed liquid, thereby reducing the demand for thermal energy during concentration. Moreover, our multi-stage FO process achieves higher concentrations (up to 600 g/L, equivalent to a mass concentration of 57.58%), surpassing the concentration thresholds necessary for various applications of acrylamide (Zheng et al., 2010).

4 Conclusion

Our work demonstrates that the multi-stage FO process provides an efficient way to concentrate high-osmotic acrylamide solution at room temperature. The high performance TFC polyamide membrane was used in the FO process to concentrate the acrylamide solution from 200 g/L to 600 g/L, and the AL-FS mode was demonstrated to be a more

efficient operation orientation than AL-DS to concentrate a high concentration acrylamide solution (>200 g/L) during the FO process. A measure of 5 M divalent MgCl_2 solution was used as an effective draw solute to provide high OP and suppress the ICP of the TFC membrane with a very low reverse salt flux. The results also illustrate that the multi-stage FO operation could dramatically improve the system efficiency for acrylamide concentration, and the draw concentration renewal at Stage II led to a water flux increase by 14.61% and to a 13.91% saving of concentration time. Moreover, the accumulated MgCl_2 in the final 600 g/L acrylamide solution was below 3.7 g/L, less than 0.62 wt% impurity in the product of acrylamide. Our research demonstrates the great potential of the multi-stage FO process for concentrating high osmotic chemicals with high system efficiency. Further investigation of regenerating draw solution is needed to achieve a sustainable operation of the FO process for scale-up operation, and membrane distillation may provide a facile approach for keeping a constant concentration of the draw solution and maintaining a stable water flux of the FO process. The integrated FO-MD system effectively harnesses the inherent strengths of both processes, enabling the production of highly concentrated acrylamide along with high-purity purified water while also achieving energy savings.

Data availability statement

The original contributions presented in the study are included in the article/Supplementary Material; further inquiries can be directed to the corresponding author.

Author contributions

SH: writing—original draft and methodology. ZZ: formal analysis, methodology, and writing—original draft. XZ: data curation, methodology, and writing—review and editing. XA: data curation and writing—original draft. YH: funding acquisition, resources, and writing—review and editing.

Funding

The author(s) declare that no financial support was received for the research, authorship, and/or publication of this article.

Acknowledgments

The authors gratefully acknowledge the support of the National Natural Science Foundation of China (No. 21978215).

Conflict of interest

The authors declare that the research was conducted in the absence of any commercial or financial relationships that could be construed as a potential conflict of interest.

The author(s) declared that they were an editorial board member of Frontiers, at the time of submission. This had no impact on the peer review process and the final decision.

Publisher's note

All claims expressed in this article are solely those of the authors and do not necessarily represent those of their affiliated organizations, or those of the publisher, the editors and the

reviewers. Any product that may be evaluated in this article, or claim that may be made by its manufacturer, is not guaranteed or endorsed by the publisher.

Supplementary material

The Supplementary Material for this article can be found online at: <https://www.frontiersin.org/articles/10.3389/fmst.2024.1407819/full#supplementary-material>

References

- Al-Kindi, S., Al-Bahry, S., Al-Wahaibi, Y., Taura, U., and Joshi, S. (2022). Partially hydrolyzed polyacrylamide: enhanced oil recovery applications, oil-field produced water pollution, and possible solutions. *Environ. Monit. Assess.* 194 (12), 875. doi:10.1007/s10661-022-10569-9
- Almoalimi, K., and Liu, Y.-Q. (2022). Fouling and cleaning of thin film composite forward osmosis membrane treating municipal wastewater for resource recovery. *Chemosphere* 288, 132507. doi:10.1016/j.chemosphere.2021.132507
- Alshehri, A., and Lai, Z. (2014). Attainability and minimum energy of single-stage membrane and membrane/distillation hybrid processes. *J. Membr. Sci.* 472, 272–280. doi:10.1016/j.memsci.2014.08.056
- Asano, Y., Yasuda, T., Tani, Y., and Yamada, H. (2014). A new enzymatic method of acrylamide production. *Agric. Biol. Chem.* 46 (5), 1183–1189. doi:10.1080/00021369.1982.10865240
- Bartels, C., Franks, R., Rybar, S., Schierach, M., and Wilf, M. (2005). The effect of feed ionic strength on salt passage through reverse osmosis membranes. *Desalination* 184 (1–3), 185–195. doi:10.1016/j.desal.2005.04.032
- Braun, O., Coquery, C., Kieffer, J., Blondel, F., Favero, C., Besset, C., et al. (2022). Spotlight on the life cycle of acrylamide-based polymers supporting reductions in environmental footprint: review and recent advances. *Molecules* 27 (1), 42. doi:10.3390/molecules27010042
- Chekli, L., Phuntsho, S., Kim, J. E., Kim, J., Choi, J. Y., Choi, J.-S., et al. (2016). A comprehensive review of hybrid forward osmosis systems: performance, applications and future prospects. *J. Membr. Sci.* 497, 430–449. doi:10.1016/j.memsci.2015.09.041
- Giagnorio, M., Morciano, M., Zhang, W., Hélix-Nielsen, C., Fasano, M., and Tiraferri, A. (2022). Coupling of forward osmosis with desalination technologies: system-scale analysis at the water-energy nexus. *Desalination* 543, 116083. doi:10.1016/j.desal.2022.116083
- Han, G., Zhang, S., Li, X., Widjojo, N., and Chung, T.-S. (2012). Thin film composite forward osmosis membranes based on polydopamine modified polysulfone substrates with enhancements in both water flux and salt rejection. *Chem. Eng. Sci.* 80, 219–231. doi:10.1016/j.ces.2012.05.033
- Hancock, N. T., and Cath, T. Y. (2009). Solute coupled diffusion in osmotically driven membrane processes. *Environ. Sci. Technol.* 43 (17), 6769–6775. doi:10.1021/es901132x
- Hao, S., Wang, J., Wang, Z., An, X., Liu, T., Qin, Y., et al. (2023a). Impact of hPG molecular size on the separation properties and antifouling performance of hPG-modified thin-film composite nanofiltration membrane. *Desalination* 548, 116296. doi:10.1016/j.desal.2022.116296
- Hao, S., Xiao, J., Liu, L., Qin, Y., Li, S., and Hu, Y. (2023b). High flux and highly fouling-resistant polyamide reverse osmosis membrane having inner and outer zwitterion-like layers. *Desalination* 565, 116823. doi:10.1016/j.desal.2023.116823
- Hu, Y. (2023). Grand challenge in membrane applications: liquid. *Front. Membr. Sci. Technol.* 2, 1177528. doi:10.3389/fmst.2023.1177528
- Ibraheem, B. M., Aani, S. A., Alsarayreh, A. A., Alsalihi, Q. F., and Salih, I. K. (2023). Forward osmosis membrane: review of fabrication, modification, challenges and potential. *Membranes* 13 (4), 379. doi:10.3390/membranes13040379
- James Munch, R. (1975) *Concentrating acrylamide solutions*. United States Patent, US3887425.
- Kambara, Y., Matsumura, M., Umeno, M., Uehara, Y., and Asao, K. (1999). Concentration method of aqueous acrylamide solution. *U.S. Pat. Appl.* 5 (922), 912.
- Lee, C. Y., Hwang, Y. B., and Chang, H. N. (1991). Acrylonitrile adaptation of *Brevibacterium* sp. CH1 for increased acrylamide production. *Enzyme Microb. Technol.* 13 (1), 53–58. doi:10.1016/0141-0229(91)90188-g
- Li, J., Guo, M., Jiao, S., Wang, Y., Luo, G., and Yu, H. (2017). A kinetic study of the biological catalytic hydration of acrylonitrile to acrylamide. *Chem. Eng. J.* 317, 699–706. doi:10.1016/j.cej.2017.02.100
- Lin, S., and Elimelech, M. (2015). Staged reverse osmosis operation: configurations, energy efficiency, and application potential. *Desalination* 366, 9–14. doi:10.1016/j.desal.2015.02.043
- Liu, X., Wu, J., Liu, C., and Wang, J. (2017). Removal of cobalt ions from aqueous solution by forward osmosis. *Sep. Purif. Technol.* 177, 8–20. doi:10.1016/j.seppur.2016.12.025
- Liu, Z., and Hu, Y. (2016). Sustainable antibiofouling properties of thin film composite forward osmosis membrane with rechargeable silver nanoparticles loading. *ACS Appl. Mater. Interfaces* 8 (33), 21666–21673. doi:10.1021/acsami.6b06727
- Long, Q., Qi, G., and Wang, Y. (2016). Evaluation of renewable gluconate salts as draw solutes in forward osmosis process. *ACS Sustain. Chem. Eng.* 4 (1), 85–93. doi:10.1021/acsschemeng.5b00784
- McGinnis, R. L., and Elimelech, M. (2007). Energy requirements of ammonia–carbon dioxide forward osmosis desalination. *Desalination* 207 (1–3), 370–382. doi:10.1016/j.desal.2006.08.012
- Munch, R. J. (1975). Concentrating acrylamide solutions. *U.S. Pat. Appl.* 3 (887), 425.
- Nagasawa, T., Shimizu, H., and Yamada, H. (1993). The superiority of the third-generation catalyst, *Rhodococcus rhodochrous* J1 nitrile hydratase, for industrial production of acrylamide. *Appl. Microbiol. Biotechnol.* 40 (2–3). doi:10.1007/bf00170364
- Nath, A., and Pande, P. P. (2020). Polyacrylamide based polymers: smart materials used in wastewater treatment. *Adv. Sci. Eng. Med.* 12 (1), 105–107. doi:10.1166/asem.2020.2531
- Ogata, N. (1960). The transition polymerization of acrylamide. I. On the polymerization condition and the property of polymer. *Bull. Chem. Soc. Jpn.* 33 (7), 906–912. doi:10.1246/bcsj.33.906
- Raj, J., Prasad, S., and Bhalla, T. C. (2006). *Rhodococcus rhodochrous* PA-34: a potential biocatalyst for acrylamide synthesis. *Process Biochem.* 41 (6), 1359–1363. doi:10.1016/j.procbio.2006.01.022
- Rastogi, N. K. (2016). Opportunities and challenges in application of forward osmosis in food processing. *Crit. Rev. Food Sci. Nutr.* 56 (2), 266–291. doi:10.1080/10408398.2012.724734
- Seybold, C. A. (2008). Polyacrylamide review: soil conditioning and environmental fate. *Commun. Soil Sci. Plant Analysis* 25 (11–12), 2171–2185. doi:10.1080/00103629409369180
- She, Q., Wang, R., Fane, A. G., and Tang, C. Y. (2016). Membrane fouling in osmotically driven membrane processes: a review. *J. Membr. Sci.* 499, 201–233. doi:10.1016/j.memsci.2015.10.040
- Smith, E. A., and Oehme, F. W. (1991). Acrylamide and polyacrylamide: a review of production, use, environmental fate and neurotoxicity. *Rev. Environ. Health* 9 (4), 215–228. doi:10.1515/reveh.1991.9.4.215
- Song, X., Liu, Z., and Sun, D. D. (2011). Nano gives the answer: breaking the bottleneck of internal concentration polarization with a nanofiber composite forward osmosis membrane for a high water production rate. *Adv. Mater.* 23 (29), 3256–3260. doi:10.1002/adma.201100510
- Sun, Y., Tian, J., Zhao, Z., Shi, W., Liu, D., and Cui, F. (2016). Membrane fouling of forward osmosis (FO) membrane for municipal wastewater treatment: a comparison between direct FO and OMBR. *Water Res.* 104, 330–339. doi:10.1016/j.watres.2016.08.039
- Sun, Y., Xue, L., Zhang, Y., Zhao, X., Huang, Y., and Du, X. (2014). High flux polyamide thin film composite forward osmosis membranes prepared from porous substrates made of polysulfone and polyethersulfone blends. *Desalination* 336, 72–79. doi:10.1016/j.desal.2013.12.036
- Tian, M., Qiu, C., Liao, Y., Chou, S., and Wang, R. (2013). Preparation of polyamide thin film composite forward osmosis membranes using electrospun polyvinylidene fluoride (PVDF) nanofibers as substrates. *Sep. Purif. Technol.* 118, 727–736. doi:10.1016/j.seppur.2013.08.021
- Tiraferri, A., Yip, N. Y., Straub, A. P., Romero-Vargas Castrillon, S., and Elimelech, M. (2013). A method for the simultaneous determination of transport and structural parameters of forward osmosis membranes. *J. Membr. Sci.* 444, 523–538. doi:10.1016/j.memsci.2013.05.023

- Truong, V.-H., and Chong, T. H. (2024). Development of a diafiltration-nanofiltration-reverse osmosis (DiaNF-RO) process for ion fractionation towards resource recovery in seawater desalination. *Desalination* 583, 117684. doi:10.1016/j.desal.2024.117684
- Wade, N. M. (1993). Technical and economic evaluation of distillation and reverse osmosis desalination processes. *Desalination* 93 (1-3), 343–363. doi:10.1016/0011-9164(93)80113-2
- Watanabe, I. (1982). Process for the production of acrylamide using microorganism. *U. S. Pat.*, US4343900.
- Watanabe, I., Ogawa, Y., and Seki, S. (1989). Method for producing acrylamide using a microorganism. *U. S. Pat.*, US4851342.
- Xudong, S., Yue, S., Huimin, Y., and Zhongyao, S. (2004). Bioconversion of acrylonitrile to acrylamide using hollow-fiber membrane bioreactor system. *Biochem. Eng. J.* 18 (3), 239–243. doi:10.1016/j.bej.2003.09.001
- Yip, N. Y., Tiraferri, A., Phillip, W. A., Schiffman, J. D., and Elimelech, M. (2010). High performance thin-film composite forward osmosis membrane. *Environ. Sci. Technol.* 44 (10), 3812–3818. doi:10.1021/es1002555
- Zhang, K., An, X., Bai, Y., Shen, C., Jiang, Y., and Hu, Y. (2021). Exploration of food preservatives as draw solutes in the forward osmosis process for juice concentration. *J. Membr. Sci.* 635, 119495. doi:10.1016/j.memsci.2021.119495
- Zhao, S., Zou, L., Tang, C. Y., and Mulcahy, D. (2012). Recent developments in forward osmosis: opportunities and challenges. *J. Membr. Sci.* 396, 1–21. doi:10.1016/j.memsci.2011.12.023
- Zheng, R.-C., Zheng, Y.-G., and Shen, Y.-C. (2010). “Acrylamide, microbial production by nitrile hydratase,” in *Encyclopedia of industrial Biotechnology*, 1–39.
- Zhu, A., Christofides, P. D., and Cohen, Y. (2009). Effect of thermodynamic restriction on energy cost optimization of RO membrane water desalination. *Industrial Eng. Chem. Res.* 48 (13), 6010–6021. doi:10.1021/ie800735q

Frontiers in Membrane Science and Technology

Forging new directions in synthetic membrane technology

An interdisciplinary journal at the interface of materials science and engineering, helping provide effective solutions to numerous modern challenges from waste water management to clean energy production.

Discover the latest Research Topics

[See more →](#)

Frontiers

Avenue du Tribunal-Fédéral 34
1005 Lausanne, Switzerland
frontiersin.org

Contact us

+41 (0)21 510 17 00
frontiersin.org/about/contact

